THE UNIVERSITY OF QUEENSLAND

AUSTRALIA

Statistical Methods and Their Applications to Rock Mechanics Problems at Scale: Factor of Safety and Probability of Failure

Aidan Ford

BEng (Mining), University of New South Wales, 2010

GradDip (Maths), Charles Sturt University, 2013

A thesis submitted for the degree of Doctor of Philosophy at

The University of Queensland in 2019

School of Civil Engineering

Abstract

The stability of rock slopes in Mining and Civil Engineering structures is typically analysed using either a Factor of Safety or a Probability of Failure method. These methods represent different assessments of the same slope stability problem, and there is currently no reliable industry-accepted method to convert a Factor of Safety to a Probability of Failure, and vice-versa, for rock slopes. Relationships between these two design philosophies are numerous in the geotechnical literature; however, these relationships typically rely on restrictive assumptions or are only applicable to a single slope failure mode. The incorporation of scale effects when considering the relationship between Factor of Safety and Probability of Failure is typically absent or it is implicitly incorporated into an empirical strength relationship. The main focus of this Thesis is to explore the relationships between Factor of Safety, Probability of Failure and problem scale for rock slopes.

After the completion of an initial literature review, it was apparent that there were several limitations in practical stability analysis, preventing the formulation of a Factor of Safety versus Probability of Failure relationship for rock slopes. Engineers are free to choose any defendable value for each relevant rock material parameter, which can create inconsistent Factors of Safety. Engineers are also free to choose how they wish to define the probabilistic behaviour of each relevant material parameter. These probabilistic descriptions are often poorly justified, rely on matching Probability Density Functions from the literature, or are based on simple assumptions such as a normal distribution. The choice of Probability Density Functions determines the calculated Probability of Failure and if incorrectly specified, unrealistic Probability of Failure can result. When scale considerations are included, the Factor of Safety versus Probability of Failure problem becomes even less well understood, with very few studies even considering the probabilistic behaviour of rock at scale, in any meaningful detail.

With these identified inconsistencies in both deterministic and probabilistic rock material parameter selection, it is highly unlikely that a usable relationship between Factor of Safety and Probability of Failure can be obtained using current industry practices, let alone considering scale effects. In order to achieve a usable relationship between Factor of Safety and Probability of Failure, including scale effects, further research is required to explore deterministic material parameter selection criteria, probabilistic material parameter selection criteria, and an appreciation of probabilistic and deterministic descriptions of material parameters at increased scales.

In order to select meaningful and consistent inputs for both Factor of Safety and Probability of Failure analyses, a greater appreciation of the intrinsic variability of rock material parameters is required. The ideal solution is to have a set of equations that can adequately describe the Probability Density Function of any material parameter from a geotechnical database, which then provides guidance as to how to complete deterministic and probabilistic analyses, including scale. With consistent selection guidelines, it should be possible to produce a usable relationship between Factor of Safety and Probability of Failure considering scale.

For this standardised approach to be possible, it is necessary to demonstrate that the distribution of rock material parameters can be universally approximated by specific Probability Density Function; that is, rock material parameters are described by Universal Distribution Functions. A similar requirement for scale effects is also required; that is, rock material parameters exhibiting a Universal Scale Function, which describes how deterministic and probabilistic parameters change as a function of problem scale. This scale consistency would then mean that a usable relationship between Factor of Safety and Probability of Failure can include consideration of any scale of interest.

The starting point of this Thesis is to provide sufficient evidence that Universal Distribution Functions are a good approximation at the laboratory scale, and are suitably generalisable to any given rock problem. An assumption-free, non-parametric test methodology is developed in order to test for and estimate this hypothesised universal behaviour. The non-parametric analysis demonstrated that Universal Distribution Functions are an applicable probabilistic model for laboratory-scale rock material parameters and demonstrated that material parameters exhibit consistent and universal correlation coefficients. The number of test samples required to achieve a desired level of accuracy was then derived for all deterministic and probabilistic rock material parameters described by the Universal Distribution Functions.

The implications of this universal probabilistic behaviour is then explored to provide supplementary evidence of their existence and to demonstrate their wider applications. The universal probabilistic behaviour was able to provide a statistical explanation as to why a linear relationship is obtained between any pair of Uniaxial Compressive Strength, Point Load Testing, and Uniaxial Tensile Strength measurements. While this explanation is able to show the existence of a linear relationship, the derivation does not produce an estimate for the magnitude of the linear relationship. A similar derivation is then used to demonstrate why a non-linear relationship is applicable for Uniaxial Compressive Strength and Young's Modulus values. This statistical description also validates two commonly used deterministic 'downgrading' methods for Uniaxial Compressive Strength, being the

use of the 35th percentile value and 80% of the mean value. The statistical theory also produces a new equation relating sonic velocity measurements to the Uniaxial Compressive Strength of rock. The applicability of this new Sonic Velocity model is compared to site data and showed to have a sufficient goodness of fit.

Due to a lack of available data for rock material parameters at increased scales, the strictly empirically based statistical analysis used to estimate laboratory-scale Universal Distribution Functions was not possible for increased scales. In order to estimate the expected Universal Scale Functions and relevant Universal Distribution Functions at increased scales, PLACEBO (Probabilistic Lagrangian Analysis of Continua with Empirical Bootstrapped Outputs) is purpose developed for this Thesis using Itasca's FLAC3D. PLACEBO is a general purpose numerical homogenisation tool able to probabilistically quantify material parameters of intact rock at arbitrarily large scales, including material nonlinearities and material parameter correlations.

It was demonstrated using PLACEBO that non-zero asymptotic rock material scale behaviours consistent with literature scaling laws are producible from heterogeneous scale analysis. It is noted that the scale response for each material parameter is dependent on input parameters and suggests that scaling laws are not universal, but must be evaluated on a case-by-case basis. The practical implications of this scale-based analysis is applied to the 'minimum shear strength' approach and is able to provide justifiably higher minimum shear strength parameters for rock by considering scale, homogenisation and correlation. Additionally, the heterogeneity of seemingly unrelated rock material parameters is observed to have considerable influence on material parameters at increased scales, and therefore the heterogeneity of all material parameters needs to be included when considering scale-dependant responses.

The probabilistic behaviour of rock material parameters at any scale show consistent and predictable changes, despite having different asymptotic-scale behaviours. Equations for the general distribution, at arbitrary volumes, for dry density and elastic Young's Modulus are also derived based on the findings of this analysis. The variability associated with the peak friction angle, peak cohesion, Uniaxial Compressive Strength and Uniaxial Tensile Strength is remarkably consistent and generally retained their associated Probability Density Functions. However, no generalised scale-dependant description is determined. This scale-invariant probabilistic behaviour meant that generalising the Factor of Safety versus Probability of Failure relationship to consider scale could produce a self-consistent relationship over changing scales of interest.

The uniaxial compressive failure process is observed to transition from strictly brittle failure at small-scale, to a dilatational, friction-hardening, cohesion-softening response at large-scale. A non-linear failure envelope with increasing triaxial stresses is produced from simple linear Mohr Coulomb assumptions, providing further evidence that the failure process of rock at practical scales is not fully represented by simple linear failure criteria. These findings demonstrate that numerical heterogeneous analysis is a powerful and cost-effective alternative to physical testing and is able to quantify emergent failure complexities and material parameter scaling laws governed by material heterogeneity.

Non-parametric statistical analysis is also completed on numerically simulated Fractional Brownian Motion paths to establish a theoretical universal probabilistic model for discontinuity roughness. This probabilistic model is then used to derive the expected scaling laws associated with discontinuity roughness, as well as simple estimates of a discontinuities fractal characteristic using Barton's length amplitude measurements. The theoretical scale behaviour is then compared and contrasted against two different natural discontinuities with measurement scales ranging from 0.05m to 7.5m. The field measurements of discontinuity roughness demonstrated the non-fractal nature of discontinuities over most measured scales, and the inability of the fractal model to produce the observed negative scaling law and associated homogenisation at increasing scales. These findings suggest that a purely fractal self-affine description of discontinuity roughness is not applicable at practical scales.

A new relationship is then derived relating fractal characteristics and Joint Roughness Coefficients. This new relationship was compared against Barton's standard profiles and Bandis' Scaling Law using the available field measurements of roughness, and showed consistency in estimates of the scale dependant Joint Roughness Coefficient up to discontinuity lengths of 7.5m. This comparison with the well tested Bandis Scaling Law demonstrates the applicability and accuracy of this new roughness index, even at very large scales. These findings suggest that even though discontinuities are not completely described by a fractal self-affine model, estimates of the Hurst Exponent are still useful characteristic values for describing roughness at increased scales.

Numerical simulation methods are then implemented using pre-existing mathematical theory in order to derive estimates of cross-joint spacing in bedded rock. The simulated indicated that the distribution of cross-joint spacing at low stress levels should follow an exponential distribution, with a more general model of cross-joint spacing being the gamma distribution.

With a greater appreciation to how rock material parameters change as a function of scale, the issue of the relationship between Factor of Safety and Probability of Failure is revisited. By decomposing each failure mechanism Factor of Safety equation into its individual material parameter components, it is possible to define in closed-form upper and lower bounds for any Factor of Safety versus Probability of Failure relationship for a number of simple to completely generalised problems. It is demonstrated that when considering the particular relationship containing multiple Factor of Safety components, the probability convolutions are not able to be calculated without the use of numerical methods and did not produce a one to one relationship between Factor of Safety and Probability of Failure. This result means that there is no simple relationship that can be proposed to relate a particular Factor of Safety to a Probability of Failure for structured rock at any scale of interest.

The main problematic feature of considering Factor of Safety and Probability of Failure at increased scale is the selection of an appropriate scale of interest, which is currently poorly defined. By changing the scale of interest or how heterogeneity is interpreted, a substantially different Factor of Safety Probability of Safety relationship is obtained for a single problem. This scale of interest problem will need to be studied in detail to determine which Factor of Safety versus Probability of Failure relationship is appropriate to practical designs.

Declaration by author

This thesis is composed of my original work, and contains no material previously published or written by another person except where due reference has been made in the text. I have clearly stated the contribution by others to jointly-authored works that I have included in my thesis.

I have clearly stated the contribution of others to my thesis as a whole, including statistical assistance, survey design, data analysis, significant technical procedures, professional editorial advice, and any other original research work used or reported in my thesis. The content of my thesis is the result of work I have carried out since the commencement of my research higher degree candidature and does not include a substantial part of work that has been submitted to qualify for the award of any other degree or diploma in any university or other tertiary institution. I have clearly stated which parts of my thesis, if any, have been submitted to qualify for another award.

I acknowledge that an electronic copy of my thesis must be lodged with the University Library and, subject to the policy and procedures of The University of Queensland, the thesis be made available for research and study in accordance with the Copyright Act 1968 unless a period of embargo has been approved by the Dean of the Graduate School.

I acknowledge that copyright of all material contained in my thesis resides with the copyright holder(s) of that material. Where appropriate I have obtained copyright permission from the copyright holder to reproduce material in this thesis.

Publications during candidature

Publications are in preparation.

Publications included in this thesis

No publications included.

Contributions by others to the thesis

No contributions by others.

Statement of parts of the thesis submitted to qualify for the award of another degree

None.

Research involving human or animal subjects

No animal or human subjects were involved in this research.

Acknowledgements

This Thesis was carried out remotely from The University of Queensland (UQ), and was entirely the work of the author. There were changes to my UQ supervisory team during the course of the Thesis, due to the departure of my initial Principal Advisor Professor Marc Ruest. He was replaced by Professor David Williams, who was joined by Dr Alan Huang. I wish to acknowledge Professor Ruest for his useful discussions on the Thesis, and Professor Williams for taking on the role of Principal Advisor, despite the topic not being his specialty, and Dr Huang for his useful comments on statistical aspects of the Thesis.

Financial support

This research was supported by a Research Higher Degree Schollarship.

Keywords

Factor of safety, fractals, heterogeneity, probability of failure, rock material parameters, rock mechanics, scaling laws, statistics, stochastic methods

Australian and New Zealand Standard Research Classifications (ANZSRC)

ANZSRC code: 091402, Geomechanics and Resources Geotechnical Engineering, 100%

Fields of Research (FoR) Classification

FoR code: 0914, Resources Engineering and Extractive Metallurgy, 100%

Table of Contents

List of Figures

List of Tables

List of Abbreviations

CDF	Cumulative Distribution Function
EDF	Empirical Distribution Function
FOS	Factor of Safety
KS	Kolmogorov Smirnov goodness of fit
KW ANOVA	Kruskal Wallis Analysis of Variance
MAD	Median Absolute Deviation
PDF	Probability Density Function
PLACEBO	Probabilistic Lagrangian Analysis of Continua with Empirical Bootstrapped Outputs
PLT	Point Load Index Test
POF	Probability of Failure
RVE	Representative Volume Element
SRF	Strength Reduction Factor
UCS	Uniaxial Compressive Strength
UDF	Universal Distribution Function
USF	Universal Scale Function
UTS	Uniaxial Tensile Strength

Thesis Overview

This section gives an overview of the individual Chapters and their contained knowledge. This Thesis has four key research focuses (Chapter Two through to Chapter Five) with each Chapter addressing an industry limitation identified during the initial literature review. A breakdown of each Chapter and the information contained is shown below.

Chapter One

Chapter One provides a general overview to the original aims of this Thesis, as well as the relevant literature review. The main literature topics covered in this Chapter include:

- how Factor of Safety is defined and calculated;
- how Probability of Failure is defined and calculated;
- how rock material parameters are treated as random variables in literature; and
- how rock and rock discontinuities change as a function of scale

Chapter One concludes with several examples highlighting the current industry limitations identified during the literature review. Chapter One also presents in detail the research methodology used for each proceeding Chapter.

Chapter Two

Chapter Two is the first of the key research Chapters. This Chapter covers the non-parametric statistical analysis providing sufficient evidence for the existence of Universal Distribution Functions. The Chapter then continues onto exploring the implications and predictions that can be made using these Universal Distribution Functions. These predictions are then compared to published findings, or are compared to laboratory data. This additional analysis is included in this Chapter to provide supplementary evidence that Universal Distribution Functions are valuable constructions with a wide range of applications. An example of how to use Universal Distribution Functions is also included in this Chapter.

Chapter Three

Chapter Three is the second key research Chapter and builds on the previous Chapter. The main focus is to extend the theory presented in Chapter two to larger problem scales. The Chapter initially describes the functionality, assumptions and measurement routines for The Probabilistic Lagrangian Analysis of Continua with Empirical Bootstrapped Outputs (PLACEBO). PLACEBO is the numerical homogenisation tool used to measure material parameters at increased scales.

The Chapter then presents the output for a number of synthetic rock types generated and measured using PLACEBO. Non-parametric statistics are used to understand the changes to material parameter variability at different scales. Comparisons to previous literature findings are also presented where possible. The Chapter concludes with a practical example for how PLACEBO can aid in selecting conservative shear strength parameters that are much stronger than typical conservative selection methods.

Chapter Four

Chapter Four is the third key research Chapter and relates to the analysis for rock discontinuities. There are three sub-focuses in this Chapter:

- deriving the probabilistic model and scaling laws for rough discontinuities using a fractal model;
- comparing the fractal model to field measurements for validation; and
- using numerical methods to estimate the probabilistic behaviour of cross joints in bedded rock.

This Chapter uses non-parametric statistics as the main tool for assessment. Where possible, comparisons are made to other results and relationships from literature.

Chapter Five

Chapter Five builds on the main findings from Chapter two, three and four and revisits the relationship between Factor of Safety and Probability of Failure. This Chapter presents the mathematical derivation and numerical validation of the closed form relationships between Factor of Safety and Probability of Failure at any scale for rock slopes. Special cases that can be derived in closed form are also presented and numerically validated.

Chapter Six

Chapter Six presents a summary of the main conclusions for each Chapter in this Thesis. This Chapter also presents the significant contributions made in the field of Rock Mechanics. Possible future research topics are also included in this Chapter based on the findings of this Thesis. No new information is presented in this Chapter.

1 Factor of Safety and Probability of Failure

The appropriate design of rock slopes in Mining and Civil Engineering structures is of major importance for the safety of people and equipment, as well as the general project risk. Rock slopes are typically designed using either a Factor of Safety or Probability of Failure method. These methods represent different assessments of the same stability problem, yet there is currently no reliable industry wide method to convert a Factor of Safety to a Probability of Failure and for rock slopes. Relationships between these two design philosophies are numerous in the geotechnical literature; however, these relationships typically rely on restrictive assumptions or are only applicable to a single failure mode. The incorporation of scale effects when considering the relationship between Factor of Safety and Probability of Failure is typically absent, or it is implicitly incorporated into an empirical strength relationship.

The main focus of this Thesis is to explore the relationships between Factor of Safety, Probability of Failure and problem scale for rock slopes. The findings of this more generalised relationship between Factor of Safety and Probability of Failure will be highly beneficial for open pit geomechanics, as it allows for:

- more accurate analysis of large scale failure mechanisms;
- complete transparency for the conversion between any Factor of Safety and Probability of Failure;
- provide consistency for future mining operations and rock mechanics problems;
- risk analysis relating to Factor of Safety values;
- removal of overly conservative design practices and
- reduces analysis time, as the Probability of Failure does not require direct calculation.

Prior to delving too far into this Thesis, it is important to understand what exactly these two design principals are and how they are currently applied to practical applications. From this initial literature review, a research direction and overall methodology can be determined based on current industry limitations.

1.1 Defining Factor of Safety

The concept of using a Factor of Safety (FOS) is one of the simplest design methods taught to engineering students during their first years of study. The actual wording of the FOS definition does vary between sources, but it is typically defined as a ratio involving strength and stress, or forces. Whitman (1984) defines FOS as the ratio of the allowable Capacity C to the calculated demand D i.e.:

$$FOS = \frac{C}{D} \qquad \text{Equation 1}$$

Equation 1 is the preferred FOS formulation when dealing with simple hand calculations. Some numerical approaches find Equation 1 difficult to implement so a Strength Reduction Factor (SRF) formulation may often be used as a substitute (Sharma & Pande 1988). The SRF is defined as the value that the shear strength parameters along a specified slip surface must be reduced to bring the rock mass to a state of limiting equilibrium. For a linear Mohr Coulomb criterion, this is given by:

$$\tau = \frac{c'}{SRF} + \sigma_n \frac{\tan \phi'}{SRF} \qquad \text{Equation 2}$$

Where τ is the acting shear stress (Pa), c' is the effective cohesive stress (Pa), σ_n is the acting normal stress (Pa) and ϕ' is the effective friction angle. It is accepted that a FOS or SRF less than one describes an unstable or failed system, a FOS or SRF greater than one described a stable system and a FOS or SRF equal to one describes a system in static equilibrium.

As the calculation of FOS or SRF is deterministic in nature, representative strength parameters need to be initially selected. For example, to use Equation 2, an initial value for c' and ϕ' need to be chosen, and hence some defensible selection must be made. Hoek and Bray (1981) recommend using a conservative estimate for each Strength parameter, however they do not provide explicit guidelines on what constitutes a conservative choice.

Deterministic estimates need to be representative of the design material with minimal excessive economic implications or over conservatism. It has been noted in literature that an overly conservative System Strength parameter selection can have a considerable economic impact on a project with no overall benefit (Terbrugge, Wesseloo, Venter & Steffens 2006) and therefore should be carefully selected to produce a reasonable estimate of the system stability with minimum excessive economic implications. The implications of having multiple selection criteria for deterministic analysis are further elaborated on in Section 1.6.1.

The System Stress components in Equation 1 are calculated on a case by case basis, and relate to the loading configuration associated with a design's geometry and boundary conditions (Sharma & Pande 1988). These System Stress relationships and overall FOS equations for various rock slope failure mechanisms are presented in the following section.

1.2 Factor of Safety Equations for Structured Rock

Rock slopes in practice are seldom comprised of intact rock. Rock often contains fractures, joints, discontinuities, faults or shears which can influence the strength and mechanical parameters of the rock mass. These features, which can collectively be defined as structures, will typically govern the overall rock slope stability. The FOS equations for rock slopes are based on simple kinematics involving these structures and are typically expressed in closed form for each possible failure mechanism.

There are three main failure mechanisms governing rock slope stability; namely, Planar Failure, Toppling Failure and Intact or Circular Failure. Each failure mechanism has a number of particular Failure Cases, which include terms for particular System Strength components. This section presents and elaborates on the closed form or analytical solution for the FOS of each failure mechanism and their main associated Failure Cases.

Practical applications will typically simplify each failure mechanisms and Failure Cases to a two dimensional problem, or a representative one meter section in the third direction (in or out of the bench). The influence of end conditions in the third direction is assumed negligible in these simplified analyses. Most FOS equations require that a failure criterion be assumed in order to calculate the overall System Strength contributions. Although the assumed failure criterion may be arbitrarily chosen, the Mohr Coulomb failure criterion is commonly used as a simple general analysis criterion. The FOS equations in this Section are typically formulated in terms of the Mohr Coulomb failure criterion, but can be easily modified to accommodate any failure criterion of interest.

1.2.1 Planar Failure mechanisms

Planar Failure is characterised by rock mass movement occurring along a pre-existing discontinuity such as a joint, a fault or some planar zone of weakness. An example Planar Failure is shown in Figure 1.

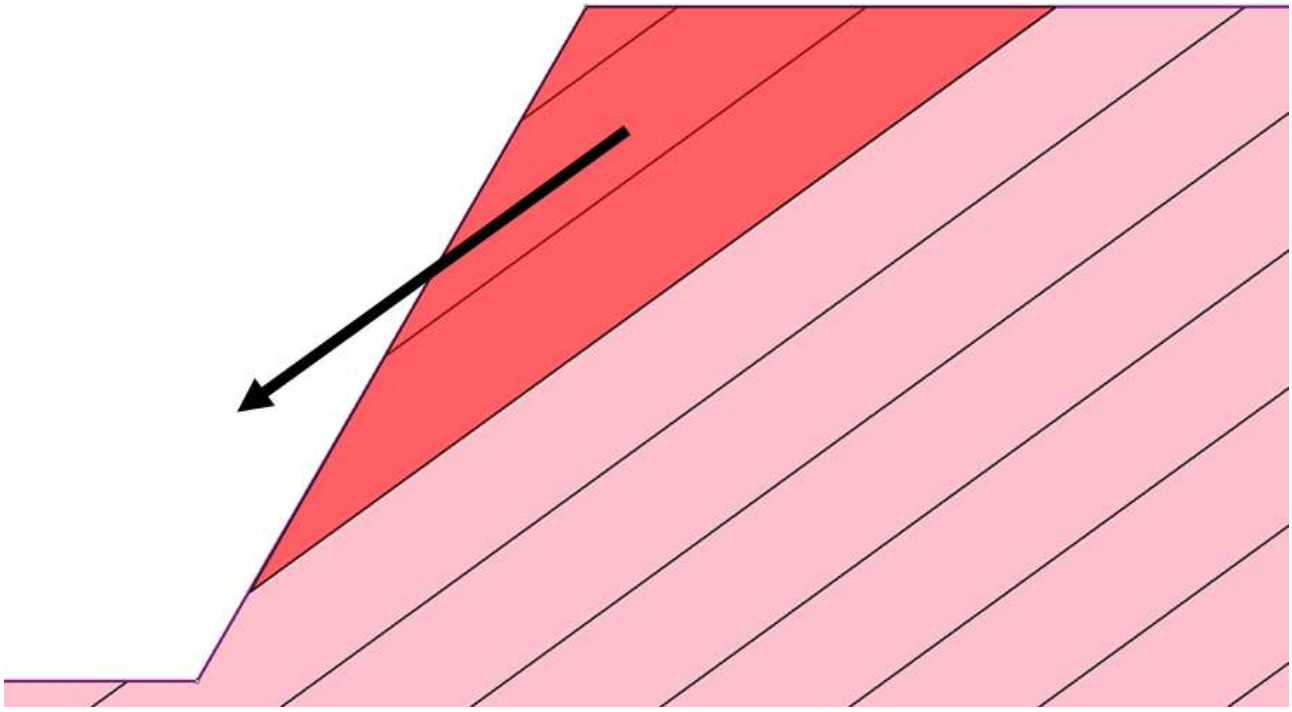

Figure 1 Example of Case 1 Planar Failure

Planar Failure additionally assumes that the rock mass is rigid and unable to deform, the forces applied to the rock mass act through the centroid and the contact area and forces remain constant. Depending on local geological conditions, planar failure can be separated into four unique cases.

Case 1 Planar Failure is defined as sliding failure occurring along a single continuous day lighting discontinuity with no intact failure occurring. If the influence of the discontinuity cohesion can be ignored, the FOS for Case 1 Planar Failure can be calculated using Equation 3:

$$FOS = \frac{\tan \phi}{\tan \theta} \qquad \text{Equation 3}$$

where θ is the apparent dip of the failure surface (˚) and ϕ is the friction angle of the discontinuity (˚). When considering a discontinuity with both cohesion and frictional components, the FOS equation for Case 1 Planar Failure is given by (Wyllie & Mah 2004):

$$FOS = \frac{cA + W\cos\theta\tan\phi}{W\ \sin\theta} \qquad \text{Equation 4}$$

where c is the discontinuity cohesion (Pa), A is the area of the cohesive surface (m²) and W is the weight of the mobile rock mass (N).

One complication that arises when trying to implement Equation 4 is in the physical interpretation and quantification of discontinuity cohesion. An alternate approach of evaluating Case 1 Planar Failure is to use the shear strength criterion presented by Barton and Choubey (1977), which was later extended to consider scale effects (Bandis, Lumsden & Barton 1981).

The Barton Bandis shear strength criterion is an empirically derived non-linear shear strength envelope that includes considerations for discontinuity roughness, infill, rock strength and discontinuity scale. The most recent version of the Barton Bandis shear strength criterion is given by Equation 5 (Bandis, Lumsden & Barton 1981):

$$\tau = \sigma'_n \tan\left(\phi_r + JRC_n \log_{10}\left(\frac{JCS_n}{\sigma'_n}\right)\right) \qquad \text{Equation 5}$$

where τ is the shear strength (Pa), σ'_n is the effective normal stress acting on the discontinuity (Pa), ϕ_r is the residual friction angle of the discontinuity after a significant amount of shearing, JRC_n is the scale dependant Joint Roughness Coefficient (0 to 20) and JCS_n is the scale dependant Joint Wall Compressive Strength (Pa). All parameters in Equation 5 can be estimated through various practical methods, with a summary presented in Table 1.

Table 1 Barton Bandis shear strength parameter estimation guidelines

Model parameter	Calculation method	Scale correction	Scale correction equation
σ'_n	Calculated from problem geometry and pore water pressure	N/A	-
JRC_0	Tilt tests to measure the tilt angle α; The amplitude-length method; Visual estimates from profile charts.	JRC_n	$JRC_n = JRC_0 \left(\frac{L_n}{L_0}\right)^{-0.02JRC_0}$
JCS_0	Field or laboratory measurements using a Schmidt hammer; JCS_0 is equal to the Unconfined Compressive Strength if the joint is unweathered; JCS_0 is reduced for weathered joints. It may reduce to 1/4 the Unconfined Compressive Strength.	JCS_n	$JCS_n = JCS_0 \left(\frac{L_n}{L_0}\right)^{-0.03JRC_0}$
ϕ_r	Direct shear tests results; Estimated using basic friction angle and Schmidt hammer measurements.	N/A	-

In Table 1, the subscript 0 denotes the reference scale of each field measurement, n refers to the scale of interest and L is the discontinuity length. More detail surrounding how each Barton Bandis parameter is calculated, as well as a detailed description of their conception can be found in a number of references, with a recent summation presented in Barton (2013). The FOS equation for Case 1 Planar Failure, using the Barton Bandis shear criterion is given by:

$$FOS = \frac{\sigma'_n \tan\left(\phi_r + JRC_n \log_{10}\left(\frac{JCS_n}{\sigma'_n}\right)\right)}{\tau_{active}} \qquad \text{Equation 6}$$

where τ_{active} is the shear stress acting on the plane of failure (Pa). τ_{active} can be estimated using Equation 7:

$$\tau_{active} = \frac{W \sin\theta}{A} \qquad \text{Equation 7}$$

When applying the scale corrections shown in Table 1, it is recommended that L_n be chosen equal to the in-situ block size to account for the increased shear strength associated with the rotational and interlocking potential of closely jointed rock (Bandis, Lumsden & Barton 1981).

Case 2 Planar Failure is defined as failure that occurs as a combination of planar sliding and mode II fracture parallel to the direction of shear. An example of Case 2 Planar Failure is shown in Figure 2

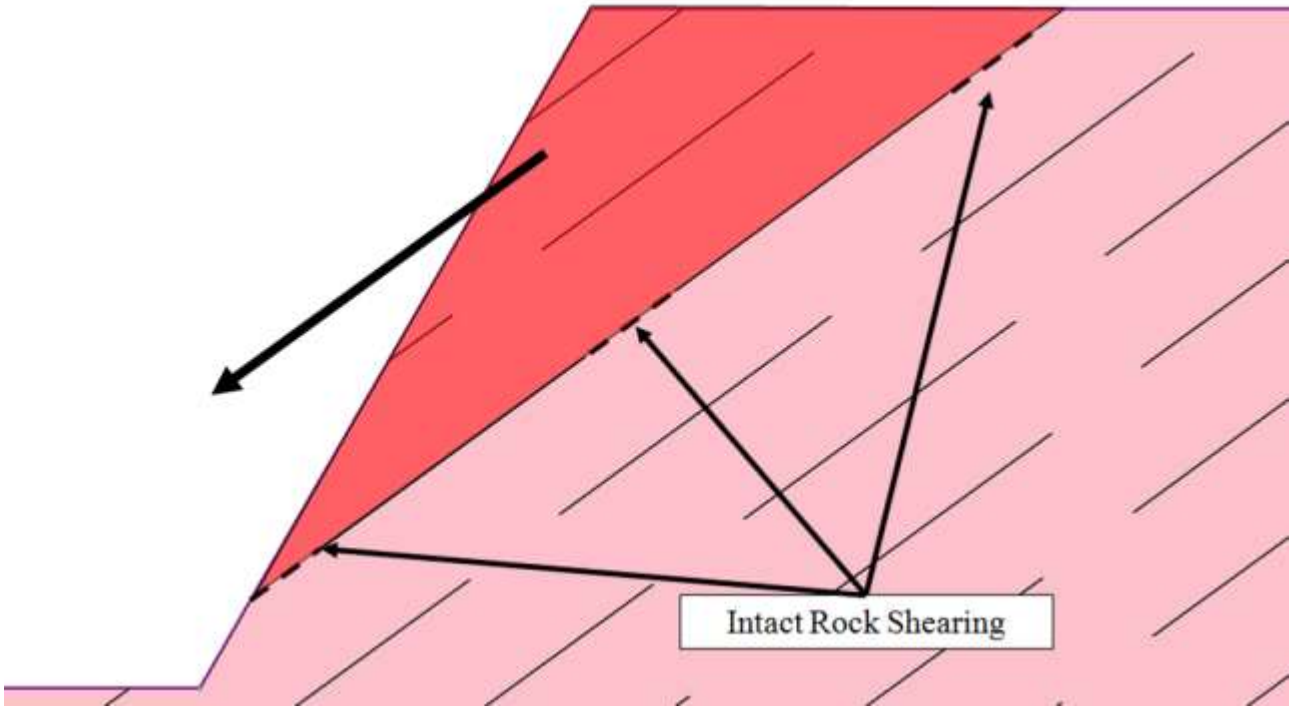

Figure 2 Example of Case 2 Planar Failure

When discontinuous joints are present within a rock mass, the variable k can be used to quantify the joint persistence (Einstein *et al* 1983):

$$k = \frac{\sum Joint\ Length}{\sum Joint\ Length + \sum Bridge\ Length} \qquad \text{Equation 8}$$

By consideration of Equation 8, k must be greater than zero and less than or equal to one. The FOS equation for Case 2 Planar Failure is obtained by modifying Equation 4 to produce Equation 9 (Einstein *et al* 1983):

$$FOS = \frac{\left[(1-k)c_i + kc_j\right]A + (W\ \cos\theta)\left[(1-k)\tan\phi_i + k\tan\phi_j\right]}{W\ \sin\theta} \qquad \text{Equation 9}$$

With the subscript j referring to the joint parameters and i referring to the intact or bridge parameters. In practice the value of k is difficult to accurately measure so some common practical approaches are to assume joints are infinitely continuous, or have some very conservative value such as $k = 0.95$.

Case 3 Planar Failure is defined as failure that occurs as a combination of shearing and mode I fracture between adjacent discontinuous joints. The direction of tensile fracturing in Case 3 Planar Failure needs to be assumed, with two reasonable assumptions being perpendicular to the major induced stress (perpendicular to the slope wall) or vertical. Figure 3 shows an example of Case 3 Planar failure with vertical tensile fracturing.

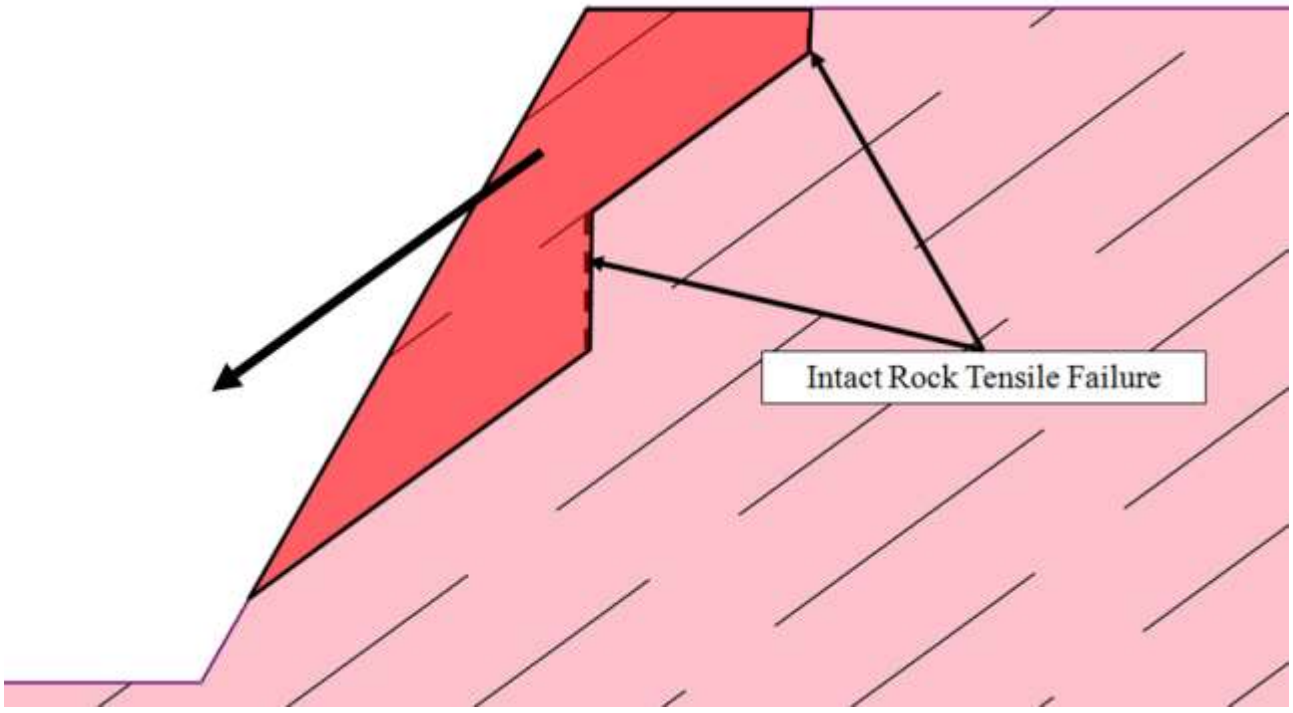

Figure 3 Example Case 3 Planar Failure. Vertical Tensile fractures Shown

When the direction of tensile failure is assumed perpendicular to the major induced stress, the FOS equation for Case 3 Planar Failure is given as (Einstein *et al* 1983):

$$FOS = \frac{c_j A' \cos(\beta - \theta) + \sigma_t A' \sin(\beta - \theta) + W \cos\beta \tan\phi_j}{W \sin\beta} \qquad \text{Equation 10}$$

where β is the apparent angle of sliding of the failed block (˚), σ_t is the tensile strength of the intact rock (Pa) and A' is the equivalent failure length (m). When the direction of tensile failure is assumed vertical, the FOS equation for Case 3 Planar Failure is given as:

$$FOS = \frac{c_j A \cos\beta + \sigma_t A \sin(\beta - \theta) + W \cos\theta \cos\beta \tan\phi_j}{W \sin\beta \cos\theta} \qquad \text{Equation 11}$$

A visual comparison of the two Case 3 Planar Failure geometries is supplied in Figure 4.

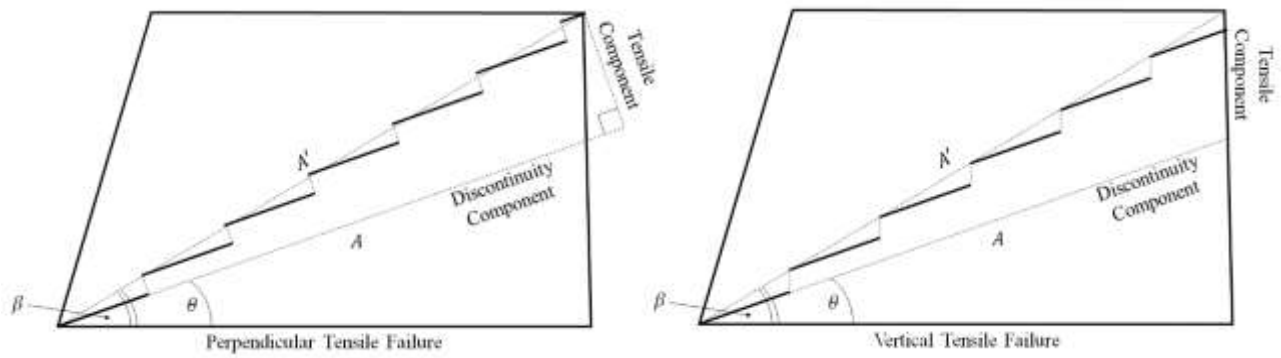

Figure 4 Geometric components for Case 3 Planar Failure

By considering Figure 4, if the failure surface start and ends are known, and a tensile failure direction is assumed, the joint spacing and persistence considerations are implicitly accounted for geometrically and therefore do not need to be considered in Equation 10 and Equation 11.

Case 4 Planar Failure defines failure that occurs when two or more discontinuities intersect, forming one or more blocks (or wedges) that are free to move. An example of Case 4 Planar Failure is shown in Figure 5.

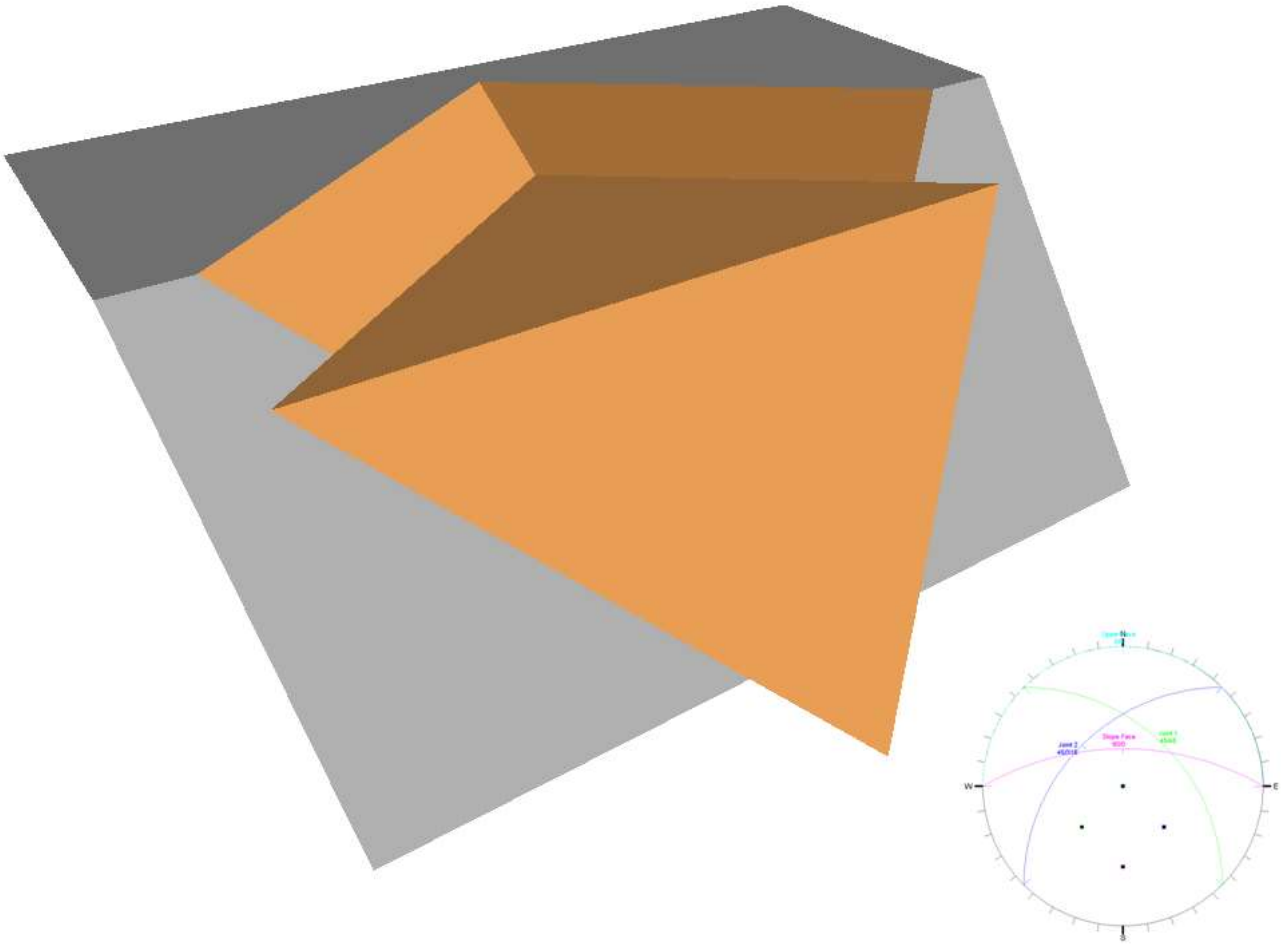

Figure 5 Example Case 4 Planar Failure

Case 4 Planar Failure differs from the other Planar Failures as sliding can occur along several surfaces or along the line of intersection of two or more discontinuities (Goodman & Shi 1985). Case 4 Planar Failure is best viewed as the three dimensional, or generalised Planar Failure where any number of the previous Failure Cases can be considered with sufficient use of vector calculus. The general FOS equation for Case 4 Planar Failure is given as:

$$FOS = \frac{\sum_{i=1}^{n} \boldsymbol{F}_{\boldsymbol{P}_i}}{\sum_{i=1}^{n} \boldsymbol{F}_{\boldsymbol{A}_i} \cdot \hat{\boldsymbol{s}}} \qquad \text{Equation 12}$$

where $\boldsymbol{F_{P_i}}$ is the i^{th} passive force vector (N) acting on the failure mass, $\boldsymbol{F_{A_i}}$ is the i^{th} active force vector (N) acting on the failure mass and $\hat{\boldsymbol{s}}$ is the unit vector in the direction of sliding. Calculating the required force vectors is tedious to do by hand so Engineers will typically use commercial software to aid in the calculation of Equation 12.

1.2.2 Toppling Failure mechanisms

Toppling Failure describes the forward rotation of a rock mass out of a slope about a point or axis below the centre of the displaced mass. Toppling Failure requires that there exists at least two discontinuity sets that are approximately perpendicular to each other, with the correct Aspect Ratio and orientation to generate unbalanced moments. An example of the required joint and slope geometry to cause toppling is shown in Figure 6.

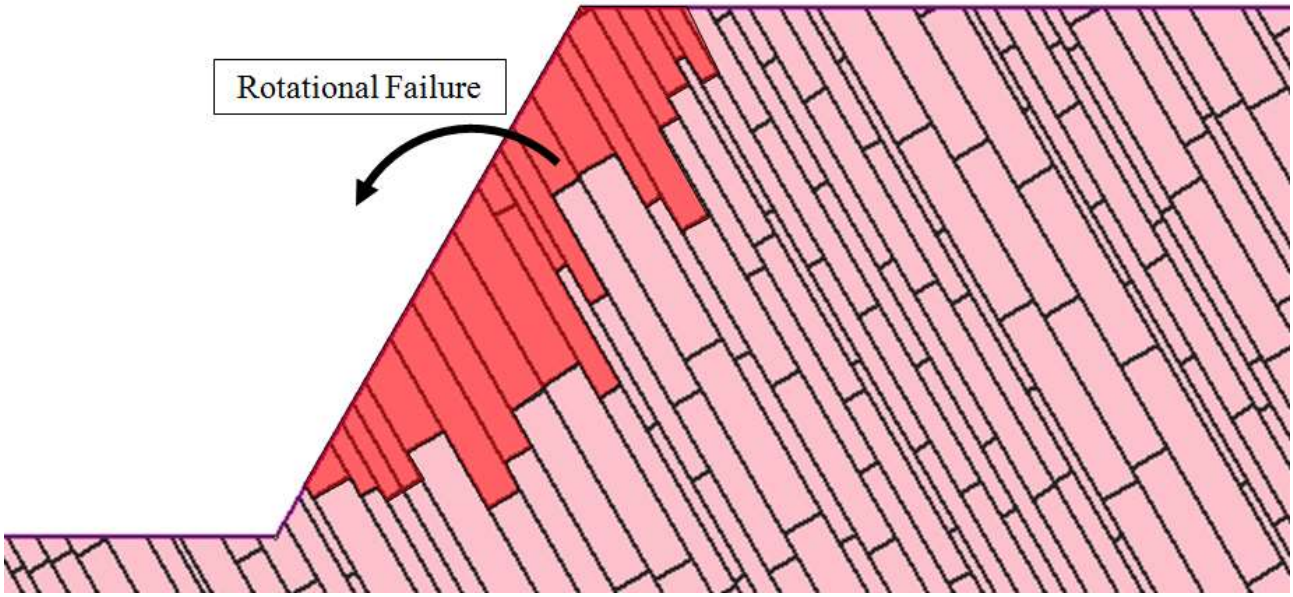

Figure 6 Example Toppling Failure

Wyllie and Mah (2004) define the Aspect Ratio of a rock block such that:

$$Aspect\ Ratio = \frac{t}{h} \qquad \text{Equation 13}$$

where t is the bed thickness (m) and h is the cross joint spacing (m). To determine if a rock mass will topple, the Aspect Ratio is assessed in conjunction with the apparent cross joint dip θ and the cross joint friction angle ϕ to determine the toppling Failure Case. There are four possible Failure Cases for Toppling Failure (Wyllie & Mah 2004):

Case 1 Toppling Failure describes a system such that:

$$\theta < \phi \; and \frac{t}{h} > \tan\theta \qquad \text{Equation 14}$$

Case 1 Toppling Failure defines a stable geometry with no sliding or toppling expected to occur. Sections of rock that fall into this region are stable. They are not prone either sliding or toppling.

Case 2 Toppling Failure describes a system such that:

$$\theta > \phi \; and \frac{t}{h} > \tan\theta \qquad \text{Equation 15}$$

Sections of rock that fall into this region have an Aspect Ratio such that moments are balanced but are able to slide. The FOS equations for Case 2 Toppling Failure are equivalent to those for Planar Failure and were presented in the Section 1.2.1.

Case 3 Toppling Failure describes a problem such that:

$$\theta < \phi \; and \frac{t}{h} < \tan\theta \qquad \text{Equation 16}$$

Case 3 Toppling Failure defines a problem where only toppling is expected to occur with no sliding. The FOS of Case 3 Toppling Failure can be determined by calculating the moments acting on a block of rock with the FOS equation given as:

$$FOS = \frac{t/h}{\tan\theta} = \frac{t}{h\tan\theta} \qquad \text{Equation 17}$$

A different FOS formulation of Case 3 Toppling Failure is also found within literature (Wyllie & Mah 2004). This formulation assumes that the direction of the induced major principal stress is parallel to the slope surface and causes shear stresses and slip on the steep dipping joint set. The FOS equation for this interpretation is given as:

$$FOS = \frac{\tan \phi}{\tan(\omega + \theta - 90)}$$ Equation 18

where ω is slope dip (˚). Equation 18 only gives the FOS of bedding planes slipping against one another and does not necessarily indicate full rotational failure of the rock mass from a slope. Equation 18 also assumes that the cohesion of the cross joints are negligible. By consideration of Equation 3 and the assumptions used to produce Equation 18 it can be seen that Equation 18 is an identical formulation to Equation 3 with a rotated coordinate system.

Case 4 Toppling Failure describes a problem such that:

$$\theta > \phi \; and \frac{t}{h} < \tan \theta$$ Equation 19

Case 4 Toppling Failure describes a multi-modal failure being a combination of both sliding and toppling. Case 4 Toppling Failure is difficult to compute by hand and must be solved on an iterative basis (Goodman & Bray 1976). Because of the tedious iterative calculations, Case 4 Toppling Failure is most commonly evaluated using a discrete element approach such as Itasca's UDEC (Itasca Consulting Group Inc. 2014) or using toppling specific software such as Rocscience's RocTopple.

Discrete Element Methods is a broad numerical method that explicitly models the motion of discrete rigid, or semi rigid blocks to assess an overall system response with respect to a time variable. Discrete Element Methods are able to model the full motion of discontinuous rock slopes and can be constructed to allow intact rock to fracture. Depending on the block dimensions and problem size simulated, the computational requirements for Discrete Element Methods can be moderate to unreasonably high for practical applications. Simplified less densely discretised models are often used to understand the likely failure mechanisms and overall system response at the loss of some numerical accuracy. Discrete Element Methods are advantageous due to their ability to analyse any and all viable kinematic failures, assess key block or passive-active style failures, assess both small and large strain, and rotational problems, incorporate the influences of field stresses, external loads and material deformability and model some degree of intact failure of rock, alongside the overall kinematic response. This increased model complexity, as previously mentioned is typically associated with long simulation runtimes.

Numerical approaches to calculate the FOS of Case 4 Toppling Failure will typically be computed using Equation 2 (the SRF formulation). A note of interest is that because Case 4 Toppling Failure is solved iteratively, the relationship between the initial problem geometry and the calculated FOS will behave chaotically depending on how the geometry is defined or generated. What this means that is very small changes in problem geometry may have considerable influences on the calculated FOS and often require numerous simulations in order to determine the likely FOS associated with a single problem geometry. A more in depth elaboration of this chaotic influence when considering iterative solutions is presented in the 3DEC user's manual (Itasca Consulting Group Inc. 2014). This chaotic nature makes it difficult to generally quantify Case 4 Toppling Failure even for well-defined problem geometries.

1.2.3 Method of Slices

When analysis is concerned with large scale multi bench failures or weak rock, the mechanism driving failure are typically not as clearly defined as the Failure Cases previously presented. These types of problems will typically have numerous failure modes and some degree of intact rock failure, forming a circular or nonplanar failure path. Typically, the analysis of these multimodal failures requires some form of numerical approximation to solve for the complex failure paths expected behaviours experienced.

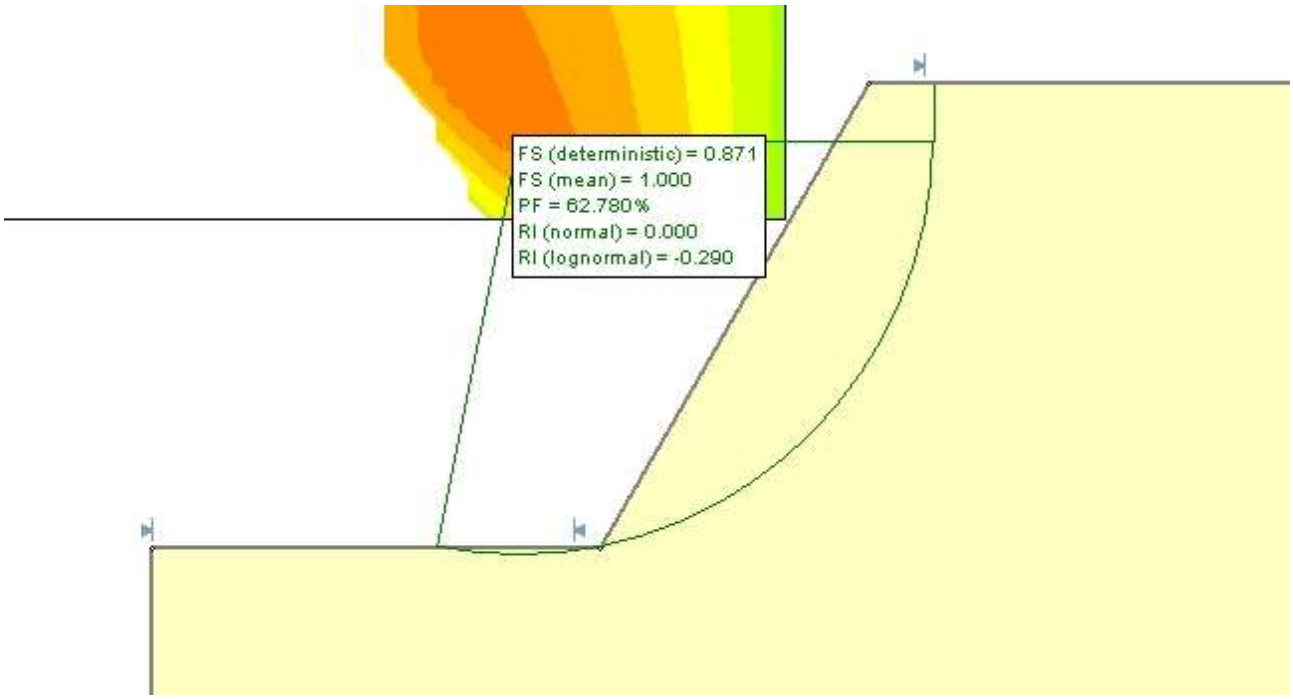

Figure 7 Example Circular Failure

Method of Slices is a very common, typically two dimensional method of determining the overall stability of a rock or soil slope (Fellenius 1936). This approach subdivides the given slope geometry into a series of slices and calculates the acting forces on each linear slice section to determine the FOS of the overall failure surface. A simple slicing method FOS equation is given by Fellenius (1936) is:

$$FOS = \frac{\sum_{n=1}^{p} c\Delta L_n + W_n \cos\alpha_n \tan\phi}{\sum_{n=1}^{p} W_n \sin\alpha_n} \qquad \text{Equation 20}$$

where p is the number of slices, c is cohesion (Pa), ΔL_n is the failure length of slice n (m), W_n is the weight of slice n (N), α_n is the dip of slice n (˚) and ϕ is the friction angle (˚). Various authors have suggested modifications to Equation 20 to include additional terms for moments and slice-slice interactions, with a large list of methods of slicing modifications presented by Fredlund (1984). Software implementations of slicing methods will typically utilise many different failure surfaces and slicing methods to determine the combination associated with the lowest overall slope FOS. Failure surfaces may also be determined using a path search algorithm to determine the weakest a non-circular failure path. Path search methods can consider local stresses, anisotropic strength and locally varying material parameters. Method of slicing are an advantageous method as they are able to include spatially different material parameters to reflect the actual rock mass conditions and local geological variations.

1.2.4 Equivalent Continuum Methods

Engineers may prefer to model the overall rock mass response instead of explicitly modelling the existing structures, in an effort to reduce the required computational time. This is achieved by modifying some combination of the laboratory scale material parameters or compatibility equations to simulate an equivalent continuous material that behaves identically to a rock mass (Sharma & Pande 1988). Equivalent continuum approaches are not limited to a single numerical method and can be implemented into various numerical methods such as Finite Element, Finite Difference or Boundary Element approaches. The main benefit of dealing with an equivalent continuum methods compared to Discrete Element Methods is that the computational effort and model discretisation are typically much less for continuum approaches and material non-linearity can be incorporated.

The FOS for equivalent continuum approaches is calculated utilising the SRF formulation given by Equation 2. Recent parametric studies by Lobbestael, Athanasopoulos-Zekkos and Colley (2013) have suggested that when numerical methods include progressive failure (i.e., strain softening) there is a potential reduction in the overall slope FOS up to 15% compared to their limit equilibum simulations. It was also noted in this study that the magnitude of the FOS reduction was more heavily influenced by the location of locally weak materials and problem geometry rather than the explicit incorporation of yielding elements.

The main limitation when dealing with equivalent continuum approaches is how to determine the combination of material parameters or modified compatibility equations that reflect the overall rock mass response. One of the most commonly used empirical method for equivalent continuum parameter selection was first proposed by Hoek and Brown (1980) and has been able to estimate the equivalent strength and stiffness of an isotropic continuum by considering both laboratory and field measurements. This method (known as the Hoek-Brown failure criterion) has been reviewed and updated over its use with a summary of the advancements available in the publication by Hoek and Marinos (2007). More recently studies (Vakili, Albrecht & Sandy 2014) (Saroglou & Tsiambaos 2007) (Dehkordi 2008) have considered how to extend the equivalent continuum approach to deal with known material anisotropy. When anisotropy is accounted for, equivalent continuum methods are more capable at approximating the material behaviour and can more clearly identify the likely failure mechanisms compared to a simpler isotropic model.

1.2.5 Factor of Safety equations for structured rock - summary

The failure mechanisms associated with rock slopes are well understood and can be grouped into three main failure mechanisms, and then further divided into several Failure Cases. The FOS for most Failure Cases are expressed in closed form, or uses a numerical approach to calculate the FOS via the SRF approach. In relation to this Thesis' aim, Table 2 presents the preferred method of calculating the FOS for each identified failure mechanism and individual Failure Cases:

Table 2 Preferred calculation method for the Factor of Safety of various failure mechanisms

Failure mechanism	Failure Case	Preferred calculation method
Sliding Failure	Case 1 - Frictional Sliding	Equation 3
	Case 1 - Frictional Cohesional Sliding	Equation 4
	Case 1 - Barton Bandis shear criterion	Equation 6
	Case 2 - Non persistent sliding	Equation 9
	Case 3 - Sliding and tensile failure	Equation 10 Equation 11
	Case 4 - Generalised sliding	Equation 12
Toppling Failure	Case 1 - Stable	-
	Case 2 - Sliding Only	See Sliding Failure
	Case 3 - Toppling Only	Equation 17
	Case 4 - Sliding and Toppling	See below
Complex	Circular and intact	Equation 20*

*In relation to quantifying the FOS of circular and intact failure, equivalent continuum methods are best suited to dealing with this failure mechanism. When contrasting the accuracy of equivalent continuum approaches compared to simpler slicing methods, the results of Lobbestael, Athanasopoulos-Zekkos and Colley (2013) suggest that the incorporation of progressive failure should be considered, however the overall impact of incorporating progressive yielding is case specific. From a general analysis of FOS for rock slopes, their incorporation of progressive yielding is far too case specific to be considered for a general assessment. Slicing methods for quantifying intact failure will offer a computationally simpler and general evaluation approach for rock slope stability.

The most problematic Failure Case was identified as Case 4 Toppling, which needs to be solved using a strictly numerical approach. Mentioned previously in Section 1.2.2 the iterative solution needed for the FOS calculation can produce a chaotic response that can be very sensitive to the problem geometry. As the behaviour of Case 4 Toppling is expected to be very unpredictable and computationally expensive to calculate, even for well-defined geological problems, the notion that a rock slope's FOS for Case 4 Toppling when dealt with in a general context has any relevant meaning is very small. For this reason, Case 4 Toppling Failure will not be considered further due to expected complications with the chaotic nature and excessively long simulation times. The findings of this Thesis can form the basis of a more in-depth assessment to considering Case 4 Toppling in isolation.

1.3 Defining Probability of Failure

When System Strength parameters and System Stresses are known and allowed to vary, Equation 1 can be defined in terms of Probability Density Functions (PDFs) such that:

$$FOS = Z(X_1, Y_1, \dots, X_n, Y_k) = \frac{F(X_1, X_2, \dots, X_n)}{G(Y_1, Y_2, \dots, Y_k)} \qquad \text{Equation 21}$$

where X_n are the PDFs associated with System Strength parameter n, Y_k are the PDFs associated with System Stress component k, F is the function that describes the System Strength, G is the function that describes the System Stress and Z is an equivalent function that describes the FOS. The Probability of Failure (POF) is then defined as the probability of obtaining a FOS value less than or equal to unity in Equation 21:

$$POF = \Pr(Z \leq 1) = \int_0^1 Z(X_1, Y_1, \dots, X_n, Y_k)\, d(X_1, Y_1, \dots, X_n, Y_k) \qquad \text{Equation 22}$$

Note that the lower integral limit is set to zero in Equation 22 as a FOS by definition cannot be negative. The proper integral notation should have the lower limit set to $-\infty$.

In relation to POF, it is accepted that the POF tends to 100% as the FOS tends to zero and POF tends to 0% as the FOS tends to infinity. Some Engineers quite strongly assert the belief that by consideration of these two previous statements the POF must be equal to 50% for a FOS equal to one. This feature is true in some specific cases but is not a general property of the relationship between FOS and POF. This feature is demonstrated further in Section 1.6.1 and is present in the FOS POF

relationships presented by Javankhoshdel and Bathurst (2014). Equation 22 is seldom defined in closed form so numerical methods are used to obtain an approximate solution. The three most commonly used numerical methods, their strengths and limitations are discussed in the following sections.

1.3.1 Monte Carlo and Latin Hypercube Sampling

Monte Carlo and Latin Hypercube Sampling methods, are simple algorithms that can be used to numerically integrate an n-dimensional problem (Brooks 1998). Monte Carlo and Latin Hypercube Sampling have every similar numerical procedures, with a general Monte Carlo procedure given by (Metropolis & Ulam 1949):

1. Define a closed-form solution or numerical approximation to a problem to be solved.
2. Define the PDF for each input variable.
3. Randomly select a value for each input variable based on their assigned PDFs.
4. Compute the value of the equation defined in Step 1 using the inputs from Step 3. Store the result.
5. Repeat Steps 3 and 4 until the required number of calculations are complete, or some convergence criteria is met.

The Latin Hypercube Sampling methodology implements a similar numerical procedure with only step 3 differing. Instead of randomly selecting each input variable, they are selected at using an evenly spaced n-dimensional grid through the input probability hypercube. This creates a finite number of non-random evaluation points:

$$\left(\prod_{n=0}^{M-1}(M-n)\right)^{N-1} = (M!)^{N-1} \qquad \text{Equation 23}$$

where M is the number of division in the PDF and N is the number of input variables. Typically, Latin Hypercube Sampling requires a fraction of the number of realisations as Monte Carlo Sampling (Cheng & Druzdzel 2000) to achieve the same relative error. A visual example comparing Monte Carlo and Latin Hypercube sampling is shown in Figure 8.

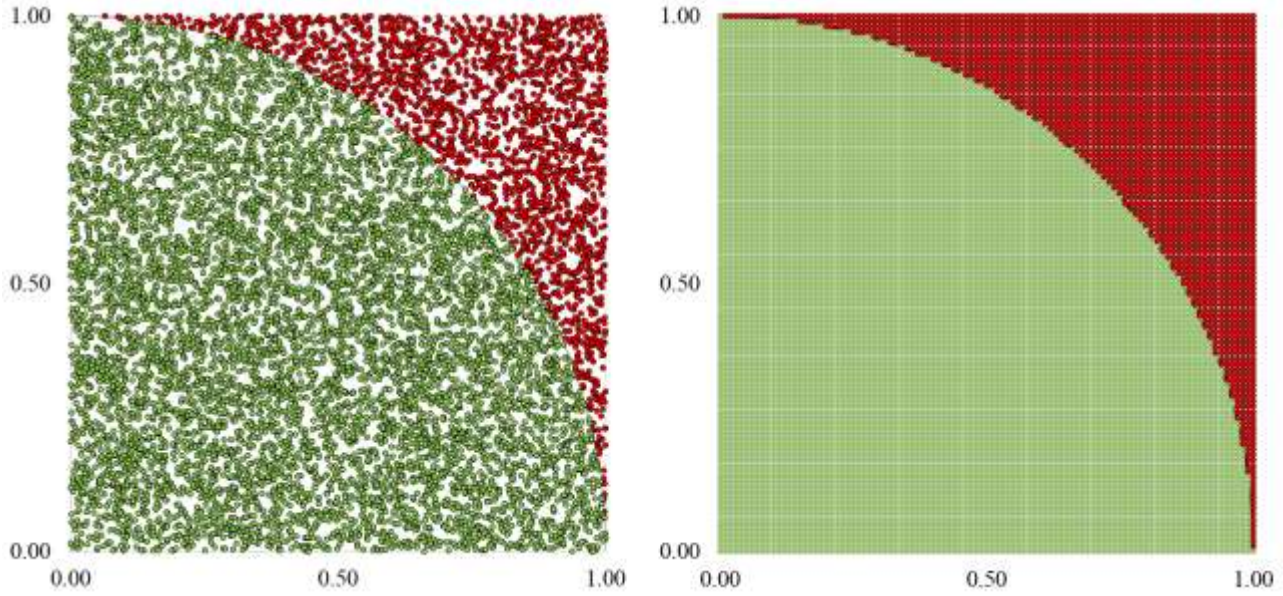

Figure 8 Comparison of integration methods for a quarter circle. Left Monte Carlo Sampling, right Latin Hypercube Sampling.

Monte Carlo Sampling and Latin Hypercube Sampling have a number of strengths and weaknesses. Monte Carlo Sampling is beneficial for the following reasons:

- Monte Carlo Sampling is very simple to implement. Depending on the specific application, it may only require one loop to implement the Monte Carlo Sampling routine. Multi-variable problems can be easily assessed using spreadsheet programs with minimal effort.
- Compatible over an n-dimensional problem (Brooks 1998). There are no limitations associated with the problem dimensionality.
- No restrictions relating to applications or functions. Any numerical procedure can be modified to incorporate Monte Carlo Sampling.
- Input PDFs can be continuous, discrete or arbitrarily defined.

Monte Carlo Sampling does have the following limitations:

- The use of Monte Carlo Sampling is restricted by the practicality of determining results for hundreds to tens of thousands of realisations. Depending on the application, it may be unfeasible to implement Monte Carlo Sampling.

- The accuracy is dependent on the law of large numbers. There is no guarantee that results from a Monte Carlo Simulation will be accurate at any number of resolutions. More calculations will result in a smaller associated error, which is at the cost of increased computational requirements.

The Latin Hypercube Sampling method has several advantages over the Monte Carlo Sampling, which include:

- Each specified realisation is only ever calculated once. This reduces the number of total calculations compared to Monte Carlo Sampling (Helton & Davis 2002) and removed redundant realisations.
- There is explicit attention to low probability events. The inputs for the Latin Hypercube are evenly sampled, results for low probability outcomes are reflected well (Iman & Conover 1980). This approach ensures that low probability events are correctly accounted for in the final output distribution.
- Fewer calculations results in faster overall computation (Cheng & Druzdzel 2000).

Some limitations that have been identified with the Latin Hypercube Sampling method include:

- The implementation of Latin Hypercube requires that the inputs are selected on an evenly spaced probability grid. Systematically selecting each evaluation point is not as simple to implement as randomly selecting values from the specified distribution.
- When a problem has more than two dimensions or is considerably nonlinear, the efficiency gained by using Latin Hypercube becomes negligible in comparison to Monte Carlo Sampling (Manteufel 2000).

Some recently published analyses using Monte Carlo Sampling include:

Pavement Performance using rock materials (Kalita & Rajbongshi 2014), Bearing Capacity of cohesionless soils (Pula & Zaskorski 2014), Probabilistic slope stability (Zhang, Zhao & Li 2010), Investigating heterogeneous slopes with cross-correlated shear strength (Minh & Le 2014), Limit state analysis of gravity dams (Carvajal, Peyras & Bacconnet 2011), Wedge stability for slopes (Vatanpour, Ghafoori & Talouki 2014), Determining critical slip surfaces in earth slopes (Metya & Bhattacharya 2014), Stability of highly weathered rock slopes utilising spatial variability (Srivastava 2012), Designing slope stability charts (Javankhoshdel & Bathurst 2014), Pillar stability for

underground mining (Guarascio & Oreste 2012) and Estimating block sizes for rock with non-persistent joints (Kim, Cai, Kaiser & Yang 2007).

Some recently published analysis using Latin Hypercube Sampling includes:

Study the behaviour of soils exposed to dynamic loads (Petrik, Hrubesova & Mohyla 2014) and Probabilistic damage around underground excavations (Fattahi, Shojaee, Farsangi & Mansouri 2013).

Industry applications of Monte Carlo Sampling are considerably more abundant than Latin Hypercube Sampling, implying some industry preference. This preference however is likely a result of built in support in commonly used software packages rather than a reflection of the method accuracy or industry standards. For typical rock slope applications (mainly limit equilibrium), there is no reason to suggest the exclusive use of Latin Hypercube Sampling over Monte Carlo Sampling. If computationally heavy analysis, for example large numerical models requires probabilistic assessment, a preference would exist to use Latin Hypercube Sampling over Monte Carlo Sampling. In these computationally heavy circumstances, Rosenblueth's Point Estimate Method may offer an even more efficient method for probabilistic assessment.

1.3.2 Rosenblueth Point Estimate Method

The Rosenblueth Point Estimate Method is a different probabilistic approach in which the input PDFs are replaced in favour of point estimates at key locations (Rosenblueth 1975). The Point Estimate Method may appear overly simple, however for many applications the results obtained are exact (Rosenblueth 1981). The Point Estimate Method procedure is given as (Griffiths, Fenton & Tveten 2002):

1. Define an output function or performance function Z. This is the function of interest and is dependent on one or more random variables $X_1, X_2, \dots, X_n$.
2. Determine the location of evaluation points $\xi_{X_{n+}}$ and $\xi_{X_{n-}}$ and weights $P_{X_{n+}}$ and $P_{X_{n-}}$ for each X_n creating a list i of 2^n evaluation points for n inputs. The evaluation points and weights are calculated by considering the first three statistical moments of each X_n. For uncorrelated X the evaluation points and weights are given by:

$$\xi_{X_{n+}} = \mu_{X_n} + C_{X_{n+}}\sigma_{X_n} \qquad \text{Equation 24}$$

$$\xi_{X_{n-}} = \mu_{X_n} - C_{X_{n-}}\sigma_{X_n} \quad \text{Equation 25}$$

$$P_{X_{n+}} = \frac{C_{X_{n-}}}{C_{X_{n+}} + C_{X_{n-}}} \quad \text{Equation 26}$$

$$P_{X_{n-}} = 1 - P_{X_{n+}} \quad \text{Equation 27}$$

$$C_{X_{n+}} = \frac{\gamma_{X_n}}{2} + \sqrt{1 + \left(\frac{\gamma_{X_n}}{2}\right)^2} \quad \text{Equation 28}$$

$$C_{X_{n-}} = C_{X_{n+}} - \gamma_{X_n} \quad \text{Equation 29}$$

where μ_{X_n} is the mean, σ_{X_n} is the standard deviation and γ_{X_n} is the skewness of X_n. Correlated input variables can also be considered, with the correlated weighting equations found in references such as Christian and Baecher (1999).

3. Evaluate $Z(i)$ at all 2^n point estimates.
4. Calculate the desired output characteristics by considering the moments of the output function Z. The first three moments are given by:

$$\mu_Z = \sum_{i=1}^{2^n} P_i Z_i \quad \text{Equation 30}$$

$$\sigma_Z^2 = \sum_{i=1}^{2^n} P_i (Z_i - \mu_Z)^2 \quad \text{Equation 31}$$

$$\gamma_Z = \frac{1}{\sigma_Z^3} \sum_{i=1}^{2^n} P_i (Z_i - \mu_Z)^3 \quad \text{Equation 32}$$

Engineers may ignore the Point Estimate Method due to its apparent mathematical complexity, however the method is simple enough to be calculated by hand using a calculator. The advantages of using the Point Estimate Method over Monte Carlo or Latin Hypercube sampling include:

- For typical applications only 2^n calculations are required (Rosenblueth 1981). This makes computations by hand possible.
- The output characteristics calculated are typically exact (Zhao & Ono 2000). Errors become more apparent when the output function is non-monotonic (i.e., higher than order 3).
- Input PDFs do not need to be definable only their key characteristics need to be quantifiable (Russelli 2008). By only defining the key characteristics, the Point Estimate Method is highly suited to real world applications that use laboratory or site data. Justification of a suitable PDF for each input variable is not required with only the mean, standard deviation and skewness of the data being needed.

The limitations associated with the Point Estimate Method include:

- The Method can be interpreted as overly approximate (Christian & Bacher 1999). This perception has influenced industry acceptance of Point Estimate Method. This is not technically a disadvantage, but it greatly limits the number of method users.
- Two point estimates are not always sufficient in evaluating functions (Rosenblueth 1981). It is not always apparent when the problem domain must be separated. This may result in inaccuracies in the results.
- In order to fully appreciate the output PDF, additional methods for example Mote Carlo Sampling are required. This makes the Point Estimate Method results redundant as the output must be calculated using a different method.
- Point Estimate Method is suited only to low variance problems. What constitutes a low variance problem is not well defined even by the method creator (Rosenblueth 1981). With ambiguity relating to the method appropriateness one may prefer not use this method.

Some examples of recent industry examples that have utilised the Point Estimate Method include:

Modelling uncertainty in underground excavations (Valley, Kaiser & Duff 2010), Assessing the bearing capacity of soils (Griffiths, Fenton & Tveten 2002 and Russelli 2008), Stability of spoil slopes in abandoned mines (Ruofen & Guangli 2013), General applications to underground drive and

development intersections risk analysis (Abdellah, Mitri, Thibodeau & Moreau-Verlaan 2014) and Rocscience SRF analysis for Phase^2 v8.0 (Rocscience, 2011).

The application of the SRF in Rocscience's finite element package Phase^2 for probabilistic analysis requires a major assumption. All input and output PDFs are assumed to follow a normal distribution (Rocscience, 2011). The Point Estimate Method implemented into Phase^2 is also limited when the output function shape changes severely. When the output function is significantly different from the input distribution or the assumed output function, results are highly inaccurate. This is best demonstrated by the work of Valley and Duff (2011).

To address a major limitation of the Point Estimate Method in relation to the FOS POF problem, consider the following example. An Engineer wants to determine the POF using the Point Estimate Method for some function Z, which describes a rock slope's FOS. Z was determined by Point Estimate Method to have the following characteristics:

$$\mu_Z = 1.5 \qquad \text{Equation 33}$$

$$\sigma_Z^2 = 0.7071 \qquad \text{Equation 34}$$

$$\gamma_Z = 0 \qquad \text{Equation 35}$$

The question is, how can these statistical characteristics be used to calculate the POF? In order to evaluate the POF (Equation 22), the PDF of Z must be known. For the above example, a uniform, Laplace, triangular and normal distribution are all plausible PDFs based on the Point Estimate Method characteristics. If the output PDF of Z is poorly defined or not assumed, then the Point Estimate Method cannot meaningfully evaluate the POF.

1.3.3 Summary and method applicability to Factor of Safety problems

This section has presented three of the most common methods of calculating a POF in geotechnical applications including some of their strengths and weaknesses. When applying these numerical methods to calculating a POF it would be preferable to use the Point Estimate Method over both Monte Carlo and Latin Hypercube Sampling due to the very efficient solution procedure. However, in order to use the Point Estimate Method the output PDF must be known, which must first be determined using either Monte Carlo or Latin Hypercube Sampling. The Monte Carlo Sampling method was chosen as the numerical method to evaluate Equation 22 for each FOS equation in Table 2. This selection was justified due to its simpler numerical implementation and ease in assessing problems with more than two variables.

1.4 Relationships Between Factor of Safety and Probability of Failure in Literature

This section presents various industry examples of the relationship between FOS and POF for rock slope designs. The objective of this section is to understand if there are any pre-existing methodologies in the relationship between FOS and POF for rock slope designs. In practice, rock slopes are required to meet some minimum accepted level of risk that is a function of a company's risk appetite or governing regulatory requirements. Depending on these standards, designs requirements may relate to either a FOS or a POF and can vary depending on the expected stand up time or economic implications of failure. Examples of general recommendations for design criteria for open pit slope design are shown in Table 3.

Table 3 Acceptance criteria for open pit mining applications (Read & Stacey 2009)

Slope scale	Consequence of failure	Acceptance criteria		
		FOS (Minimum) static case	FOS (Minimum) dynamic case	POF (maximum)
Bench	Low to high	1.10	N/A	25% - 50%
Inter-ramp	Low	1.15 – 1.20	1.00	25%
	Medium	1.20	1.00	20%
	High	1.20 – 1.30	1.10	10%
Overall	Low	1.20 – 1.30	1.00	15% - 20%
	Medium	1.30	1.05	5% - 10%
	High	1.30 – 1.50	1.10	≤ 5%

Other examples of open pit design guidelines can be found in other publications such as Sullivan, Duran and Eggers (1992), and From the Department of Minerals and Energy (1999). Although the design guidelines in Table 3 specify both a FOS and POF for each configuration, these guidelines do not imply any direct relationship between FOS and POF.

1.4.1 Literature relationships between Factor of Safety and Probability of Failure

Publications considering design FOS and POF for rock slopes do not typically focus on producing a general relationship between FOS and POF. A recent study looking into such a FOS POF relationships that does have parallels to rock slope designs is that by Javankhoshdel and Bathurst (2014) where a series of design charts relating circular failure FOS and POF for a range of soil types including purely cohesive, cohesive frictional and correlated cohesive frictional are presented. Although these relationships are for soils, the analogue to cohesive frictional materials (a common model for rock) means that they do produce some insight into a similar FOS POF relationship for rock. A collection of FOS POF relationships obtained through communications with Geotechnical practitioners and various literature sources relating to rock slope stability is presented in Figure 9.

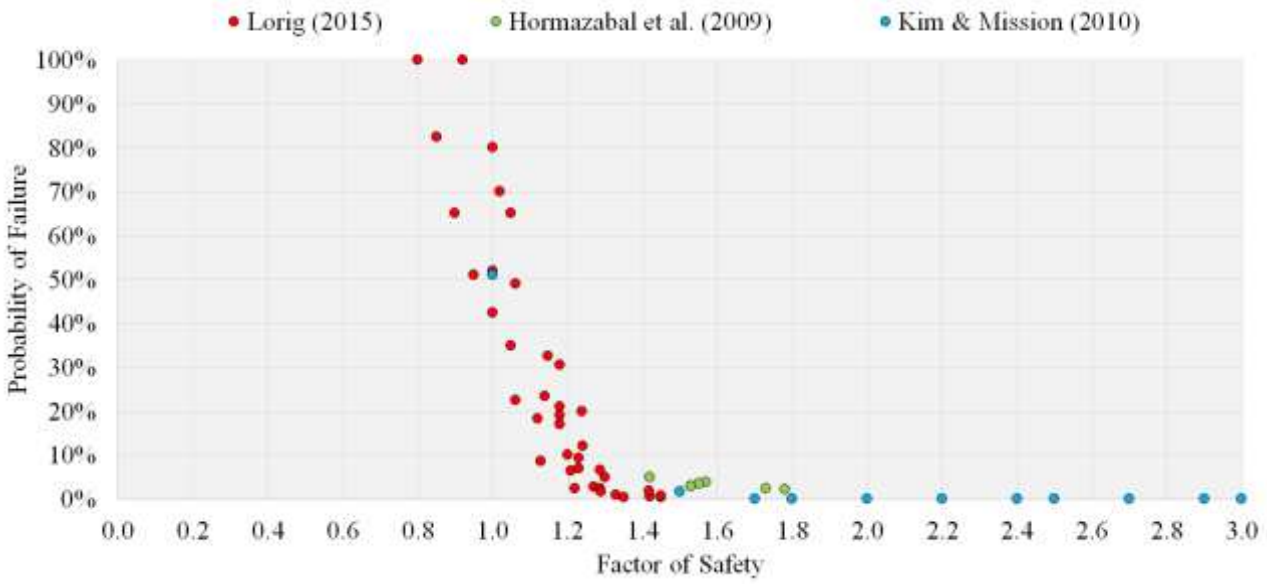

Figure 9 Documented Factor of Safety Probability of Failure relationships

The data points shown in Figure 9 relate to numerical predictions of the FOS and POF associated with various numerical analyses. From the FOS POF pairs shown in Figure 9 it appears that there is some consistent underlying relationship between FOS and POF based on multiple author's analysis. When applying the FOS POF equations given by Javankhoshdel and Bathurst (2014) to produce the relationship with the best fit Figure 10 is produced:

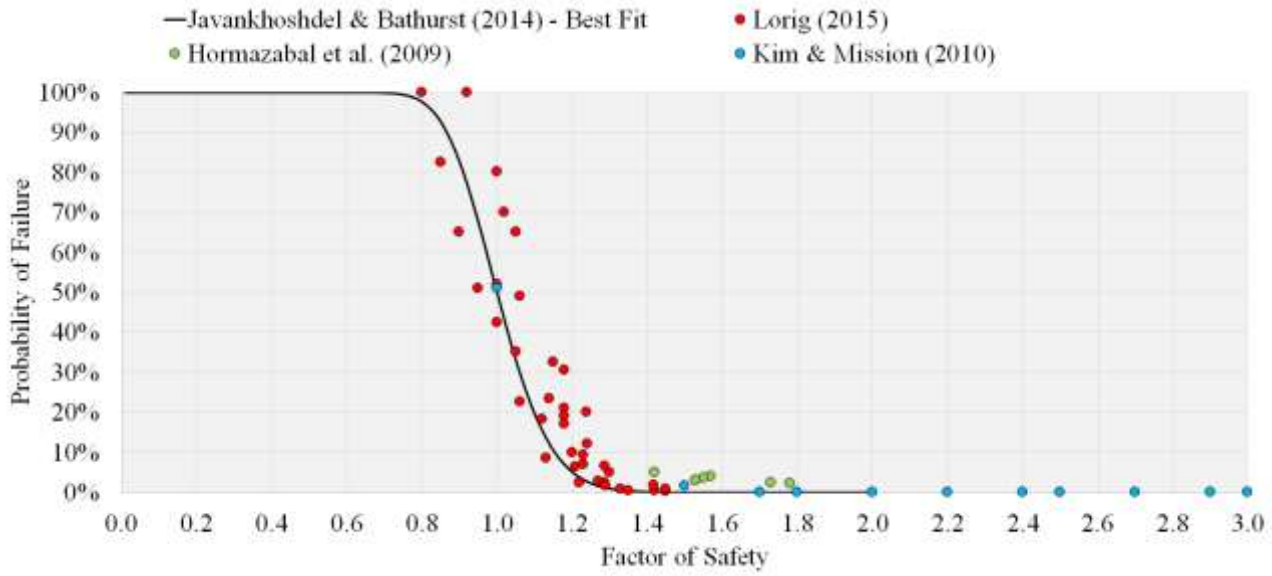

Figure 10 Documented Factor of Safety Probability of Failure relationships with fitted equation

Based on Figure 10 the available FOS POF pairs and the FOS POF Equation by Javankhoshdel and Bathurst (2014) appear reasonably consistent. The FOS POF relationship shown in Figure 10 is calculated by using the following equation:

$$POF = \Pr(FOS < 1) = \Phi\left(\frac{\ln\left(\sqrt{\frac{1+COV_{su}^2}{1+COV_\gamma^2}}/\overline{FOS}\right)}{\sqrt{\ln\left((1+COV_{su}^2)(1+COV_\gamma^2)\right)}}\right) \qquad \text{Equation 36}$$

where COV_{su} is the Coefficient of Variation associated with the shear strength and COV_γ is the Coefficient of Variation associated with the unit weight. The relationship shown in Figure 10 is equal to a COV_{FOS} given by:

$$COV_{FOS} = \sqrt{COV_{su}^2 + COV_\gamma^2} = 11.18\% \qquad \text{Equation 37}$$

This 'one fit all' relationship does appear promising, however there are several aspects and assumptions that need further consideration:

The FOS POF Relationship given by Equation 36 assumes that the shear strength, unit weight and FOS are all described by log-normal distributions (Javankhoshdel & Bathurst 2014). This assumption may be appropriate for soils, but may not be appropriate for rock material parameters. Further review is required in order to identify if this material parameter assumption is consistent and representative for rock parameters.

The FOS POF Relationship is presented for circular failure. It is suspected that each FOS equation presented in Table 2 will produce a different FOS POF relationship due to the formulation of the Failure Mechanism that has been previously identified are significantly different. More insight is required to determine if the relationship shown in Figure 10 is Failure Mechanism specific or a truly global FOS POF relationship.

The incorporation of scale effects are not apparent in the equation or design charts given by Javankhoshdel and Bathurst (2014). Although some appreciation can be considered, a more transparent appreciation of scale effects when considering FOS and POF for rock is ideal.

1.4.2 Rock material parameter variability in literature

In order to determine if the assumptions used by Javankhoshdel and Bathurst (2014) are appropriate for rock, an extensive literature review was completed in order to identify any trends or consistencies within rock material parameter PDF descriptions. Table 4 through Table 7 summarise the elastic, mechanical, geological and rock mass PDF used in literature respectfully.

Table 4 Elastic parameters Probability Density Functions from literature

Parameter	PDF used	References
Dry density	Normal	(Carvajal, Peyras & Bacconnet 2011); (Metya & Bhattacharya 2014); (Zhang, Zhao & Li 2010)
	Log-normal	(Javankhoshdel & Bathurst 2014)
	Uniform	(Saliba, Saliba, Panitz, Figueiredo & Duarte 2014)
Young's Modulus	Normal	(Kim & Mission 2011); (Abdellah, Mitri, Thibodeau & Moreau-Verlaan 2014)
	Normal (Truncated at 0)	(Idris, Saiang & Nordlund 2012)

	Log-normal	(Bauer & Pauła 2000)
	Gamma	(Canbulat 2010)
Poisson's Ratio	Log-normal	(Canbulat 2010)

Table 5 Mechanical parameters Probability Density Functions from literature

Parameter	PDF used	References
Uniaxial Compressive Strength	Normal	(Guarascio & Oreste 2012); (Jefferies, Lorig & Alvares 2008); (Wiles 2006); (York, Canbulat & Jack 2000)
	Normal (Truncated at 0)	(Carvajal, Peyras & Bacconnet 2011); (Idris, Saiang & Nordlund 2012)
	Weibull	(Maheshwari, Valadkar & Venkatesham 2009); (Lu & Xie 1995); (Krumbholz, Hieronymus, Burchardt, Troll, Tanner & Friese 2014)
	Log-normal	(Canbulat 2010)
Point Load Index	None found	Normal, normal (Truncated at 0), Weibull and log-normal Can all be inferred from the relationship between Point Load Index and Uniaxial Compressive Strength (Franklin et al 1985)
Uniaxial Tensile Strength	Normal	(Perras & Diederichs 2014)
	Normal (Truncated at 0)	(Carvajal, Peyras & Bacconnet 2011); (Idris, Saiang & Nordlund 2012)
	Weibull	(Amaral, Cruz Fernandes & Guerra Rossa 2008); (Lobo-Guerrero & Vallejo 2006)
Peak friction	Normal	(Baecher & Christian 2003); (Zhang, Zhao & Li 2010); (Abdellah, Mitri, Thibodeau & Moreau-Verlaan 2014); (Wiles 2006)

	Normal (Truncated at 0)	(Metya & Bhattacharya 2014); (Idris, Saiang & Nordlund 2012)
	Log-normal	(Minh & Le 2014); (Javankhoshdel & Bathurst 2014); (Baecher & Christian 2003)
Residual friction	None found	N/A
Cohesion	Normal	(Zhang, Zhao & Li 2010); (Abdellah, Mitri, Thibodeau & Moreau-Verlaan 2014); (Metya & Bhattacharya 2014); (Baecher & Christian 2003)
	Normal (Truncated at 0)	(Idris, Saiang & Nordlund 2012)
	Log-normal	(Javankhoshdel & Bathurst 2014); (Baecher & Christian 2003)
Dilation	None Found	N/A

Table 6 Geological parameters Probability Density Functions from literature

Parameter	PDF used	References
Joint dip and dip direction	Normal	(Young 1987); (Kulatilake 1986); (Vantanpour, Ghafoori & Talouki 2014); (Robertson 1977); (Barton 1976); (Baecher, Lanney & Einstein 1977); (Kulatilake, Chen, Teng, Pan & Shufang 1995); (Sjoberg 1996)
	Fisher	(Sjoberg 1996)
Joint spacing / frequency	Normal	(Hammah & Yacoub 2009)
	Exponential	(Baecher 1983); (Gumede & Stacey 2007)
	Weibull	(Rabinovitch, Bahat & Greenber 2012); (Tang, Liang, Zhang, Chang, Tao, Wang, Zhang, Liu, Zhu & Elsworth 2008)
	Log-normal	(Canbulat 2010); (Gumede & Stacey 2007)

Joint persistence / trace*	Normal	(Hammah & Yacoub 2009)
	Log-normal	(Baecher 1983); (Villaescusa & Brown 1992); (Zadhesh, Jalali & Ramezanzadeh 2014)
	Exponential	(Zadhesh, Jalali & Ramezanzadeh 2014)
	Gamma	(Zadhesh, Jalali & Ramezanzadeh 2014)
Joint roughness	Log-normal	(Morelli 2014)
	Uniform	(Saliba, Saliba, Panitz, Figueiredo & Duarte 2014)
	Gamma	(Kveldsvik, Nilsen, Einstein & Nadim 2008)
Joint stiffness	None Found	N/A
Joint Compressive Strength	Uniform	(Saliba, Saliba, Panitz, Figueiredo & Duarte 2014)
Joint friction	Normal	(Irigaray, El Hamdouni, Jiménez-Perálvarez, Fernández & Chacón 2012); (Park, Um, Woo & Kim 2012); (Vantanpour, Ghafoori & Talouki 2014);
	Uniform	(Saliba, Saliba, Panitz, Figueiredo & Duarte 2014)
Residual joint friction	None found	N/A
Joint cohesion	Normal	(Vantanpour, Ghafoori & Talouki 2014); (Park, Um, Woo & Kim 2012);
	Normal (Truncated at 0)	(Irigaray, El Hamdouni, Jiménez-Perálvarez, Fernández & Chacón 2012)
Joint dilation	None found	N/A
Far field stresses	None found	N/A

*Zadhesh, Jalali and Ramezanzadeh (2014) has an abundance of trace length references. Typically, authors have suggested that joint traces are either log-normal or exponentially distributed.

Table 7 Rock mass parameter Probability Density Functions from literature

Parameter	PDF used	References
Rock Quality Designation	None found	N/A
Rock Mass Rating	Weibull	(Nejati, Ghazvinian, Moosavi & Sarfarazi 2014)
Rock Tunnelling Quality Index	None found	N/A
Mathew's stability number	None found	N/A
Hoek-Brown criterion	Normal	GSI - (Guarascio & Oreste 2012); (Jefferies, Lorig & Alvares 2008) M_i - (Guarascio & Oreste 2012)
	Normal (Truncated at 0)	GSI - (Idris, Saiang & Nordlund 2012) M_i - (Idris, Saiang & Nordlund 2012)
Block size / volume	Log-normal	(Kim, Cai, Kaiser & Yang 2007)
Shear Strength models	Log-normal	(Griffiths & Fenton 2003); (Javankhoshdel & Bathurst 2014)
	Normal	(Wiles 2006)
Factor of Safety	Normal	(Sjoberg 1996)
	Log-normal	(Srivastava 2012), (Javankhoshdel & Bathurst 2014), (Hammah & Yacoub 2009)

Upon consideration of a vast literature search, the following conclusions can be made:

- Geomechanics parameters appear to vary considerably between studies and therefore there is currently no consistent PDF for each material parameter.
- There is limited statistical understanding of input variability, with the 'natural assumption' of a normal distribution being common practice. Some authors enforce the condition of non-zero values by using a log-normal distribution or a truncated normal distribution.

- Studies that are more recent have begun to acknowledge that Geomechanics parameters can be described by less traditional PDF families such as the gamma or Weibull distribution. The adoption of these functions implies that statistical rigour for Geomechanics applications is becoming increasingly popular.

Based on the review of material parameter PDF assumptions in literature, it is apparent that there are no consistent PDF or consistent assumption for rock material parameters across multiple authors. This uncertainty in PDF descriptions and its implications to the FOS POF relationship is further discussed in Section 1.6.2. This review has also demonstrated that the assumptions used to produce the relationship shown in Figure 10 is sufficiently doubted, and warrant further research into quantifying material parameter variability in terms of representative PDFs for rock material parameters.

1.5 Rock, Rock Material Parameters and Discontinuities at Scale

Scaling laws in geotechnical engineering are used to describe how the measurable response of rock changes when the volume or characteristic dimension being assessed is varied. Scaling laws within brittle and quasi-brittle material literature consistently identify decreasing strengths (Bažant 1999) at increasing scales. This decrease in strength is also referred to as a negative scaling law. The most common empirical scaling law for laboratory to describe rock strength is in the form (Hoek & Brown 1980):

$$\frac{x_{V_n}}{x_{V_0}} = \left(\frac{V_n}{V_0}\right)^C \qquad \text{Equation 38}$$

where V_0 is the characteristic dimension or Representative Volume Element (RVE), V_n is the scale of interest, x_{V_0} is the strength component at the associated subscript scale and C is a constant. The size of the characteristic dimension or RVE is defined as the smallest indivisible volume with measurable behaviour (Le & Bažant 2011). For intact rock, this is often taken as the test diameter or volume of an NQ sized laboratory sample. The constant C in Equation 38 is determined experimentally (Hoek & Brown 1980) with the most publicised value for brittle compressive failures in hard rock having C equal to -0.18 for a V_0 of 50mm. It does need to be noted that Hoek and Brown's database did not contain samples that were larger than 200mm in diameter, or smaller than 0.8 times the typical laboratory sizes. They also did not suggest that Equation 38 could be extrapolated beyond their data.

Using Equation 38 as a generalised scaling law for strength does have some problems. As V_n tends to infinity, the strength also tends to zero. Although it can be argued that the convergence of Equation 38 to zero is sufficiently slow, such that it can provides accurate estimates for 'in-situ block strength', some authors (Goldstein *et al* 1966) (Zengchao, Yangsheng & Dong 2009) (Zhang, Zhu, Zhang & Ding 2011) have added an asymptote to Equation 38 to produce:

$$\frac{x_{V_n}}{x_{V_0}} = \left(\frac{V_n}{V_0}\right)^C + x_\infty \qquad \text{Equation 39}$$

where x_∞ is the asymptotic strength at an infinite scale. The asymptote in Equation 39 is calculated on a case by case basis from some regression model, with no real physical basis or representation to its selection. This asymptotic approach implies limitations of the typical scaling law to describe all conceivable problems. Scaling laws in brittle materials are often described using the statistical theory arguably first proposed by Weibull (1951) and was the basis of his '*statistical distribution function of wide applicability'* to describe heterogeneous systems that are said to fail if one component within a larger system fails. This failure model is often referred to as the weakest link model. In practice this weakest link failure is not observed in either laboratory or field responses of rock. Laboratory scale samples at low confining stresses produce detectable acoustic emissions starting at 40% to 60% of the peak compressive strength (Hoek & Martin 2014) (Cho, Martin, Sego & Christiansson 2004) while in-situ seismic responses are detectable during the loading process and prior to failure. These observations suggest that independent of scale, rock failure is a gradual process and is not fully represented by a weakest link model.

More complex failure models do exist to describe failure of multiple RVEs. These models include Daniel's Fibre Bundle Mode (Daniels 1945) and Series-Parallel Coupling Models (Pang, Bažant & Le 2008). Unlike the Weibull model, load shedding capabilities are captured in these models and progressive failure can occur prior to reaching a peak strength. The increased model complexity means that analytical solutions are seldom possible, with numerical methods being used to determine an equivalent response. For stress related problems in rock, stochastic finite element (Liu 2004) (Wong, Wong, Chau & Tang 2006) (Zhu 2008), finite difference (Sainsbury, Pierce & Mas Ivars 2008) and DEM (Mas Ivars *et al* 2011) (Poulsen, Adhikary, Elmouttie & Wilkins 2015) (Zhang, Stead & Elmo 2015) have been successfully used to model progressive failure in heterogeneous models to obtain scale dependant responses. These approaches are analogues to a complex failure model like those mentioned previously, with the load shedding rules explicitly defined by the compatibility

equations. Literature studies considering heterogeneity and scale in rock can be broadly grouped into two categories; mesoscopic modelling and synthetic rock mass modelling.

1.5.1 Numerical scale analysis

Mesoscopic modelling refers to simulations that consider the behaviour of 'intermediate' volumes of intact rock. Within these mesoscopic simulations, material parameters are randomly distributed throughout the model to reflect microscopic strength variability. Failure in mesoscopic modelling typically initiates at some localised zone of weakness, which then propagates to cause complete failure. Examples of mesoscopic modelling studies include the work by Liu (2004), Wong *et al* (2006) and Zhu (2008). Within these studies, each strength parameter was assumed to follow a Weibull distribution, and the mechanical parameters were deterministic. Zhu (2008) did extend their analysis to consider heterogeneity associated with Young's Modulus, however a sensitivity of the influences of including this heterogeneity for Young's Modulus was not considered within the study.

Macroscopic heterogeneity or synthetic rock mass modelling refers to modelling methodologies that consider the influences and failure of both intact rock and structure within a rock mass. The typical synthetic rock mass approach involves simulating the behaviour of a large volume of rock containing a randomly generated fracture network. The fracture network is generated from a statistical description of joint set orientation, spacing and persistence that is generated on a case by case basis. These synthetic rock masses are then evaluated to obtain an equivalent continuum response of the rock mass assuming some failure model. Approaches using synthetic rock masses are primarily done using Discrete Element Methods (Mas Ivars *et al* 2011) (Poulsen, Adhikary, Elmouttie & Wilkins 2015) (Zhang, Stead & Elmo 2014), however continuum based approaches (Sainsbury, Pierce & Mas Ivars 2008) are possible.

Failure in synthetic rock masses is primarily related to the presence of comparatively weaker joints and partially contributed by failure of the stronger intact rock bridges. The applications of heterogeneity in synthetic rock mass models are noted to differ across studies. For example, the approaches used by Sainsbury *et al* (2008), Mas Ivars *et al* (2011) and Poulsen *et al* (2015) utilise calibrated deterministic intact rock and joint parameters, with the heterogeneity arising from the fracture network. Different approaches by Zhang and Zhao (2016) or Zhang *et al* (2014) extend their analysis to also consider heterogeneity associated with intact rock strength but utilise deterministic joint parameters. Within all of the mentioned synthetic rock mass modelling studies, no considerations were given to the influences of mechanical parameter heterogeneity that is, the influences of locally varying Young's Modulus and Poisson's Ratio.

Numerical scale analysis is typically done considering an ultimate deterministic output. This is done, as the result is to obtain equivalent material parameter to be used in continuum modelling for general design applications. The considerations of probabilistic scale effects are not dealt with in any of the previously mentioned studies, with the probabilistic behaviour at scale being implied from Author's presented summary statistics. Stochastic numerical methods are general enough to produce a probabilistic description of scale behaviours if sufficiently modelled and interpreted.

1.5.2 Experimental scaling laws

Experimental studies considering scale effects of rock tend to focus primary on the overall intact strength (e.g., compression or tension) with limited considerations to the constitutive material parameters (e.g., friction, cohesion, Young's Modulus etc.). Some notable studies considering scale and material parameters include those by Masoumi (2013), Simon and Deng (2009) Wong, Wong, Chau and Tang (2006), Zhu (2008). Another common feature of scale studies is that as sample sizes increase, the number of test samples relating to increased scales typically reduces (Masoumi 2013). This reduction in tested samples is likely a function of the practicality of sourcing samples, the specialty equipment required or the cost of materials and testing.

A similar style of review to material parameter assumptions in Section 1.4.2 was completed to identify if there are any major studies or consistent probabilistic and deterministic trends for rock material parameters at various scales. After completing this review, it was found that there are very few studies relating to material parameter variability and scale with only two notable references. Weiss, Girard and Amitrano (2013) mentions that rock under uniaxial compression at any scale follows a normal distribution. Weiss' result was obtained by modelling the behaviour of numerically simulated materials at various sizes. Another study by Arioglu (1999) suggested the following equation to explain the variability or rock at increased scales:

$$Variability = \frac{S^2}{nV} \qquad \text{Equation 40}$$

where S^2 is the variance, n is the number of samples and V is the sample volume. Equation 40 was only stated and has very little confidence due to no new information or experimental data being provided. The author also uses the term variability as a more general term with no indication as to which statistical parameter it relates.

As previously mentioned, publications considering rock generally at scale do have some rather consistent trends for rocks over various scales. A summary of these phenomenon are listed in Table 8.

Table 8 Literature conclusions about rock at different scales

Finding of study	References
As a sample's size increases, its strength **increases**	(Hawkins 1998); Many listed in (Masoumi 2013) Note that this influence is only noted for samples smaller than 50mm diameter
As a sample's size increases, its strength **decreases**	(Marcel & Vliet 2000); (Thuro & Plinninger 2001); (Hoek & Brown 1980); (Sainsbury, Pierce & Mas Ivars; 2008), (Bažant 2008); (Weiss, Girard & Amitrano 2013); (Pratt *et al* 1972); (Bieniaswski 1968); (Hustrulid 1976); (Pierce, Gadia & DeGagne 2009); (Sahawne 2013); (Borr-Brunetto, Carpinteri & Chiaia 1999); (Bieniawski & Van Heerden 1975); (Marsland 1971)
As a sample's size increases, its strength remains **constant**	(Kuehn *et al* 1992); (Van Mier 1986); (Mogi 1962)
As a sample's size increases, the standard deviation for strength **decreases**	(Marcel & Vliet 2000); (Sainsbury, Pierce & Mas Ivars 2008); (Bažant 2008); (Weiss, Girard & Amitrano 2013); (Kuehn *et al* 1992); (Pierce, Gadia & DeGagne 2009); (Molenda *et al* 2013)
As a sample's size increases, the standard deviation for strength remains constant	(Thuro *et al* 2001)

Based on the literature search shown in Table 8 the most consistent behaviour is that rocks (strength) at scale exhibits the well documented negative scaling law and an associated homogenisation, or reduction in variance. A visual example of this idealised behaviour at scale is shown in Figure 11.

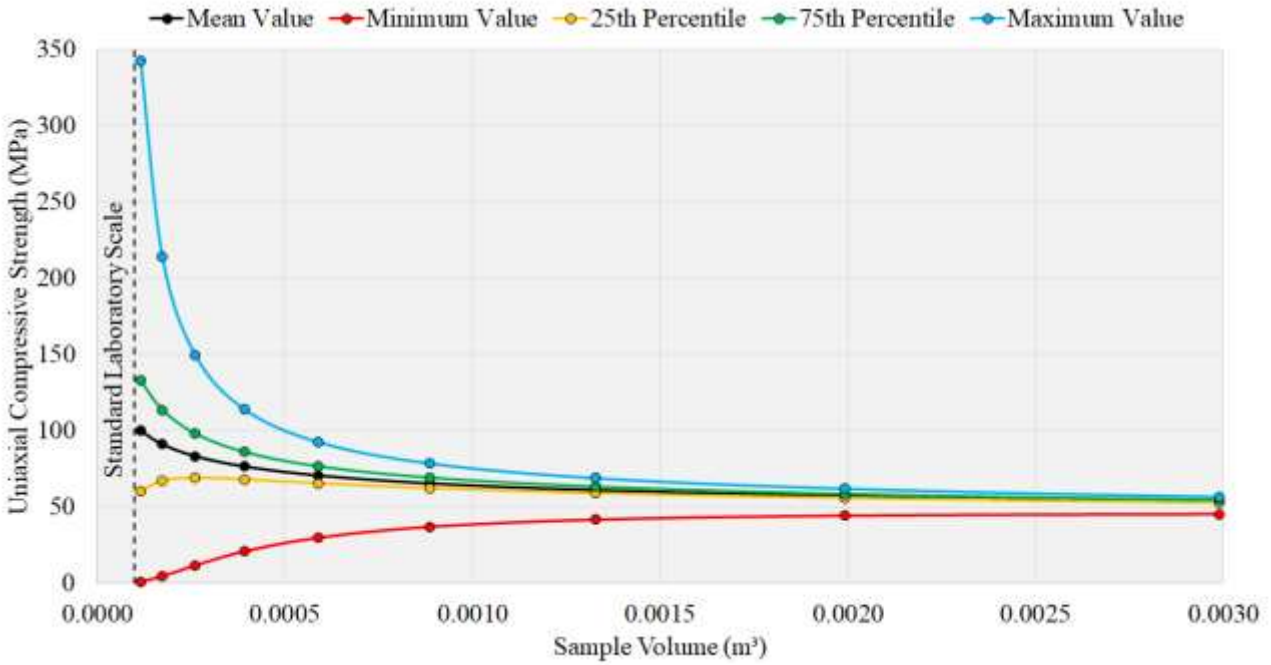

Figure 11 Idealised scale response - underlying scaling law and associated homogenisation

By considering this documented phenomenon shown in Figure 11, and the FOS POF charts presented by Javankhoshdel and Bathurst (2014) some appreciation can be included for scale by selecting the relationship line that describes the scale of interest's Coefficient of Variation. For this approach to be practical, the assumption that the shear strength at any scale is described by a log-normal distribution needs to be validated, and the Coefficient of Variation for a particular scale of interest needs to be routinely quantifiable. When considering the initial PDF assumptions for rock presented in Table 4 through Table 7, it is doubtful this relationship is currently present for rock parameters and warrants further research into quantifying how problem scale effects the associated material parameter PDF.

1.5.3 Rock discontinuities and scale

The behaviour of rock discontinuities at scale is fundamentally a complex problem to evaluate. Reasons for this include the highly variable nature of quantitative discontinuity features, and the accompanying complex failure processes. A non-exhaustive list of quantitative discontinuity features, which have been demonstrated to influence a discontinuities' shear strength, include the surface roughness (Barton & Choubey 1977) including anisotropy (Belem, Homand-Etienne & Souley 2000), the degree of surface interlocking (Johansson 2016), the orientation of the discontinuity with respect to loading (Bahaaddini 2014), discontinuity persistence (Bahaaddini 2014)**,** spacing (Bahaaddini 2014), intact rock and infill strength (Barton & Choubey 1977) and infill thickness (Karakus, Liu, Zhang & Tang 2016).

The failure process during shear is of equal complexity with some factors influencing the process including the applied normal stress (Goodman, Taylor & Brekke 1968), the rate of applied loading (Meemum 2014), intact failure verse dilatational failure (Goodman, Taylor & Brekke 1968), surface degradation while shearing (Lee, Park, Cho & You 2001), residual shear strength parameters (Barton 1982) and interactions between nearby discontinuities (Bahaaddini 2014).

The shear strength of any discontinuity may exhibit scale dependant behaviour and is often described by a negative scaling law. The notion of scaling laws for discontinuity shear strength remains somewhat contested in rock mechanics literature with summations of various scale studies presented by authors such as Johansson (2016), Bahaaddini (2014) and Li, Oh, Mitra and Canbulat (2017) implying that there is no consistently identifiable scaling law for discontinuity shear strength in rock mechanics literature. Research focusing on the nature of discontinuities and scale may proceed by using numerical or fractal methods.

Numerical methods can be used simulate the expected behaviour of discontinuities. The main aim of numerical methods is to produce a deterministic equivalent continuum material for applications in larger numerical models, or parameter estimates for empirical criterion at some desired orientation or scale. Most numerical approaches considering discontinuity shear strength utilise Discrete Element Methods (Itasca Consulting Group 2014) or particle element (Itasca Consulting Group 2014) approach such that the entire shear failure process can be quantified. Numerical methods are able to assess any problem scale or complexity as long as a representative discontinuity geometry is available. Numerical applications will typically deal with this geometry requirement in one of three approaches:

- Idealised profiles (Giacomini, Buzzi & Krabbenhoft 2008) (Shrivastava, Rao & Rathod 2012) - Simple repeating geometry such as a saw tooth or stepped triangular profiles are used as simple approximations.
- Digitising the standard roughness profiles (Karami & Stead 2008) (Park & Song 2009) - Barton's standard profiles are digitised and used as representative geometry. This approach limits the analysis to a two dimensional case and 10 representative geometries.
- Surface scanning or tomography representation (Bahaaddini 2014), (Karakus, Liu, Zhang & Tang 2016), (Lambert & Coll 2009), (Lazzari 2013) - two or three dimensional surface scans are obtained and used as representative geometry. This approach would constitute the current best practice as site based conditions are directly quantified and any measurable scale can be

considered. Advances in scanning technology are making this method more practically applicable. In order to use surface scanning techniques at large scales, a sufficiently large daylighting section of a discontinuity must be available to measure. This requirement does limit which discontinuities can be assessed in a practical setting.

A recent study by Tatone and Grasselli (2013) has brought to light some issues associated with the accuracy surface scanning methods, in particular resolution and noise. Their findings suggest that the measurement resolutions had a more significant influence on the measurable discontinuity roughness than the sampling window did, meaning scanning techniques at very large scales may have undesirable accuracy and misrepresent roughness. This means that a mutual limiting factor when considering scale and discontinuities is the inability to accurately quantify large scale discontinuity features, in particular discontinuity roughness.

Another approach that is common in rock mechanics literature is fractal descriptions of discontinuities. Fractal approaches are typically more mathematically complex than empirical or numerical methods and revolve around the notion that rock exhibit self-similar geometric properties (Mandelbrot 1982). The geometric complexity, scalability and self-similarity of an object is quantified by either its fractal dimension D or Hurst exponent H. The two fractal parameters are related to one another such that:

$$H = 2 - D \qquad \text{Equation 41}$$

The term fractal is a broad definition, which covers two classifications of self-similarity; namely, fractal self-similar describing geometry that isotopically scales (Mandelbrot 1982), and fractal self-affine describing geometry that scales anisotropically (Mandelbrot 1982). Fractal analysis considering rock discontinuities (Li, Oh, Mitra & Canbulat 2017), (Malinvero 1990)**,**(Kwašniewski & Wang 1993)**,** (Seidel & Haberfield 1995)**,** (Belem, Homand-Etienne & Souley 1997)**,** (Um 1997)**,** (Fardin 2003)**,** (Lanaro 2001)**,** (Pearce 2001)**,** (Jiang, Li & Wang 2013)**,** (Wei, Liu, Li & Wang 2013) have shown that fractal self-affine is a more appropriate description of discontinuities than fractal self-similar.

The fractal characteristics D and H can be estimated for a discontinuity using various techniques, with an extensive list of fractal measurement methods presented by Annadhason (2012). Methods used in rock mechanics literature include the roughness-length methods (Malinvero 1990)**,** variogram methods (Belem, Homand-Etienne & Souley 1997), compass walking methods (Lee, Carr, Barr &

Hass 1990), divider or modified divider methods (Brown 1987) and spectral methods (Guohua 1994). The main premise of fractal approaches is to relate H or D to some discontinuity roughness feature, with a prominent general relationship being:

$$R = a \times L^H \qquad \text{Equation 42}$$

where R is some analogue to roughness such as the asperity height (Johansson 2016) or the standard deviation of the asperity height (Li, Oh, Mitra & Canbulat 2017) (Tatone & Grasselli 2013), a is a proportionality constant and L is the discontinuity length (m). Equation 42 or similar is then used estimate JRC from these fractal characteristics, with a large summary of equations relating JRC and D being found in Li and Huang (2015). Although from an academic perspective the relationship between fractal characteristics and JRC is an interesting property, A practitioner may prefer to use direct measurements of JRC using the methods recommended by Barton (2013) (i.e. Table 1) as they are direct and practically applicable measurements of roughness. The main benefit of fractal methods is that they are mathematical models, which describe natural phenomenon. This mathematical basis means that fractal models have predictable and well-defined characteristics, which may prove useful when considering discontinuity roughness at unmeasurable scales, including probabilistic influences.

1.5.4 Rock at scale - summary

In summary when considering probabilistic descriptions of rock material parameters at scale, there is very limited information in relation to the variable behaviour of rock mechanics parameters at different scales. Any study that did look at these influences typically related to scaling the Uniaxial Compressive Strength or the shear strength of surfaces rather than the fundamental parameters. In general, studies considering scale effects contain the following three limitations:

- Very small sample sizes. Typically less than 10 with samples reducing in number for larger sizes.
- The strength is explained through Weibull statistics or some power law; that is, they predict zero strength at infinite scales or some arbitrarily chosen asymptotic value.
- Material constants and curve fitting parameters are used to fit data. These constants have no physical meaning other than increasing the relationship fit and vary greatly between rock types. With an inability to directly measure these constants, it makes it difficult to routinely calculate them without site specific testing.

Heterogeneous stochastic modelling was presented as a cost effective alternative to physical testing in order to approximate scaling laws for rock. The limiting feature of forward prediction by numerical modelling is that the output is a direct result of the assumed inputs. For heterogeneous stochastic modelling, the problem requires not only the selection of an appropriate constitutive model, but also valid approximations for the PDF of each relevant material parameter. Without a sufficient understanding of the PDF of all key material parameters, there can be limited confidence in numerically obtained scaling laws.

When considering scale effects for discontinuities, it is evident that a common limiting factor of understanding the shear strength of discontinuities at scale is the inability to accurately quantify large scale discontinuity features, in particular discontinuity roughness. Fractal methods are a mathematical description of discontinuity roughness meaning that their behaviour is well defined mathematically at any conceivable scale and parameter combination. Fractal methods may provide practical solutions to quantifying the nature of discontinuity roughness at scales, which are unpractical or costly to measure. Fractal methods can also be numerically generated in both two and three dimensions to arbitrary precision and may remove the issues associated with surface scanning methods for numerical analysis. This mathematical approach also lends itself to exploring probabilistic descriptions of discontinuity roughness, which can aid in scale-dependant, risk based designs.

In relation to this Thesis, heterogeneous stochastic modelling offers a reasonably cheap method of estimating general probabilistic scaling laws for rock parameters, but first requires the determination of representative PDFs for all input material parameters associated with one RVE. Fractal methods also offer a sound method of quantifying probabilistic scaling laws for rock discontinuities in terms of practical measurements, which can be compared to experimental evidence to justify their applicability. If these fractal methods are applicable, they can be used in conjunction with heterogeneous stochastic methods to quantify all shear strength parameters of the Barton Bandis criterion for application in scale dependant POF analysis.

1.6 Research Direction Based on Literature

In order to summarise and demonstrate the main identified industry limitations from the completed literature review, consider the following FOS POF example problems each highlighting a particular limitation.

1.6.1 Industry limitation example one

A mine wants to construct a simple bench that contains a single cohesionless daylighting joint. The joint has a constant dip of 27° and is subparallel to the slope. It is known from field testing that the average joint friction angle is 30°, the minimum joint measurement is 20°, the most commonly recorded joint friction angle is 25° and a back analysis from a similar failure at the operation estimates the joint set friction angle to be 27.5°. The design FOS and POF are obtained by using Equation 3 and Equation 22 respectfully. Four different site Engineers are asked to calculate the FOS and POF for the slope design and provide a defendable justification for their deterministic design choices. The calculated FOS, POF and justification of each engineer is shown in Table 9. Note that the POF is calculated using a triangular distribution for the joint friction, easily constructible and justifiable from the problem description.

Table 9 Example one - calculations and Engineer justifications of Factor of Safety

	Friction angle used	Justification	Calculated FOS	Closed form POF
Engineer 1	30°	Using the mean friction angle is commonly used in literature to describe joint friction when considering FOS.	1.13	35.20%
Engineer 2	20°	A conservative choice to account for the most adverse conditions.	0.71	
Engineer 3	25°	This friction angle is the most commonly measured value and is therefore the best estimate	0.92	
Engineer 4	27.5°	The back analysis failure is representative of in-situ conditions and is therefore the best estimate	1.02	

Each Engineer's result in Table 9 relates to the exact same stability problem, yet all Engineers have calculated a different FOS and the same POF. The deterministic value selection criteria used by each Engineer is reasonable and therefore one may ask, which of the four FOS values is most representative or most intuitive for the design's stability? Based on current industry practices, each FOS POF evaluation in Table 9 produces four equally valid yet drastically different FOS POF relationships. If each Engineer extended their analysis to consider a larger range of joint orientations, the FOS POF relationship each engineer would produce is shown in Figure 12.

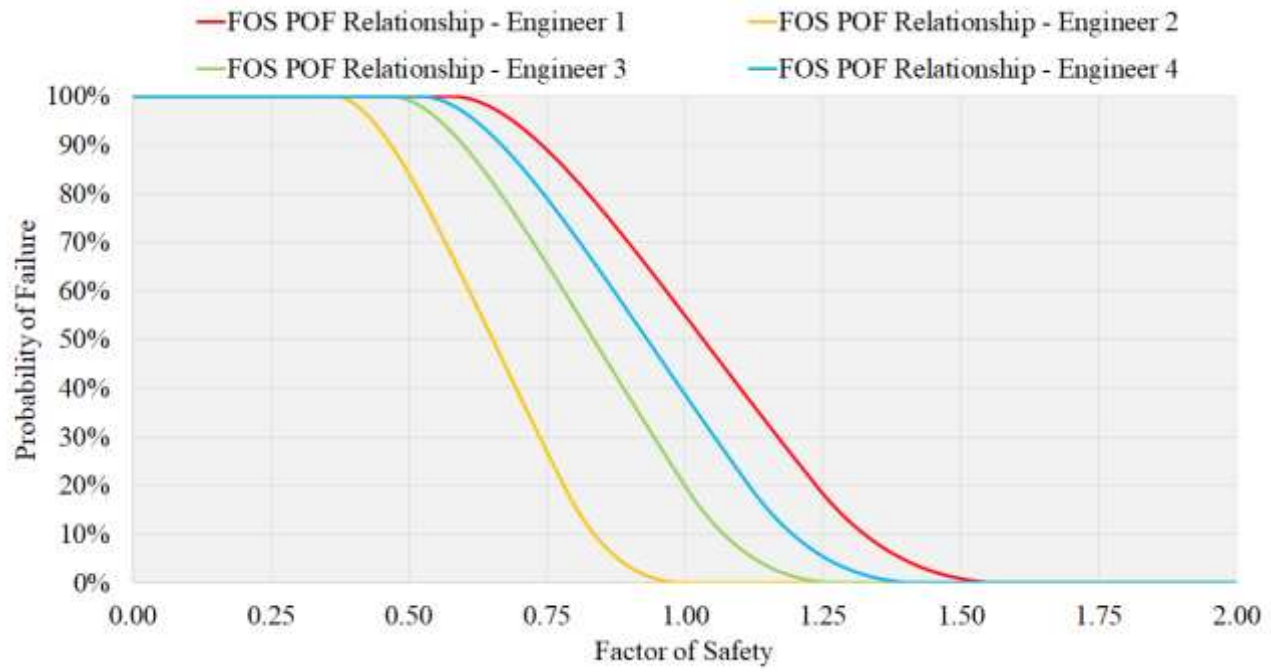

Figure 12 Example one - Factor of Safety Probability of Failure relationship for each Engineer

The results shown in Table 9 and Figure 12 demonstrate that without consistent deterministic selection criteria for material parameters, it is impossible to produce a consistent relationship between FOS and POF as each selection criterion alters the relationship between FOS and POF. Also of interest is that no Engineer has produced a POF equal to 50% for a FOS equal to one from their analysis, refuting the claim that this feature must be true in all FOS POF relationships.

1.6.2 Industry limitation example two

Consider a different mining scenario where three Engineers agree on what deterministic FOS to use but have conflicting views on how to describe probabilistically, each material parameter. Each Engineer assesses the same bench using Rocscience's Slide and calculates the FOS and POF for a proposed slope design, but choose to describe all material parameters using different PDF assumptions:

- Engineer one - uniform distributions for each material parameter;
- Engineer two - normal distributions for each material parameter; and
- Engineer three - triangular distributions for each material parameter.

Also of note is that the PDFs chosen by each Engineer have identical minimums, maximums, means, modes and median values. The model parameter inputs are shown in Table 10 with the analysis results being shown in Table 11. Note that the standard deviations for the normal distribution assumptions are chosen such that the minimum and maximum values align with the third standard deviation.

Table 10 Example two - input Probability Density Function summary

	Minimum value	Mean value	Maximum value
Slope angle (˚)	-	60	-
Slope height (m)	-	52	-
Unit weight (kN/m³)	25.0	27.5	30.0
Cohesion (kPa)	0.0	2.5	5.0
Friction (˚)	30	35	40

Table 11 Example two - slide simulation Probability of Failure summary. 5000 realisations used in each simulation

	Engineer one - uniform distributions	Engineer two - normal distributions	Engineer three - triangular distributions
Minimum slip circle	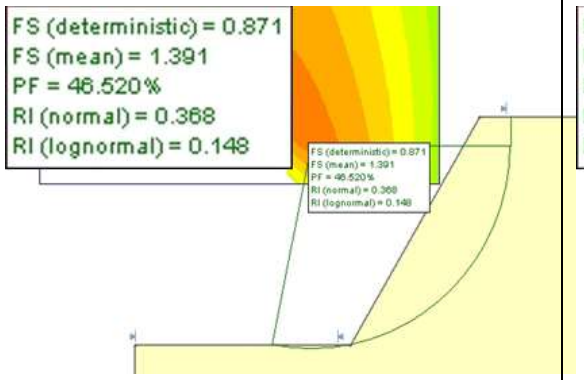	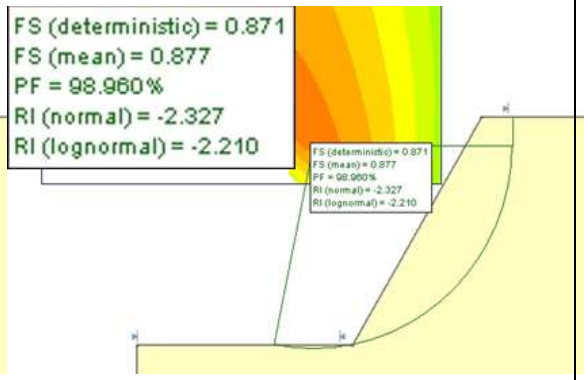	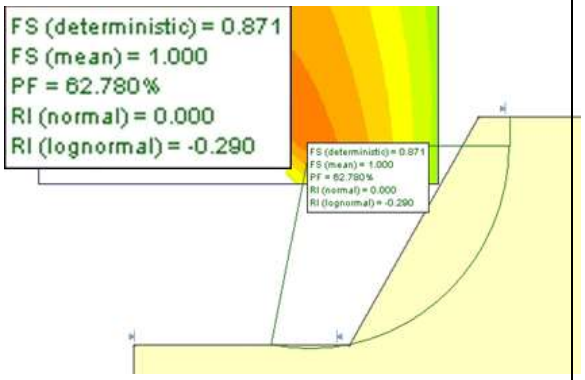
Deterministic FOS	0.87	0.87	0.87
Mean FOS	1.39	0.88	1.00
POF	46.52%	98.96%	62.78%

Note that in Table 11 FS(deterministic) is the FOS obtained using mean value inputs, FS(mean) is the average FOS obtained from the probabilistic simulation, PF is the POF and is defined in the usual manner and RI is the Reliability Index calculated by assuming either a normal or log-normal FOS distribution.

By consideration of Table 11, it can be seen that each Engineer produces the same deterministic FOS, but produce drastically different values for the POF. By considering how the POF is calculated, it is unsurprising that all three produce different values of the POF. By considering Equation 22 for each Engineer's assumptions, $F(\cdot)$, $G(\cdot)$ and $Z(\cdot)$ have changed. The integral may still have the same bounds but a different function is being integrated and therefore there is no reason why the integral should produce an identical value. A further implication of this is that unless the function $Z(\cdot)$ varies in a systematic and predictable way across all rock slope designs, it is again impossible to determine a general relationship between FOS and POF. Worded differently, without a consistent PDF assumption or sufficiently strict guidelines to what PDFs are representative for each material parameter, no relationship between FOS and POF can be obtained.

1.6.3 Industry limitation example three

A third limitation associated with current practises deals with a fundamental uncertainty in data collection. Rock can have essentially an unlimited combination of relevant mechanical or strength related material parameters that can vary considerably even between identical lithologies or even over a local distance. The only method of quantifying local conditions is to complete a range of laboratory tests, which form an estimate of the true in-situ conditions. This approach will always incur some degree of error between measured values and the true value, with this error systematically decreasing with increasing numbers of measurements. For a practical application of a FOS or POF, a design must meet some acceptance criteria, for example a FOS greater than 1.5 or a POF less than 1% and there is little or no considerations given to sampling error influences. When this is worded as a question, does a FOS or POF calculated using 5 field measurements have the same meaning or significance as a FOS or POF calculated using 500 measurements?

To explore this influence, consider a flat underground mineral deposit that is mined by four independent companies using an identical room and pillar mining method. All companies use and simple pillar stability equation defined in terms of the mean pillar strength $\bar{\mu}$ (Pa) and the equivalent pillar stress σ_{zz} (Pa) such that:

$$FOS = \frac{\bar{\mu}}{\sigma_{zz}} \qquad \text{Equation 43}$$

For this example, each mine is designing a pillar where the equivalent pillar stress σ_{zz} is 30 MPa. Each company has completed a different number of laboratory Uniaxial Compressive Strength (UCS)

tests, which range from 20 tests through to 1000 tests and do not share their laboratory measurements with other companies. Unknown to all companies the true UCS distribution is described by a log-normal distribution with a log-location of 3.912 and a log-scale of 0.5. For clarification, this example differs from the example two in Section 1.6.2 as all companies are using identical deterministic estimates and in theory, the same (unknown) PDF with different levels of understanding based on sampling errors.

Each company uses their own strength database to calculate the FOS and POF of the example pillar. Their estimates of FOS and POF as well as the true values are presented in Table 12. Note that the POF is calculated from the Empirical Distribution Function derived from each company's database and does not assume any particular PDF.

Table 12 Example three - Factor of Safety and Probability of Failure as a function of measurement sizes

	Number of laboratory samples	Mean UCS	Calculated FOS	Calculated POF
Company one	20	54.00 MPa	1.80	30.00%
Company two	50	61.20 MPa	2.04	10.00%
Company three	250	55.80 MPa	1.86	14.80%
Company four	1000	56.40 MPa	1.88	14.60%
True State	-	56.66 MPa	1.89	15.35%

By review of Table 12, it is apparent that all companies produce reasonably consistent FOS values, but do produce a larger range of POF values. The results in Table 12 are visually compared to the true underlying relationship in Figure 13.

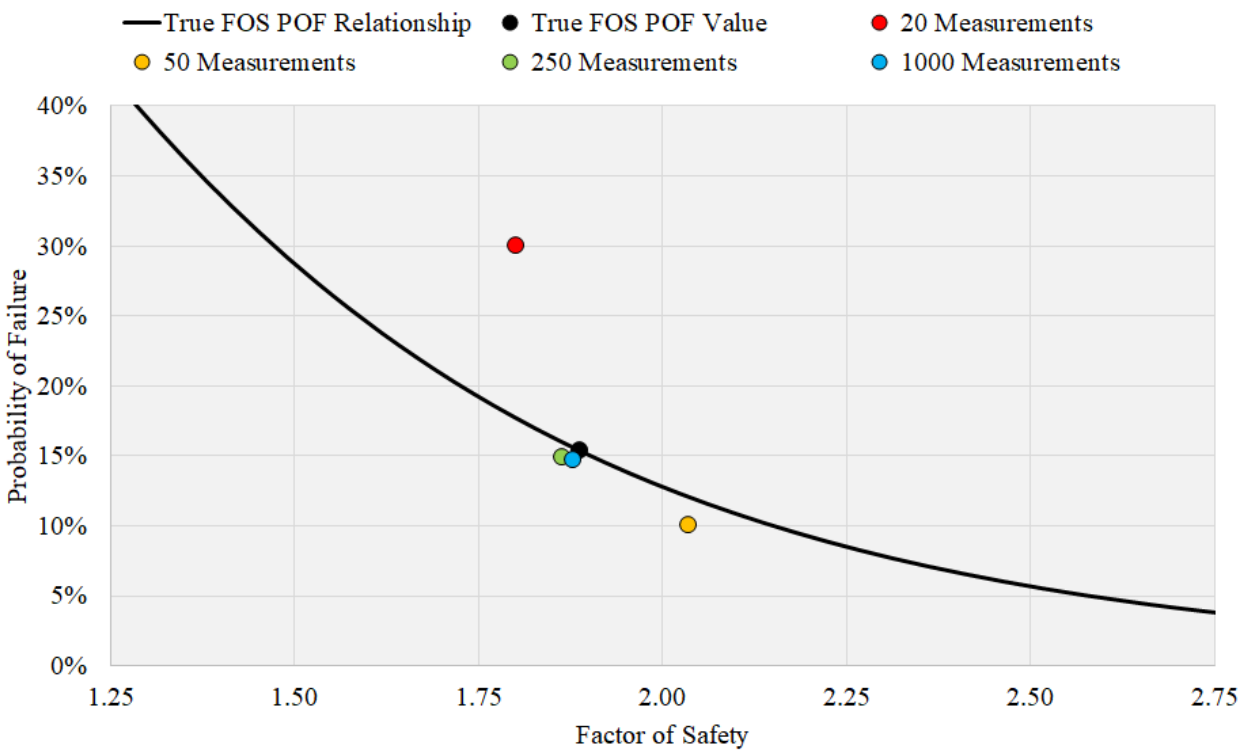

Figure 13 Example three - comparisons of calculated Factor of Safety and Probability of Failure for different sample sizes

It can be seen in Figure 13 that the higher the number of samples, the closer the FOS and POF tend to the true value. The results presented in Table 12 are single evaluations of a much larger range of possible results obtained for a given number of measurements. If each operation repeated their testing campaign 350 times each, Figure 14 shows the spread of possible FOS POF relationships that could have been presented in Table 12.

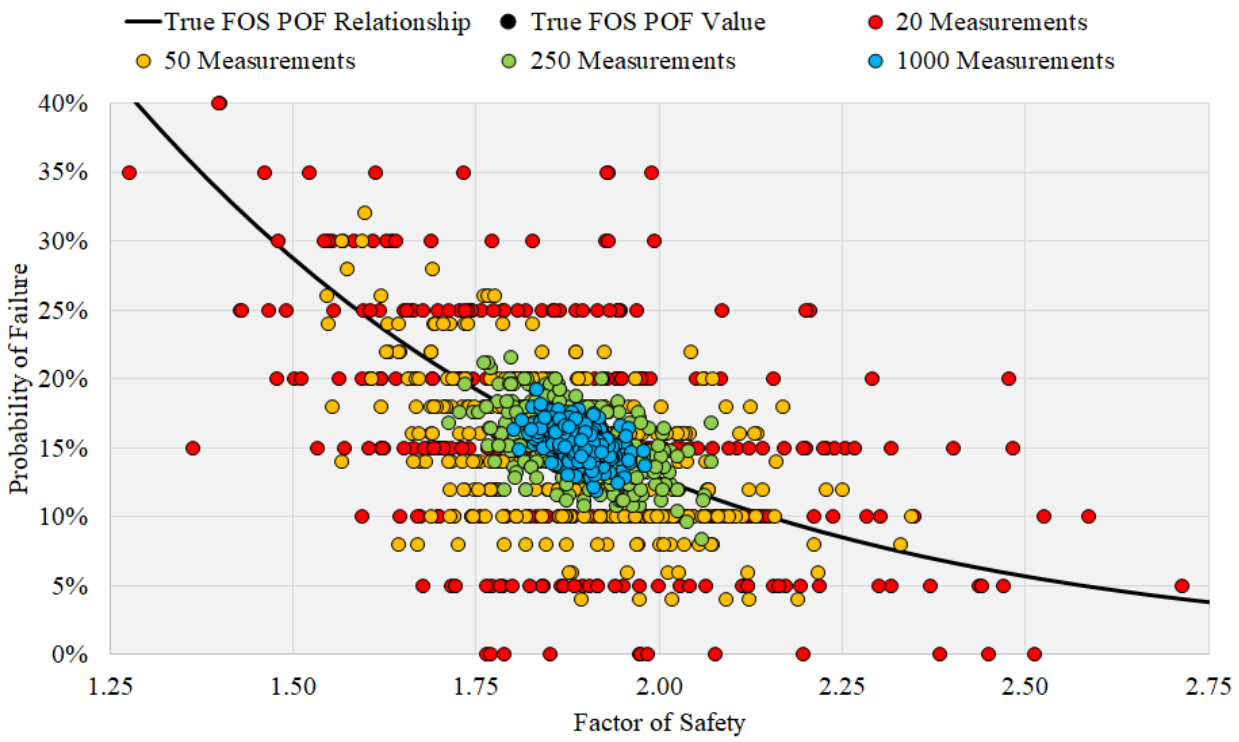

Figure 14 Example spread of possible Factor of Safety and Probability of Failure evaluations based on random sampling

The findings shown in Figure 14 highlight an overlooked issue when dealing with FOS and POF relationships. Based on current practices, each estimate shown in Figure 14 are equally valid estimates of the FOS POF relationship. This sampling error will also influence which PDF appears reasonable when considering statistical fitting techniques. A summary of the possible ranges that could have been obtained are suppled in Table 13.

Table 13 Possible Factor of Safety and Probability of Failure ranges based on sample size

	Number of laboratory samples	FOS Range	POF Range
Company one	20	1.28 - 2.71	0.00% - 40.00%
Company two	50	1.55 - 2.34	4.00% - 32.00%
Company three	250	1.71 - 2.07	8.40% - 21.60%
Company four	1000	1.80 - 1.98	11.90% - 19.20%
True State	-	1.89	15.35%

Based on current industry approaches, this fundamental uncertainty is not really dealt with in any robust manner. Two typical approach would be to complete a sensitivity analysis to calculate the stability over some finite range of material parameter inputs, or use a very conservative value such as the lowest observed strength. These minimum strength approaches do have practical implications as Engineers are 'incentivised' to test fewer and fewer samples. This is because the more laboratory samples that are measured, it is more likely that a very low value will be obtained. Insight into the fundamental sampling error and its implications to practical designs is an important feature that needs to be considered not only for design stability but also for personnel safety and project economics.

1.6.4 Requirement for Universal Distribution Functions and proof of concept

In attempting to find a representative relationship between FOS and POF, a review of literature and several examples have demonstrated that current industry knowledge is insufficient to produce a meaningful relationship between FOS and POF for rock slopes. Engineers are currently free to choose any defendable value for each relevant material parameter, which can create inconsistent FOS relating to a POF (presented in Section 1.6.1). Engineers are also free to choose how they wish to define the PDF of each relevant material parameter with their selection ultimately changing the POF. This PDF selection is often poorly justified and relies on matching PDF assumptions from literature or simple assumptions like a normal distribution. When the same problem is analysed using different PDF assumptions, significant changes in the calculated POF are observed (presented in Section 1.6.2).

With these current inconsistencies for both deterministic and probabilistic material parameter selection, it is highly unlikely that a usable relationship between FOS and POF can be obtained from current industry practices. When the scale considerations are included, the FOS POF problem becomes even less understood, with very few studies even considering the probabilistic behaviour of rock at scale, in any meaningful detail. In order to achieve a usable relationship between FOS and POF considering scale, further research is required in the following four areas:

- deterministic selection criteria;
- probabilistic selection criteria;
- influences of sampling errors on deterministic and probabilistic estimates; and
- probabilistic descriptions of material parameters at scale.

In order to select meaningful and consistent inputs for both FOS and POF analysis, a greater appreciation of the intrinsic variability of material parameters is required. The ideal solution would be to have a set of equations that can adequately describe the variability of any material parameter from a geotechnical database, which provide appropriate guidance to perform the desired deterministic or probabilistic analysis. For this to be possible, it needs to be demonstrated that the variability of material parameters of rocks can be universally approximated by some specific PDF family; that is; each material parameter can be described by a **Universal Distribution Function** (UDF). If this is not possible then a routine can be developed in order to approximate appropriate parameter inputs on a case by case basis. From these UDF descriptions, it should be possible to define intuitive and consistent guidelines for calculating either a FOS or POF and hence compute a usable FOS POF relationship. This Thesis will therefore focus primarily on the approximation, and quantification of these hypothesised UDFs, and how they are influenced by changing problem scales. The qualitative governing hypothesis relating to material parameter variability to be explored in this Thesis is given as:

Irrespective of lithology or formation, there are statistically justified, universally definable Probability Density Functions that sufficiently describe the in-situ variability of mechanical and geological parameters for rock.

This hypothesis can be written as an equivalent mathematical proposition:

There are some constants $s_1, s_2, \dots, s_n$ *such that* $F(xs_1) = F(xs_2) = \cdots = F(xs_n)$ *where* F *is the distribution of the unscaled measurement for variable i.*

The intent of the above hypotheses is not to suggest that all rocks have identical PDFs for their material parameters, but rather they have a specific PDF family associated with each parameter. The constants s_i in the above proposition are such that the material specific PDF is produced for each unique rock type. Practically, the intent is to answer the following (example) question: Can the basic friction angle of rock always be approximated by a normal distribution? If not, how can the case specific PDF for the basic friction angle be routinely estimated for engineering purposes?

In order to demonstrate how this concept of UDFs in conjunction with a standardised deterministic selection criteria resolves some current industry limitations, reconsider the underground pillar example from Section 1.6.3. Now suppose much more is known about material parameter variability. It has been shown that the UDF that describes rock's UCS is known, and is described by a log-normal

distribution, whose log-scale is always 0.5. It has also been decided that all deterministic FOS calculations must to be calculated using the average UCS.

Under these restrictions, the FOS equation is fixed and given by Equation 43, the deterministic inputs are consistent and the PDF (i.e., the UDF) is also consistent. With all these known properties, it is then possible to calculate the closed form relationship between FOS and POF using Equation 43 and Equation 22:

$$POF = \frac{1}{2} + \frac{1}{2}\text{erf}\left(\frac{1 - 8\ln FOS}{4\sqrt{2}}\right) \qquad \text{Equation 44}$$

where erf is the Gauss Error Function. By consideration of Equation 44, the POF is only dependant on the specified FOS and will always return the exact POF. This means that the only sampling error in the calculation comes from the uncertainty associated with the average UCS measurement. This is visually shown by updating Figure 14 to produce Figure 15 using Equation 44.

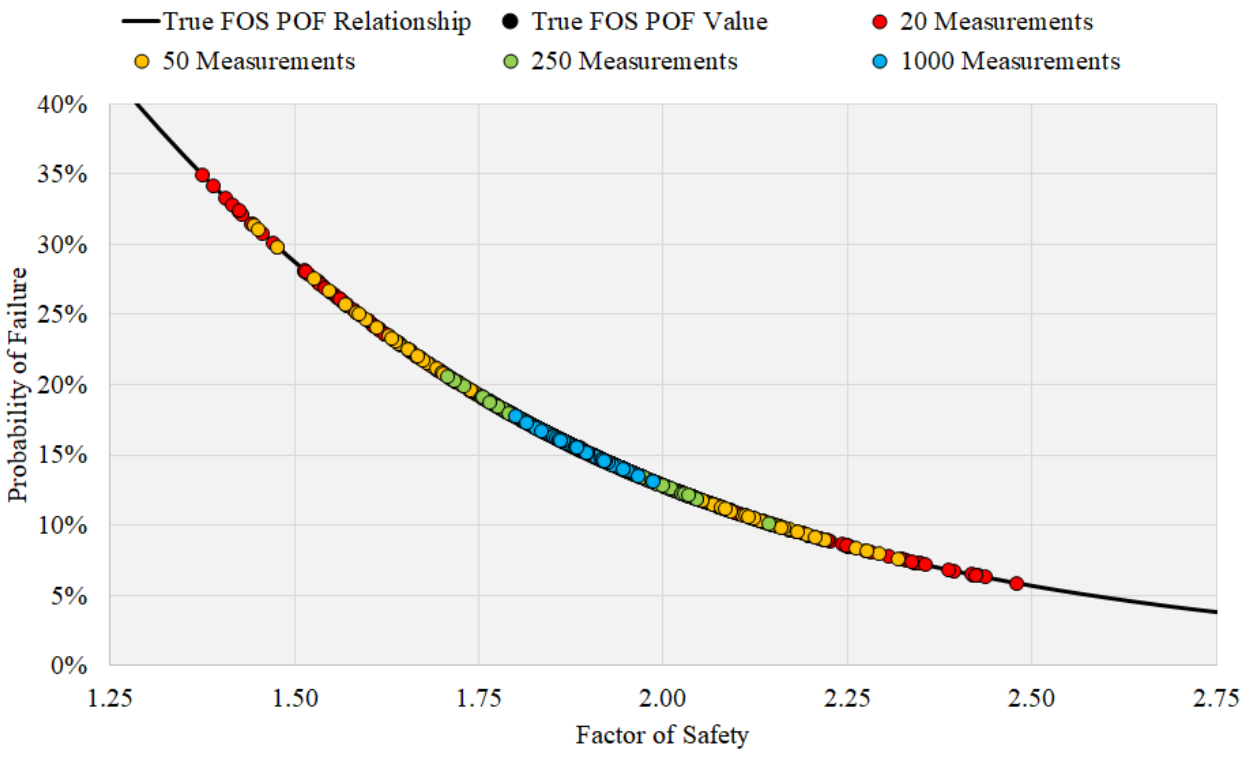

Figure 15 Example spread of possible Factor of Safety and Probability of Failure evaluations based on Universal Distribution Functions

For clarification, this approach only has an uncertainty in the value of FOS, verse the original case when there was an uncertainty associated with both the FOS and the POF calculation. As the UDF is known and the deterministic FOS is calculated using the average UCS, the sampling error associated with the calculated FOS is also known and can be calculated using Equation 46:

$$\sigma_{\bar{\mu}} = \frac{S}{\sqrt{n}} \qquad \text{Equation 45}$$

$$\bar{\mu} = \hat{\mu} \pm Z_{\alpha}\sigma_{\bar{\mu}} \qquad \text{Equation 46}$$

where $\sigma_{\bar{\mu}}$ is the mean standard error, S is the UDF standard deviation, n is the number of samples, $\hat{\mu}$ is the mean value estimate and Z_{α} is the standard normal distribution. For a 95% confidence interval:

$$\bar{\mu} = \hat{\mu} \pm 1.96\sigma_{\bar{\mu}} \qquad \text{Equation 47}$$

From this known relationship, each company can calculate their unique FOS as well as an appreciation for what the true POF is, given their understanding of the rock's UCS. Table 14 presents an updated version of Table 12 with the known and quantifiable uncertainty.

Table 14 Factor of Safety Probability of Failure bounds using Universal Distribution Functions

	Mean UCS with 95% confidence interval	Calculated FOS	Calculated POF
Company one	54.00 ± 13.23 MPa	1.80 ± 0.44	8.63% - 35.82%
Company two	61.20 ± 8.37 MPa	2.04 ± 0.28	7.60% - 18.89%
Company three	55.80 ± 3.74 MPa	1.86 ± 0.12	13.11% - 19.70%
Company four	56.40 ± 1.87 MPa	1.88 ± 0.06	14.06% - 17.23%
True state	56.66 MPa	1.89	15.35%

To demonstrate the implications of this quantifiable sampling error, say for this example the acceptable pillar POF is 20%. Using this criteria and the information presented in Table 14, Company one has enough insight and doubt about the particular pillar meeting the desired criteria and may choose to further quantify the rock's UCS or modify their pillar design to meet the required POF.

Companies two, three and four are confident their design meets this requirement and may go for slightly more risky pillar designs to achieve a POF equal to 20%.

This UDF approach can also be generalised to consider scale effects. Suppose that similarly to the UDF of laboratory scale UCS, the scale dependant UDF is also known. There is also known to exist a **Universal Scale Function** (USF), which describes how the deterministic input (i.e., the average UCS) changes as a function of scale. For this example, the scale dependant UDF is a log-normal distribution with the log-scale given by:

$$S_{V_n} = \frac{S_{V_0}}{\sqrt{V_n}} \qquad \text{Equation 48}$$

where S_{V_n} is the log-scale (Pa) associated with a pillar volume V_n (m³) and S_{V_0} is the log-scale (Pa) associated with laboratory scale measurements. The accompanying USF is given by:

$$\bar{\mu}_{V\,n} = \frac{\bar{\mu}_{V\,0} - \bar{\mu}_{V\,\infty}}{\sqrt[3]{V_n}} + \bar{\mu}_{V\,\infty} \qquad \text{Equation 49}$$

where $\bar{\mu}_{V\,n}$ is the mean strength (Pa) associated with a pillar volume V_n (m³), $\bar{\mu}_{V\,0}$ is the mean strength (Pa) associated with laboratory scale measurements and $\bar{\mu}_{V\,\infty}$ is the asymptotic UCS (Pa). For this example the value of $\bar{\mu}_{V\,\infty}$ is given as 35% of the mean UCS and V_0 is equal to 1 m³. The USF and UDF are then presented in terms of the scale dependant FOS, FOS_{V_n}:

$$FOS_{V_n} = \frac{\bar{\mu}_{V\,n}}{\sigma_{zz}} \qquad \text{Equation 50}$$

Note: σ_{zz} is always calculated from the problem geometry and is always correct for the scale of interest. If Equation 44 is updated to consider FOS_{V_n} then the scale dependant POF is described by:

$$POF = \frac{1}{2} + \frac{1}{2}\,\mathrm{erf}\left(\frac{1 - 8V_n \ln FOS_{V_n}}{4\sqrt{2V_n}}\right) \qquad \text{Equation 51}$$

Equation 51 then expresses how to account for all literature documented scale phenomena and still produces a closed form equation relating the FOS and POF for any desired problem scale. Some scale dependent FOS POF relationships using Equation 50 and Equation 51 are shown in Figure 16.

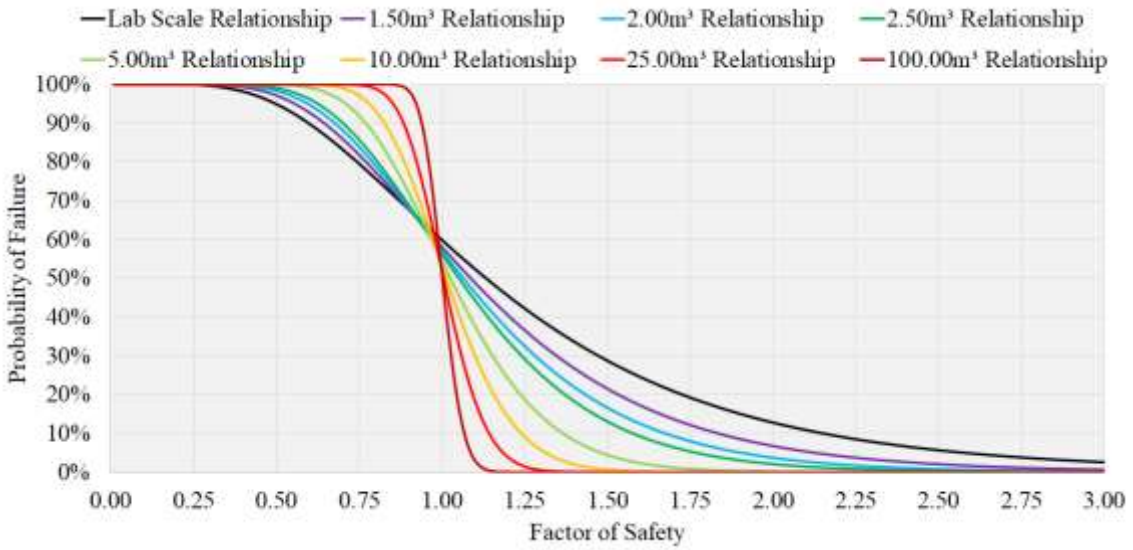

Figure 16 Example scale dependant Factor of Safety Probability of Failure relationship - scale dependant Factor of Safety

Depending on which measure of FOS (laboratory scale or scale dependant) is used, two different scale dependant relationships between FOS and POF relationships are produced. The scale dependant FOS POF relationships using the laboratory scale FOS are shown in and Figure 17.

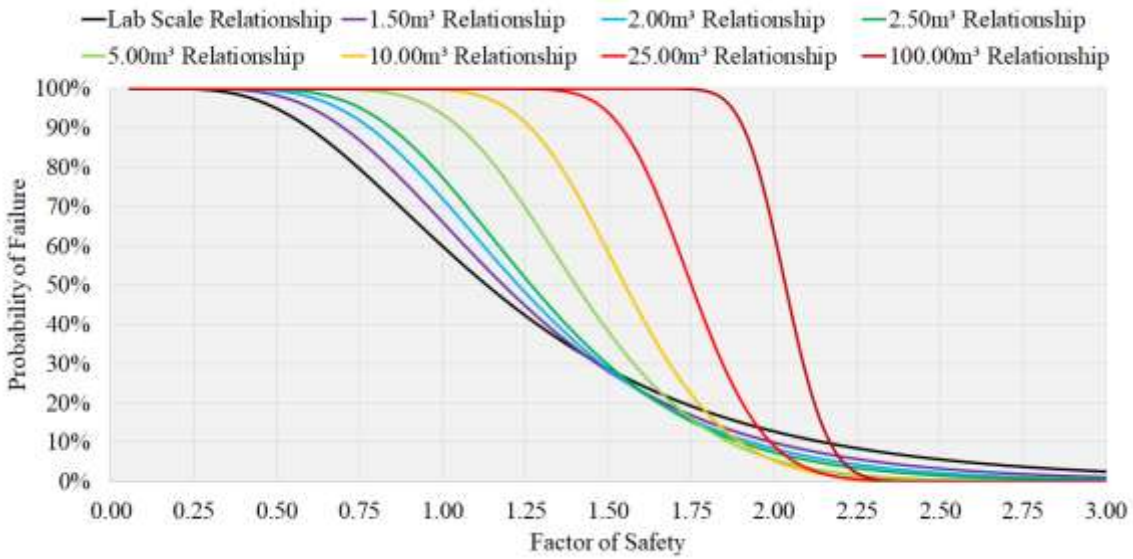

Figure 17 Example scale dependant Factor of Safety Probability of Failure Relationship - laboratory scale Factor of Safety

The scale dependant UDF USF formulation can also utilise the known measurement error and propagate this to consider the uncertainty in the POF at arbitrary sizes. An example of the FOS and POF uncertainty at a pillar volume of 25m³ is shown in Table 15.

Table 15 Example of scale dependant Factor of Safety and Probability of Failure error propagation

	Mean UCS with 95% confidence interval	Calculated FOS at 25m³	Deterministic POF	Calculated POF range
Company one	31.63 ± 4.52 MPa	1.05 ± 0.15	31.62%	3.47% - 85.67%
Company two	34.09 ± 2.86 MPa	1.14 ± 0.10	10.97%	2.10% - 36.28%
Company three	32.24 ± 1.28 MPa	1.07 ± 0.04	25.11%	14.45% - 39.50%
Company four	32.45 ± 0.64 MPa	1.08 ± 0.02	23.13%	17.62% - 29.61%
True state	32.54 MPa	1.09	22.30%	22.30%

Based on this proof of concept it is apparent that an approach considering UDFs is able to overcome many of the currently experienced industry limitations and produce meaningful and consistent scale dependant FOS POF relationships. Currently these UDFs and USFs are hypothesised to exist and needs to be either mathematically derived or experimentally validated.

1.7 Research Methodologies and Key Research Focuses

In order to achieve the aims and address the limitations presented, this Thesis has been separated into four key research focuses, each addressing a major limitation associated with current industry practices. A common underlying theme for all key focuses is the notion that rock exhibits an approximate universal probabilistic behaviour. Although this is most heavily assessed in Chapter Two, this assessment methodology is a common feature of all Chapters. The following sections outline the aim and test methodology for each proceeding Chapter in this Thesis.

1.7.1 Research focus one - testing for Universal Distribution Functions

The initial starting point of this Thesis is to provide sufficient evidence that UDFs are a sufficient approximation and are suitably generalisable as to apply to any given rock problem at the laboratory scale. To date, no such large scale variability analysis has been completed on rock material parameters. The methodology of assessment must be robust enough to identify these hypothesised UDFs as well as make as few initial assumptions as possible. To test for UDFs, the governing hypotheses presented previously in Section 1.6.4. To test whether a UDF exists for rock material parameters at the laboratory scale, the following methodology was used to build a sufficiently strong argument to accept or reject their existence:

Step 0 - Selection of an appropriate test type and level of significance

Statistical testing methods can be broadly categorised as either parametric or non-parametric. Although there is no set definition of what constitutes a parametric or non-parametric test (Walsh 1962), non-parametric tests make fewer model assumptions compared to their parametric counterparts. Generally, non-parametric tests have broader applications at the expense of statistical power for the same sample size (Mumby 2002). A comparison of the typical assumptions associated with each testing method is shown in Table 16.

Table 16 Comparison between parametric and non-parametric test assumptions

Statistical test type	Parametric testing	Non-parametric testing
Probability Density Function assumption (Glass, Peckham & Sanders 1972)	Samples assumed to follow a normal distribution	No assumption about sample Probability Density Function
Variance assumption (Glass, Peckham & Sanders 1972)	Assumed equal variance across all groups	No assumption of equal variances
Measure of central tendency (Mehotcheva 2008)	Mean	Median
Statistical power (Walsh 1962)	Generally higher power	Generally lower power
Data type (Walsh 1962)	Quantitative only	Qualitative and quantitative
Number of samples (Hoskin 2009)	Typically >30	Small sample sizes allowed

The significance level of a test, α is a measure of how statistically different a test result must be in order to reject the associated test hypothesis (Motulsky 2007). Typically α is set to 0.05 (5%) for most engineering and scientific applications and means that for a given test there is a 5% (or 1 in 20) chance of obtaining a false positive (Motulsky 2007). To align with common engineering and scientific applications, all statistical tests were conducted at a 5% statistical significance. Where applicable, binomial confidence intervals are also used to verify if the overall acceptance or rejection of the test hypothesis was consistent with the expected Type I errors. This additional step is synonymous with repetition testing to ensure that consistent results are being obtained across many statistical realisations.

Step 1 - Amass a large geological database covering numerous lithologies and spatial locations

The laboratory scale geological database was been amassed from 25 different data sources, of which most were the geotechnical database of operating mines in Australia. Each source typically contained between one and ten individual lithological units. The following rock parameters and associated data ranges are stored in the database:

Table 17 Intact rock material parameter database summary

Intact rock material parameter	Number of data sets	Range of mean values
Uniaxial Compressive Strength	41	4.065 MPa – 240.500 MPa
Point Load Test Index	34	0.17 MPa – 7.52 MPa
Uniaxial Tensile Strength	20	1.167 MPa – 23.454 MPa
Peak friction	17*	21.54° – 43.03°
Residual friction	10*	23.95° – 38.29°
Dry density	35	1.27 g/cm^3 – 3.32 g/cm^3
Young's Modulus	27	1.52 GPa – 75.50 GPa
Poisson's Ratio	27	0.035 – 0.310

*Many friction data sets were sourced from two PhD theses completed by Coulson (1970) and Tse (1979). This covered a wide range of prepared direct shear tests and lithology types in each study. More detail for each data set is presented in the Appendix.

Step 2 - Transformations to obtain the unscaled measure for each data set

In order to directly compare very different data sets, a descaling process needed to be completed to obtain the unscaled measure of each material parameter. All data was transformed by dividing each data point by the sample's median value. The median value was chosen over the mean value as it is far less susceptible to outlying values and is the typical measure of central tendency associated with non-parametric testing.

Step 3 - Test for the existence of a UDF by using non-parametric bootstrapping techniques

Two tests for the appropriateness of a UDF were used for this Thesis, the Kruskal Wallis Analysis of Variance (KW ANOVA) and non-parametric bootstrapping. The KW ANOVA is a comparative rank based method similar to the parametric Analysis of Variance (Van Hecke 2012). The KW ANOVA is used to test whether different samples are drawn from the same underlying PDF (Kruskal & Wallis 1952). The test hypothesis for the KW ANOVA is stated as:

k Independent random samples have the same distribution function, $F_1(\cdot) = \cdots = F_k(\cdot) = F$*;*

The Kruskal-Wallis test statistic H, is calculated using Equation 52:

$$H = \frac{12}{N(N+1)} \sum_{i=1}^{k} \frac{R_i^2}{n_i} - 3(N+1) \qquad \text{Equation 52}$$

where, N is the total number of observations over all samples, R_i is the sum of the ranks in the ith sample group, n_i is the number of observations in the ith sample and k is the number of sample groups. For sample groups containing more than five observations (Moore & McCabe 2006), H follows approximately a Chi-Squared distribution, $\mathcal{X}^2_{k-1,\alpha}$. These critical Chi-Squared distribution values are widely available in look-up tables, statistical software or common spreadsheet applications. If the test hypothesis is rejected, it is possible to determine whether the data completely, partially, or totally does not support the hypothesis (Acar & Sun 2013). This is done by performing pair-wise comparisons using KW ANOVA.

When datasets were transformed about the median value, comparisons using the KW ANOVA would generally accept the test hypothesis. To compensate for this influence, non-parametric bootstrapping was used to test for a common underlying PDF for descaled data. Bootstrapping is a statistical resampling method first introduced by Efron (1979) and is a simple method for estimating sample characteristics based on randomly resampling with replacement, an available dataset. Bootstrapping techniques were used to check to some significance level that Independent Identically Distributed samples are drawn from the same underlying PDF. The test hypothesis for the non-parametric bootstrapping is identical to the test hypothesis for the KW ANOVA. The bootstrapping test logic and methodology is detailed below:

Suppose that n descaled samples follow some UDF (i.e., the test hypothesis is true). If additional descaled samples are obtained and tested it stands that these samples should also follow the same UDF under the assumption the test hypothesis is true. It is possible to compute the $\binom{n}{2}$ pairs of observable statistical differences between each pair combination and determine the largest difference associated with the $\binom{n}{2}$ descaled pairs.

If the n descaled samples are pooled together, it stands that there should be no discernible method of determining the origin of any single sample. If the pooled data are sufficiently large and resampled (bootstrapped) using the n sample sizes, the resamples will approximate the underlying PDF. By computing the largest statistical difference between each $\binom{n}{2}$ bootstrapped pair, a single approximation of the maximum statistical difference between any random samples that may occur by chance alone can be obtained. This may be repeated k times to gain a distribution of the largest statistical difference.

The largest statistical difference associated with the n descaled samples can be compared with the range of bootstrapped statistical differences to see how consistent the assumption of a UDF is. If the statistical significance α percent of the bootstrapped largest statistical difference is larger than the largest statistical difference from the n descaled samples, then it can be concluded that the data are consistent with the test hypothesis (i.e., there exists some UDF). If the associated percentage of the largest statistical difference is smaller than statistical significance α then the test hypothesis must be rejected.

Step 4 - Estimate the characteristics of plausible distributions using Maximum Likelihood Estimation techniques and mathematical properties associated with each characteristic distribution

With evidence for some underlying UDF, the next step is to estimate what this distribution may be. Maximum Likelihood Estimates (2009) were calculated for each chosen PDF family to estimate the most likely nature of the underlying UDF for each material parameter. Maximum Likelihood Estimates are a statistical technique aimed at estimating the PDF parameter values $\theta_1, \theta_2, \dots, \theta_n$ of an assumed underlying statistical distribution that is most likely to produce the observed data (Ramachandran & Tsokos 2009).

The seven PDF types primarily used are the normal, log-normal, gamma, Weibull, Rayleigh and Laplace distributions. These distributions were chosen as they cover a wide range of general distribution shapes as well as being relatively well known distribution types. It must be noted that although the Maximum Likelihood Estimates do provide the most likely combination of PDF parameter values that would produce the observed data assuming a specified underlying distribution, it does not guarantee a statistically acceptable fit. Maximum Likelihood Estimates need to be verified for their applicability through a goodness of fit test to ensure they are sufficiently accurate.

Step 5 - Test for the goodness of fit of plausible UDFs using the Kolmogorov Smirnov goodness of fit test

The next step is to verify the goodness of fit of the Maximum Likelihood Estimates, to determine the leading approximation for the underlying UDF of each material parameter. As the PDF for each material parameter is expected to be continuous, the Kolmogorov Smirnov goodness of fit (KS) (Chakravarti *et al* 1967) is favoured over the Chi-squared goodness of fit test (Fisher 1922) as it is a more applicable test for continuous distributions. The KS tests if a continuous PDF is sufficient at explaining the observed distribution of Independent Identically Distributed samples. The test hypothesis for the KS test is given as (Chakravarti *et al* 1967):

The Empirical Distribution Function follows the specified continuous Cumulative Distribution Function.

In order to compute the required test statistic, the expected Cumulative Distribution Function (CDF) is compared to the data's Empirical Distribution Function (EDF). EDFs are step functions that describe the CDF of the individual observations, with the equation given as (DuFour *et al* 1998):

$$\widehat{F_n}(x) = \frac{number\ of\ observations\ in\ the\ sample \leq x}{n} = \frac{1}{n}\sum_{i=1}^{n} 1\{x_i \leq x\} \qquad \text{Equation 53}$$

where $\widehat{F_n}(x)$ is the EDF for x, and n is the number of individual samples. The KS test statistic D_n, is calculated using Equation 54 (Chakravarti *et al* 1967):

$$D_n = \sup_x \left|\widehat{F_n}(x) - F(x)\right| \qquad \text{Equation 54}$$

Equation 54 is the correct expression for the maximum absolute vertical distance between the EDF and the assumed CDF. The Critical Statistic for KS can be found in various lookup tables such as Miller (1956).

For each PDF family assessed, initial inputs were based on the Maximum Likelihood Estimates and then varied to obtain the statistically significant range of PDF parameters, which are consistent with the underlying UDF approximation and Type I error. In conjunction to using KS, data was additionally assessed using the Shaprio Wilk (1965) test. This test is a supplementary test to accept or refute the UDF approximation of an underlying normal distribution. The Shapiro Wilk test is chosen for its high statistical power when testing for normality compared to other commonly implemented statistical tests (Razali & Wah 2011). The test hypothesis is given as:

The data follows a normal distribution with unspecified mean and standard deviation.

This additional test was used to help accept or rule out a normal distribution when multiple UDFs were applicable.

Step 6 - Test for possible model simplifications and variable substitutions

As mentioned in Step 3, the data are subjected to a descaling process to allow comparative analysis. A statistical side effect of this process is that the UDF's input parameters are then defined in terms of the scaling variable (i.e., the median value). For completeness, the goodness of fit needs to be replicated for all raw data, as well as assessed for any simplified models or viable variable substitutions. In order to check for these simplifications and substitutions, the leading UDF approximation for each distribution was then subjected to additional KS tests to assess the statistical fit of using the mean value as a substitute for the median value, using a constant scale value instead

of one defined in terms of the median value and all permutations. This reanalysis ensures that all possible UDF formulations are checked and verified for their applicability to real world problems.

Step 7 – Test for multivariate correlations using Pearson's product moment correlation coefficient test

For any pair of measurable material parameters, it is possible that some degree of correlation exists between them. These correlations are important when assessing any problem requiring two or more material parameters to be defined (e.g., strength and elastic parameters). In these scenarios, the conditional distributions need to be correctly generated to ensure the overall probabilistic behaviours are correct. The Pearson's Product Moment Correlation Coefficient Test (Fisher 2016) is used in conjunction with bootstrapping techniques to both test and estimate the correlation coefficients associated with each pair of concurrently measured rock parameters.

Pearson's Product Moment correlation coefficient ρ is a measure of the tendency for two random variables to follow some underlying collinearity. The value of ρ can vary between -1 and 1, with these extremes corresponding to a perfectly negative linear and perfectly positive linear relationship respectfully between observations. The statistical test associated with this variable is the Pearson's product moment correlation test, which tests to some statistical significance if a pair of concurrent observations are correlated or not. The test hypothesis is given as:

The correlation coefficient ρ between the two variables is equal to 0.

Correlation coefficients were initially tested for using Matlab to determine if a general correlation exists within raw samples between different rock parameters, with additional bootstrapping techniques used to estimate a range of plausible ρ. The test logic for estimating rock parameter correlation coefficients is detailed below:

It is unknown if there exists correlation coefficients for any pair rock parameters, but from the geological database (i.e., the untransformed data) it is possible to calculate the correlation coefficient ρ and the associated statistical significance for each combination of concurrently measured parameters for each sample and accept or reject the test hypothesis. From this information, the binomial confidence interval can be used to verify if there is or is not evidence for some general statistically significant correlation between each pair of parameters. This initial test cannot determine what the correlation coefficient is, only if it exists or not.

A similar non-parametric bootstrapping routine used in Step 3 can then be used to estimate the underlying correlation coefficient for each pair of rock parameters. In this test, random pools of sample pairs were generated, with each estimate of ρ being stored. This was repeated 10000 times for each pair of rock parameters. From the bootstrapped ρ values, it is possible to calculate the central region containing 95% of all observed values of ρ across all resamples. This range can be used as a confidence interval containing the value of ρ with 95% confidence. The non-parametric bootstrapping method of estimating ρ was preferred as it makes no assumptions about the distribution of ρ between each pair of rock parameters and is therefore non-parametric.

1.7.2 Research focus two - Universal Distribution Functions at different scales

Due to a lack of available data for rock parameters at increased scales, the strictly empirically based statistical analysis used in research focus one was not applicable. Numerical methods offer a cost effective alternative to physical testing but require a well-defined understanding of all constitutive components and material parameter variability. Although mesoscopic heterogeneous analysis is not new method in geotechnical research, no single study has considered the influences of varying all constitutive model parameters and their associated correlations when modelling scale effects and heterogeneity.

From the findings of research focus one, it stands to reason that if UDFs are modelled to create a large heterogeneous volume of intact rock, when simulated the output should produce reasonable approximations of the true scaling laws for intact material parameters. This process can then be repeated many times to gain an appreciation of the PDF associated with material parameters for any given volume. These results can then be used to estimate the scale dependant UDF relationships and the associated USFs for each material parameter. In order to estimate these scale dependencies the following methodology was used:

1. Generate a three dimensional numerical model that approximates some multiple of one RVE. For example, a numerical sample 5 times larger than a single RVE would be comprised of 125 RVEs arranged in a 5 by 5 by five array.
2. Randomly seed each RVE as per the appropriate UDF and associated correlation coefficients from research focus one.
3. Apply external loads and numerically measure various peak and residual material parameters associated with each sample.

4. Repeat steps 2 and 3 until a sufficient number of numerical measurements are obtained for a given size.
5. Repeat step 1 through 4 for different sample sizes, input values and material responses to look for consistent behaviours with increasing scales using the methodology from research focus one.

In order to achieve this research focus, the purpose built program *The Probabilistic Lagrangian Analysis of Continua with Empirical Bootstrapped Outputs* (PLACEBO) was written which currently operates using Itasca's FLAC3D, and is partially implemented for applications using Itasca's PFC2D, PFC3D and 3DEC. Detail, validation of, and fundamental assumptions for PLACEBO are documented and presented in Chapter Three.

1.7.3 Research focus three - Universal Distribution Functions for rock discontinuities

As the overall aim of this Thesis is to evaluate the FOS POF relationship for structured rock, an appreciation for the probabilistic behaviour of discontinuities at scale is required. The aim of research focus three is to explore the applicability of using fractal methods to derive the UDF and USF for discontinuity roughness at arbitrary scales. The governing hypothesis for this research focus is given as:

Given some roughness measurement $\hat{r}_0$ associated with length L_0, estimate $\widehat{H}$ such that the behaviour of $\hat{r}_n$ is known for any L_n.

A particular emphasis of this research focus was to keep field measurements and mathematical concepts to a minimum such that the methods presented are applicable practical problems. In order to achieve this aim, the following methodology was used:

Step 1 - Selection of a representative roughness measurements and a reasonable fractal simulation method.

Multiple quantitative measures of discontinuity roughness are common in rock mechanics literature. A simple representative roughness measurement needs to be selected to form the basis for the analysis. Numerous methods of simulating fractal geometry are also available, which vary in terms of accuracy, numerical complexity and problem dimensionality. With many simulation methods available, a choice of a representative fractal simulation method applicable to rock engineering problems was selected.

Step 2 - Quantify the expected behaviour of discontinuity roughness measurements as a function of model parameters.

Fractals can be numerically generated for any conceivable combination of input parameters. By simulating and measuring the roughness of numerical discontinuities with multiple input combinations, one can gain an appreciation as to how each parameter influences the measured output and its associated distribution. These simulations can then be used to build a probabilistic description of discontinuity roughness as a function of each parameter. The quantification of roughness was assessed using the general non-parametric framework described in research focus one.

Step 3 - Develop a method of estimating fractal parameters from physical measurements.

Each fractal parameter needs to be estimated from simple field measurement such that all values can be estimated. Equations relating to the mean, mode, median, variance and measurement scale were derived using statistical regression techniques. The fractal parameter estimates associated with Barton's standard profiles where then compared to estimates from other authors.

Step 4 - Compare the expected behaviour of discontinuity roughness to real world measurements.

Any mathematical model needs to be validated with physical measurements to demonstrate the method's applicability. Roughness measurements associated with two different discontinuities over varying scales were assessed to determine the applicability of a fractal based model at practical scales.

Additionally, toppling FOS equations require a probabilistic description of cross joint spacing in order to calculate the associated POF. Theory presented by Hobbs (1967) was used to derive a probabilistic scale dependant model for cross joint spacing in bedded material.

1.7.4 Research focus four - revisiting Factor of Safety and Probability of Failure

The final research focus of this Thesis is to take the findings and revisit the relationships between FOS and POF. The governing hypothesis for this research focus is given as:

If a geological system is sufficiently definable in terms of both variability and mechanical behaviour, a one to one relationship between Factor of Safety and Probability of Failure can be routinely calculated.

The following methodology was used for this research focus:

Step 1 Construct Monte Carlo simulations for each relevant Failure Mechanism. In order to evaluate all identified failure mechanisms for a general slope, commercial software is far too time consuming to consider a wide range of slope geometries and input combinations. In order to evaluate numerous geometries, input combinations and failure mechanisms Monte Carlo simulators were purpose built to randomly generate a mine scale pit slope and material parameter inputs to evaluate the FOS and POF over general conditions for each failure case. The Monte Carlo simulators constructed relate to each FOS equation shown in Table 2.

Step 2 Derive the closed-form approximations for the relationship between Factor of Safety and Probability of Failure. By using various statistical techniques, the relationship between FOS and POF can be explored. Various particular, special and generalised cases for each FOS relationship in Table 2 were assessed to mathematically derive the expected FOS POF relationships for each FOS equation in Table 2.

Step 3 Compare and contrast the closed form relationships to Monte Carlo Sampling. By using the Monte Carlo simulation engines from Step 2, each failure mechanism FOS POF relationship from Step 3 can be compared to Monte Carlo simulations to verify their applicability over a number of input scales, problem geometry and material parameter combinations.

1.7.5 Knowledge gaps addressed

This section gives a brief summary of the key knowledge gaps this Thesis aims to address.

1. Do UDFs exist? Current industry knowledge suggests that there is no consistent probabilistic model for rock parameters. UDFs are required to resolve some of the issues associated with calculating a relationship between FOS and POF.

2. If UDFs exist, do they support previous published finding or provide new insights and relationships for rock parameters?

3. How do all rock material parameters change as a function of scale? Previous numerical analysis only focus on strength parameters and neglect elastic parameters. Is there more to be gained from numerical scale analysis? Rock parameters at scale are treated deterministically, what is the probabilistic behaviour of rock parameters at larger than laboratory scales?

4. If rock discontinuities are fractal, what is the expected probabilistic behaviour? What scaling laws are expected using a fractal model? Is the fractal model supported by field measurements?

5. Can a generalised model for cross joint spacing be calculated from first principals?

6. Do the new findings in this Thesis help address the industry problems for FOS and POF and scale?

2 Universal Distribution Functions at the Laboratory Scale

2.1 Testing for Universal Distribution Functions

2.1.1 Initial friction analysis

Prior to completing the main statistical analysis, some terminology needs to be defined. This section deals with peak and residual friction. As stated in Krahn and Morgenstern (1979) the use of the term residual strength, particularly for rock can be misleading and the value is dependent on many factors such as the original joint profile or surface roughness. In this Thesis, when the term residual friction and or cohesion is used, this is in referring to the equivalent strength parameter values for which deformation can continue with no further change in resistance (Krahn & Morgenstern 1979). As mentioned in Coulson (1970) the residual strength conditions in their database were typically obtained after one to two inches of shear had occurred for the 6 inch samples. As noted in Section 1.6.4 this analysis is concerned with understanding what PDF family and can accommodate for differences in how parameters are defined.

The friction data found in Coulson (1970) was initially subjected to a series of KW ANOVA tests. This initial analysis was completed to determine if surface preparation methods used in Coulson (1970), had any influence on the distribution associated with measured friction angles. The friction data in Coulson (1970) contained both peak and residual friction angles from direct shear tests for a number of lithologies in both wet and dry surface conditions as well as including a number of different surface preparation methods. A summary of the statistical analysis comparing the distribution of friction angles over surface preparation methods is shown in Table 18.

Table 18 Kruskal Wallis Analysis of Variance test decision summary - the distribution of friction vs sample preparation methods

Lithology	Peak friction	Residual friction	Peak friction	Residual friction
	Dry samples		Wet samples	
Granite Basalt	✗	✓	✗	✓
Dolomite	✗	✗	✗	✗
Bedford Limestone	✗	✓	✓	✗
Solenhofen Limestone	✓	✓	✓	✗
Fine Coulee Granite	✗	✓	✗	✗
Coarse Coulee Granite	✓	✓	✓	✓
Berea Sandstone	✗	✗	✗	✓
Schistose Gneiss	✗	✓	✗	✗
Hackensack Siltstone	✗	✓	✓	✓
Overall Conclusion	✗	✓	✗	✗

For clarification, cells in Table 18 containing a tick (✓) have accepted the test hypothesis (i.e., the PDF of each grouping shows no difference across preparation methods) at a 5% significance, and cells containing a cross (✗) reject this test hypothesis at the same significance. From Table 18, it can be concluded from the sample of data at a 5% significance that surface preparation techniques have a significant impact of the distribution of peak friction in dry conditions, the peak friction in wet conditions and the residual friction in wet conditions. There is insufficient evidence to suggest that the residual friction in dry conditions is effected by surface preparation techniques.

The results in Table 18 are not surprising, as it would be suspected that by smoothing down a shear surface, potential interlocking asperities or fragments would be removed. Once failure had occurred, some degree of material breakup would be expected to have occurred, which would be independent of surface preparation. It is interesting to note that this influence is not apparent in wet surfaces, which would not have been expected. Based on the results of the KW ANOVA, the residual dry friction

samples per lithology were grouped prior to obtaining their unscaled measures used in the following sections.

2.1.2 Non-parametric bootstrapping

After descaling all available data, each material parameter was analysed using non-parametric bootstrapping. Each resampling process was repeated 10,000 times for each material parameter to obtain an accurate estimate of the distribution of statistical differences. Additionally, for parameters that may have larger underlying similarities (e.g., all strength components and all frictional components) additional resampled pools were tested spanning all relevant material parameters. The non-parametric bootstrapping test decision summary is shown in Table 19.

Table 19 Non-parametric bootstrapping test decision summary

Sample description	Decision
Uniaxial Compressive Strength	✓
Point Load Index	✗
Uniaxial Tensile Strength	✓
All intact strength parameters (all direct strength tests combined)	✗
Peak dry friction	✓
Peak wet friction	✓
Residual dry friction	✓
Residual wet friction	✓
All material friction (all friction values combined)	✓
Dry density	✓
Young's Modulus	✗
Poisson's Ratio	✗

The results in Table 19 containing a tick (✓) have accepted the test hypothesis (i.e., the unscaled measure shows no difference across a particular material parameter) at a 5% significance, and cells containing a cross (✗) reject this test hypothesis at the same significance.

From Table 19, it can be concluded at a 5% significance that UCS is consistent with some UDF, Point Load Indices (PLT) are not consistent with a single UDF, Uniaxial Tensile Strength (UTS) is consistent with some UDF, intact strength parameters (combining UCS, PLT and UTS) are not consistent with a single UDF, all frictional parameters are consistent with some UDF, dry density is consistent with some UDF, Young's Modulus is not consistent with a single UDF, and Poisson's Ratio is not consistent with a single UDF.

Although some rock parameters do not appear to follow a universal family of distributions, it may still be possible to find accurate approximations that are a practically useful for each variable. To put this into perspective, with a big enough sample size, any statistical procedure will discriminate between very similar PDFs and hence conclude they are significantly different. For example given sufficiently large data sets, two normal distributions with mean values equal to 0.95 and 1.05 with the same standard deviation can be discriminated. For practical purposes, these two datasets may very well be approximated by a normal distribution with mean value 1.00 and a common standard deviation. This feature may still hold true for the rock parameters that reject the test hypothesis during the non-parametric bootstrapping and hence were included in all further analysis.

2.1.3 Verifying the goodness of fit

In order to accept any viable UDF approximation identified by the KS test, for each material parameter, the following criteria must also be met:

- The proportion of samples accepting the test hypothesis for each test type must be such that the binomial confidence interval of results is consistent with a 5% Type I error.
- For a single UDF to be accepted to describe numerous test types, the proportion of samples accepting the test hypothesis for each test type and all the samples together must be such that the binomial confidence interval is consistent with a 5% Type I error.
- The UDF must produce logical results (e.g., non negative values, obey physical upper limits, etc.).

A summary of the KS test decisions for each viable UDF family for unscaled measures is shown in Table 20.

Table 20 Kolmogorov Smirnov goodness of fit test decision summary

Parameter	Probability Density Function family					
	Normal	Log-normal	Gamma	Weibull	Rayleigh	Laplace
Point Load Index	✗	✗	✗	✓	✓	✗
Indirect Tensile Strength	✓	✓	✓	✓	✓	✗
Uniaxial Compressive Strength	✓	✓	✓	✓	✓	✗
Intact strength parameters (UCS, UTS and PLT)	✗	✗	✗	✓	✓	✗
Material friction peak dry	✓	✓	✓	✓	✓	✓
Material friction residual dry	✓	✓	✓	✓	✗	✓
Material friction peak wet	✓	✓	✓	✓	✓	✓
Material friction residual wet	✓	✓	✓	✓	✗	✓
Material friction (all friction values combined)	✓	✓	✓	✓	✗	✓
Dry density	✗	✗	✗	✓	✗	✓
Young's Modulus	✗	✓	✓	✓	✗	✗
Poisson's Ratio	✗	✓	✓	✓	✓	✗

For clarification, Table 20 shows which UDF families are applicable, a tick (✓) for viable UDF families and a cross (✗) for insufficient fits to unscaled measures based on the KS test. The decision to accept viable UDFs in Table 20 included the three criteria as previously mentioned.

From Table 20, it can be concluded at a 5% significance that the intact strength components (UCS, PLT and UTS) of rock are consistent with a Rayleigh or Weibull distribution, material friction components (peak and residual in wet and dry conditions) are consistent with many PDF families, dry density is consistent with a Weibull or Laplace distribution, Young's Modulus is consistent with a log-normal, gamma or Weibull distribution and Poisson's Ratio is consistent with by many PDF families.

The intact strength (UCS, PLT and UTS) UDF estimates (i.e. Rayleigh and Weibull) are identical as a Rayleigh distribution is equivalent to a Weibull distribution with shape parameter equal to 2, so there is in essence only one UDF that covers all tested intact strength parameters. Due to the large number of acceptable UDF types for material friction, friction data was subjected to a series of Shapiro Wilk tests to refute or accept a normal distribution approximation. The summary of the Shapiro Wilk test decisions for friction parameters are shown in Table 21.

Table 21 Shaprio Wilk test decision summary - material friction

Friction type	Decision
Peak dry friction	✓
Peak wet friction	✓
Residual dry friction	✗
Residual wet friction	✗
Material friction (all friction parameters)	✗

Cell in Table 21 containing a tick (✓) have accepted the test hypothesis (i.e., a normal distribution is appropriate) at a 5% significance, and cells containing a cross (✗) reject this test hypothesis at the same significance. Table 21 concludes that instantaneous friction values are sufficiently described by a normal distribution for both wet and dry cases, while residual friction values are some other distribution that is quite similar to but is not a normal distribution. With the available data and statistical results, a normal distribution is a reasonable approximation for all frictional components.

2.1.4 Verifying Universal Distribution Functions on raw data

Once approximations of viable UDFs have been obtained for the unscaled measure of each parameter, their applicability to the raw data was assessed. A summary of the applicability of UDFs on raw data and variable substitution is shown in Table 22. The notation used in Table 22 is consistent with statistical notation. 'Hatted' values (e.g., $\hat{k}$) denote parameter estimates while 'barred' values $\bar{M}$ and $\bar{\mu}$ indicate the random sample's median and mean values respectfully. This notation is used as these values are not the 'true' value of the overall population, but estimates based on samples.

Table 22 Universal Distribution Function simplification and variable substitution analysis summary

	UDF family	Median value with variable scale	Median value with constant scale	Mean value with variable scale	Mean value with constant scale
Intact strength grouping (UCS, PLT and UTS)	Weibull	$\hat{k} = 2.00$ $\hat{\lambda} = \frac{\bar{M}}{(\ln(2))^{\frac{1}{\hat{k}}}}$	✗	✗	✗
	Rayleigh	$\hat{\lambda} = \frac{\bar{M}}{\sqrt{2\ln 2}}$	N/A	✗	N/A
Material friction	Normal	$\hat{\sigma} = 2.07\% - 12.57\%\ of\ \bar{M}$	$\hat{\sigma} = 0.77 - 4.42$	$\hat{\sigma} = 3.14\% - 14.48\%\ of\ \bar{\mu}$	$\hat{\sigma} = 1.04 - 5.44$
Dry density	Weibull	$\hat{k} = 24.44 - 27.14$ $\hat{\lambda} = \frac{\bar{M}}{(\ln(2))^{\frac{1}{\hat{k}}}}$	✗	✗	✗
	Laplace	$\hat{\sigma} = 2.62\% - 5.54\%\ of\ \bar{M}$	$\hat{\sigma} = 0.08 - 0.13$	$\hat{\sigma} = 4.00\% - 6.26\%\ of\ \bar{\mu}$	$\hat{\sigma} = 0.08 - 0.15$
Young's Modulus	Log-normal	✗	$\hat{\sigma}$ = 1.82 – 2.09	✗	✗
	Gamma	$\hat{k} = 1.88 - 3.63$ $\hat{\sigma} \approx \frac{3\hat{k} + 0.2}{3\hat{k} - 0.8}\frac{\bar{M}}{\hat{k}}$	✗	$\hat{k}$ = 1.52 – 2.60 $\hat{\sigma} \approx \frac{\bar{\mu}}{\hat{k}}$	✗
	Weibull	$\hat{k} = 1.43 - 1.93$ $\hat{\lambda} = \frac{\bar{M}}{(\ln(2))^{\frac{1}{\hat{k}}}}$	✗	✗	✗
Poisson's Ratio	Log-normal	✗	✗	✗	✗
	Gamma	✗	✗	✗	✗
	Weibull	✗	✗	✗	✗
	Rayleigh	✗	N/A	✗	N/A

For clarification, cells in Table 22 containing a cross (✗) indicates an insufficient goodness of fit. Cells containing N/A are not possible to calculate. Table 22 additionally shows which UDF estimates are applicable when converted back to their raw form. This table presents the substitutions that must be tested and are mentioned in Step 6 of the test methodology in Section 1.7.1. The equations shown in Table 22 are obtained from known relationships between PDFs and their statistical parameters and are used to convert the problem to a practical form, where there is one universal constant and one measurable value (the median or mean value). Although Table 23 in the following Section only presents one main UDF for each material parameter, all UDFs presented in Table 22 are statistically acceptable and meet the required definition of a UDF. The specific UDFs in Table 23 were selected based on their implications to further analysis.

All attempts to analyse Poisson's ratio from the raw data provided no viable UDF estimate. In general, no statistically significant UDF estimate adhered to the physical upper limit that is associated with Poisson's ratio and hence no viable UDF was obtained. By consideration of both the lower and upper limit associated with Poisson's ratio, it would be suspected that the skewness of the associated PDF would change as the median or mean value approaches either 0 or 0.5, for this reason it is difficult to generalise the PDF associated with Poisson's ratio. A triangular distribution was trialled for its effectiveness but also failed to produce consistently significant results among all samples therefore fails to meet the definition of a UDF. The triangular distribution is however a very simple 'temporary general approximation', which can deal with both the physical upper and lower limits and changing skewness. The triangular distribution approximation for Poisson's Ratio needs to be manually constructed on a case by case basis.

2.1.5 The Universal Distribution Functions for rock parameters at the laboratory scale

The aim of this analysis was to determine whether or not there exists consistent underlying distributions associated with various parameters of rocks. After the completion of a series of non-parametric statistical tests on an extensive materials database, it can be shown that such UDFs do exist for a number of parameters and hence an acceptance of the overarching hypothesis (i.e., proof that UDFs exist). Table 23 presents the leading approximations for both deterministic and probabilistic estimates of many key rock parameters.

Table 23 Universal Distribution Function approximation for intact rock material parameters at the laboratory scale

	Intact strength (UCS, PLT and UTS)	Material friction (peak and residual)	Dry density	Young's Modulus	Poisson's Ratio
UDF family	Rayleigh	Normal	Laplace	Weibull	No true UDF Reasonable approximation is a triangular distribution
PDF	$f(x) = \frac{x}{\lambda^2} e^{-\frac{x^2}{2\lambda^2}}$	$f(x) = \frac{1}{\sigma\sqrt{2\pi}} e^{-\frac{1}{2}\left(\frac{x-\mu}{\sigma}\right)^2}$	$f(x) = \frac{1}{2\sigma} e^{-\frac{\lvert x-\mu\rvert}{\sigma}}$	$f(x) = \begin{cases} \frac{k}{\lambda}\left(\frac{x}{\lambda}\right)^{k-1} e^{-\left(\frac{x}{\lambda}\right)^k} & x \geq 0 \\ 0 & x < 0 \end{cases}$	$f(x) = \begin{cases} 0 \; for \; x < a \\ \frac{2(x-a)}{(b-a)(c-a)} \; for \; a \leq x < c \\ \frac{2}{b-a} \; for \; x = c \\ \frac{2(b-x)}{(b-a)(b-c)} \; for \; c < x \leq b \\ 0 \; for \; b < x \end{cases}$
Parameter estimates using the mean	N/A	$\hat{\mu} = \bar{\mu}$ $\hat{\sigma} = 3.14\% - 14.48\% \; of \; \bar{\mu}$ Or $\hat{\sigma} = 1.04 - 5.44$	$\hat{\mu} = \bar{\mu}$ $\hat{\sigma} = 4.00\% - 6.26\% \; of \; \bar{\mu}$ Or $\hat{\sigma} = 0.08 - 0.15$	N/A	$\hat{a} = minimum \; observation \; or \; 0$ $\hat{b} = maximum \; observation \; or \; 0.5$ $\hat{c} = 3\bar{\mu} - (\hat{a} + \hat{b})$
Deterministic estimate using the mean		$\widehat{Mo} = \bar{\mu}$	$\widehat{Mo} = \bar{\mu}$		$\widehat{Mo} = \hat{c}$
Parameter estimates using the median	$\hat{\lambda} = \frac{\bar{M}}{\sqrt{2\ln 2}}$	$\hat{\mu} = \bar{M}$ $\hat{\sigma} = 2.07\% - 12.57\% \; of \; \bar{M}$ Or $\sigma = 0.77 - 4.42$	$\hat{\mu} = \bar{M}$ $\hat{\sigma} = 2.62\% - 5.54\% \; of \; \bar{M}$ Or $\hat{\sigma} = 0.08 - 0.13$	$\hat{k} = 1.43 - 1.93$ $\hat{\lambda} = \frac{\bar{M}}{(\ln(2))^{\frac{1}{\hat{k}}}}$	$\hat{c} = \hat{b} - \frac{2(\hat{b}+\bar{M})^2}{(\hat{b}-\hat{a})}$ for positively skewed data Or $\hat{c} = \hat{a} + \frac{2(\hat{a}-\bar{M})^2}{(\hat{b}-\hat{a})}$ for negatively skewed data
Deterministic estimate using the median	$\widehat{Mo} = \frac{\bar{M}}{\sqrt{2\ln 2}}$	$\widehat{Mo} = \bar{M}$	$\widehat{Mo} = \bar{M}$	$\widehat{Mo} = \hat{\lambda}\left(\frac{\hat{k}-1}{\hat{k}}\right)^{\frac{1}{\hat{k}}}$	$\widehat{Mo} = \hat{c}$

In Table 23, the deterministic estimate is specified by the UDF's mode value $\widehat{Mo}$. The mode value was chosen as the representative deterministic value, as it defines the rock parameter value that is most likely to occur within the specified UDF. The mode value is considerably more intuitive when describing random variables, compared to other possible methods such as the mean or median value and was therefore chosen. It is noted that the deterministic material parameter estimates in Table 23 should be used cautiously when dealing with some empirical design methods. These empirical methods (a particular emphasis for those empirical methods which require specification of a representative UCS) were potentially developed using other statistical measures (e.g., using the mean UCS), which may produce poor comparisons when using the mode value. This potential issue when long standing empirical design methods should be verified for their effectiveness in further studies. It is also recommended based on the results summarised in Table 23 that the median value formulation with the variable scale parameter be used over the mean value. The reasoning for this is that the associated UDF parameter ranges have the smallest associated error based on the analysis and the variable scale parameter generally adheres to logical values.

The following figures show a comparison between each UDF approximation with the associated database EDFs shown in blue. The data presented relate to the highest sample count data sets and are used to demonstrate just how effective each UDF equation is at describing each material parameter. The solid black line is the CDF associated with the underlying UDF. These images plot the unscaled measure to better reflect the distribution across all encountered conditions in a single figure. The UDF approximation for all intact strength components (UCS, PLT and UTS) is shown in Figure 18.

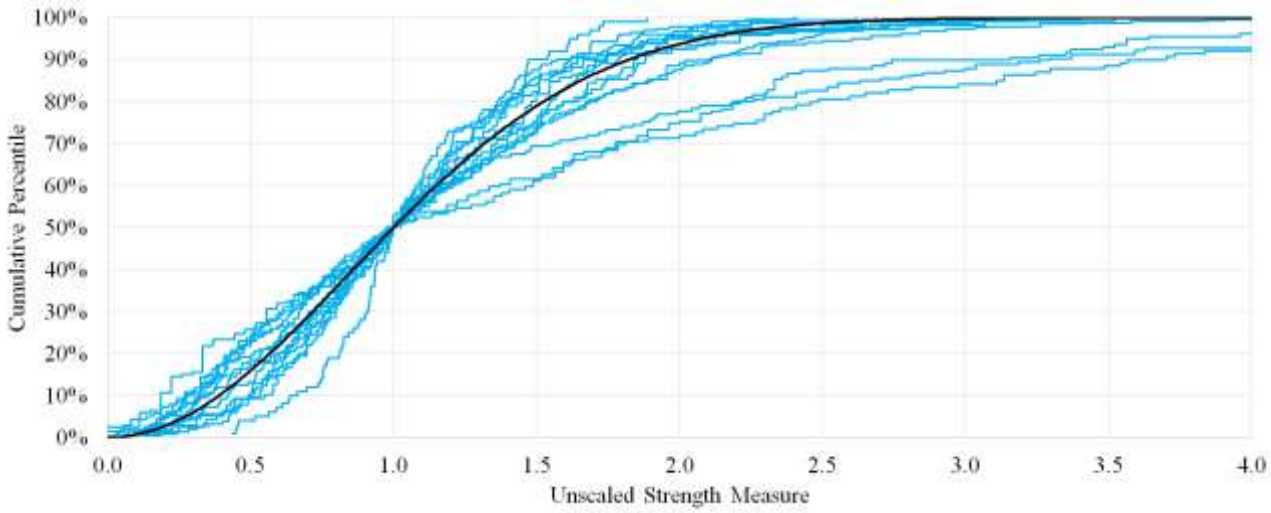

Figure 18 Empirical Distribution Function for intact strength with the Rayleigh distribution UDF

The distribution shown in Figure 18 has the scale parameter $\hat{\sigma}$ selected such that the median value is one (i.e., the unscaled measure). For unscaled samples the value of $\hat{\sigma}$ is selected based on the recommendations shown in Table 23. An interesting feature of Figure 18 can be observed by comparing the three lowest EDFs. This highly peculiar deviation from the expected CDF is due to dissimilar materials being logged as a single geological unit. This feature is suspected to be the leading cause of the rejection of the test hypothesis when completing the non-parametric bootstrapping in Table 19. To demonstrate that this was the case, two artificial UCS samples with median values 50 MPa and 150 MPa were generated and assessed as if they were a single unit. The resultant EDF and corresponding CDF according to UDF theory is shown in Figure 19.

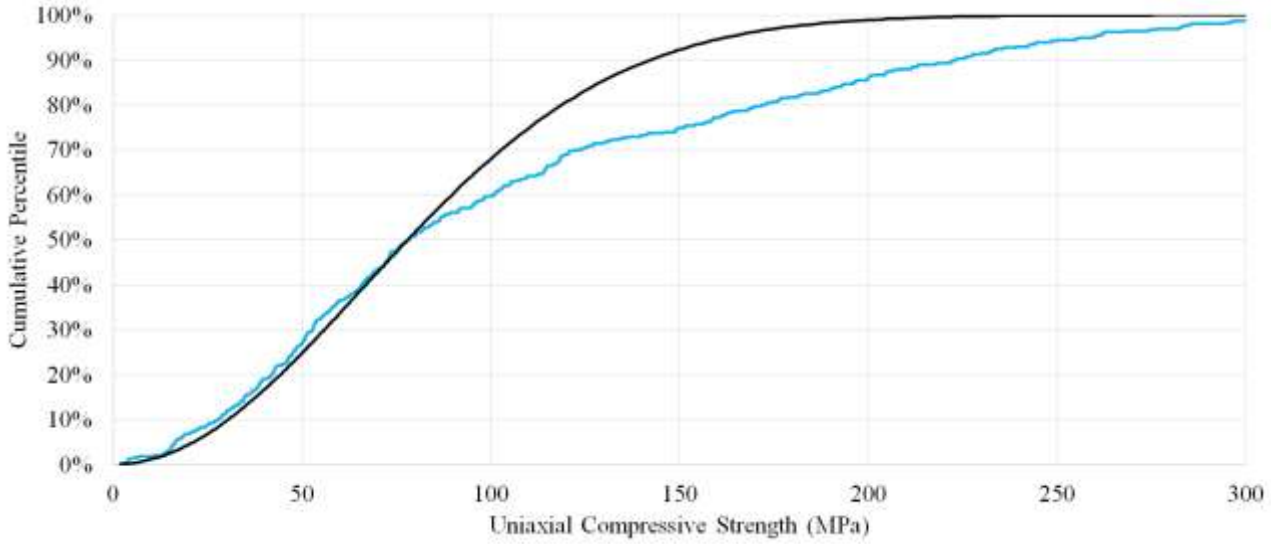

Figure 19 Artificial data simulating excessive deviation from the expected Cumulative Distribution Function in Uniaxial Compressive strength data

It is obvious from Figure 19 that the observed deviation apparent in Figure 18 has been accurately reproduced using the presented UDF theory. The more dissimilar the median values are, the more pronounced the deviation from the assumed CDF becomes. Fortunately, this deviation can be advantageous when constructing geotechnical domains. If a database containing UCS, UTS or PLT data shows significant deviation like that in Figure 19, then there is implicit evidence that two or more distinctively different materials have been grouped together in the same classification. The process for separating out this data may be straight forward if there are notable lithological differences (e.g., weathering, mineralisation, veining etc.) or spatial separations, however it can become increasingly difficult to implement when these features are not readily apparent difference, such as in weak and strong interbedded sedimentary layers.

The UDF for material friction is shown in Figure 20.

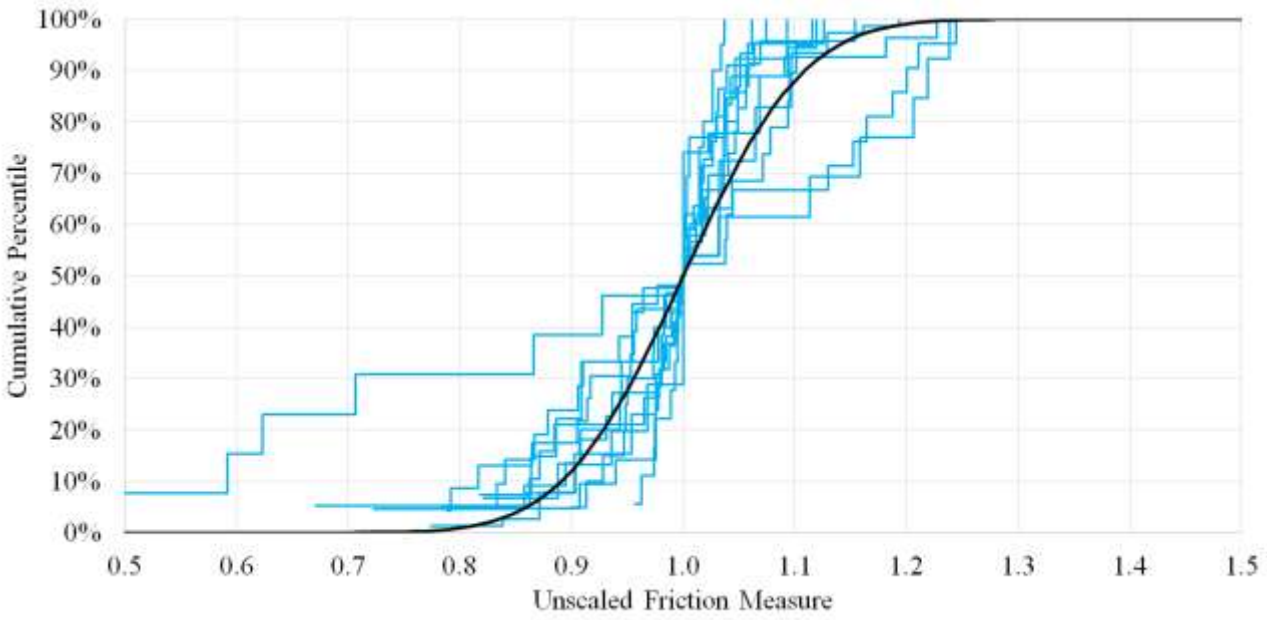

Figure 20 Empirical Distribution Functions for material friction with normal distribution UDF. $\hat{\sigma}$ = 0.085

Note that the UDF shown in Figure 20 is in not more accurate than any of the statistically viable values for $\hat{\sigma}$. This single estimate is only used to illustrate the nature of the underlying UDF. It is noted that all values shown in Table 23 are viable parameter estimates. The UDF for dry density is shown in Figure 21.

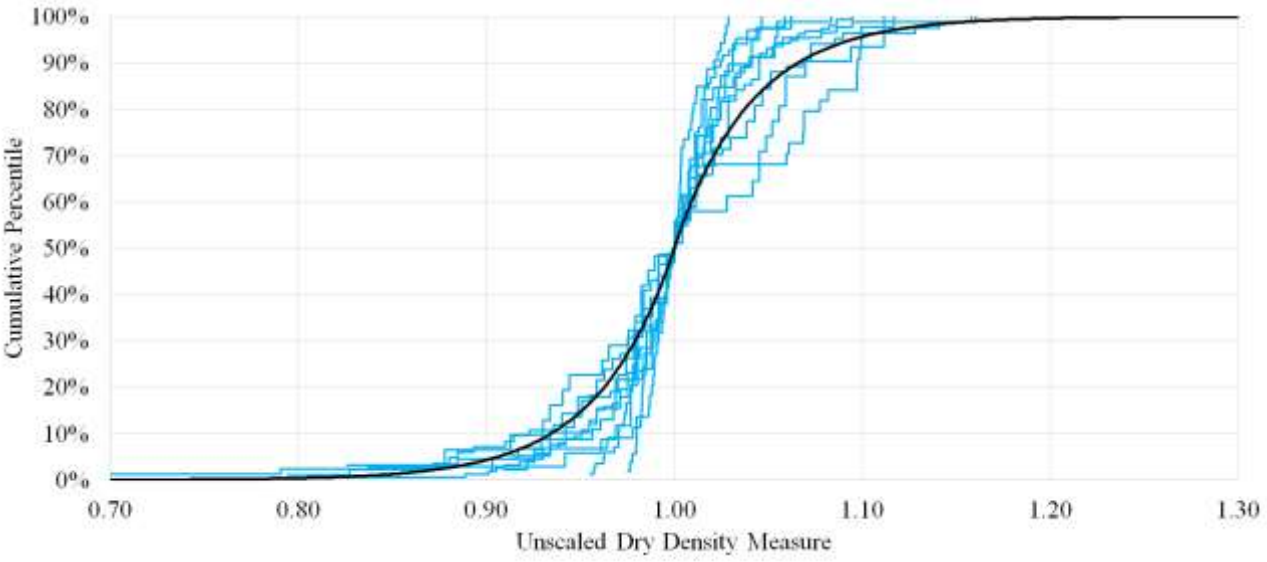

Figure 21 Empirical Distribution Functions for dry density with Laplace distribution UDF $\hat{\sigma}$=0.0408

Note that the UDF shown in Figure 21 is in not more accurate than any of the statistically viable values for $\hat{\sigma}$. This single estimate is only used to illustrate the nature of the underlying UDF. The UDF for Young's Modulus is shown in Figure 22.

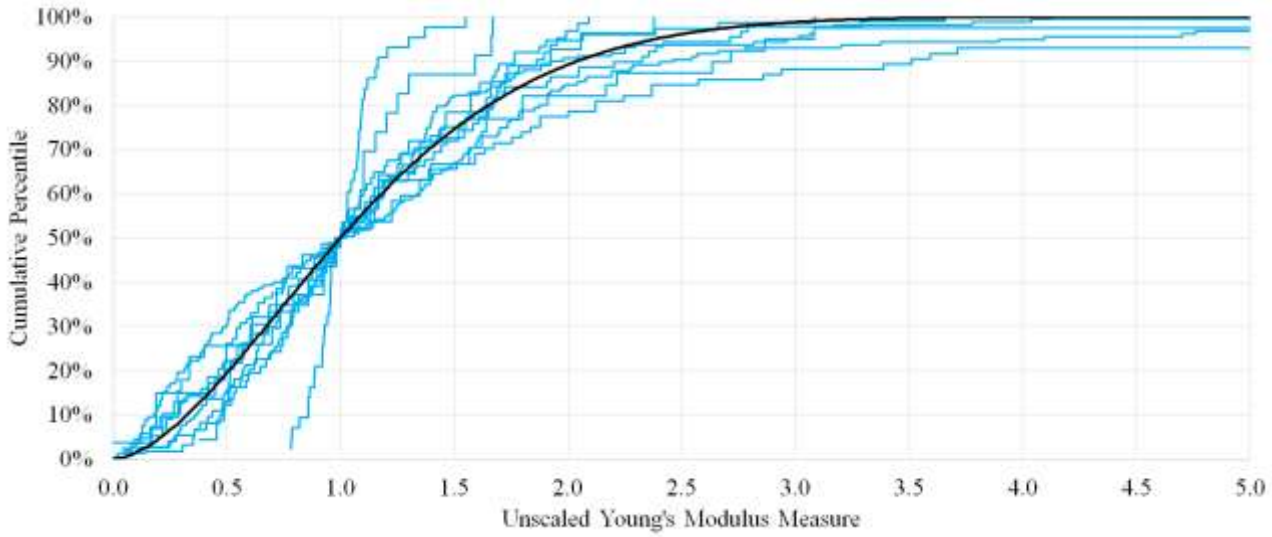

Figure 22 Empirical Distribution Functions for Young's Modulus with Weibull distribution UDF $\hat{\lambda}$= 1.68

Note that the UDF shown in Figure 22 is in not more accurate than any of the statistically viable values for $\hat{\lambda}$. This single estimate is only used to illustrate the nature of the underlying UDF. The EDFs for Poission's Ratio are shown in Figure 23 with a triangular distribution superimposed.

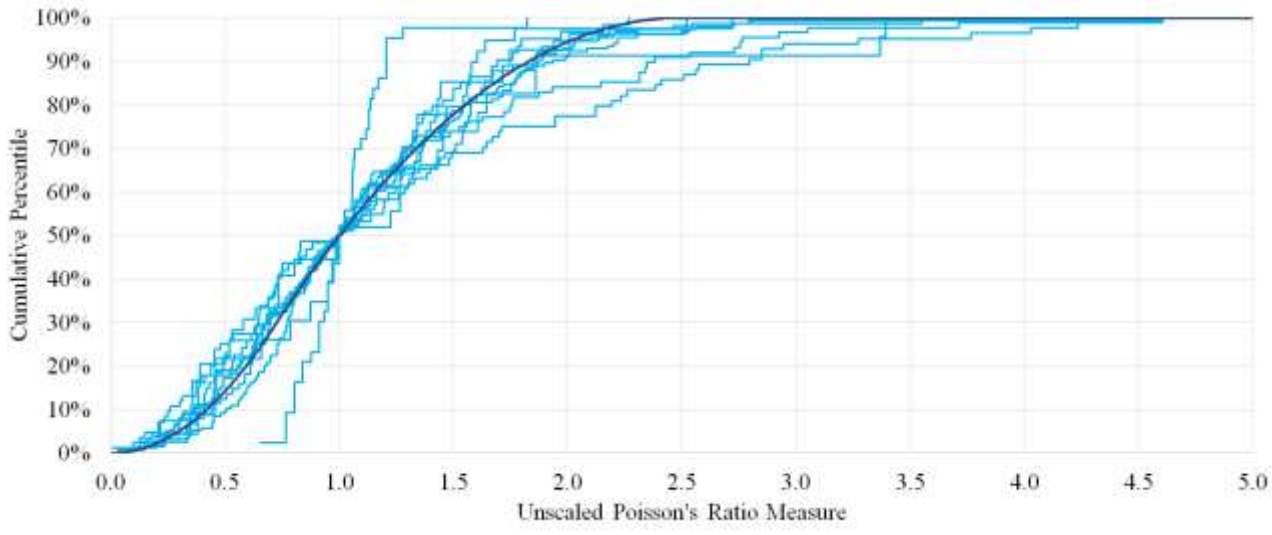

Figure 23 Empirical Distribution Functions for Poisson's Ratio. A triangular distribution is shown

Figure 23 does appear to show some underlying trend in most EDFs, however the trialled distribution fails to meet the upper physical limit of Poisson's Ratio and hence fails to meet the definition of a UDF (see Section 2.1.3). The triangular distribution estimate shown in Figure 23 is only plotted to show its effectiveness at approximating the distribution of Poisson's Ratio and its applicability as a 'temporary approximation'.

2.1.6 Universal material correlations

To assess if there is some general underlying correlation ρ, Pearson's product moment correlation coefficient test was completed to identify if parameter correlations exist and if so, what the likely values are. The summary of the initial correlation coefficient analysis is shown in Table 24.

Table 24 Product moment correlation coefficient test decision summary

Material parameter pairs	Decision
Dry density vs Uniaxial Compressive Strength	$\boldsymbol{\rho \neq 0}$
Dry density vs Young's Modulus	$\boldsymbol{\rho \neq 0}$
Dry density vs Poisson's Ratio	$\rho = 0$
Uniaxial Compressive Strength vs Young's Modulus	$\boldsymbol{\rho \neq 0}$
Uniaxial Compressive Strength vs Poisson's Ratio	$\rho = 0$
Young's Modulus vs Poisson's Ratio	$\boldsymbol{\rho \neq 0}$

From Table 24, it can be concluded at a 5% significance that correlation coefficient between dry density and UCS, dry density and Young's Modulus, UCS and Young's Modulus, and Young's Modulus and Poisson's Ratio are consistent with some non-zero correlation coefficient. The analysis also showed that calculated correlation coefficient between dry density and Poisson's Ratio, and Young's Modulus and Poisson's Ratio are consistent with no true correlation.

The non-parametric bootstrapping routine was then completed to determine the 95% confidence interval for ρ. Each resample process was repeated 10000 times for each pair of material parameters to obtain an appropriately large spread of correlation coefficients. The non-parametric bootstrapping results for correlation coefficients is shown in Table 25.

Table 25 Correlation coefficients for rock parameters

Correlated pairs	95% confidence interval containing ρ
Dry density vs Uniaxial Compressive Strength	$+0.3050 \leq \rho \leq +0.4982$
Dry density vs Young's Modulus	$+0.2489 \leq \rho \leq +0.4302$
Dry density vs Poisson's Ratio	$\rho = 0.0$
Uniaxial Compressive Strength vs Young's Modulus	$+0.5281 \leq \rho \leq +0.8481$
Uniaxial Compressive Strength vs Poisson's Ratio	$\rho = 0.0$
Young's Modulus vs Poisson's Ratio	$-0.0966 \leq \rho \leq -0.0224$
All other permutations	Unknown*

*No correlation coefficients can be calculated between material parameters not shown in Table 25. This is because these values (e.g., UCS and UTS) are obtained from destructive testing methods and hence no two measurements of these parameters can be obtained simultaneously.

2.1.7 The implicit Universal Distribution Function for cohesion

Unlike the other mentioned material parameters, cohesion cannot be directly measured in laboratory tests. Typically, cohesion is computed from direct shear tests, uniaxial compressive or triaxial tests by finding the linear regression intercept of the observed failure, in terms of acting normal and shear stresses. Being an indirectly measured material parameter it is difficult to obtain a single measurement of cohesion and hence an associated PDF. In relation to a Mohr Coulomb material, given a UCS and an appropriate friction angle, cohesion is calculated using Equation 55:

$$c = \frac{UCS(1 - \sin\phi)}{2\cos\phi} \qquad \text{Equation 55}$$

where c is the material cohesion (Pa), UCS is the Uniaxial Compressive Strength (Pa) and ϕ is the material friction (°). The mode (deterministic) estimate for cohesion can then be calculated using Equation 55 and the mode values for UCS and friction found in Table 23. The probabilistic UDF estimate for material cohesion becomes difficult to express in closed form, but can be defined implicitly and routinely generated:

1. Randomly generate a UCS value.
2. Randomly generate a friction angle.
3. Compute Equation 55 using the random estimates to obtain a random estimate for material cohesion.

This calculation is only expressed in terms of the UCS, however the probabilistic behaviour can be extended to incorporate triaxial behaviours of a Mohr Coulomb material by considering that the behaviour is linearly dependant to the applied normal stress, which for all intents and purposes is some finite value (known or unknown). The shear strength at this normal stress can be probabilistically calculated as per the above routine to obtain the generalisation to triaxial stress states for any value of confinement.

2.1.8 Additional parametric analysis - peak and residual friction

As the UDF identified for friction is reasonably well approximated by a normal distribution with equal variance (i.e., the requirements for parametric testing), this allows parametric testing methods to be used to better understand the frictional data. To further quantify some issues associated with friction, a series of paired t-tests where completed to determine if there is a difference between the mean peak and residual friction angles for rock. The hypothesis for this test is given as:

The mean difference ($\phi_{peak} - \phi_{residual}$) is equal to zero.

The results of these tests are summarised in Table 26.

Table 26 T-test decision summary

Surface preparation	Dry samples	Wet samples	Dry and wet
Sandblasted	-1.365° to -0.0818°	ND	ND
Smoothed with #80 silicon-carbide grit paper	ND	+0.563° to +3.004°	ND
Smoothed with #600 silicon-carbide grit paper	-7.256° to -2.745°	-6.993° to -0.592°	-6.385° to -2.328°
Surface preparation independent	-2.931° to -0.505°	ND	-2.025° to -0.159°

For clarification, cell in Table 26 displaying ND have accepted the test hypothesis (i.e., no difference between peak and residual friction angles) at a 5% significance. All other cells have rejected the test hypothesis, and present the 95% confidence interval of the mean difference between peak and residual friction angles.

The results shown in Table 26 present rather inconsistent behaviours across all test groupings. The results indicate at 5% significance that for sandblasted surfaces, the residual friction angle is higher than the peak friction angle for dry conditions and no significant difference in wet conditions. There was no significant difference when considering all sandblasted surfaces. Surfaces prepared with #80 silicon-carbide grit paper indicate at 5% significance that the peak friction angle his higher than the residual friction angle in wet conditions and no significant difference in dry conditions. There was no significant differences when considering all surfaces prepared with #80 silicon-carbide grit paper. Surfaces prepared with #600 silicon-carbide grit paper showed consistently that the residual friction angle is higher than the peak friction angle at a 5% significance. When all surface preparations were grouped, the results indicate at 5% significance that the residual friction angle is higher in dry samples, there is no difference in friction angles for wet samples, and the residual friction angle is higher when combining both wet and dry samples.

Based on the physical interpretation of these surface preparation methods, one would have suspected that there would be some consistent response (e.g., higher or lower residual friction angles) when considering surface preparation or the influences of water. The inconsistencies in which friction value is higher for sandblasted or #80 silicon-carbide grit paper in wet or dry conditions implies that there is likely no significant difference between the residual and peak friction angle. The #600 silicon-carbide grit paper surfaces consistently identify a higher residual friction angle, which again is consistent with the previously presented interpretation that there likely is some true detectable difference. As a general conclusion, these results can be interpreted as there being no significant difference between peak and residual friction angles for relatively natural surfaces and that well prepared surfaces will typically have a higher residual friction angle compared to the peak friction angle.

2.2 Implications of Universal Distribution Functions

This section focuses on providing additional evidence that the UDFs identified can be used to produce a variety of results, which are consistent with literature findings over a wider range of applications. The consistency of these new results with documented phenomenon provides additional support to the validity of UDFs as well as demonstrates the broad range of applications that they can offer.

2.2.1 Deterministic and probabilistic applications

With the discovery of UDFs, the issues associated with inconsistent FOS and POF selection criteria that were demonstrated in Section 1.6.1 and Section 1.6.2 using laboratory scale parameters have now been addressed. To demonstrate how to apply the notion of UDFs and more generally Table 23, a fictitious laboratory database with 10 samples for each material parameters was randomly generated from their respective UDF. These raw data are supplied in Table 27.

Table 27 Example laboratory data used to demonstrate Universal Distribution Functions

Sample number	UCS (MPa)	UTS (MPa)	Friction (°)	Density (t/m^3)	Young's Modulus (GPa)	Poisson's Ratio
1	55.65	5.06	21.07	2.52	49.66	0.087
2	70.94	4.98	30.51	2.39	31.31	0.021
3	38.98	5.68	24.86	2.77	33.99	0.036
4	61.06	5.15	24.92	2.34	37.11	0.094
5	12.38	2.10	22.08	2.36	17.34	0.077
6	9.35	1.39	26.22	2.46	9.38	0.171
7	41.31	4.65	23.04	2.52	42.98	0.139
8	16.68	1.88	34.06	2.43	14.22	0.162
9	34.53	1.26	21.79	2.72	15.51	0.102
10	24.37	4.18	28.42	2.60	19.54	0.122
Calculated median	36.76	4.42	24.89	2.49	25.43	0.10
Calculated mean	36.53	3.63	25.70	2.51	27.10	0.10

Also provided in Table 27 are the mean and median values of each material parameter, which are required for calculations. The recommended deterministic value is the mode value for each material parameter. The mode value as previously mentioned, relates to the most likely, or highest probability value from the specified distribution. When calculating the FOS of a slope the mode value is recommended to be used due to the intuitiveness to slope stability.

For a deterministic analysis, the only required value is the mode value. From Table 23 it can be seen that the mode value of dry density and material friction is equal to the median value. The mode value of the UCS and UTS are calculated using the given equations. Using the mode values of friction and UCS, the mode value of cohesion for a Mohr Coulomb material can be calculated using Equation 55. Poisson's Ratio utilises the mean value to calculate mode value. The mean value is used in this instance, as the formulation of the mode value in terms of the mean value is simpler than using of the median value. The minimum and maximum values of Poisson's Ratio are also required to compute the mode value of Poisson's Ratio, which are obtained from reviewing the data in Table 27. The calculation for the mode value of Young's Modulus is not as straight forward as other deterministic estimates as it requires the selection of an appropriate value of the UDF shape parameter k. How this is achieved is discussed along with the probabilistic parameter estimates.

Probabilistic analysis or when the POF is being assessed, requires the PDF of all relevant material parameters to be specified. As the UDF family (e.g., normal, Weibull etc.) for each material parameter is fixed, no PDF selections techniques need to be considered. Most UDFs have two statistical parameters, which are calculated from the available data to correct the shape, scale and location of each PDF to site specific conditions. Probabilistic parameters in Table 23 are presented either as either a fixed range or as a function of the median or mean value.

Although all values within a specified parameter ranges in Table 23 are statistically viable approximations, the chosen value must still be a reasonable reflection of the available data. In the absence of many individual measurements or a more in depth statistical assessment, it is recommended that the highest variance UDF be chosen from the statistically applicable range for each material parameter. The practitioner should always check for compatibility of parameter estimates by ensuring that the data makes logical sense. For example, the mode value of Poisson's Ratio must be larger than the minimum value and all material parameters values must be non-negative. If a more rigorous approach is desired, values can be easily calculated using the associated Maximum Likelihood Estimate applicable to each UDF. The Maximum Likelihood Estimate for the UDF parameters are shown in Table 28.

Table 28 Maximum Likelihood Estimation for example Universal Distribution Function parameters

Material parameter	Maximum Likelihood Estimate equations	Parameter estimate
Friction (Montgomery & Runger 2014)	$\hat{\sigma} = \sqrt{\frac{1}{n}\sum_{i=1}^{n}(x_i - \hat{\mu})^2}$	$\hat{\sigma} = 4.20$ or 16.88% of $\bar{M}$
Density (Norton 1984)	$\hat{\sigma} = \frac{\sum_{i=1}^{n}\lvert x_i - \bar{M}\rvert}{n}$	$\hat{\sigma} = 0.115$ or 4.62% of $\bar{M}$
Young's Modulus (Cohen 1965)	Solve simultaneously: $\hat{k} = \frac{\sum_{i=1}^{n} x_i^{\hat{\lambda}}}{n}$ $\frac{\sum_{i=1}^{n} x_i^{\hat{\lambda}} \ln x_i}{\sum_{i=1}^{n} x_i^{\hat{\lambda}}} - \frac{1}{\hat{\lambda}} - \frac{1}{n}\sum_{i=1}^{n} \ln x_i = 0$	$\hat{\lambda} = 30.75$ $\hat{k} = 2.26$

As expected, the parameter estimates in Table 28 typically fall within the specified statistically significant ranges given in Table 23. The value of $\hat{k}$ associated with Young's Modulus Maximum Likelihood Estimate is noted to fall outside the specified range, which contains 95% of the calculated values of $\hat{k}$. The Weibull distribution Maximum Likelihood Estimate in Table 28 is difficult to solve without the aid of statistical software, so practitioners may prefer to use a graphical methods such as using the KS test. The KS test for the example Young's Modulus data is shown in Figure 24.

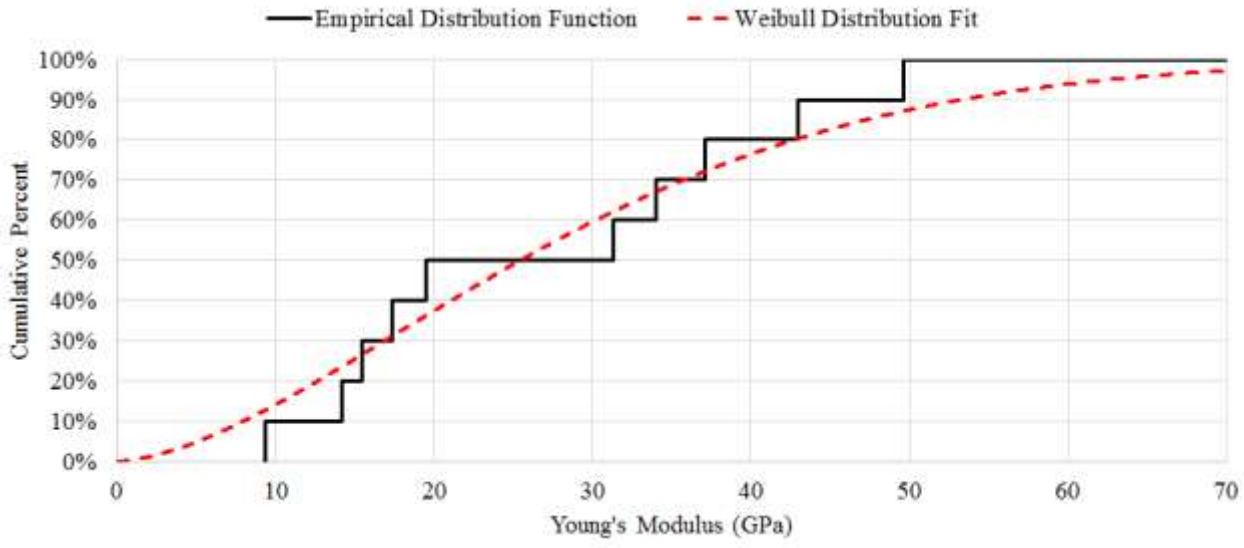

Figure 24 Graphical parameter estimation by Kolmogorov Smirnov goodness of fit

The Weibull distribution shown in Figure 24 is characterized by $\hat{\lambda} = 31.87$ and $\hat{k} = 1.62$ with associated KS test statistic $D_n = 0.1364$. Note that the parameter estimates obtained by graphical and Maximum Likelihood Estimates are both equally applicable based on the available data. For this example, the graphical estimate was used as the value of $\hat{k}$ falls within the specified shape range in Table 23.

An advantage of a graphical approach compared to the use of an equation is that it allows for a visual assessment of the goodness of fit, which is often overlooked when dealing with strictly mathematical descriptions of variability. With a calculated value of $\hat{k}$ for Young's Modulus the mode value can then be calculated using the equations presented in Table 23. When all values are computed using the data supplied in Table 27 and Table 28, Table 29 is produced to summarise the deterministic (FOS) and probabilistic (POF) material parameter estimates using UDFs.

Table 29 Example Universal Distribution Function calculations verse true values

Value	UCS (MPa)	UTS (MPa)	Cohesion (MPa)	Friction (°)	Density (t/m³)	Young's Modulus (GPa)	Poisson's Ratio
Parameter estimates							
PDF Distribution	Rayleigh	Rayleigh		Normal	Laplace	Weibull	Triangular
Parameter one	$\hat{\lambda} = 31.22$	$\hat{\lambda} = 3.75$	Implicit	$\hat{\mu} = 24.89$	$\hat{\mu} = 2.49$	$\hat{\lambda} = 31.87$	$\hat{a} = 0.021$
Parameter two	N/A	N/A	Implicit	$\hat{\sigma} = 4.20$	$\hat{\sigma} = 0.115$	$\hat{k} = 1.62$	$\hat{b} = 0.171$
Parameter three	N/A	N/A	N/A	N/A	N/A	N/A	$\hat{c} = 0.108$
Mode value (FOS input)	31.22	3.75	9.97	24.89	2.49	17.68	0.108
True values							
Parameter one	$\lambda = 30.66$	$\lambda = 3.42$	Implicit	$\mu = 26.10$	$\mu = 2.51$	$\lambda = 25.01$	$a = 0.013$
Parameter two	None	None	Implicit	$\sigma = 3.22$	$\sigma = 0.13$	$k = 1.86$	$b = 0.303$
Parameter three	None	None	None	None	None	None	$c = 0.045$
Mode value	30.66	3.42	9.56	26.10	2.51	16.48	0.045

Table 30 Example Universal Distribution Function percentage errors

Value	UCS (MPa)	US (MPa)	Cohesion (MPa)	Friction (°)	Density (t/m³)	Young's Modulus (GPa)	Poisson's Ratio
Parameter one	+1.83%	+9.65%	N/A	-4.64%	-0.80%	+27.43%	+61.54%
Parameter two	N/A	N/A	N/A	+30.43%	-11.54%	-12.90%	-43.56%
Parameter three	N/A	N/A	N/A	N/A	N/A	N/A	+140.00%
Mode value	+1.83%	+9.65%	+4.29%	-4.64%	-0.80%	+7.27%	+140.00%

For clarification, using the information provided in Table 29, the row labelled 'mode value should be used to calculate the FOS. If the information in Table 29 was to be used to calculate the POF, the PDF distribution family shown and the corresponding parameters should be used as the input.

Also supplied is Table 30, which presents the percentage errors associated with each parameter estimate and the true value used to generate the sample data. Some parameter estimates can be seen to have a considerable sampling error associated with their estimates, particularly the UDF parameters. This sampling error in practical settings is unknown, but can be estimated from statistical analysis. Quantification of sampling errors for each material parameter is detailed in the following section.

2.2.2 Sampling errors

Deterministic and probabilistic selection will always produce some error between the estimates and the true value, an associated sampling error. The sampling error cannot be directly measured, but can be shown to reduce with an increasing number of samples (Gill, Corthésy & Leite 2005). Varying guidelines (Bieniawski 1979) (Ruffolo & Shakoor 2009) are available, which specify the minimum number of laboratory tests required for various rock material parameters. These guidelines relate to estimates of the mean material parameter value with no recommendations to aid in the number of samples required for probabilistic parameter accuracy. As the PDF family for each UDF is fixed, it is possible to calculate the number of samples required to obtain a desired accuracy for both deterministic and probabilistic parameters for different rock material parameters.

In order to estimate the sampling errors associated with the median value and probabilistic parameters for each material parameter, the largest scale parameter UDF estimate for each material parameter was used to generate random laboratory sample pools with varying sample numbers. Each sample pool then had the median value and the associated Maximum Likelihood Estimate for each PDF parameter calculated and then the associated percentage error for each random sample pool was calculated. This process was then repeated 1000 times for six different inputs and sample pools with the number of samples ranging from 2 to 2000.

For clarification, the ‘largest scale parameter’ refers to selecting UDF parameters, which produce the highest associated variance. For example, the scale parameter associated with the highest variance for friction is given by 12.57% of the median value and Young’s Modulus is given by a shape parameter of 1.43. Justification of selecting the largest scale parameter was to provide an upper limit to sample size requirements and to account for the most variable statistically acceptable UDF model. From the resulting distribution of sampling errors, the central 95^{th} percentile was used to estimate the required sample numbers to meet a specified sampling error for each parameter. The sample number estimates for each parameter based on UDFs are shown in Table 31.

Table 31 Sample size estimates for specified accuracies using the median value

Material parameter	Value	±50% of true value	±25% of true value	±15% of true value	±10% of true value	±5% of true value
UCS	Median	9	33	90	203	809
PLT						
UTS						
Friction	Median	1	2	4	9	36
	Scale parameter	6	24	72	172	763
Density	Median	1	1	2	3	8
	Scale parameter	15	59	163	367	1465
Young's Modulus	Median	18	67	178	387	1454
	Shape parameter	25	73	164	310	925
Poisson's Ratio	Behaviour poorly understood. No estimate possible					

Note that for UCS, PLT and UTS only one sample number is specified. This is because the probabilistic parameter is only dependant on the median value. Estimates for the number of samples to achieve some specified percentage error cannot be calculated for Poisson's Ratio, as there is currently no associated UDF for Poisson's Ratio.

Table 31 may appear to suggest that you must have the number of samples specified in order to achieve the desired level of accuracy. However, reviewing the percentage errors in Table 30, most deterministic estimates fall within ±10% of their true value while probabilistic parameters are typically within ±30%. The results presented in Table 31 imply an error of up to ±50% for the number of available samples. These estimates are the number of samples needed to be 'almost surely' within the required accuracy level. It is possible to obtain very accurate estimates with fewer samples but these results are not guaranteed and their true accuracy cannot be verified.

It is interesting to note how greatly different the sample size estimates for intact strength are compared to recent published estimates of the requirements for UCS tests by Ruffolo and Shakoor (2009) shown in Table 32. These estimates are also based on a central 95th percentile confidence interval, and use a similar estimation technique.

Table 32 Estimates for the sample numbers of Uniaxial Compressive Strength by Ruffolo and Shakoor (2009)

Accuracy range	Within ±5%	Within ±10%	Within ±15%	Within ±20%	Within ±25%
Bera Sandstone	6	4	3	3	3
Indiana Limestone	25	9	5	4	4
Marble	29	9	6	5	4
Milbank Granite	42	13	7	5	5
Wissahickon Schist	n/a	25	13	9	7

One possible explanation for the difference is that the sample size estimates presented in Table 31 are for the median value while the ranges shown in Table 32 are for the mean value. The rate of convergence of the sample mean and sample median to the true mean and true median are different. The rate of convergence and the associated sampling error for the mean and median values can be compared by considering the associated mean and median confidence intervals in terms of the associated standard errors (Harding, Tremblay & Cousineau 2014):

$$Mean\ Confidence\ Interval = \bar{\mu} \pm Z_{n,\alpha}\left(\frac{\hat{s}}{\sqrt{n}}\right) \qquad \text{Equation 56}$$

$$Median\ Confidence\ Interval = \bar{M} \pm Z_{n,\alpha}\left(1.253\frac{\hat{s}}{\sqrt{n}}\right) \qquad \text{Equation 57}$$

where $Z_{n,\alpha}$ is the standard normal distribution, n is the number of samples, $\bar{\mu}$ is the calculated mean, $\bar{M}$ is the calculated median and $\hat{s}$ is the calculated standard deviation. Even when correcting for the convergence of the median value by multiplying the estimates of Ruffolo and Shakoor by 1.25, the discrepancies are still noticeable. The second and more likely reason for these differences is due to the low measured standard deviation for each lithology in Ruffolo and Shakoor's database compared to those measured for the initial UDF study database. A comparison of this data to the values used to derive the intact strength (i.e., PLT, UCS and UTS data) UDF is shown in Figure 25.

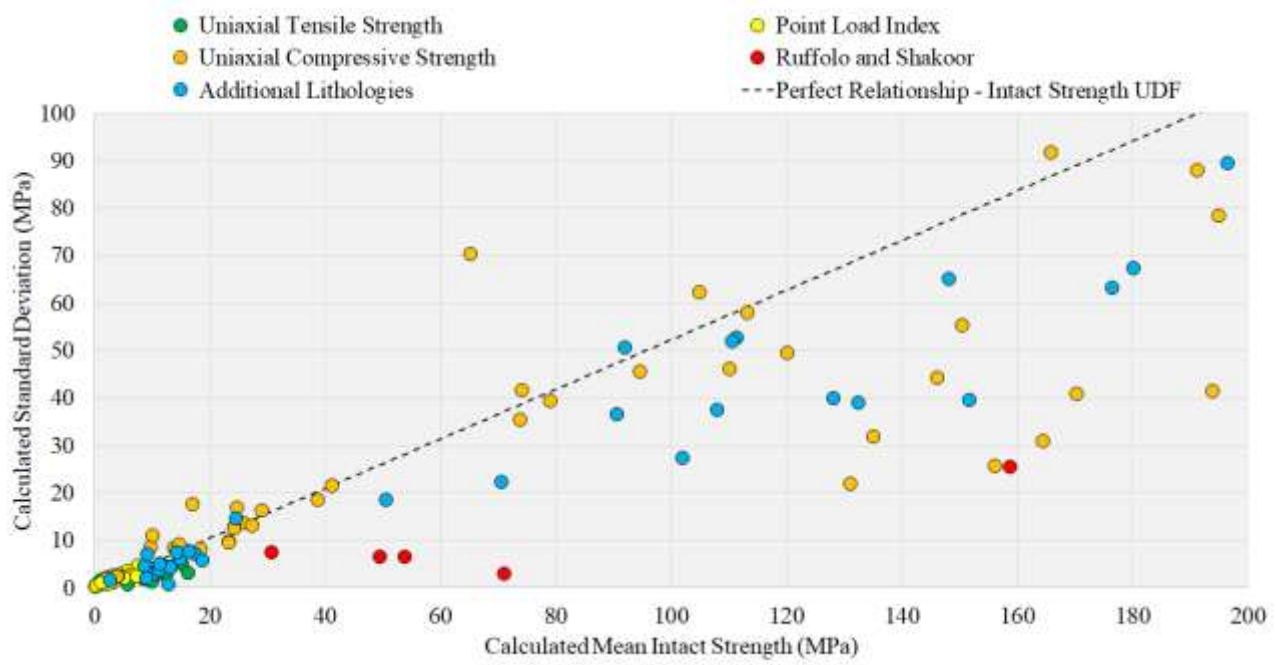

Figure 25 Scatter plot of mean strength vs standard deviation for intact rock strength measurements

The scatter plot shown in Figure 25 shows that most of the rock types that were used as part of Ruffolo and Shakoor's work show considerable deviation from the general data trend and the idealised perfect relationship given by UDFs. For comparison, additionally sourced UCS data (blue dots) not used during the initial UDF analysis follow the same general trend predicted by the UDF. As the standard deviations calculated by Ruffolo and Shakoor are lower than those predicted by UDFs the rate of

convergence to the mean value, and in term, the associated percentage error for a given number of samples will be lower than those calculated using UDFs. The low calculated standard deviations from Ruffolo and Shakoor may be due to sampling errors for the standard deviation or some influence that is currently unaccounted for when applying UDFs.

By consideration of the mean and median standard errors (Equation 56 and Equation 57), the mean value, in theory should produce a 'more accurate' measure of the data as the mean standard error is smaller than the median standard error for some number of samples; that is, it is more likely to be closer to the true value. In order to compare the applicability of the mean value over the median value, the percentage errors at various sample sizes and confidence intervals for UCS were constructed using the above mentioned method. These results are shown in Table 33.

Table 33 Percentage error confidence intervals for Uniaxial Compressive Strength using the mean and median value

Samples	25% confidence interval		50% confidence interval		68% confidence interval		95% confidence interval	
	Median value	Mean value	Median value	Mean value	Median value	Mean value	Median value	Mean value
5	± 10.00%	± 9.50%	± 20.50%	± 20.00%	± 30.50%	± 29.50%	± 60.00%	± 58.00%
10	± 7.00%	± 6.50%	± 14.50%	± 14.50%	± 21.50%	± 21.00%	± 42.00%	± 41.50%
20	± 5.00%	± 4.50%	± 10.50%	± 10.00%	± 15.50%	± 15.00%	± 30.50%	± 30.00%
30	± 4.00%	± 4.00%	± 8.50%	± 8.50%	± 12.50%	± 12.50%	± 25.00%	± 24.50%
40	± 3.50%	± 3.50%	± 7.50%	± 7.50%	± 11.00%	± 11.00%	± 22.00%	± 21.50%
50	± 3.00%	± 3.00%	± 7.00%	± 7.00%	± 10.00%	± 10.00%	± 19.50%	± 19.50%
100	± 2.50%	± 2.50%	± 5.00%	± 5.00%	± 7.00%	± 7.50%	± 13.50%	± 14.00%
200	± 1.50%	± 2.00%	± 3.50%	± 4.00%	± 5.00%	± 5.50%	± 10.00%	± 10.50%

Table 33 shows that although the convergence rates for the mean and median values are different, the percentage errors at various confidence intervals and sample sizes are very similar and show no real differences in sampling errors. The median value was still chosen as the representative value to describe each UDFs as it produces a better statistical estimator of the entire PDF for real world samples. For this reason, the median value remains the recommended estimator of a sample pool.

For any individual problem, if a sufficiently rigorous statistical analysis provides justification that the mean value provides a better estimate site conditions than the median value, there is no reason not to use it. If the mean value is used over the median value, the UDF parameter relationships must be formulated in terms of the mean value to ensure that the correct PDF is used. Equivalent relationships between UDF parameters and the mean value are simple to derive using the associated underlying PDF.

2.2.3 Linear and non-linear relationships between rock parameters

Having single approximations for the PDF of various rock parameters and evidence that they are correlated can help estimate underlying linear and nonlinear relationships between them. If two variables are positively correlated, it is possible to use a perfectly correlated relationship ($\rho = +1$) to compute the underlying linear or nonlinear relationship between these variables. Linear relationships between PLT, UCS, UTS and Young's Modulus are commonly reported in rock mechanics literature (Nazir, Momeni, Armaghani & Amin 2013) (Rusnak & Mark 2000) (Kumar, Asce, Bhargava, Choudhury & Asce 2017). To demonstrate that these relationships are predicted by UDFs, the UDF associated with all intact strength components (i.e., PLT, UCS and UTS) must first be transformed from a Rayleigh distribution to a Weibull distribution. A Rayleigh distribution is a special case of a Weibull distribution where the Weibull distribution shape parameter k is equal to 2 and the scale parameter λ, equal to $\sqrt{2}$ times the Rayleigh scale parameter. This PDF transformation simplifies the derivation and allows for considerations of Young's Modulus, which is described by a Weibull distribution. The CDF for a generic Weibull distribution is given by:

$$F_X(x) = 1 - e^{-\left(\frac{x}{\lambda}\right)^k} \qquad \text{Equation 58}$$

Equating the CDFs of any two perfectly correlated Weibull distributions with parameters of each distribution denoted by subscripts 1 and 2, the following expression is obtained:

$$x_2 = \lambda_2 \left(\frac{x_1}{\lambda_1}\right)^{\frac{k_1}{k_2}} \qquad \text{Equation 59}$$

This is the general equation for the relationship between two perfectly correlated Weibull distributions. For the UDF approximations for PLT, UCS and UTS, the value of k equal to 2, with λ being related to the median value M. By substituting the value of $k_1 = k_2 = 2$ into Equation 59:

$$\frac{x_2}{x_1} = \frac{\lambda_2}{\lambda_1} = Constant$$ Equation 60

Equation 60, suggests that if any two correlated Weibull distributions have identical shape parameters, then there is an underlying linear relationship with gradient equal to the ratio of the median values or scale parameters. From the available UDFs, this implies that any pair of PLT, UCS or UTS are correlated, then the underlying relationship between them must be linear. These linear relationships are known to exist and are often the focus of published studies (Nazir, Momeni, Armaghani & Amin 2013) (Rusnak & Mark 2000). This replication of this known linear relationship by use of UDFs provides evidence that the UDFs associated with PLT, UCS and UTS are correct for each of these material parameters.

Although a linear relationship can be shown to exist, there is no available information about what the gradient of this relationship is or what the 'conversion factor' from one material parameter to the other is. Published conversion factors between UCS and PLT listed by Rusnak and Mark (2000) show variations in conversion factors between rock types, which is also supported by their own findings.

Equation 59 can be used to describe the relationship between two Weibull distributions, which have different shape parameters. This equation can be used to describe the underlying relationships between Young's Modulus and any of the PLT, UCS or UTS material parameters. When the shape parameters are not equal, a nonlinear underlying relationship is produced, with a greater difference in shape parameters producing a more pronounced nonlinear response. Examples of this underlying nonlinear relationship between UCS and Young's Modulus in both synthetic and real data are shown in Figure 26.

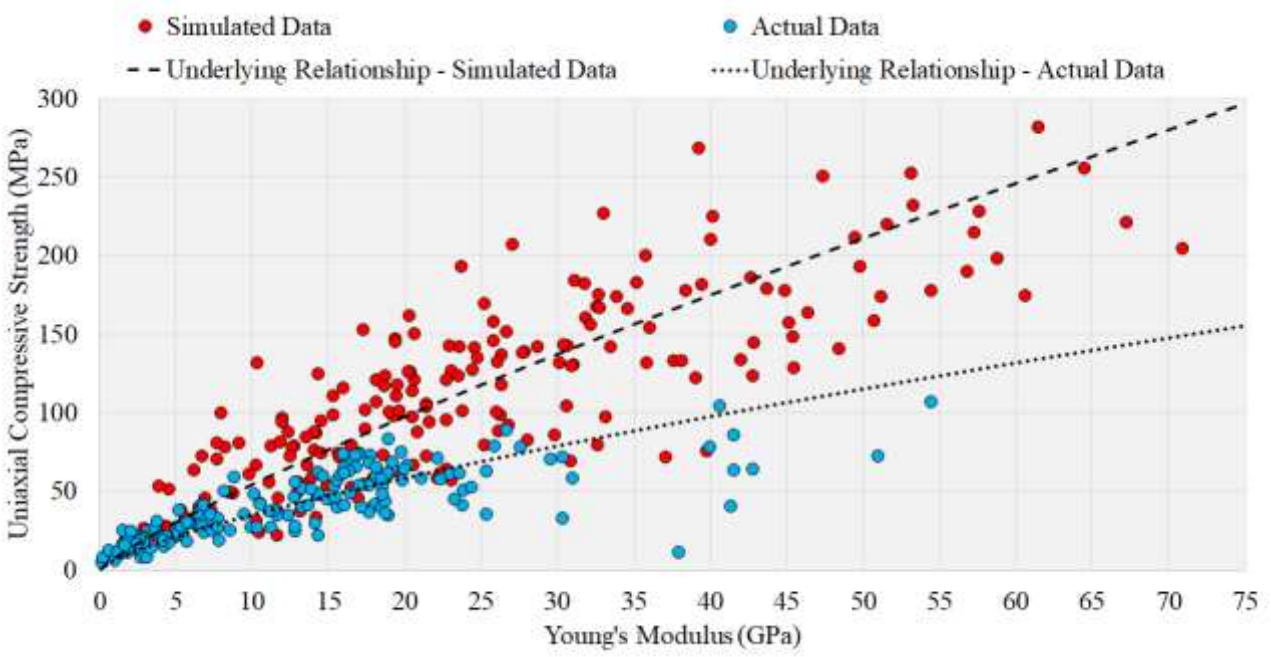

Figure 26 Scatter plot showing the curvature between the relationship of Uniaxial Compressive Strength and Young's Modulus

Depending on how different the associated shape parameters are, the nonlinear response may be subtle and can produce reasonably high R^2 values when using linear regression to estimate the relationship. For the simulated example data (red dots) shown in Figure 26, an R^2 of 0.61 is obtained for a linear model with zero intercept. The goodness of fit obtained by fitting a linear model to this subtle nonlinear relationship may also explain why linear relationships are commonly quoted in literature (Kumar, Asce, Bhargava, Choudhury & Asce 2017). The nonlinearity is more pronounced in the real data set (blue dots) in Figure 26.

2.2.4 Relationships between Uniaxial Compressive Strength and sonic velocity

Equation 59 can also be used to help formulate much more complex relationships. It is possible to derive a new relationship between the sonic velocity through rock and the associated UCS. The most common models used to describe this relationship between these two parameters is to fit an exponential model in the form (Butel, Hossack & Kizil 2014):

$$UCS \approx Ae^{Bc_p} \qquad \text{Equation 61}$$

where A and B are site specific constants calculated from the regression model and c_p is the velocity of a pressure wave (m/s). Note that some authors express this relationship not in terms of velocity but

in terms of the time interval between sending and receiving the sonic pulse, a similar exponential model is also used in these instances. Alternative empirical relationships are also common with many examples listed by Chang *et al (*2006), which consider other parameters including porosity These alternative empirical relationships still rely on site specific constants obtained from regression analysis to describe the data. By using UDFs, an alternative description of the relationship between sonic velocity and UCS can be derived in terms of measurable quantities and does not require the calculation of site specific constants. From fundamentals, the speed of pressure waves through any solid material is given by (Rienstra & Hirschberg 2009):

$$c_p = \sqrt{\frac{E(1-\nu)}{\rho(1+\nu)(1-2\nu)}} \qquad \text{Equation 62}$$

where c_p is the speed of a pressure wave (m/s), E is Young's Modulus (Pa), ν is Poisson's Ratio and ρ is density (kg/m^3). Since a relationship for Young's Modulus in terms of UCS can be expressed by Equation 59, this can be substituted into Equation 62 and rearranged to obtain:

$$UCS = M_{UCS}\sqrt{\left(\frac{c_p^2\rho(1+\nu)(1-2\nu)}{M_E(1-\nu)}\right)^{k_E}} \qquad \text{Equation 63}$$

Where M_E is the median Young's Modulus (Pa), M_{UCS} is the median UCS (Pa) and k_E is the Weibull distribution shape parameter for Young's Modulus. This solution can also be verified in terms of units, a feature that cannot be done in Equation 61. Similar to pressure waves, the relationship between shear wave velocity and UCS can be derived. Consider the equation for the speed of a shear wave (Rienstra & Hirschberg 2009):

$$c_s = \sqrt{\frac{G}{\rho}} \qquad \text{Equation 64}$$

where c_s is the shear wave velocity (m/s) and G is the shear modulus (Pa). An identical derivation used to obtain Equation 63 can be used to obtain the following relationship between UCS and shear velocities:

$$UCS = M_{UCS}\sqrt{\left(\frac{2c_s^2\ \rho(1+\nu)}{M_E}\right)^{k_E}} \qquad \text{Equation 65}$$

This relationship is beneficial, as it does not require curve fitting parameters as all variables are quantifiable from laboratory or field tests. The values of ρ and ν that should be used when using Equation 65 are mode values for density and Poisson's Ratio. How to calculate the mode values based on their associated UDFs have previously been presented in Table 23.

To check the applicability of this new model, the joint distribution of sonic velocity and UCS values in real samples was compared to the joint distribution randomly generated by using UDFs by means of the two-dimensional Kolmogorov Smirnov goodness of fit test (Friedman 2004). The real data and simulated data based on UDF theory are shown in Figure 27. Additionally the exponential relationship like Equation 61 was included to compare this new model to currently industry methods.

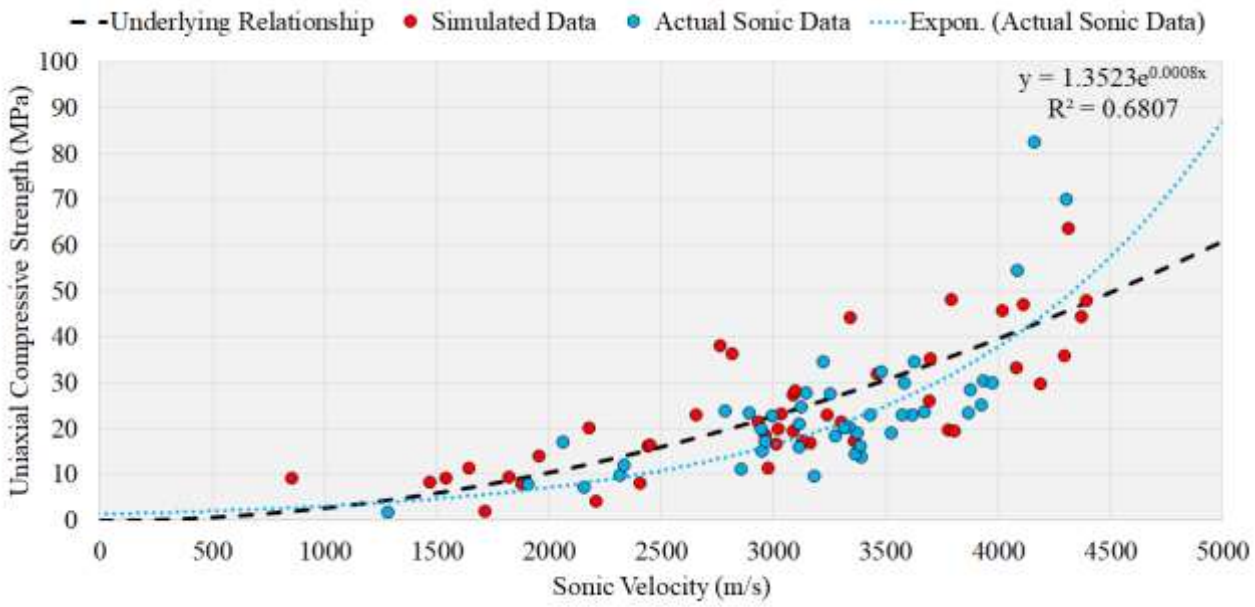

Figure 27 Sonic velocity vs Uniaxial Compressive Strength for real and simulated data sets

Note that the data shown in Figure 27 related to laboratory sonic and compressive measurements for an ironstone from Australia. The data shown formed part of the UDF material database. Visual comparisons between the underlying relationship (Equation 63) and the typical exponential relationship show notable discrepancies near the central portion of the data (15 MPa verse 25 MPa UCS at 3000 m/s) and much larger discrepancies at high sonic velocities (past 4000 m/s). Statistically, the distribution of synthetic samples compared to the actual data distribution suggested that there was

no statistically significant difference at a 5% significance between the distribution of real data and synthetic data, with a calculated KS test statistic equal to 0.3209 and a P-value of 0.1833. From first impressions, Equation 63 appears promising in predicting the relationship between sonic velocity and UCS as the behaviour is based on physical measurements rather than site specific constants. This relationship should be compared to more site data in order to determine its effectiveness compared to the typical exponential model over a wide range of geological conditions.

2.2.5 A statistical justification for the 35th percentile and 80% Uniaxial Compressive Strength for rock blocks

Geotechnical practitioners often use the '35th percentile' rule of thumb, or some downgrading factor (e.g., 80% of the mean UCS (Laubscher & Jakubec 2001)) when selecting representative UCS for analysis of rock. This use of percentiles is most evident in the work by Lacey (2015) with this study focused on determining 'characteristic' strength estimates to be used in civil designs involving rock. Based on Lacey's findings the following percentiles of an assumed normal distribution were recommended to be used as 'characteristic' strengths for rock:

Table 34 Percentile estimates of characteristic strengths (After Lacey 2015)

Test type	Percentile range*
Point Load Index	25th to 45th percentile. Average of 35th
Uniaxial Compressive Strength	20th - 30th percentile

*the ranges are produced from statistical analysis over different lithologies and encompass 95% of all evaluations.

Through the use of UDFs, these percentile recommendations can be shown to be approximately equal the mode value of their underlying UDF, the deterministic value recommended in Table 23. The mathematic derivation is shown below. Note this example uses the UCS but an identical derivation can be done for PLT and also UTS as the UDF that describes all of these material parameters is the same Rayleigh distribution:

The UCS UDF has been shown to be consistent with a Rayleigh distribution. For any sufficiently large random sample drawn from a Rayleigh distribution, the sample variance, $Var(X)$ and mean value μ_R will approach:

$$Var(X) = \frac{4-\pi}{2}\,\lambda_R^2 \qquad \text{Equation 66}$$

$$\mu_R = \lambda_R\sqrt{\frac{\pi}{2}} \qquad \text{Equation 67}$$

where λ_R is both the Rayleigh distribution's scale parameter and mode value Mo_R. By rearranging Equation 67 and solving for λ_R, it can be shown to be approximately equal to 80% of the mean value (79.79% of the mean) and confirms the estimate of using 80% of the mean UCS for the intact rock strength (Laubscher & Jakubec 2001). Percentiles are calculated as the value that corresponds to a particular cumulative percent of an assumed PDF. As the underlying distribution is assumed by Lacey (2015) to be normal with associated mean μ_N and standard deviation σ_N. If the standard deviation of any sufficiently large random sample drawn from a Rayleigh distribution were calculated, the standard deviation $Std(X)$ would approach:

$$Std(X) = \sigma_N = \sqrt{\frac{4-\pi}{2}}\lambda_R \qquad \text{Equation 68}$$

It is of interest to evaluate the percentile of a normal distribution at the value of Mo_R. The equation for evaluating this percentile is given by calculating the CDF of a normal distribution at Mo_R. This is calculated as:

$$CDF(Mo_R) = \frac{1}{2}\left[1 + \text{erf}\left(\frac{Mo_R - \mu_N}{\sigma_N\sqrt{2}}\right)\right] \qquad \text{Equation 69}$$

Where erf is the Gauss Error Function. Substituting Equation 66 and Equation 67 into Equation 69 yields:

$$CDF(Mo_R) = \frac{1}{2}\left[1 + \text{erf}\left(\frac{\lambda_R - \lambda_R\sqrt{\frac{\pi}{2}}}{\sqrt{\frac{4-\pi}{2}}\,\lambda_R\sqrt{2}}\right)\right] \qquad \text{Equation 70}$$

With some algebraic simplification, Equation 70 becomes:

$$CDF(Mo_R) = \frac{1}{2}[\,1 + \text{erf}(-0.2734)] \qquad \text{Equation 71}$$

As erf value is undefined in close-form, the numerical approximation is used to compute Equation 71:

$$CDF(Mo_R) = 0.3497\ or \sim 35th\ percentile \qquad \text{Equation 72}$$

This mathematical approach using UDFs matches the estimates for PLT proposed by Lacey and is close to the estimate for UCS. The reason for the discrepancy between the mathematical percentile estimate for UCS and estimates derived by Lacey is most likely due sampling errors associated with the UCS test database. PLT numbers in Lacey's study were orders of magnitude greater than UCS test numbers, which may explain why the mean percentile for PLT matches the theoretical value. An identical percentile 'characteristic' strength for both PLT and UCS makes sense considering the known and mathematically derived linear relationship between these two variables. This 35th percentile selection method by consideration of an identical derivation using the UTS shows that this value is also the suggested deterministic value.

The derivation presented provides a 'statistical explanation' as to why in situ rock appears to be weaker than laboratory tests. One thing to be weary of with these 'downgraded' values is that they relate only to the intact strength (UCS and UTS) and not the entire rock mass. A secondary strength reduction due to the presence of joints is also expected, and must still be estimated by using common empirical methods for example Hoek *et al* (2002). Another influence that is not fully captured by this approach is scale dependant strength. Although part of this scale effect can be described by this statistical influence, strength in brittle materials (Bažant 1999), and rock (Sing 1981) at increased scales produce strengths that are much lower than a purely statistical influence, suggesting some true 'non-statistical' scale response. An analysis of scale effects and the applicability of UDFs is assessed in the Chapter Three.

3 Extending Universal Distribution Functions to Consider Scaling Laws

As mentioned in Chapter One, the a-typical nature of non-standard laboratory testing practices means there are limited data that can be used to meaningfully assess probabilistic scale effects in rock material parameters. In lieu of this, heterogeneous modelling techniques were used to estimate the associated probabilistic scaling laws associated with material parameters. This Chapter outlines a general overview, fundamental assumptions, limitations, and calculation routines of the numerical program purpose built to quantify probabilistic scale effects for rock. This program was given the title The Probabilistic Lagrangian Analysis of Continua with Empirical Bootstrapped Outputs (PLACEBO), which currently operates using Itasca's FLAC3D.

3.1 PLACEBO Functionality Overview

PLACEBO is a general purpose numerical homogenisation tool used to quantify the probabilistic material parameters of intact rock at arbitrarily large scales. PLACEBO achieves this by constructing large heterogeneous laboratory samples using the known UDFs associated with mesoscopic scale zones. These large heterogeneous samples are then simulated using various laboratory test configurations to estimate the material parameters at the specified macroscopic scale, including material nonlinearities and material parameter correlations. The mesoscopic scale is used to describe the input scale over microscopic, as the scale in which the known probabilistic behaviour is quantified is larger than the grain size problems (i.e., explicitly able to include fracture mechanics and crack growth) but smaller than a typical assumed continuum scales.

The outputs produced by PLACEBO are emergent behaviours or bootstrapped, as the complex behaviours are not explicitly accounted for as model inputs and emerge as a result of simple justifiable assumptions. PLACEBO operates similarly to Itasca's PFC3D in terms of failure initiation and may occur randomly throughout the sample at any point due to local 'weaknesses' or 'defects'. The key difference between these two approaches (PLACEBO and PFC3D) is that PLACEBO uses a strain softening continuums instead of ridged spheres, particles or clumps. PLACEBO is advantageous over PFC3D in some notable ways:

It is simpler to incorporate real world measurements - PLACEBO operates on measurable laboratory scale values of which are used to simulate larger volumes. Depending on which contact model is used, PFC3D required inputs specified in terms of force and elastic components in terms of stiffness, which are not as easily measured or replicated without extensive numerical calibration. It is also difficult to calibrate a PFC3D model that can replicate all laboratory scale material parameters simultaneously (e.g., tensile strength, compressive strength, Poisson's Ratio and Young's Modulus). The PFC3D manual does make note that laboratory samples testing in this numerical environment are good at replicating UCS strengths **or** UTS strengths but not both simultaneously. Because PLACEBO uses laboratory parameters as the fundamental model inputs, each zone will always produce a valid combination of all material parameters.

Material parameter inputs are well defined probabilistically - From the initial UDF work completed in Chapter 2, most key inputs are definable probabilistically and universally. There is no need to trial various material parameter PDFs as they are well defined at the discretised scale.

Material correlation is accounted for - PLACEBO correctly applies all conditional probabilities to all relevant material parameters to ensure correct material parameter relationships are accounted for during each simulation. Shear strength parameters are often modelled with implicit negative correlation coefficients (Zengchao, Yangsheng & Dong 2009) (Zhang, Zhu, Zhang & Ding 2011) to better reflect measurable correlations in shear strength parameters. In these studies, only the frictional and cohesion components are modelled as correlated random variables with all other material parameters remaining uncorrelated. As many other material parameters in Chapter Two were shown to be correlated, all of these correlated influences are required for accurate heterogeneous analysis. The importance of including correlation coefficient is discussed later in this Chapter.

Model discretisation is orders of magnitude greater than PFC3D - Although it can be argued that PFC3D doesn't restrict the size of individual particles, PFC3D typically models small scale problems (i.e., grain-sized problems), which are heavily limited by runtimes. PLACEBO operates using mesoscopic zones, which means modelling practical problem sizes is more computationally efficient.

Material parameter non-linearity is explicitly accounted for at the discretisation scale- Although some degree of explicit progressive failure can be incorporated into PFC3D using the flat joint contact model, this progressive failure and associated non-linearity is typically an emergent property in PFC3D analysis. PLACEBO does model this emergent non-linearity but can also utilise an initially implemented nonlinearity for tensile, cohesive, frictional and dilatational influences.

3.1.1 PLACEBO limitations

Although care was taken to most accurately represent reality, there are a number of known limitations with the current implementation of PLACEBO. The following detail the known limitations associated with the use of PLACEBO. Justifications for these known assumptions and limitations are detailed below:

RVEs are rectangular and not cylindrical. One RVE is based on a NQ uniaxial UCS sample, which are cylindrical in shape. To implement a routine tessellating approximation, square rectangular prism zones are used.

Uniaxial Tensile Strength is associated with one RVE – UTS for intact rock are typically inferred from Brazilian Tensile Strength tests (ISRM 1978). The sample geometry, although similar to a UCS tests in terms of characteristic dimension (the sample diameter), it is noticeably different in term of volume. The assumption that one RVE is associated with both the UTS and UCS was made as partial discretization of material parameters was not possible to implement without violating the associated correlations.

Micro mechanics are ignored in favour for a continuum – The intergranular fracture process observed in practice and analysis using software such as PFC3D is acknowledged to occur. These processes were considered too small and poorly quantifiable to be directly considered in PLACEBO. A statistically equivalent continuum based on the measurable statistical behaviours of material at one RVE was used as a well-defined substitution. This means that features smaller than one RVE were deemed too small to influence the overall behaviour and cannot be measured. A comparison of failure observed across different testing methods is shown in Figure 28.

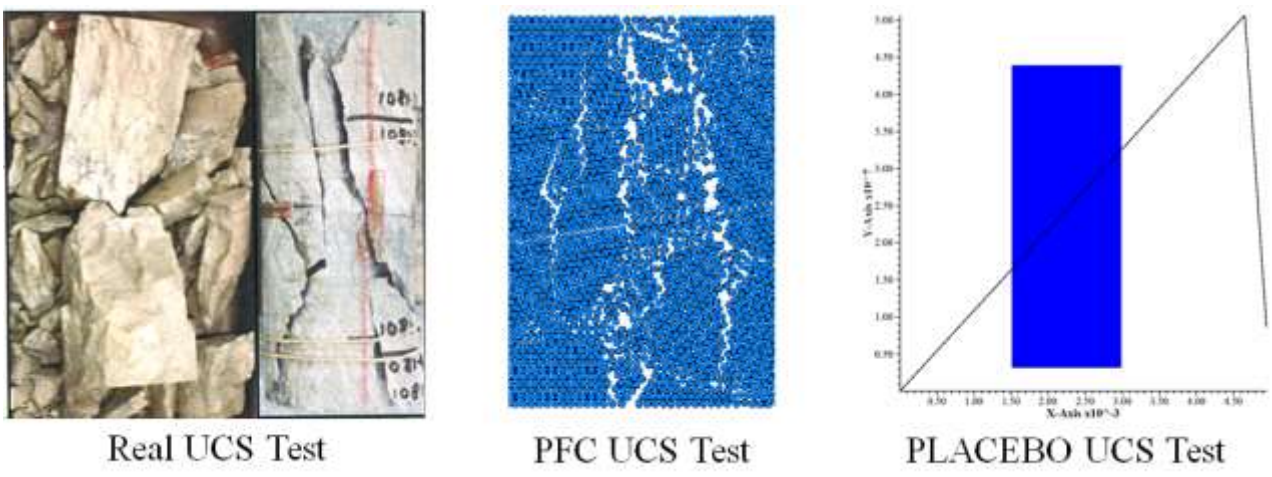

Figure 28 Failure observed in real test samples, PFC3D and PLACEBO

Fracture mechanics interactions are accounted for but are limited – It is known that stress concentrations about crack tips play an important role in tensile failure propagation in brittle materials (Griffith 1921). The stress concentrations may be underestimated numerically, as the model discretization used will result in blunt numerical cracks after yielding. To explore the influence of blunt cracks two aspects were checked:

- If FLAC3D strain softening tensile failure honour stress fields about cracks (Mode I).
- If blunt cracks (limited by PLACEBO discretisation) honour stress fields sufficiently for proper fracture mechanic responses (Mode I).

To test for the failure mode response, the tensile stresses (i.e., Mode I Fracture) about three different numerical cracks in a semi-infinite (open vertically with finite bounds laterally) were considered. This crack configuration does not have an analytical solution for stress intensities so the stress field about a two dimensional plane-strain line crack was considered as the replication standard. Numerical models were constructed in FLAC3D using an open (i.e., zones are set as *Null*) and strain softened crack (all other zones less the crack are elastic). Zone volumes were $1cm^3$ with the numerical sample being 1m wide in both the x and y directions. A uniaxial tensile stress of 5 MPa was then applied to the open end. The stress fields for various zone types are shown in Figure 29.

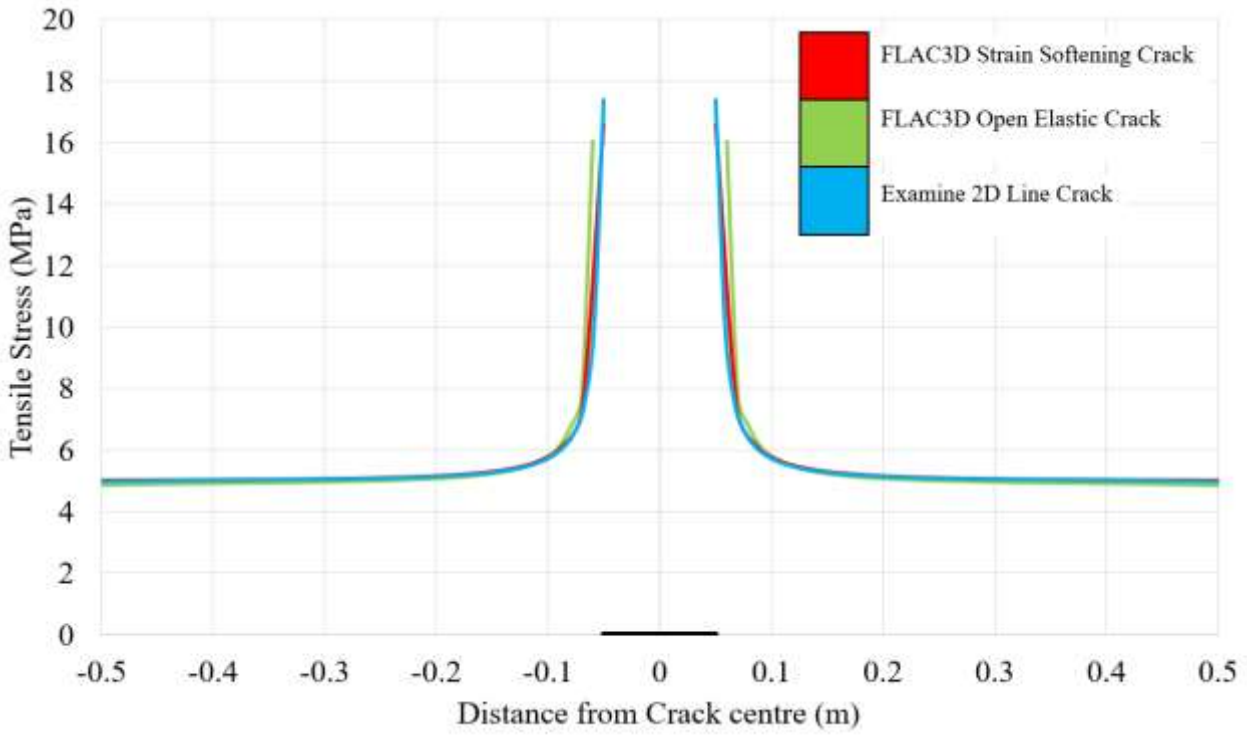

Figure 29 Comparisons of stresses about a crack tip using various numerical methods

It can be seen in Figure 29 that field stresses about open or strain-softened cracks in FLAC3D are sufficiently accurate to say that the stress field response can accommodate a fracture mechanics response. To test the influence of a blunt crack, a single zone was modelled and compared to the two dimensional line crack. The fields about these crack geometries are shown in Figure 30.

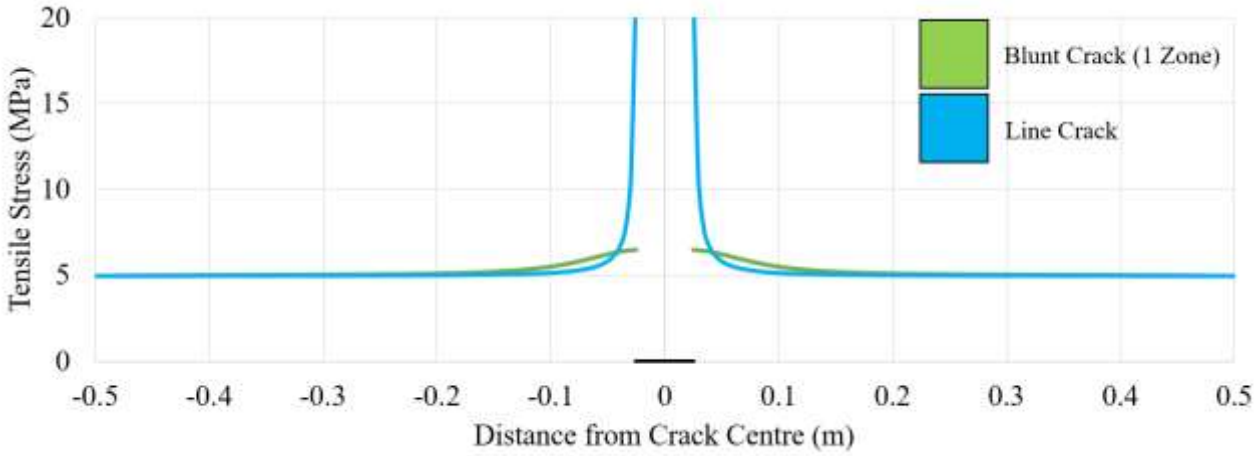

Figure 30 Comparisons of stresses about two dimensional line and a two dimensional 'blunt' crack

By considering Figure 30 it can be seen that the blunt cracks are poor at replicating the expected stress field. While the implemented procedure in PLACEBO does allow cracks to form and coalesce, there is some doubt concerning the accuracy with respect to a completely realistic fracture propagation response near a crack tip. These results indicate that PLACEBO will almost surely over-estimate the UTS of any sample due to lower than expected stress intensities at the crack tip surface. This problem could be reconciled in the future in three ways:

- By using smaller zones - Zone sizes are set based on the leading understanding of material variability at a given scale and cannot change in volume without considerable doubts concerning model accuracy. The tensile stress partial discretisation (mentioned previously) may alleviate some of the errors associated with this issue, but as previously mentioned is very difficult to correctly implement.
- By changing zone aspect ratios - The aspect ratio for each zone is that of a single UCS sample and is done in case some geometric influence is present. This initial zone aspect ratio influence is demonstrated later in this Chapter.
- Checking for any tensile failure and assuming instantaneous crack propagation - This approach may fix the issues with zone sizes/ aspect ratios, but may also under estimate the true UTS. This is because any crack that forms, the stress intensity factor may not exceed the Mode I fracture

toughness and hence will not fail instantaneously. The best approximation for UTS estimation would be obtained using fracture mechanic specific software (Nakamura, Gu, Tajima & Hazama 2015) to estimate scale dependent tensile failure. The issue is then that fracture toughness needs to be defined probabilistically, which is seldom studied for rock engineering problems. A pinching method would give upper and lower bounds, but this also does not give much guidance for practical problem inputs.

Material is linear over varying confinement. The UDF analysis from Chapter Two presented a probabilistic model for a Mohr Coulomb criterion over varying confinement. Although this is a reasonable assumption for geotechnical problems, studies (Hoek & Brown 1980) have shown that materials do exhibit nonlinear strengths over varying confinements. The reason for using the Mohr Coulomb criterion is that the UDF behaviours for nonlinear relationships like the Hoek Brown criterion (Hoek & Brown 1980) are currently undefined in terms of UDFs. PLACEBO is general enough that any conceivable failure criterion can be implemented once a probabilistic description is available.

Only intact responses are considered - UDFs are currently only applicable at describing intact rock behaviour and currently are not applicable at describing rock structure. Due to this limited information, only intact behaviours can be assessed using PLACEBO currently.

3.1.2 PLACEBO assumptions

As mentioned in Chapter Two, many material parameters are currently unquantified using UDFs. In their absence, the following behaviours were assumed due to a current incomplete probabilistic understanding:

Tensile Strength correlation coefficients are similar to compressive strength correlation coefficients. Destructive tests are used to quantify intact strength (UTS and UCS), meaning correlation coefficients cannot be measured for destructive test pairs. This assumption is reasonable and produces higher UTS for RVEs of higher UCS. This assumption also aligns with the published findings of Nazir, Momeni, Armaghani and Amin (2013) and others (See Nazir *et al 2013*).

Each RVE has identical peak and residual friction angles and no softening. From Chapter Two it was shown that there is generally no statistical difference between the mean peak and mean residual friction angles for rock. The assumption of unchanging friction is reasonable based on these previous findings and does not require a softening or hardening friction response to be specified at one RVE.

Cohesion softens to some specified percentage of peak zone cohesion. As the UDF of cohesion is implicitly defined, residual values of cohesion should also follow the same UDF. A perfectly correlated ratio reduction was used to apply similar implicit distribution for residual cohesion. This means that each RVE retains some percentage of its peak cohesion after some specified plastic shear strain. The cohesion softening table was assumed linear to some specified plastic shear strain, with a zone dependant softening rate based on each zone's peak cohesion. This implementation produces a similar implicit distribution for the rate of softening (i.e., the distribution of the cohesion softening table) as that of cohesion. The critical shear strain is set at a default 0.000001 to simulate brittle failure. This softening response can be arbitrarily specified as required.

Tensile strength soften to zero. This is a typical brittle material assumption and is stated for completeness. The critical tensile strain is set at a default 0.000001 to simulate instantaneous crack propagation within a single zone. This softening response can be arbitrarily specified as required.

Dilation per zone Deterministic. This assumption was made due limited information for rock dilation. This value can be arbitrarily set as required.

End plate influences are implicitly incorporated. The influences of loading plattens is frequently assessed as a sensitivity in numerical modelling (Liu 2004) (Sainsbury, Pierce & Mas Ivars 2008). End plate influences were implicitly defined in the UCS seed in this analysis to limit the number of definable unknowns. This means that a single RVE model always produces statistically indistinguishable results from real world tests that is, it correctly accounts for unknown end effects at laboratory scales without explicitly defining the influence. It is possible that this method results in end effects being present in each RVE, which may distort results to some unknown level. It is a considerably difficult task to quantify real world end effects and then separate them from intrinsic material parameters based on current understandings.

3.1.3 PLACEBO measurement routines

In order to measure all material parameters for each sample, a wide range of numerical laboratory are conducted on each numerical sample:

Density

Density is measured after each sample is randomly generated. The density of an n RVE sample is calculated using:

$$\rho_n = \frac{1}{n\,V_0}\sum_{i=1}^{n}\rho_i V_0 \qquad \text{Equation 73}$$

where ρ_n is the material density (kg/m³) of n RVEs, V_0 is the volume of the RVE (m³).

Elastic parameters

Strain measurements are required when considering elastic and plastic responses of each sample. For each sample, two distinctively different elastic measurements are measured:

- the elastic components obtained from elastic simulations; and
- the equivalent elastic components (named the secant values) obtained from plastic analysis. The secant measurement is the value of Young's Modulus and Poisson's Ratio at the point of sample failure.

The reason for including both measurements is that models larger than 1 RVE begin to yield before the peak strength is attained, which influences the equivalent elastic response (i.e., the scale effect on elastic parameters). In order to measure the elastic components, the average face displacements and strains in the x, y and z directions are used. This averaging is used to align with how elastic components (mainly the vertical direction) are calculated for laboratory samples. From Elasticity theory. The stain-stress relationship is governed by:

$$\epsilon = \frac{\sigma}{E} \qquad \text{Equation 74}$$

where σ is the acting stress (Pa), E is Young's Modulus (Pa) and ϵ is the strain in the direction of loading. For each simulation in PLACEBO, ϵ is measured using the standard definition of strain:

$$\epsilon = \frac{\Delta L}{L} \qquad \text{Equation 75}$$

where L is the initial side length (m); and ΔL is the change in side length when exposed to some stress (m). The average displacement δ (m) of each surface on the sample is calculated by using:

$$\delta_{top} = \frac{1}{n}\sum_{i=1}^{n} \delta_i \qquad \text{Equation 76}$$

where n is the number of grid points on the measured face. ΔL in Equation 75 is then calculated by:

$$\Delta L = \delta_{top} - \delta_{bottom} \qquad \text{Equation 77}$$

The Young's modulus is only calculated for the Z direction. Poisson's Ratio is calculated using the standard definition:

$$v = -\frac{\epsilon_x}{\epsilon_z} = -\frac{\epsilon_y}{\epsilon_z} \qquad \text{Equation 78}$$

where v is Poisson's Ratio and ϵ_i is the strain in the direction i. As the sample is three dimensional (and by chance partially anisotropic) both x and y values of Poisson's Ratio are measured along with the average of both measurements.

Stresses

One routine is used to tack both the peak and residual strength for each test the stress is calculated by:

$$\sigma = \frac{\sum_{i=1}^{n} F_i}{Area} \qquad \text{Equation 79}$$

where σ is the active stress (Pa) and F_i is the force acting on grid point i (N). The force is calculated from the unbalanced force on one of the loading platters and divided by the sample area. Tensile stresses and compressive stresses are tracked in 'real time' for the entire duration of each test. The maximum value of stress observed through the entire test is deemed the peak strength for each sample.

The residual compressive strength is taken as the value of the tracked stress at some point far past the peak strength is achieved. This is manually set as a function of the test volume to minimise how long the numerical routine takes to run for a given sample size. Typically 250,000 to 300,000 model cycles past the peak stress measurement was chosen as the residual strength.

Strength parameters

In terms of numerical modelling strength parameters, the peak or residual compressive or triaxial strengths are not definable model inputs. These measured strengths need to be converted to material parameters. UCS in a Mohr Coulomb model is defined using a value of cohesion c and a friction angle ϕ. The value for c in terms of the UCS and friction is previously presented in Equation 55. From the FLAC3D manual, the Mohr Coulomb equation for shear failure f^s implemented is given by:

$$f^s = \sigma_1 - \sigma_3 \left(\frac{1+\sin\phi}{1-\sin\phi}\right) + 2c\sqrt{\frac{1+\sin\phi}{1-\sin\phi}} \qquad \text{Equation 80}$$

where σ_1 is the Major stress (Pa) and σ_3 is the Minor stress (Pa) (for triaxial cases this is the confining stress). Failure is assumed to occur when f^s >0 with the limit state given when f^s = 0. Using this limit state for two different triaxial stress states, ϕ can be calculated using:

$$\phi = \sin^{-1}\left(\frac{\sigma_{1_1} - \sigma_{1_2} - \sigma_{3_1} + \sigma_{3_2}}{\sigma_{3_1} - \sigma_{3_2} + \sigma_{1_1} - \sigma_{1_2}}\right) \qquad \text{Equation 81}$$

When the value for ϕ (°)is determined, Equation 55 can then be evaluated to determine the value of cohesion. This process is applicable for both the peak and residual as previously mentioned. In an ideal world, the perfect Mohr Coulomb criterion is quantifiable using only two measurements to calculate both friction and cohesion from a single simulation. From initial testing, it was determined that due to small incurrences of numerical rounding errors, a pair of triaxial measurements produces

slightly different values for friction and cohesion for an idealised model. To compensate for this four strength tests (one uniaxial and three triaxial) are simulated for each sample, with a line of best fit being used to generate the variable inputs for Equation 81. The confining stresses for each numerical sample are calculated as a function of the material inputs, and correspond to 5%, 10% and 15% of the median UCS. The linear regression model implemented is given in the form:

$$\widehat{\sigma_1} = \hat{m}\sigma_3 + \widehat{\sigma_0} \qquad \text{Equation 82}$$

where $\hat{m} = \left(\frac{1+\sin\phi}{1-\sin\phi}\right)$ and $\hat{\sigma}_0 = 2c\sqrt{\frac{1+\sin\phi}{1-\sin\phi}}$. The linear regression equations are given as:

$$\hat{m} = \frac{(\sum \sigma_1)(\sum {\sigma_3}^2) - (\sum \sigma_3)(\sum \sigma_3\sigma_1)}{n(\sum {\sigma_3}^2) - (\sum \sigma_3)^2} \qquad \text{Equation 83}$$

$$\widehat{\sigma_0} = \frac{n(\sum \sigma_3\sigma_1) - (\sum \sigma_3)(\sum \sigma_1)}{n(\sum {\sigma_3}^2) - (\sum \sigma_3)^2} \qquad \text{Equation 84}$$

where σ_1 is the peak or residual strength (Pa) and σ_3 is the applied confining stress (Pa). To validate the accuracy of this approach numerous combinations of hardening and softening models were simulated to determine the accuracy of the above calculation routines. Table 35 shows the accuracy validation of this regression technique to quantify various combinations of input and residual friction values for validation of the above equations.

Table 35 Mohr Coulomb calculation accuracy check

Input values		PLACEBO output			
Peak values	Residual values	Peak friction	Peak cohesion	Residual friction	Residual cohesion
35° 4 MPa	35° 0.00 MPa	34.98 (0.06%)	4.02 (0.50%)	35.02 (0.07%)	0.00 (0.00%)*****
20° 2 MPa	20° 0.00 MPa	20.11 (0.55%)	2.01 (0.50%)	20.12 (0.58%)	0.00 (0.00%)*****
40°	30°	39.97	6.00	30.00	1.00

6 MPa	1.00 MPa	(0.08%)	(0.00%)	(0.00%)	(0.00%)
25° 9 MPa	35° 2.50 MPa	25.03 (0.12%)	9.00 (0.00%)	35.01 (0.02%)	2.50 (0.00%)
45° 5 MPa	10° 5.00 MPa	44.88 (0.27%)	5.03 (0.60%)	10.00 (0.02%)	5.00 (0.00%)
45° 5 MPa	45° 5.00 MPa	45.01 (0.02%)	5.02 (0.40%)	45.00 (0.00%)	5.00 (0.00%)

*these residual values, despite being zero are perfectly replicated within PLACEBO. Ideally, these should have an undefined accuracy but it can be taken that the error is zero in these cases. The numerical accuracy for calculating both peak and residual under strain softening / hardening and perfectly plastic are correctly accounted for and replicated with typically less than 0.5% error in accuracy.

As previously mentioned, PLACEBO operates using a strain softening/hardening Mohr Coulomb model with non-associated shear and associated tension flow rules. In order to quantify the softening response, the plastic components of strain need to be quantified. Using the standard definitions, the total stain ϵ^{Total} can be decomposed into the elastic $\epsilon^{Elastic}$, and plastic $\epsilon^{Plastic}$ components:

$$\epsilon^{Total} = \epsilon^{Elastic} + \epsilon^{Plastic} \qquad \text{Equation 85}$$

The value of ϵ^{Total} is the only quantity that can be directly measured for large heterogeneous samples. This becomes problematic as the problem cannot be broken down into the key components as for any multiple zone model as the equivalent elastic components are unknown. The solution to this is that each sample is simulated twice, once to calculate $\epsilon^{Elastic}$ at failure, then a second simulation to track the plastic components by:

$$\epsilon^{Total}_{Failure} - \epsilon^{Elastic}_{Failure} = \epsilon^{Plastic} \qquad \text{Equation 86}$$

Tensile plastic strain according to the FLAC3D manual implements the following associated plastic flow rule:

$$\Delta\epsilon_3^{Pt} = \frac{\sigma_3^I - \sigma^t}{K + \frac{4}{3}G}$$ Equation 87

$$\Delta\epsilon_3^{Pt} = \frac{(1-2v)(1+v)(\sigma_3^I - \sigma^t)}{E(1-v)} = \frac{(\sigma_3^I - \sigma^t)}{M}$$ Equation 88

where σ_3^I is the new trial stress at the next time step (Pa), σ^t is the peak tensile stress (Pa) and M is the P-wave modulus (Pa). From Equation 88 it can be seen that when a trial tensile stress is applied, the difference between the stress and the peak is calculated as a linear strain and added to the plastic strain increment. This is an identical formulation to calculating the plastic component in isolated tension. By considering that the plastic flow rule for tension is associative, this would have been expected.

In order to validate the measurement routine accuracy for Equation 88, a single zoned UTS test was modelled with various tensile softening tables assigned to compare the numerical accuracy of the plastic strain routine. The results of these simulations are shown in Table 36.

Table 36 Errors in plastic measurements - tensile strain

Assigned critical softening	PLACEBO measurement	Error (%)
5.0×10^{-2}	5.0×10^{-2}	0.00%
1.0×10^{-2}	9.9×10^{-3}	1.00%
1.0×10^{-3}	8.4×10^{-4}	16.00%
1.0×10^{-4}	2.6×10^{-6}	97.40%
1.0×10^{-5}	1.0×10^{-6}	90.00%
1.0×10^{-6}	3.7×10^{-6}	270.00%

From Table 36 it can be seen that for large values of plastic strains there is minimal errors associated with the measurement routine. When the critical tensile strain becomes small, there are substantial errors. This unreasonably high error for the measured plastic tensile strain means that analysis cannot accurately estimate the equivalent plastic tensile strain. For this reason plastic tensile strain considerations as a function of scale cannot be considered in any meaningful detail currently.

Plastic shear strain utilises a non-associated flow rule, which means that the direction of plastic flow doesn't have to be in the direction of applied loads (for example, in a compressive test, loads are applied vertically but the failure may have plastic strains in a direction that make some angle to the applied load). From the FLAC3D manual, the plastic shear strain increment used for softening responses is a measure of the second invariant of the plastic shear-strain increment tensor given as:

$$k^s = \frac{1}{\sqrt{2}}\sqrt{\left(\epsilon_1^{ps} - \epsilon_m^{ps}\right)^2 + \left(\epsilon_m^{ps}\right)^2 + \left(\epsilon_3^{ps} - \epsilon_m^{ps}\right)^2} \qquad \text{Equation 89}$$

where ϵ_1^{ps} is the major plastic shear strain component, ϵ_3^{ps} is the minor plastic shear strain component and ϵ_m^{ps} is the volumetric plastic shear strain. ϵ_m^{ps} is defined as:

$$\epsilon_m^{ps} = \frac{1}{3}\left(\epsilon_1^{ps} + \epsilon_3^{ps}\right) \qquad \text{Equation 90}$$

This formulation is difficult to generalise with very little supporting documentation to how it is executed. The Von Mises criterion offers a more applicable definition, with the plastic shear strain component given by:

$$k^s \approx \frac{\sqrt{2}}{3}\sqrt{\left(\epsilon_{xx}^p - \epsilon_{yy}^p\right)^2 + \left(\epsilon_{yy}^p - \epsilon_{zz}^p\right)^2 + \left(\epsilon_{zz}^p - \epsilon_{xx}^p\right)^2} \qquad \text{Equation 91}$$

where $\epsilon^p$is the plastic strain component associated with the global coordinate directions. The numerical implementation of Equation 91 was checked for its numerical accuracy, with the results shown in Table 37.

Table 37 Errors in plastic measurements - shear strain

Assigned critical softening	PLACEBO measurement	Error (%)
5.0×10^{-2}	4.9×10^{-2}	2%
1.0×10^{-2}	9.6×10^{-3}	4%
1.0×10^{-3}	1.3×10^{-3}	30%
1.0×10^{-4}	4.8×10^{-4}	380%
1.0×10^{-5}	7.6×10^{-4}	7500%
1.0×10^{-6}	5.4×10^{-4}	53900%

From Table 37 is can be seen that for large values of critical plastic strains (e.g., 5%) there are acceptable errors associated with the measurement routine. When the strain becomes small, there are substantial errors. Due to these errors, it is currently unfeasible to use PLACEBO to quantify shear strain responses. It is suspected that the main reason for this inaccuracy of both the plastic tensile and shear measurement routines are rounding errors incurred from successive calculations. As the strain values in question are very small, they are easily influenced by rounding errors. Better measurement techniques are required to bypass this issue in future iterations of PLACEBO.

Dilation is calculated using plastic strain components. The most usable definition utilises the equations presented in the Odometer test within the FLAC3D manual. From Equation (1.103) in the manual, the plastic strains are related to dilation such that (Note: rearranged such that loading is aligned with the Z axis):

$$\epsilon_{xx}^{p} = -\omega N_{\psi} \qquad \text{Equation 92}$$

$$\epsilon_{yy}^{p} = -\omega N_{\psi} \qquad \text{Equation 93}$$

$$\epsilon_{zz}^{p} = -2\omega \qquad \text{Equation 94}$$

Note that ω is a function that relates to the material's stiffness and strength. From simple rearranging of Equation 94 and substituting into Equation 92:

$$\frac{2\epsilon_{xx}^{p}}{\epsilon_{zz}^{p}} = N_{\psi}$$ Equation 95

From the FLAC3D manual, the dilation function is given as:

$$N_{\psi} = \frac{1 + \sin(\psi)}{1 - \sin(\psi)}$$ Equation 96

Using this substituting Equation 96 into Equation 95 and solving for ψ:

$$\psi = \sin^{-1}\left(\frac{2\epsilon_{xx}^{p} - \epsilon_{zz}^{p}}{\epsilon_{zz}^{p} + 2\epsilon_{xx}^{p}}\right)$$ Equation 97

The numerical accuracy of Equation 97 was checked against single zoned models with an initially seeded known value for dilation and a randomly seeded value of Poisson's ratio and Young's Modulus to ensure the plastic measurements were correctly measured. The results of the dilation routine are shown in Table 38.

Table 38 Error in dilation angle measurements

Assigned dilation angle	PLACEBO measurement	Error (%)
50°	50.67°	1.34%
40°	41.32°	3.30%
30°	32.46°	8.20%
20°	21.08°	5.40%
10°	9.25°	7.50%
0°	0.78°	N/A

Even though PLACEBO was unable to replicate the plastic strain rates, it was reasonable at estimating and measuring sample dilation using Equation 97, as the measured value was typically within one degree of the actual dilation. When considering larger samples, the measurement routine for dilation in PLACEBO did occasionally produce negative dilation angles, which had questionable physical

representations. These negative values raised enough doubt that dilation was not sufficiently measured within PLACEBO simulations. For this reason, dilation was not included in further analysis.

3.1.4 PLACEBO extension - path dependant Probability of Failure

As the heart of PLACEBO is essentially a sophisticated random number generator, it does have applications to more general problems. PLACEBO can be used to numerically evaluate the POF integral on a zone by zone basis for any problem geometry. While FLAC3D has been previously used for POF analysis considering heterogeneity, the POF integral in these applications is calculated outside of FLAC3D using the output of the FOS solver (Shen 2012) or using an assumed POF model (Chiwaye 2010). This direct implementation within FLAC3D gives the ability to consider the POF for all possible progressive failures, includes considerations for material parameter heterogeneity. The application of this POF calculation can be done using the following loop:

- Define a model geometry and material parameter inputs.
- Simulate model for some number of steps.
- Search for ‘failure’ based on some criteria; for example, plastic strain, displacement, etc.
- Reseed model and simulate.
- Calculate the POF for each zone based on the outputs of all simulations.

An example model computed with this zone dependent POF approach is shown in Figure 31.

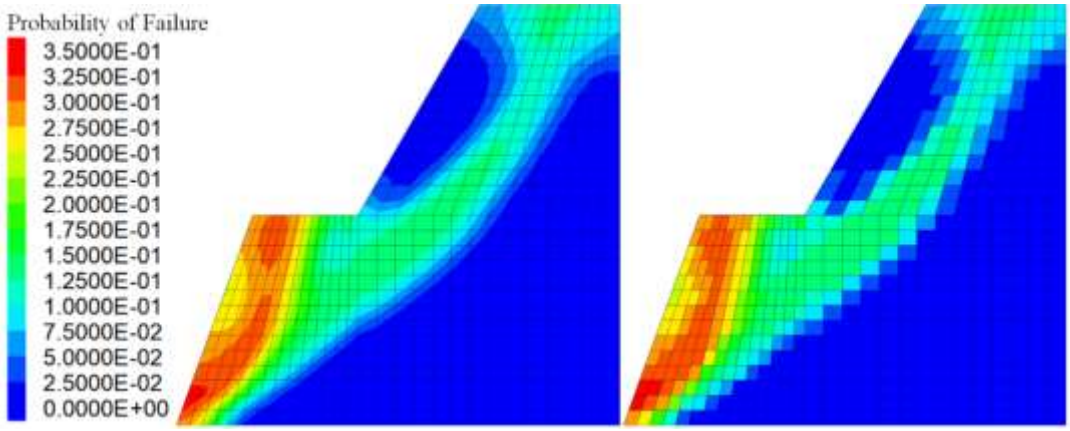

Figure 31 Example path dependent Probability of Failure considering heterogeneity

In the example shown in Figure 31 the POF for the lower bench is roughly 35%, while the POF for both benches is 15%. In terms of practical applications of this POF approach, there are currently some limitations:

Mesh dependencies need to be considered - The material behaviour is tied to a specific zone volume, which need to be corrected in terms of both scaling laws and variability based on the generated problem mesh. While this influence is ignored in Figure 31, it needs to be included to produce realistic failure probabilities and paths. Using a uniformly zoned model does eliminate this mesh dependency, but based on the current volume in which UDFs are quantified would result in models with unreasonably long simulation times, even for single bench models. It is noted that including this mesh dependency is trivial in PLACEBO.

Simulation times are unreasonably long - As a rough estimate, a mine scale numerical model may take 6 hours or more to simulate the excavation of several pit cutbacks. In order to calculate the POF, the problem would need to be simulated 500 - 1000 times to gain an appreciable probabilistic response. This would produce a run time of several months, which would not be a practical numerical assessment tool. For practical applications, this limits the complexity of problems that can be solved currently.

3.2 Numerical analysis at scale using PLACEBO

In order to test for and approximate general material parameter scale behaviours, representative material characteristics over a wide range of conditions and inputs were considered. Five separate synthetic 'lithologies' were generated to simulate a wide range of commonly encountered geological conditions, with each lithology being loosely based on actual test results from Chapter Two. Statistical parameters for each synthetic lithology were randomly selected from the statistical viable range in Table 23 in order to better reflect all viable probabilistic conditions. The median value M and associated probabilistic parameters, for each synthetic lithology is shown in Table 39.

Table 39 Synthetic lithology peak and elastic material parameter inputs

Lithology	UTS (MPa)	UCS (MPa)	Poisson's Ratio	Young's Modulus (GPa)	Friction (°)	Sample height to width ratio	Dry density (t/m^3)
UDF	Rayleigh	Rayleigh	Triangular	Weibull	Normal	Constant	Laplace
Lithology one (L1)	$M = 2.010$	$M = 13.500$	$a = 0.018$ $b = 0.066$ $c = 0.022$	$M = 11.700$ k =1.437	$M = 39.000$ $\sigma = 4.538$	2.63	$M = 2.370$ $\sigma = 0.050$
Lithology two (L2)	$M = 2.850$	$M = 36.100$	$a = 0.013$ $b = 0.303$ $c = 0.045$	$M = 20.530$ k =1.856	$M = 26.100$ $\sigma = 3.217$	2.52	$M = 2.510$ $\sigma = 0.053$
Lithology three (L3)	$M = 8.500$	$M = 95.900$	$a = 0.200$ $b = 0.335$ $c = 0.279$	$M = 68.150$ k =1.480	$M = 36.000$ $\sigma = 1.263$	2.84	$M = 2.670$ $\sigma = 0.026$
Lithology four (L4)	$M = 12.300$	$M = 116.300$	$a = 0.180$ $b = 0.350$ $c = 0.279$	$M = 66.800$ k =1.605	$M = 37.000$ $\sigma = 1.844$	2.57	$M = 2.750$ $\sigma = 0.052$
Lithology five (L5)	$M = 14.400$	$M = 149.000$	$a = 0.189$ $b = 0.363$ $c = 0.238$	$M = 87.450$ k =1.921	$M = 32.00$ $\sigma = 1.788$	2.71	$M = 2.830$ $\sigma = 0.042$

Note that in Table 39, UCS is not a material parameter. This value is provided as it is used in conjunction with the friction angle to implicitly calculate the UDF for cohesion. Correlation coefficients were also required for each variable pair to correctly account for conditional material parameter probabilities. The correlation coefficient matrix for each synthetic lithology is shown below.

$$R(x) = \begin{bmatrix} r_\rho^2 & r_{\rho,\sigma_t} & r_{\rho,\sigma_c} & r_{\rho,E} & r_{\rho,v} & r_{\rho,\phi} \\ r_{\rho,\sigma_t} & r_{\sigma_t}^2 & r_{\sigma_t,\sigma_c} & r_{\sigma_t,E} & r_{\sigma_t,v} & r_{\sigma_t,\phi} \\ r_{\rho,\sigma_c} & r_{\sigma_t,\sigma_c} & r_{\sigma_c}^2 & r_{\sigma_c,E} & r_{\sigma_c,v} & r_{\sigma_c,\phi} \\ r_{\rho,E} & r_{\sigma_t,E} & r_{\sigma_c,E} & r_E^2 & r_{E,v} & r_{E,\phi} \\ r_{\rho,v} & r_{\sigma_t,v} & r_{\sigma_c,v} & r_{E,v} & r_v^2 & r_{v,\phi} \\ r_{\rho,\phi} & r_{\sigma_t,\phi} & r_{\sigma_c,\phi} & r_{E,\phi} & r_{v,\phi} & r_\phi^2 \end{bmatrix} \quad \text{Equation 98}$$

$$R(L1) = \begin{bmatrix} 1.000 & 0.498 & 0.429 & 0.341 & 0.000 & 0.000 \\ 0.498 & 1.000 & 0.516 & 0.650 & 0.000 & 0.000 \\ 0.429 & 0.516 & 1.000 & 0.649 & 0.000 & 0.000 \\ 0.341 & 0.650 & 0.649 & 1.000 & -0.028 & 0.000 \\ 0.000 & 0.000 & 0.000 & -0.028 & 1.000 & 0.000 \\ 0.000 & 0.000 & 0.000 & 0.000 & 0.000 & 1.000 \end{bmatrix} \quad \text{Equation 99}$$

$$R(L2) = \begin{bmatrix} 1.000 & 0.463 & 0.387 & 0.462 & 0.000 & 0.000 \\ 0.463 & 1.000 & 0.523 & 0.840 & 0.000 & 0.000 \\ 0.387 & 0.523 & 1.000 & 0.621 & 0.000 & 0.000 \\ 0.462 & 0.840 & 0.621 & 1.000 & -0.077 & 0.000 \\ 0.000 & 0.000 & 0.000 & -0.077 & 1.000 & 0.000 \\ 0.000 & 0.000 & 0.000 & 0.000 & 0.000 & 1.000 \end{bmatrix} \quad \text{Equation 100}$$

$$R(L3) = \begin{bmatrix} 1.000 & 0.433 & 0.467 & 0.361 & 0.000 & 0.000 \\ 0.433 & 1.000 & 0.725 & 0.718 & 0.000 & 0.000 \\ 0.467 & 0.725 & 1.000 & 0.734 & 0.000 & 0.000 \\ 0.361 & 0.718 & 0.734 & 1.000 & -0.042 & 0.000 \\ 0.000 & 0.000 & 0.000 & -0.042 & 1.000 & 0.000 \\ 0.000 & 0.000 & 0.000 & 0.000 & 0.000 & 1.000 \end{bmatrix} \quad \text{Equation 101}$$

$$R(L4) = \begin{bmatrix} 1.000 & 0.407 & 0.432 & 0.424 & 0.000 & 0.000 \\ 0.407 & 1.000 & 0.615 & 0.573 & 0.000 & 0.000 \\ 0.432 & 0.615 & 1.000 & 0.673 & 0.000 & 0.000 \\ 0.424 & 0.573 & 0.673 & 1.000 & -0.026 & 0.000 \\ 0.000 & 0.000 & 0.000 & -0.026 & 1.000 & 0.000 \\ 0.000 & 0.000 & 0.000 & 0.000 & 0.000 & 1.000 \end{bmatrix} \quad \text{Equation 102}$$

$$R(L5) = \begin{bmatrix} 1.000 & 0.503 & 0.433 & 0.325 & 0.000 & 0.000 \\ 0.503 & 1.000 & 0.680 & 0.595 & 0.000 & 0.000 \\ 0.433 & 0.680 & 1.000 & 0.662 & 0.000 & 0.000 \\ 0.325 & 0.595 & 0.662 & 1.000 & -0.052 & 0.000 \\ 0.000 & 0.000 & 0.000 & -0.052 & 1.000 & 0.000 \\ 0.000 & 0.000 & 0.000 & 0.000 & 0.000 & 1.000 \end{bmatrix}$$ Equation 103

Based on these inputs and the testing methodology presented in Chapter One, the following results were obtained. For consistency and to allow for comparative analysis over multiple lithologies, results were typically expressed in terms of percentages of the median input value (the value of M shown in Table 39). The presentation of scale sizes was chosen as multiples of one RVE to reduce the exaggeration of a volume based x-axis. These scale measurements are converted to a volume by multiplying the RVE volume by the third power of the sample size.

3.2.1 Dry density at scale

Dry density was not influenced by interacting complexities like other material parameters. A closed form approximation of the general behaviour of dry density at scale was derived algebraically. The density of an n RVE sample volume is given by:

$$\rho_n = \frac{1}{n\,V_0}\sum_{i=1}^{n}\rho_i V_0 = \mu_{\rho_0}$$ Equation 104

where ρ_n is the material density of n RVEs (kg/m³), V_0 is the volume of the RVE (m³) and μ_{ρ_0} is the mean density of the RVE (kg/m³). As the dry density UDF has an unchanging mean value, the scale parameter σ. will vary with the sample volume in accordance with the central limit theorem. The scale parameter as a function of the number or RVEs is then calculated by:

$$\sigma_n = \frac{\sigma_0}{\sqrt{n}}$$ Equation 105

where σ_0 is a value between 2.62% and 5.54% of the median RVE density (t/m^3). Converting Equation 105 to a function of the overall volume V produces Equation 106:

$$\sigma_V = \frac{\sigma_0}{\sqrt{V}}\sqrt{V_0} \qquad \text{Equation 106}$$

When the upper and lower bounds given in Table 23 are included:

$$\frac{0.0262\,\mu_{\rho_0}\sqrt{V_0}}{\sqrt{V}} \lesssim \sigma_V \lesssim \frac{0.0554\,\mu_{\rho_0}\sqrt{V_0}}{\sqrt{V}} \qquad \text{Equation 107}$$

The arbitrary scale UDF for dry density ρ_V, in t/m^3 is then given as:

$$f(\rho_V \mid V, \mu_{\rho_0}, \sigma_0) \approx \frac{1}{2\sigma_V} e^{-\frac{|\rho_V - \mu_{\rho_0}|}{\sigma_V}} \qquad \text{Equation 108}$$

Equation 108 is expected to be accurate for volumes greater than one RVE, but decrease significantly in accuracy for volumes that approach the material's grain size. It is expected that the PDF near this volume will transition to a multi modal distribution, reflecting the mineral composition and density distributions rather than the rock.

3.2.2 Deterministic strength at scale

The change in the measured median UTS for each sample size and lithology are shown in Figure 32.

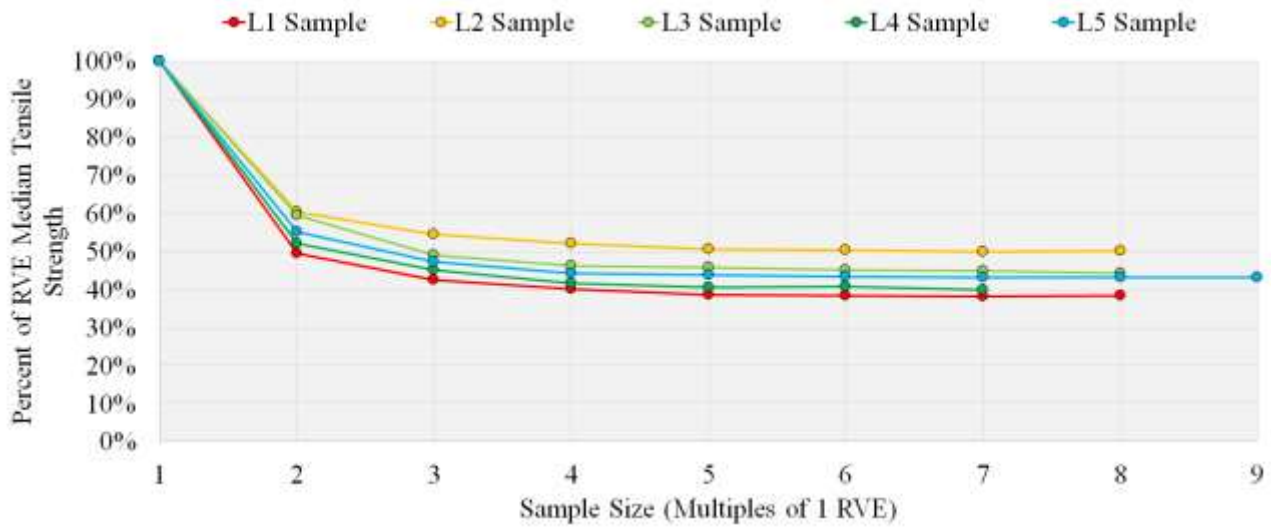

Figure 32 Influences of scale on the median tensile strength of each synthetic lithology

The measured UTS can be seen to follow the 'typical' strength reduction found in literature, but appears to have a well-defined asymptotic strength beyond 5 times one RVE. There was also notable differences in the asymptotic strengths associated with each lithology, with asymptotes ranging between 50% and 40% of the median laboratory scale value. Mentioned previously, the UTS was expected to be significantly higher than what would be observed in real world direct tensile tests. The accumulated plastic tensile strains at failure within these numerical samples produced 'non rock like' tensile failure, with fracture patterns similar to tensile failure in high fracture toughness materials like steel or tungsten. Examples of these tensile failure patterns produced as part of this study are shown in Figure 33.

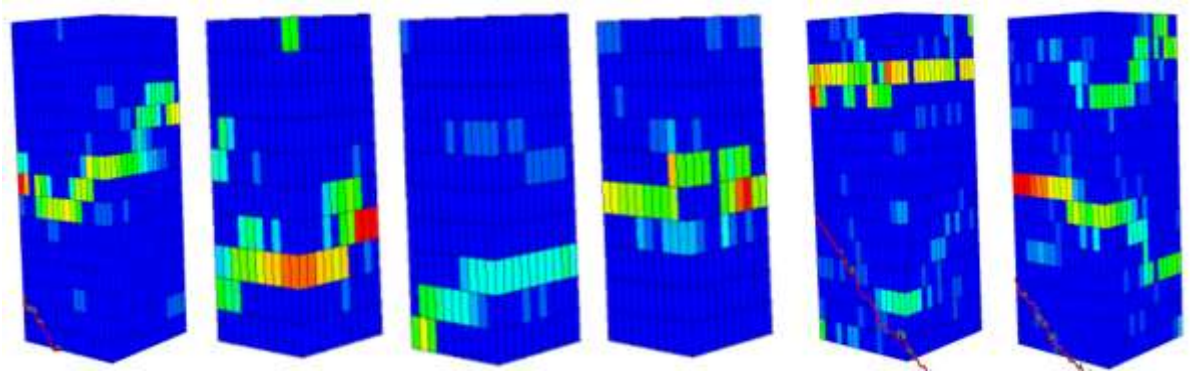

Figure 33 Plastic tensile strain at peak tension

In Figure 33, any zone that is not dark blue indicates tensile failure with a pattern analogous to fractures. The multiple parallel tensile 'cracks' were observed to form prior to peak stress. Isolated zones were also observed to fail in tension, forming 'pits' and not propagating. These fracture patterns imply a slow and stable fracture process unlike the instantaneous fracture propagation seen in rock or other brittle materials. Based on these findings, the median UTS strength at increased scales shown in Figure 32 provide an upper limit to the median UTS of intact rock as this is the highest achievable UTS with non-instantaneous fracture propagation.

The change in the measured median UCS obtained by the simulations follow a similar trend to those observed from the tensile tests. The median UCS at various scales shown in Figure 34.

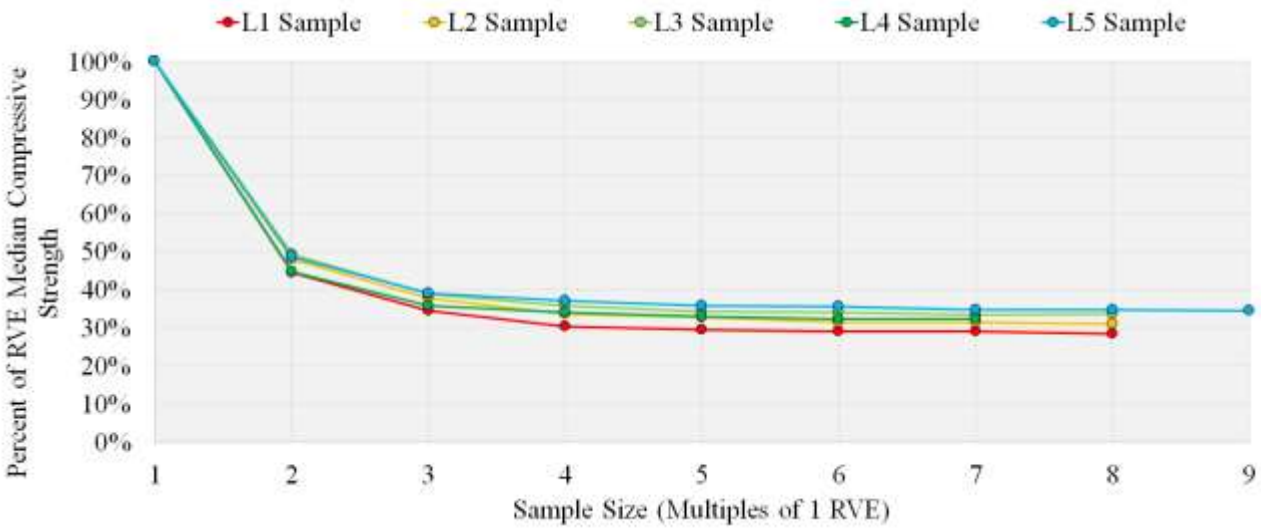

Figure 34 Influences of scale on the median Uniaxial Compressive Strength of each synthetic lithology

Notable differences between the results shown in Figure 32 and Figure 34 are that the asymptotic range and magnitudes are less than the tensile strength range, with asymptotes ranging between 30% and 35%. The typical mode of failure for these numerical compressive samples were axial splitting, but shear style failures were occasionally observed. Comparing the observed scale response to published data showed a closer agreement with the scale behaviour of cubes of coal, summarised by Singh (1981) than for the 'hard rock' relationship calculated by Hoek (1980) (Equation 38). When the UCS was separated into friction and cohesion components of the Mohr Coulomb failure criterion, unexpected behaviours emerge. Consider Figure 35 showing the scale behaviour associated with the peak friction angle.

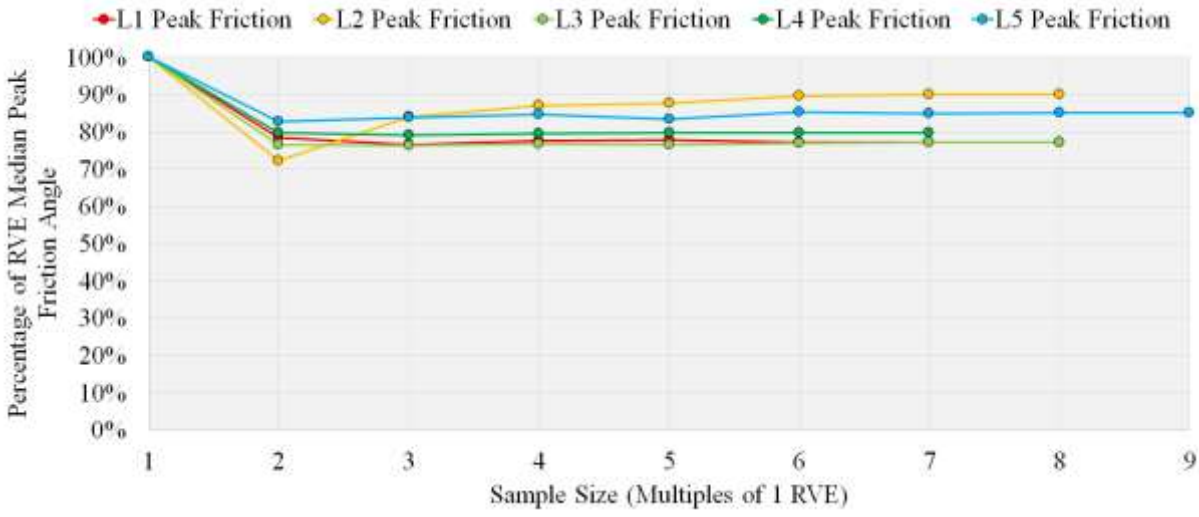

Figure 35 Influence of scale on the median peak friction angle of each synthetic lithology

Figure 35 indicates a significantly lower median peak friction angle than the input value specified for one RVE. The peak friction angle appears to asymptote near 6 times one RVE, with asymptotes ranging from 90% to 77% of the specified median peak friction angle. The median residual friction angle at increased scale is shown in Figure 36.

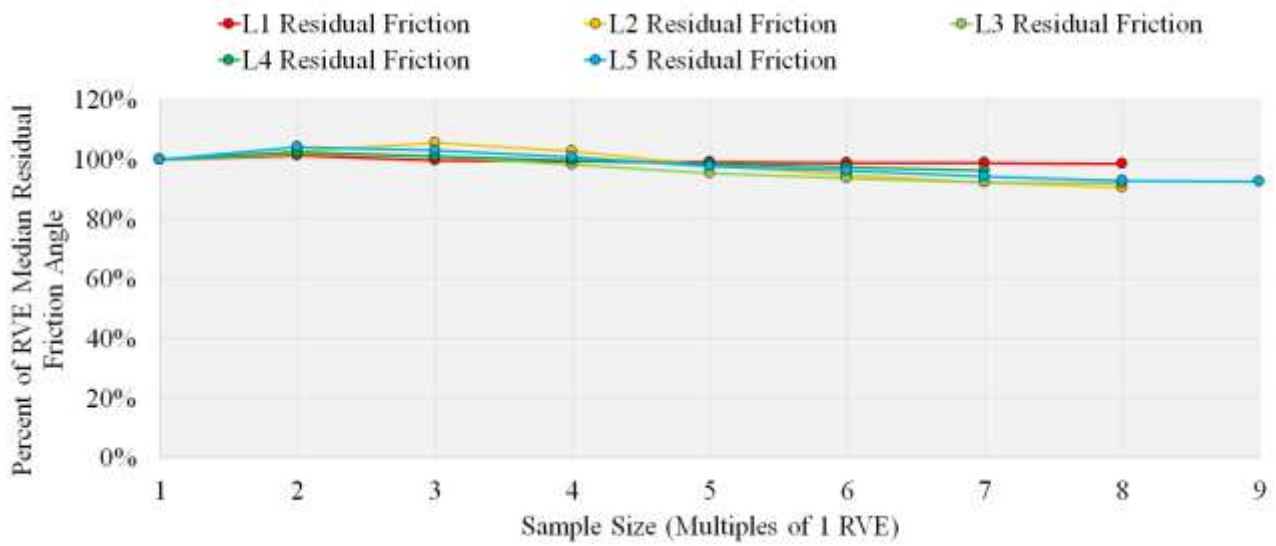

Figure 36 Influence of scale on the median residual friction angle of each synthetic lithology

Figure 36 shows that the scale relationships for the median residual friction is very slight, if present at all. The median residual friction angle remained relatively consistent with the initial input value, but does appear to drop to a between 90% and 100% of the specified median value near 5 times one RVE. When comparing values of peak and residual friction it was evident that a distinct friction hardening response emerges, even at relatively small model sizes like 2 times one RVE. A friction hardening response is often used by numerical modellers (Barton, Pandey 2011) (Martin, Christiansson & Soderhall 2001) (Gao & Kang 2016), and has been shown to be representative of real world responses (Marton & Chandler 1994). The fact that this friction hardening response better reflects practical scale problems and was numerically reproduced without assumption suggests it is the correct response for rock at increased scales and can be attributed to material parameter heterogeneity. Another response observed in the friction tests that agrees with literature scale findings is that the residual friction component remained essentially unchanging with scale. Scale dependant shear strength model presented by Bandis, Lumsden and Barton (1981) for discontinuities suggest that the friction component is unaffected by scale. These findings also align with Antomon's Second law of friction stating that friction is independent of area (Baumberger & Caroli 2006).

The median peak and residual cohesion as a function of sample size are shown in Figure 37.

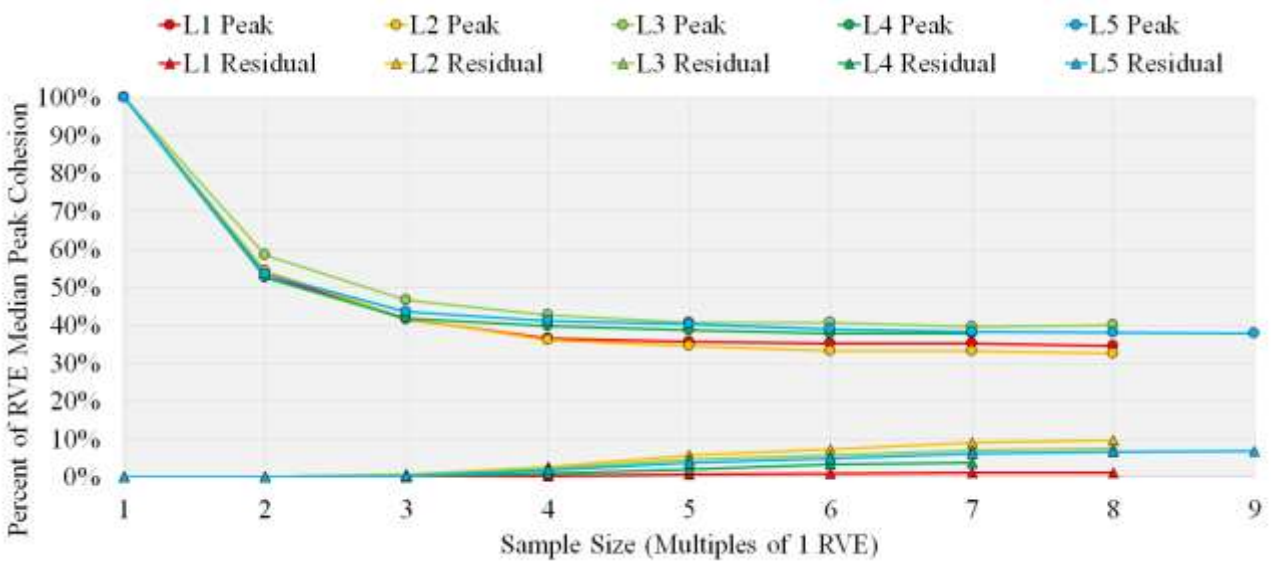

Figure 37 Influences of scale on the median peak and residual cohesion of each synthetic lithology

The intact behaviour of the median peak cohesion was seen to follow the typical scale behaviour for rock. The asymptotes for cohesion are slightly higher than for the overall compressive strength, due to the measured reduction in peak friction shown previously in Figure 35. The emergence of a non zero residual cohesion term became increasingly prominent at large scales and appears to asymptote near 7 times one RVE. Residual cohesion values differed greatly between lithologies, with the median value being less than 10% of the peak cohesion for all lithologies. The validity of these results can be substantiated using the following arguments:

As the value of cohesion was calculated using multiple triaxial tests results in combination with UCS test results, the residual cohesion component can be envisioned as an ‘apparent cohesion’ caused by shear stresses acting on the newly formed failure surface. This interpretation would have a roughness shear strength component acting with a frictional component, like in Barton’s Shear strength model (Bandis, Lumsden & Barton 1981) producing this ‘apparent cohesion’. If the numerical modelling methodology was able to account for a continually degrading shear surface, a cohesionless planar failure surface could be produced from continual loading. This limitation is a numerical side effect caused by a fixed model geometry and an inability to model progressive failure with an updating failure profile. This shear surface degradation from an initially rough surface to a more planar surface has been considered in other discrete element based analysis considering large shear displacements (Ge, Tang, Eldin, Wang, Wu & Xiong 2017). It was noted that some numerical modelling approaches do use a finite residual cohesion when selecting material parameters for practical scale problems (Itasca 2011).

The emergent residual cohesion at scale is probably valid for some highly confined or low shear displacement system like failure deep within rock. Close surface or high shear displacements would not be expected have this feature with comparable back analysis of physical phenomenon of such systems (Strouth & Eberhardt 2009) using this final cohesionless state. Based on the results, this emergent residual cohesion can be seen to be a feature of rock failure at scale with more research is required to identify if the residual cohesion obtained from this study is a realistic response for large shear displacement problems.

3.2.3 Probabilistic strength behaviour at scale

Along with the deterministic responses, probabilistic behaviours of material parameters at scale were also considered. An interesting feature of all the intact strength tests (UTS and UCS) was that they had remarkably consistent probabilistic responses although they differed in asymptotic values at increased scales. To demonstrate this result, it is convenient to talk about the UDF of both UTS and UCS (i.e., a Rayleigh distribution) in terms of Weibull distributions. A Rayleigh distribution as previously mentioned is a special case of a Weibull distribution where the Weibull distribution shape parameter k is equal to 2 and the scale parameter λ equal to $\sqrt{2}$ times the Rayleigh scale parameter. This transformation allows for simpler representation of probabilistic scale effects. The variations in the Weibull shape parameters at scale appeared to be invariant of each lithology and scale asymptote. To illustrate this, Figure 38 shows the Maximum Likelihood Estimate for the Weibull shape parameter of each lithology and size for both UTS and UCS tests.

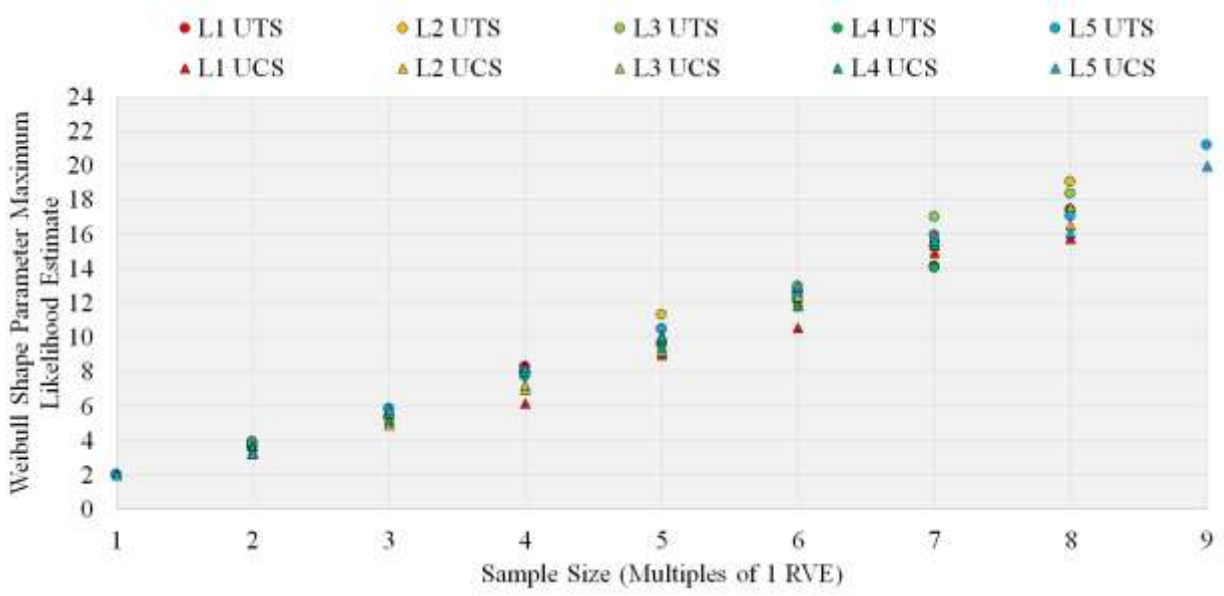

Figure 38 Maximum Likelihood Estimates of the Weibull distribution shape parameter for Uniaxial Compressive Strength and Uniaxial Tensile Strength at various scales

By inspection of Figure 38, it the relationship between sample size and the Weibull shape parameter for intact measurements of UTS and UCS at scale is linear with the following general equation:

$$k_{V_n} \approx 2 \times Sample\ Size \qquad \text{Equation 109}$$

where k_{V_n} is the Weibull shape parameter at the associated subscript volume. To test the appropriateness of Equation 109 as a viable model for estimating the Weibull shape parameter at a given scale, a series of statistical regressions were completed to compare Equation 109 to the observed Maximum Likelihood Estimate to determine the model's applicability. Additionally, a series of KS tests were completed to verify if the UDF predicted by Equation 109 was sufficient at describing the simulated data at a given size. The KS test results are summarised in Table 40 and Table 41. The test hypothesis for this regression analysis is given as *the gradient of the linear relationship is 2 with a zero intercept*. A summary of the results and test decisions are shown in Table 42.

Table 40 Kolmogorov Smirnov goodness of fit test decision summary for Uniaxial Tensile Strength

Scale	L1	L2	L3	L4	L5
1x RVE	Model Input	Model Input	Model Input	Model Input	Model Input
2x RVE	✓	✓	✓	✓	✓
3x RVE	✓	✓	✓	✓	✓
4x RVE	✓	✓	✓	✓	✓
5x RVE	✓	✗	✓	✗	✓
6x RVE	✗	✓	✗	✗	✓
7x RVE	✓	✓	✗	✗	✓
8x RVE	✓	✓	✗	-	✗
9x RVE	-	-	-	-	✓
Overall Conclusion	✗				

Table 41 Kolmogorov Smirnov goodness of fit test decision summary for Uniaxial Compressive Strength

Scale	L1	L2	L3	L4	L5
1x RVE	Model Input	Model Input	Model Input	Model Input	Model Input
2x RVE	✓	✓	✓	✓	✗
3x RVE	✓	✓	✓	✗	✓
4x RVE	✓	✓	✓	✓	✓
5x RVE	✓	✓	✓	✓	✓
6x RVE	✗	✓	✓	✓	✓
7x RVE	✓	✓	✗	✗	✗
8x RVE	✗	✗	✗	-	✗
9x RVE	-	-	-	-	✗
Overall Conclusion	✗				

Table 42 Weibull distribution shape parameter regression analysis summary

Lithology	Uniaxial Tensile Strength test decision	Uniaxial Compressive Strength test decision
L1	✓	✓
L2	✗	✓
L3	✗	✓
L4	✓	✓
L5	✗	✗
Overall conclusion	✗	✗*
Combined conclusions	✗	

*Although Equation 109 was acceptable in terms of the regression analysis for UCS, Equation 109 produced an insufficient goodness of fit when tested using the KS test. Due to this result, Equation 109 was ultimately rejected for its applicability to describe the observations.

Based on the summary suppled in Table 42 it was concluded at a 5% significant that the estimated Weibull shape parameter of UTS and UCS as a function of scale is not consistent with Equation 109. No additional analysis was completed on determining a statistically significant relationship as numerous complex models may produce statistically significant model fits. Simple alternative models could include a nonzero intercept, a gradient not equal to two or some nonlinear relationship. In order to best estimate this probabilistic scale response, substantial physical testing would offer the most 'assumption free' method of evaluation. Physical testing would focus mainly on the region between 0 and 3 times one RVE as this is both a practical testing region and would be able to detect if an intercept exists as well as any distinctive nonlinear change in real world measurements.

The probabilistic response for peak and residual friction were specified as normal distributions and have two associated parameters, the location (the mean or median value) and the scale (standard deviation) parameter. The location parameters for the peak and residual friction angles are equivalent to the median value and have previously been shown in Figure 35 and Figure 36. The Maximum Likelihood Estimates at various scales for the standard deviation of the peak friction angle is shown in Figure 39.

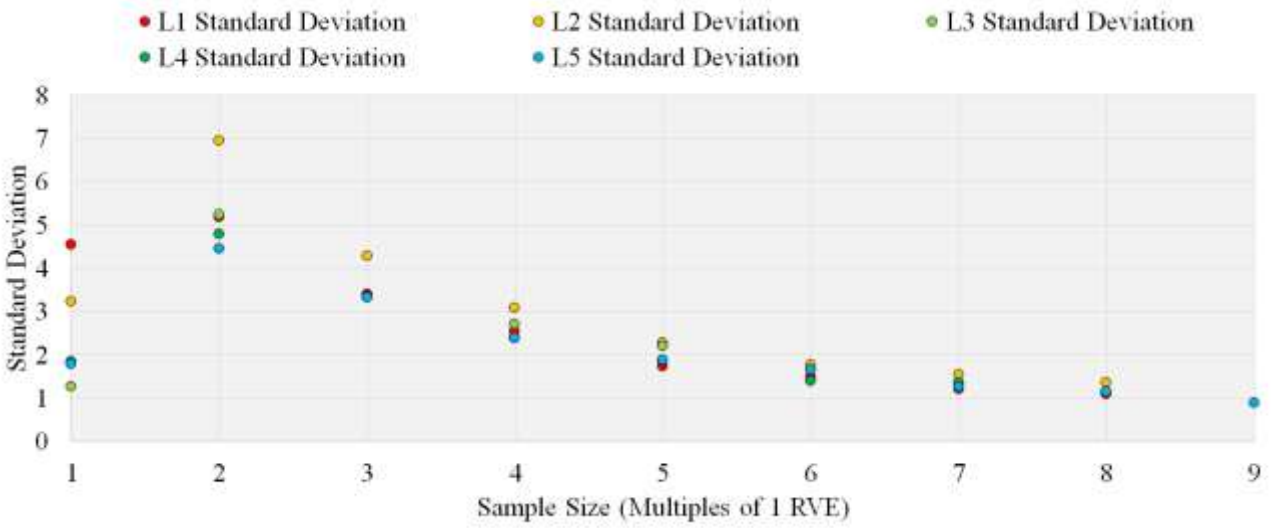

Figure 39 Maximum Likelihood Estimates standard deviation as a function of scale for peak friction angle

The results shown in Figure 39 suggest that the standard deviation of the peak friction angle undergoes a drastic deviation from the initial input and then follows an unknown, input invariant relationship (i.e., the standard deviation at some scale is approximately constant). A likely explanation for these results is that some internal process or interaction is dictating the peak frictional response, with only a token contribution from the initial input value. To explore this notion further, a series of normality tests were completed to check if the distribution associated with the peak friction angle retains its specified normal distribution. This test was completed using the Shapiro Wilk test. The test hypothesis is given as *the data follows a normal distribution with unspecified mean and standard deviation.* The summary of these analysis are shown in Table 43.

Table 43 Shaprio Wilk test decision summary for peak friction angles at various scales

Scale	L1	L2	L3	L4	L5
1x RVE	Model Input	Model Input	Model Input	Model Input	Model Input
2x RVE	✓	✗	✗	✓	✗
3x RVE	✓	✗	✓	✓	✓
4x RVE	✓	✓	✗	✗	✗
5x RVE	✓	✗	✗	✓	✓
6x RVE	✓	✓	✓	✓	✓
7x RVE	✓	✓	✓	✓	✓
8x RVE	✓	✗	✓	-	✓
9x RVE	-	-	-	-	✓
Overall conclusion	✓	✗	✗	✓	✓
Combined conclusion	✗				

From Table 43, it was concluded at 5% significance that the distribution of peak friction angles at scale are not normally distributed. The fact that the results showed a statistically significant deviation from the assumed normal distribution adds evidence that some internal influence is controlling the response of the peak friction angle. As to what mechanism is behind these observations is difficult to

say. Physical testing completed on samples between one and three times one RVE would offer insights into if this invariant frictional behaviour is observed in practice and if not, provide a comparable baseline behaviour for future analysis.

The Maximum Likelihood Estimates for the standard deviation for the residual friction angle is shown in Figure 40.

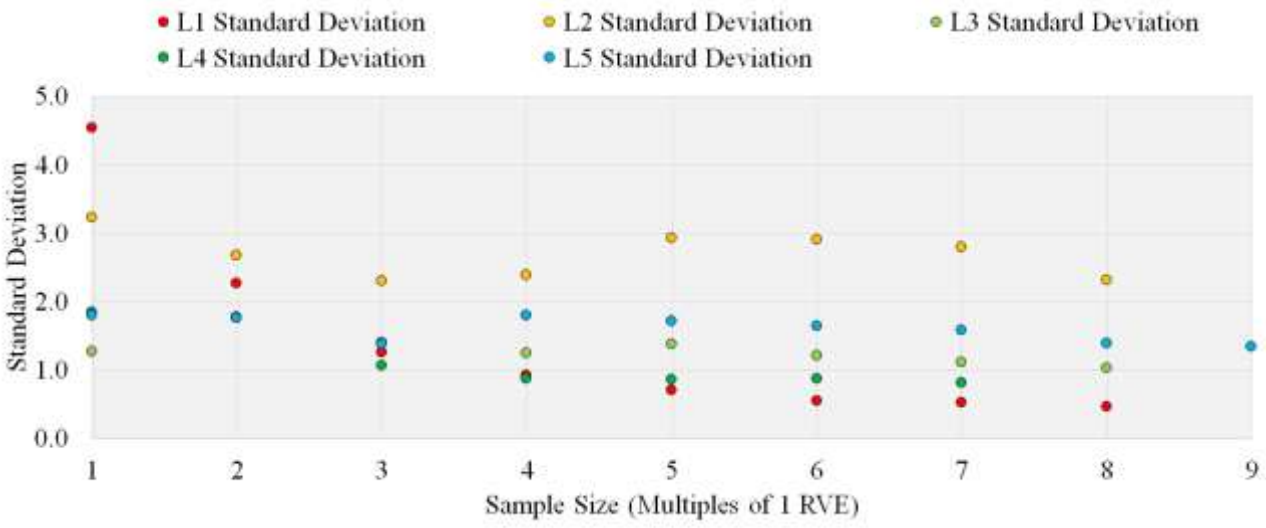

Figure 40 Maximum Likelihood Estimates for the standard deviation as a function of scale for residual friction angle

Figure 40 shows a considerably different response to the standard deviation of the residual friction angle compared to the peak friction angle. The change in standard deviation with respect to scale differs considerably between lithologies, with L1 and L4 showing a well defined reduction with scale, while L3 and L5 show no significant change in standard deviation. These findings show that the probabilistic behaviour of the residual friction angle must be evaluated on a case by case basis and does not appear to be as consistent as previously presented material parameters. Normality tests were also completed on the residual friction angle data to test for similar influences of scale on the associated distribution, with the summary of results presented in Table 44. The same statistical test, significance and hypothesis used for the peak friction angle was used.

Table 44 Shaprio Wilk test decision summary for residual friction angles at various scales

Scale	L1	L2	L3	L4	L5
1x RVE	Model Input	Model Input	Model Input	Model Input	Model Input
2x RVE	✗	✗	✗	✗	✗
3x RVE	✗	✗	✗	✗	✓
4x RVE	✓	✗	✗	✗	✓
5x RVE	✗	✗	✗	✗	✗
6x RVE	✓	✗	✗	✗	✗
7x RVE	✓	✗	✓	✓	✗
8x RVE	✓	✗	✓	-	✓
9x RVE	-	-	-	-	✓
Overall conclusion	✗	✗	✗	✗	✗
Combined conclusion	✗				

From the summary presented in Table 44, it was concluded at 5% significance that the distribution of residual friction angles at scale is not normally distributed. In order to understand this deviation more thoroughly physical testing offers the best method of assessment.

While there was evidence to suggest a normal distribution is insufficient to describe the peak friction angle of rock, the normal distribution is still a very good approximation. Figure 41 shows the normal distribution approximation for a lithology and scale, which failed the Shapiro Wilks test.

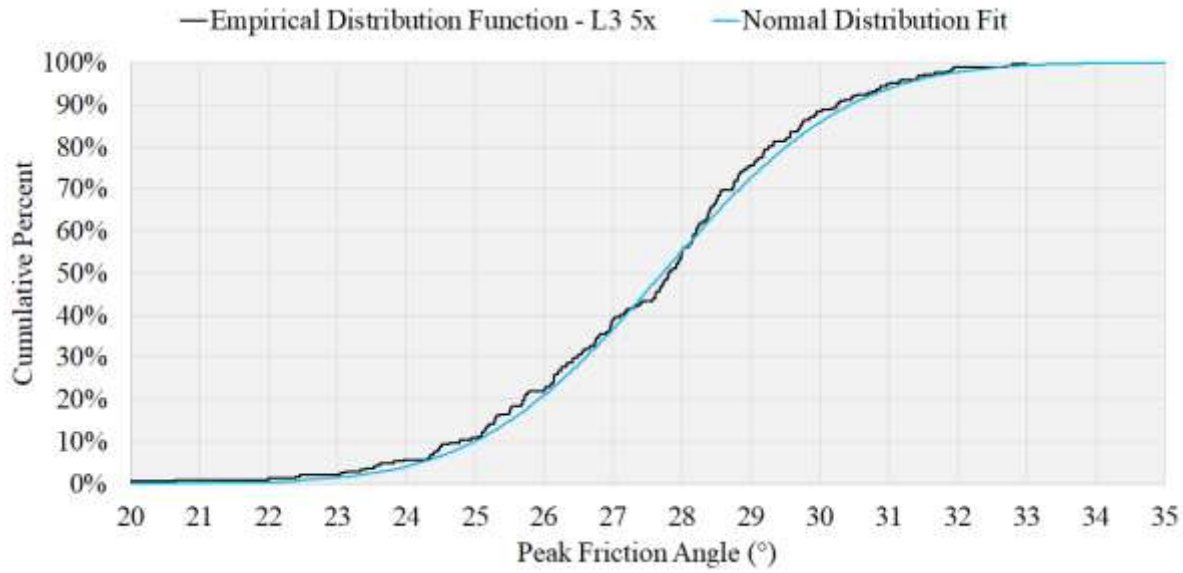

Figure 41 Example normal distribution approximation for the peak friction angle of L3 5x RVE

It is evident in Figure 41 that a reasonably accurate fit is obtained using a normal distribution approximation. Again further insight by physical testing will lead to a better understanding of the probabilistic nature of rock friction at increased scales.

A probabilistic analysis of cohesion can only be partially considered. As the cohesion UDF is implicitly defined using the UCS and the peak friction angle, the exact PDF is undefined. The variance associated with the peak cohesion at scale does show a consistent behaviour with scale. The calculated variance for the peak cohesion as a function of scale is shown in Figure 42. Note that the y axis is plotted using a Log10 scale.

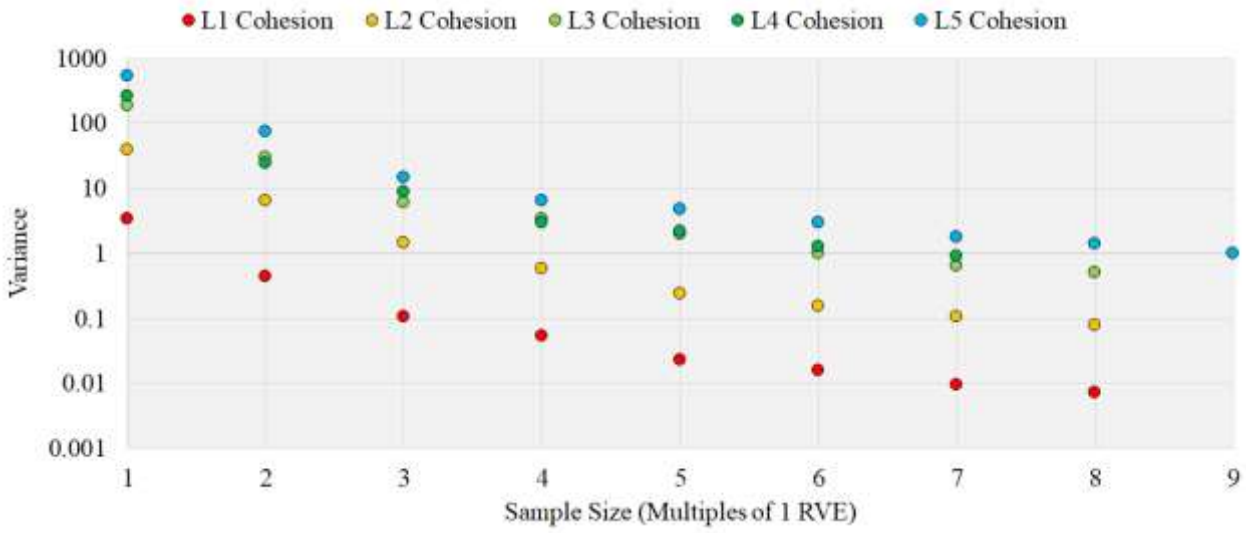

Figure 42 Variance for the peak cohesion as a function of scale

By considering Figure 42 it can be seen that the variance of peak cohesion decreases with increasing scale and the relationship is pronounced. A simple model that may be suitable at describing the measured variance is given by:

$$Var(C_n) \approx \frac{Constant}{\sqrt[3]{Sample\ Size}} \qquad \text{Equation 110}$$

where C_n is the peak cohesion at the associated subscript. To test Equation 110 as suitable model to describe the variance of peak cohesion as a function of sample size, a series of statistical regressions were completed to compare Equation 110 to the observed data. The test hypothesis is given as *the exponent of the power regression is equal to the negative cube root of the sample size*. A summary of these statistical tests are shown in Table 45.

Table 45 Regression test decision summary for peak cohesion variance

Lithology	Test decision
L1	✓
L2	✗
L3	✗
L4	✗
L5	✓
Overall Conclusion	✗

Based on the results suppled in Table 45 it can be concluded at a 5% significant that the estimated variation in the variance of peak cohesion is not consistent with Equation 110.

The calculated variance associated with the residual cohesion at various scales is shown in Figure 43.

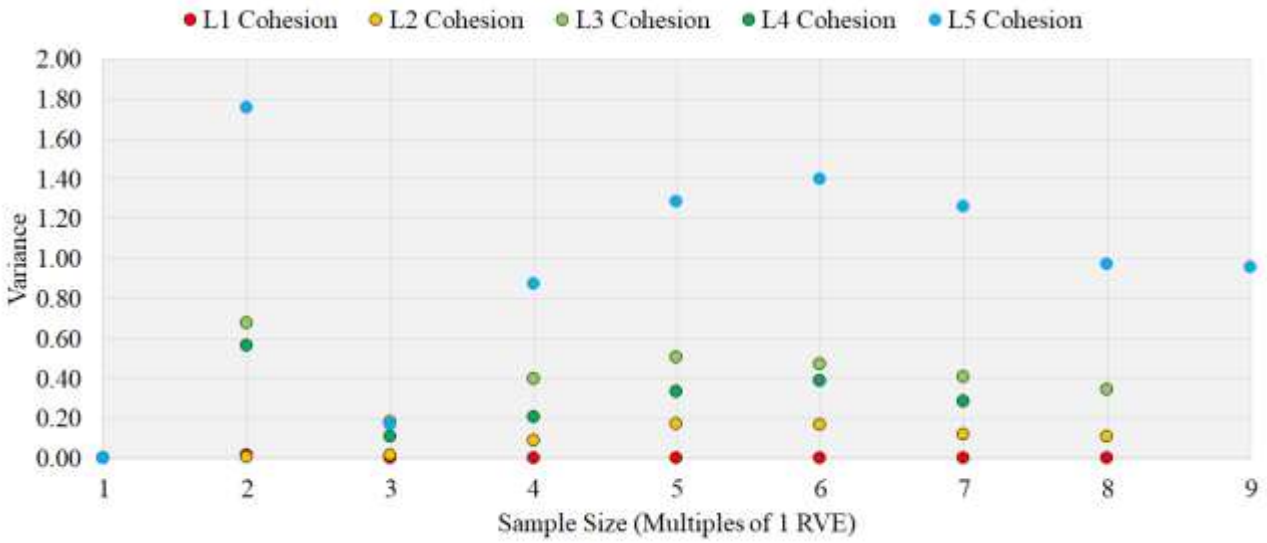

Figure 43 Variance for the residual cohesion as a function of scale

It can be seen in Figure 43 that the variance associated with residual cohesion increases, and peaks near 6 times one RVE, before decreasing. There is also a large spike at 2 times one RVE, which is likely attributed to the relatively small model sizes and the initial emergence of a residual cohesion value. As the residual cohesion is an emergent behaviour, limited conclusions can be drawn. An understanding as the behaviour and variability of residual cohesion at 2 to 4 times one RVE would offer an increased understanding and form comparative baseline for the variable and emergent nature of residual cohesion for rock.

3.2.4 Mechanical parameters at scale

For each sample, two mechanical parameters were quantified, Young's Modulus and Poisson's Ratio. Each of these material parameters had two individual measurements, an elastic and a secant measurement were obtained to gain some appreciation for pre peak yielding. A visual representation of how the elastic and secant Young's Modulus are determined in each model is shown in Figure 44.

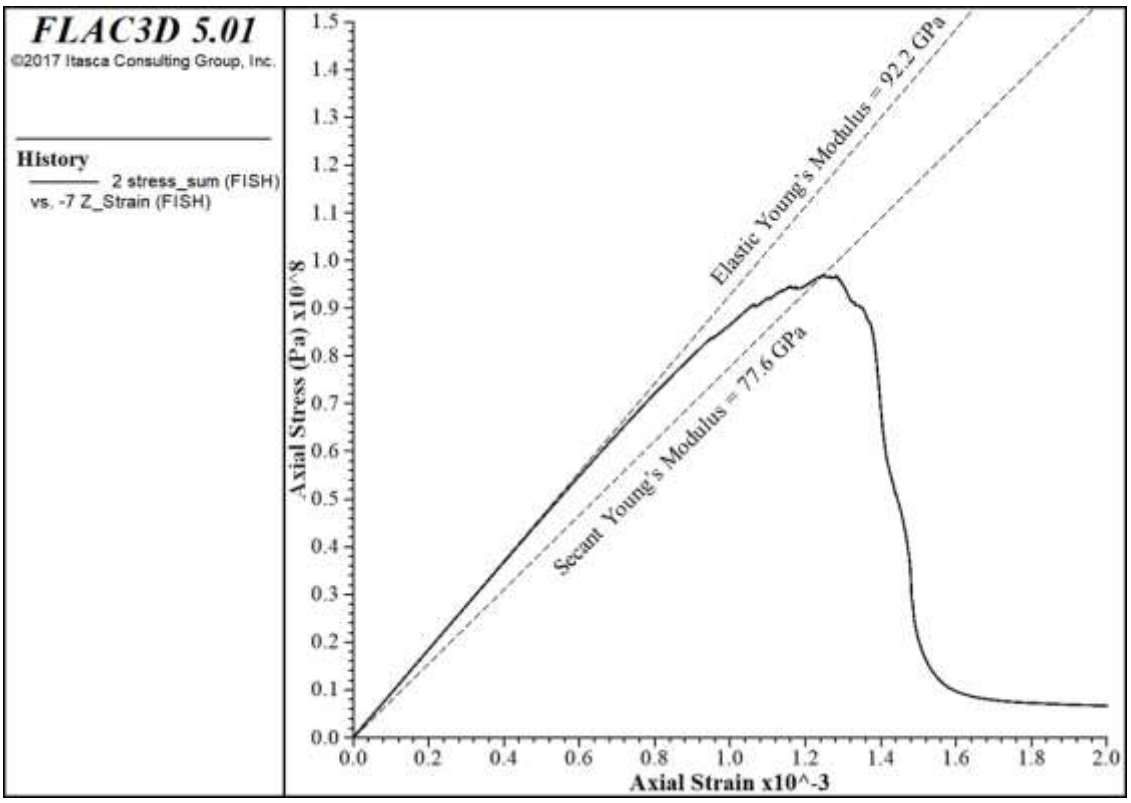

Figure 44 Example representation of elastic and secant Young's Modulus measurements

The elastic Young's Modulus represents the linear material response until internal elements begin to yield. For the example shown in Figure 44, this corresponds to the tangent of the cure below an axial stress at roughly 45% of the peak compressive strength. It is interesting to note that the onset of this yielding does align with the onset of acoustic emissions in laboratory testing (Hoek & Martin 2014). The variation in elastic and secant Young's Modulus at various scales is shown in Figure 45.

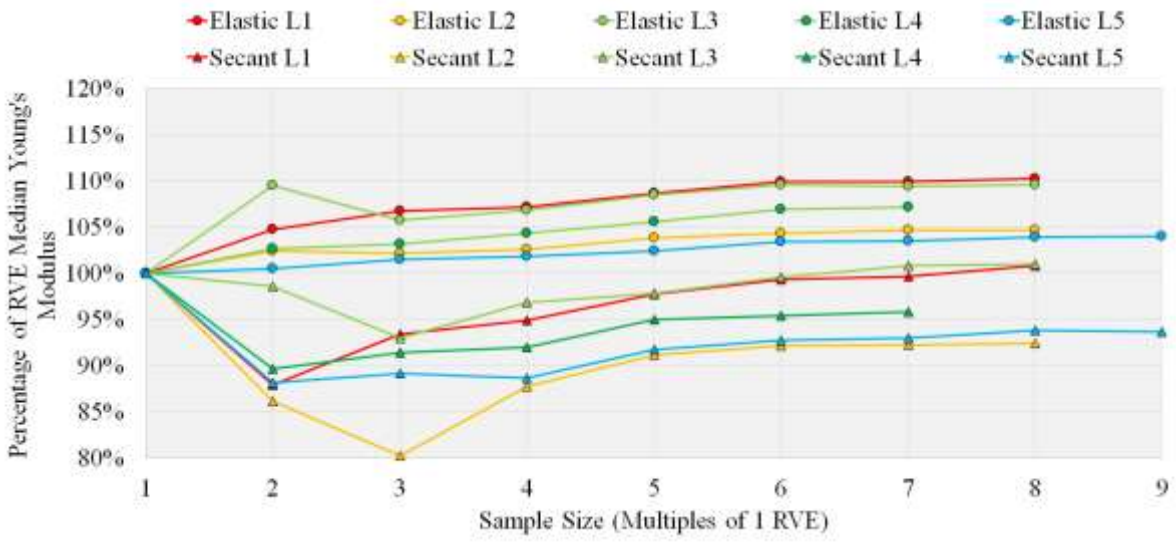

Figure 45 Influences of scale on the median elastic and secant Young's Modulus

From Figure 45, there is an increase in the median value of the elastic Young's Modulus with increasing scale while there is a decrease in the median value of the secant Young's Modulus. These results suggest that depending on which measurement of Young's Modulus is used, either a positive and negative scaling law can be produced. The literature on the behaviour of Young's Modulus at increased scale also shows conflicting findings, with Masoumi (2013) reporting a notable increase in mean elastic Young's Modulus with increased scale while Simon and Deng (2009) reporting an arguably negligible change in mean elastic Young's Modulus with scale. The findings of this study align with Masoumi's findings and suggest some positive scaling law is associated with Elastic Young's Modulus. The asymptotic value of both elastic and secant Young's Modulus appears at 7 times one RVE, with ranges of 104% to 110% of the median value for elastic and 92% to 101% of the median value for secant measurements.

From a probabilistic perspective, the variation in the associated Weibull shape parameters for both elastic and secant Young's Modulus at scale are remarkably consistent for each lithology. The Maximum Likelihood Estimates for the Weibull shape parameter of the elastic Young's Modulus is shown in Figure 46 and the secant Young's Modulus is shown in Figure 47.

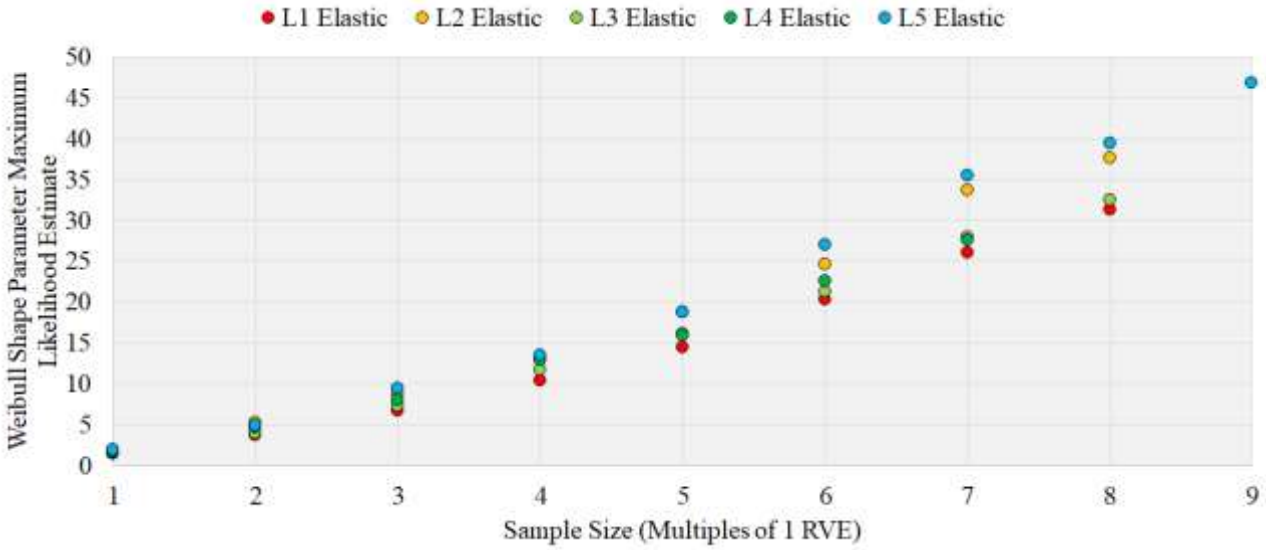

Figure 46 Maximum Likelihood Estimate of the elastic Young's Modulus shape parameter at various scales

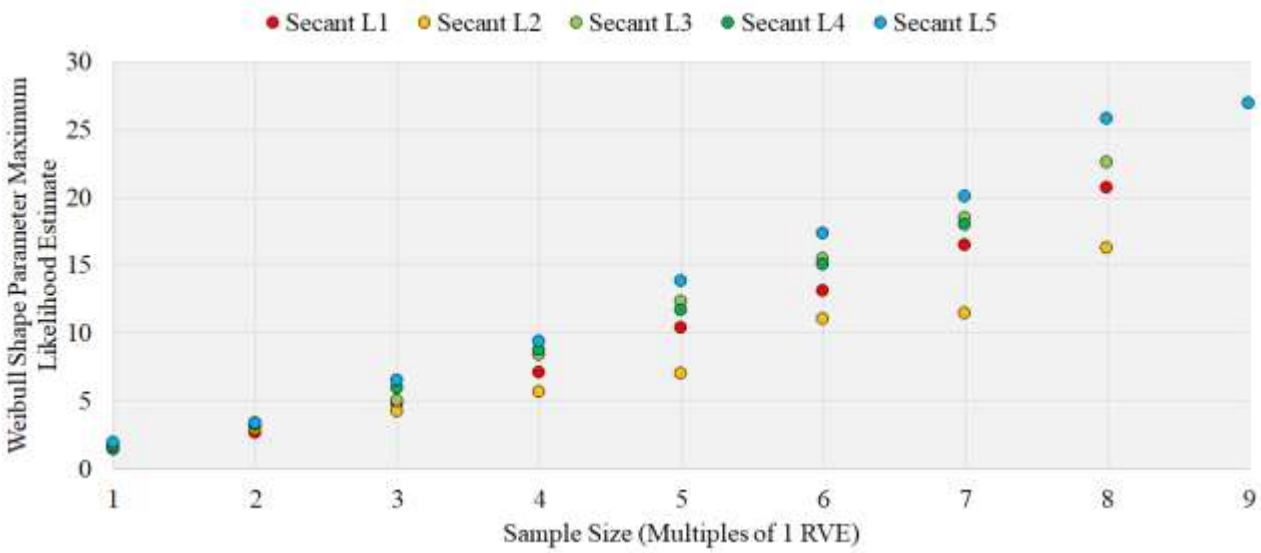

Figure 47 Maximum Likelihood Estimate of the secant Young's Modulus shape parameter at various scales

A simple model to explain the observed Weibull shape parameters as a function of sample size is given by:

$$k_{V_n} \approx k_{V_0} \times \sqrt{Sample\ Size^3} = k_{V_0} \times Sample\ Size^{1.5} \qquad \text{Equation 111}$$

where k_{V_n} is the Weibull shape parameter at the associated subscript. To test Equation 111 as a viable model to describe the Weibull shape parameter at scale, a series of statistical regressions were completed to compare Equation 111 to the observed data. Additionally, a series of KS tests were completed to verify if the UDF predicted by Equation 111 was sufficient at describing the simulated data at a given size The test hypothesises are given as *the constant of the power regression is equal to the Weibull shape parameter at 1 RVE* and *the exponent of the power regression is equal to 1.5*. A summary of these statistical test decisions for both elastic and secant Young's Modulus are shown in Table 46, with associated KS test decisions shown in Table 47.

Table 46 Regression statistical analysis summary - Equation 111

Lithology	Elastic Young's Modulus test decision		Secant Young's Modulus test decision	
	Constant term	Power term	Constant term	Power term
L1	✗	✗	✗	✓
L2	✓	✓	✗	✓
L3	✓	✓	✓	✓
L4	✓	✓	✗	✗
L5	✓	✓	✓	✗
Overall conclusion	✓		✗	

Table 47 Kolmogorov Smirnov test decision summary elastic Young's Modulus

Scale	L1	L2	L3	L4	L5
1x RVE	Model Input	Model Input	Model Input	Model Input	Model Input
2x RVE	✓	✓	✓	✓	✓
3x RVE	✓	✓	✓	✗	✓
4x RVE	✓	✓	✓	✓	✓
5x RVE	✓	✓	✓	✓	✗
6x RVE	✓	✗	✓	✓	✓
7x RVE	✗	✓	✗	✓	✓
8x RVE	✓	✓	✓	-	✓
9x RVE	-	-	-	-	✓
Overall Conclusion	✓				

Based on the results suppled in Table 46 it can be concluded at a 5% significant that the estimated Weibull shape parameter of elastic Young's Modulus as a function of scale is consistent with Equation 111 and that the estimated Weibull shape parameter of secant Young's Modulus as a function of scale is not consistent with Equation 111. No additional analysis was completed on determining a statistically significant relationship for secant Young's Modulus as numerous complex models may be statistically significant. Similarly to the conclusions of the statistical analysis of the scale response of UCS and UTS, physical testing would offer the most meaningful method of assessment. The same testing region of between 0 and 3 times one RVE is recommended for exploring this concept further.

As Equation 111 is applicable at describing the observed Weibull shape parameter for the elastic Young's Modulus, Equation 111 can be generalised and expressed in terms of volume to give:

$$k_{V_n} \approx \frac{k_{V_0}}{\sqrt{V_0}} \times \sqrt{Volume} = Constant \times V_n^{0.5} \qquad \text{Equation 112}$$

The same statistical testing methodology was used to validate Equation 112 use at describing the observed Weibull shape parameter. A summary of the statistical analysis for Equation 112 is shown in Table 48.

Table 48 Regression statistical analysis summary - elastic Young's Modulus using actual volume

Lithology	Constant term	Power term
L1	✓	✗
L2	✓	✓
L3	✓	✓
L4	✓	✓
L5	✓	✓
Overall conclusion	✓	

Based on the results suppled in Table 48 it can be concluded at a 5% significant that the estimated Weibull shape parameter of elastic Young's Modulus as a function of volume are consistent with Equation 112. The goodness of fit analysis by the KS test showed sufficient goodness of fit testing across all samples using Equation 112. Of note though is that in order to produce the Weibull scale parameter for each lithology and volume, the case specific median elastic Young's Modulus had to be used. Based on these findings the associated Weibull scale parameter for elastic Young's Modulus must be generated on a case by case basis and currently cannot be readily generalised.

The median elastic Poisson's Ratio as at various scales is shown in Figure 48.

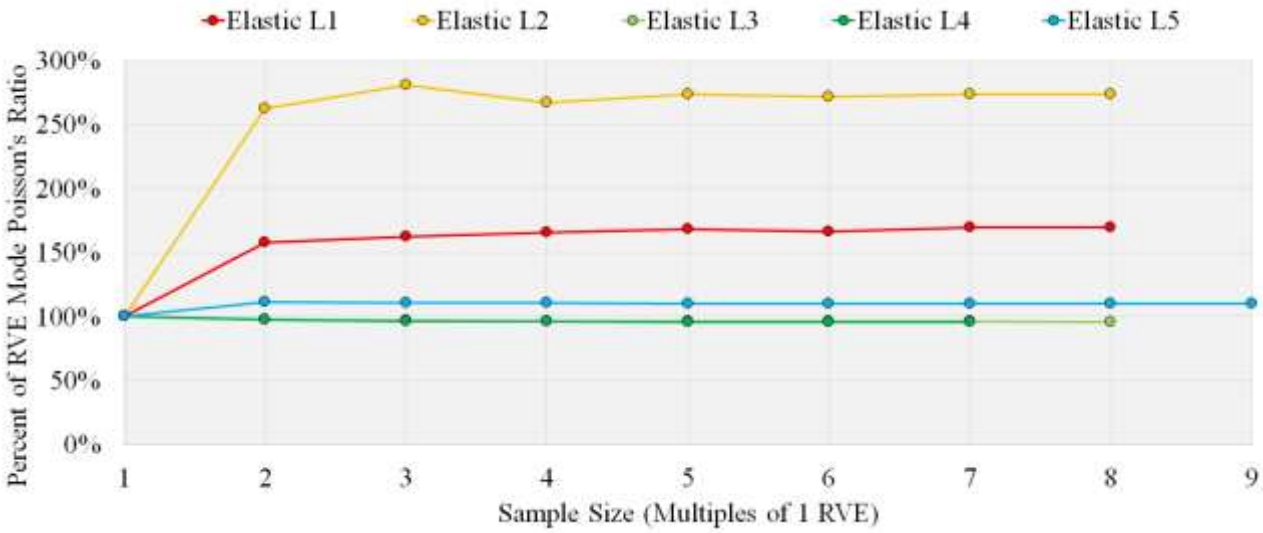

Figure 48 Influences of scale on the median elastic Poisson's Ratio

From review of Figure 48, there does not appear to be a consistent behaviour for the Elastic Poisson's Ratio for each lithology. By considering the input distributions, the asymptotic value for the elastic Poisson's Ratio can be seen to converge to the average Poisson's Ratio of one RVE. Convergence of Poisson's Ratio to the mean value does align with common modelling selection justifications (Mas Ivars et al 2011) (Gao, Stead & Kang 2014).

The median secant Poisson's Ratio as a function of scale is plotted in Figure 49.

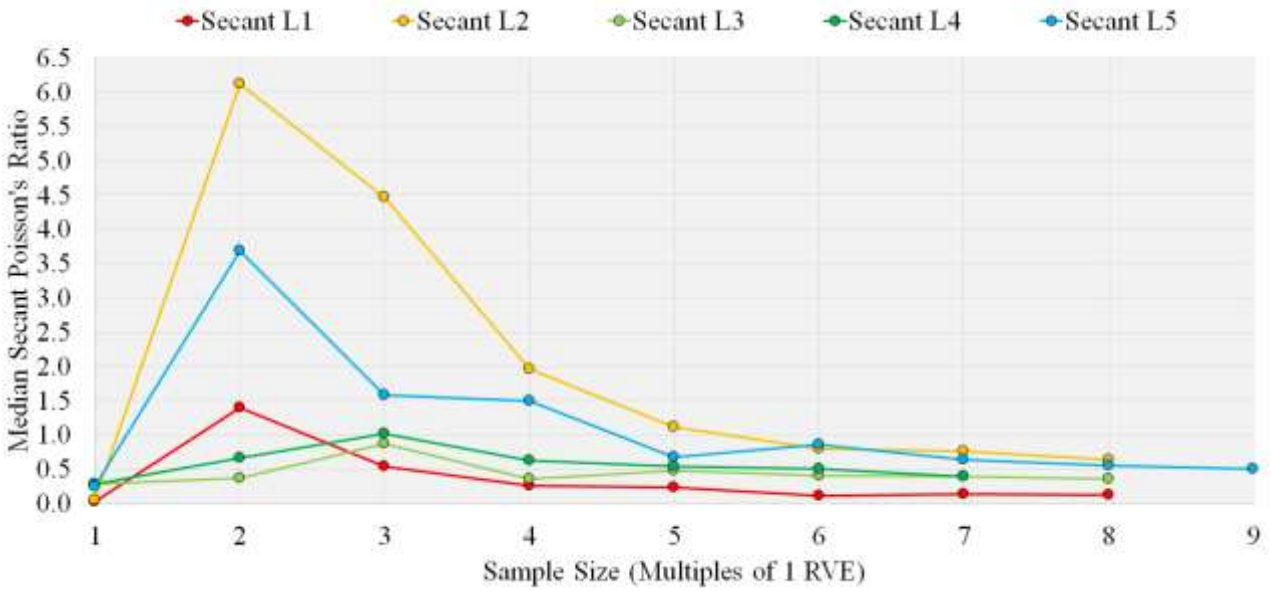

Figure 49 Influences of scale on the median secant Poisson's Ratio

Note that the values plotted in Figure 49 are the raw median value. It was seen that the measurements of Poisson's Ratio at the point of failure were far beyond the compatibility and physical upper limit for elastic materials ($0 < \nu < 0.5$). A comparison of the elastic and secant Poisson's Ratio suggests that at some point prior to peak stress, a considerable amount of plastic dilation occurs within the sample. The implications of these findings are elaborated below:

From an equivalent continuum modelling approach for practical scales, these results suggest that assuming an equivalent linear response until failure does not account for all observed mechanical behaviours. In order to correctly model the equivalent dilatational response at the peak strength, the sample must yield at some point prior to the peak strength. This modelling response has been shown effective in practice by Hajiabdolmajid, Kaiser and Martin (2002) and was used to replicate in situ responses. The results of this study extend this idea and suggest the inclusion of some dilatational consideration at this point would be required to fit the observed mechanical response. How this pre peak yielding relates to all constitutive model parameters values is unknown at this time. The results obtained for the peak and residual behaviour can be interpreted as point evaluations along an extended failure response. A more in depth revaluation would be required to firstly identify the initial yield point, possibly done by checking for 'significant' deviations from the elastic response and quantifying all constitutive components at that point. A more complete understanding of Poisson's Ratio should be quantified before completing such an analysis to limit possible errors with forward prediction associated with using incorrect PDFs.

A probabilistic description of Poisson's Ratio was not included. As the distribution of Poisson's Ratio must be defined on a case by case basis, no reasonable generalisation is possible currently. If a UDF can be found that describes Poisson's Ratio, a greater appreciation to its generalised probabilistic behaviour may be possible.

3.2.5 Numerical input sensitivity analysis

A sensitivity analysis was completed to understand the influences that each model component has on the measurable response of all material parameters. To form a comparative baseline, the material parameter sensitivity was completed for lithology 'L5' at 6 times one RVE. This model size was chosen as most material parameters reach an asymptotic value at or near this size and are computationally efficient compared to larger model sizes. Each sensitivity was completed using 200 random realisations to also consider changes the associated PDF. To test for differences associates with the distribution of each material parameter, the KW ANOVA was used. A summary of the statistical analysis and the change in the median material parameter for sensitivity is shown in Table 49.

Table 49 Sensitivity statistical analysis summary

Sensitivity	Value Change	UTS (MPa)	UCS (MPa)	Elastic Young's Modulus (GPa)	Secant Young's Modulus (GPa)	Elastic Poisson's Ratio	Secant Poisson's Ratio	Peak Friction (°)	Peak cohesion (MPa)	Residual friction (°)	Residual cohesion (MPa)	Elastic Young's Modulus Equation 112
Base Line	-	6.238	53.238	90.410	81.087	0.262	0.854	27.330	16.079	30.925	1.971	✓
Reduced RVE H:W Ratio	H:W = 2.5 -7.75% H:W	ND	-1.203 -2.26%	ND	ND	ND	ND	ND	-0.253 -1.57%	-0.896 -2.90%	ND	✓
Increased RVE H:W Ratio	H:W = 3.0 +10.70%	ND	+0.724 +0.54%	ND	ND	+0.01 +0.43%	ND	ND	+0.461 +2.86%	-0.608 -1.97%	ND	✓
Limited Correlations	Only known correlations used	-1.205 -19.32%	-2.624 -4.93%	ND	ND	ND	ND	+0.886 +3.24%	-0.969 -6.03%	-0.339 -1.10%	ND	✓
No Correlations	All correlations equal 0	-1.433 -22.97%	-14.145 -26.57%	ND	-14.532 -17.92%	ND	+0.511 +59.84%	+1.043 +3.82%	-4.456 -27.71%	ND	+0.439 +22.27%	✓
Reduced sample H:W Ratio	6x9x4 RVEs	+0.198 +3.17%	+1.815 +3.41%	+0.868 +0.96%	ND	+0.001 +0.38%	ND	ND	+0.740 +4.60%	ND	-0.430 -21.82%	✓
Increased sample H:W Ratio	6x4x9 RVEs	-0.377 -6.04%	-3.501 -6.58%	-0.860 -0.95%	ND	-0.001 -0.38%	ND	ND	-0.760 -4.73%	ND	-0.229 -11.62%	✓
Equivalent Cube RVEs	Cubic RVE.	-0.977 -15.66%	-9.836 -18.48%	-3.260 -3.61%	-1.356 -1.67%	-0.006 -2.29%	-0.437 -51.17%	+0.398 +1.46%	-2.992 -18.61%	+1.778 +5.75%	-1.060 -53.78%	✓
Reduced UTS	UTS = 10.0 MPa -30.56%	-1.885 -30.22%	-1.913 -3.59%	ND	ND	ND	+0.024 +2.81%	+0.391 +1.43%	-0.576 -3.58%	-1.526 -4.93%	+1.301 +66.01%	✓

Increased UTS	UTS = 20.0 MPa +38.89%	+2.234 +35.81%	ND	ND	ND	ND	ND	ND	ND	+0.889 +2.87%	-1.471 -74.63%	✓
Reduced UCS	UCS = 100.0 MPa -32.89%	ND	-16.790 -31.54%	ND	ND	ND	-0.210 -24.59%	-0.441 -1.61%	-4.886 -30.39%	+0.915 +2.96%	-1.733 -87.92%	✓
Increased UCS	UCS = 200 MPa +34.23%	ND	+15.583 +29.27%	ND	ND	ND	ND	ND	+4.668 +29.03%	-1.343 -4.34%	+2.448 +124.20%	✓
Reduced Young's Modulus	E = 75 GPa -14.24%	ND	ND	-12.860 -14.22%	-11.676 -14.40%	ND	ND	ND	ND	-0.814 -2.63%	+0.232 +11.77%	✓
Increased Young's Modulus	E = 95 GPa +8.63%	ND	ND	+7.963 +8.81%	+7.455 +9.19%	+0.001 +0.38%	-0.339 -39.70%	ND	ND	-0.879 -2.84%	ND	✓
Reduced Young's Modulus Shape Parameter	k = 1.43 -25.56%	-0.425 -6.81%	-4.389 -8.24%	+5.879 +6.50%	+3.269 +4.03%	-0.001 -0.38%	-0.276 -32.32%	-3.028 -11.08%	-0.385 -2.39%	-1.231 -3.98%	+0.642 +32.57%	✓
Increased Young's Modulus Shape Parameter	k = 1.93 +0.47%	ND	ND	ND	ND	ND	ND	ND	ND	-0.769 -2.49%	ND	✓
Reduced Poisson's Ratio	a = 0.1134 b = 0.2178 c = 0.1428 -40.00%	ND	ND	ND	ND	-0.106 -40.46%	-0.143 -16.74%	ND	ND	-0.815 -2.64%	+0.307 +15.58%	✓

Increased Poisson's Ratio	a = 0.2646 b = 0.4999 c = 0.3332 +40.00%	ND	-1.316 -2.47%	ND	ND	+0.108 +41.22%	ND	-0.555 -2.03%	ND	-0.629 -2.03%	ND	✓
Reduced Friction	ϕ = 25 -21.88%	ND	+1.597 +3.00%	ND	ND	ND	+0.141 +16.51%	-5.695 -20.84%	+2.577 +16.03%	-7.039 -22.76%	+0.853 +43.28%	✓
Increased Friction	ϕ = 40 +25.00%	ND	-3.444 -6.47%	ND	ND	+0.001 +0.38%	-0.385 -45.08%	+6.424 +23.51%	-2.788 -17.34%	+8.164 +26.40%	-0.841 -42.67%	✓
Reduced Friction Standard Deviation	σ = 0.6624 -62.95%	ND	ND	ND	ND	ND	ND	ND	ND	-0.736 -2.38%	+0.280 +14.21%	✓
Increased Friction Standard Deviation	σ = 4.0224 +124.97%	ND	ND	ND	ND	ND	ND	ND	ND	-0.715 -2.31%	ND	✓
Initial RVE dilation	5 degrees dilation	ND	-1.007 -1.89%	ND	ND	ND	+0.270 +31.62%	ND	ND	-0.695 -2.25%	+0.407 +20.65%	✓
Initial residual cohesion	15% residual cohesion	ND	+3.639 +6.84%	ND	-1.919 -2.37%	0.001 +0.38%	-0.514 -60.19%	+0.653 +2.39%	ND	ND	+5.228 +265.25%	✓
Non instantaneous softening	0 MPa cohesion at 1% plastic shear strain	ND	+56.157 +105.48%	ND	-13.422 -16.55%	ND	-0.384 -44.96%	+6.676 +24.43%	+12.903 +80.25%	+4.025 +13.02%	-1.302 -66.06%	✓
Non instantaneous softening and residual cohesion	15% residual cohesion at 1% plastic shear strain	ND	+58.031 +1.09%	ND	-14.274 -17.60%	ND	-0.371 -43.44%	+6.958 +25.46%	+13.302 +82.73%	+3.059 +9.89%	+3.891 +197.41%	✓

Note in Table 49, ND signifies no difference. Cells containing values indicate a statistically significant difference at a 5% significance due to the sensitivity change. The values specified present the difference in median values and percentage differences. The results of the sensitivity analyses presented in Table 49 indicate that material parameters at scale are influenced by seemingly unrelated values. For example, changing the shape parameter associated with Young's Modulus at one RVE has a significant influence on all measured material parameters.

Probably the most significant behaviour to emerge during the sensitivity analysis is the impact of plastic components on sample behaviour. By comparing the failure envelopes for different softening responses, Figure 50 was produced.

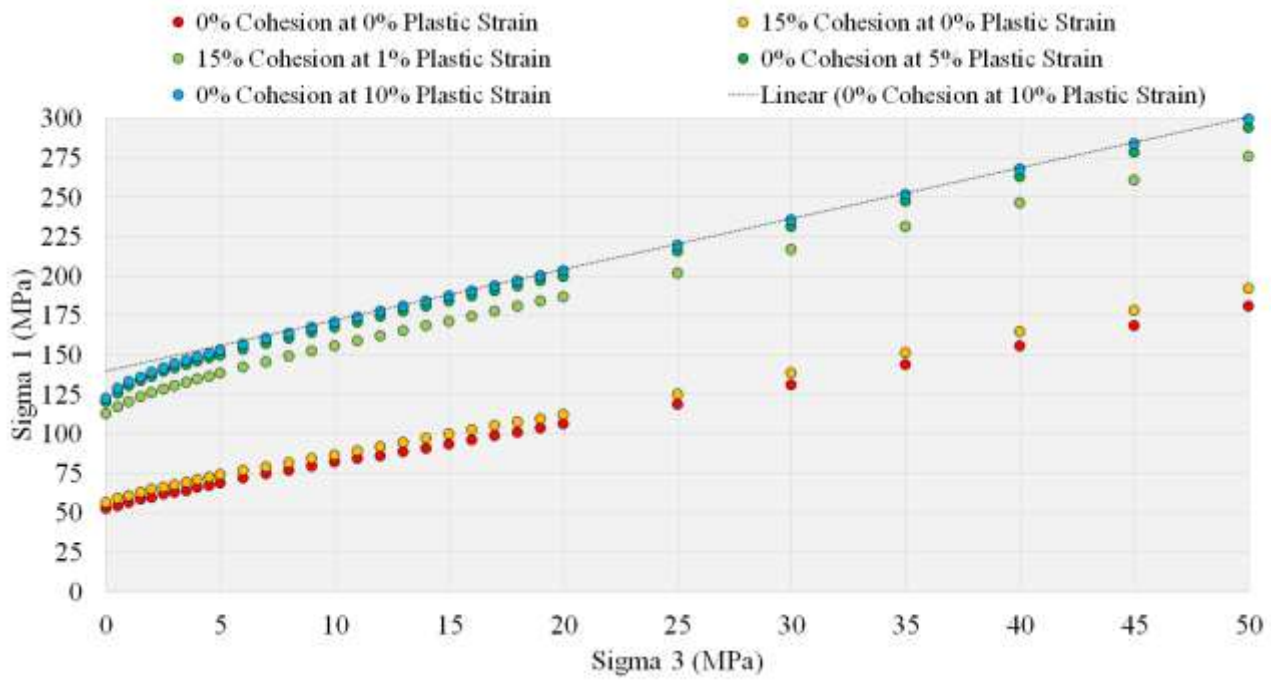

Figure 50 Triaxial stress at failure for varying softening responses. Linear line shown to better illustrate the nonlinearity

Note that to produce Figure 50, one random realisation was used, with only the softening tables being varied (i.e. all simulations use the same random material parameters). From review of Figure 50, it can be seen that by defining a large residual cohesion component to each RVE, a small but noticeable increase in peak strength is obtained. By increasing the plastic strain at which the residual values are achieved drastically increases the measured strength, almost doubling the UCS and producing a UCS that closely matches Hoek's Scaling Law (Hoek & Brown 1980) given by Equation 38. More importantly, a non-instantaneous drop in post peak strength parameters produces a distinctively non-linear failure envelope with increasing confinement, a feature that has also been demonstrated

experimentally (Hoek & Brown 1988). The findings of the sensitivity suggest that the following model components have the biggest influences on the general behaviour of rock at scale:

Selection of a non instantaneous cohesion softening - The softening cohesional response, which is rarely measured at one RVE, is arguably the most important parameter affecting material behaviour at larger scales. Without a proper description of strain softening response at one RVE, the analysis indicates that significantly lower strength estimates at scale are calculated. Inclusion of this non-instantaneous softening also produces the confinement dependent strength response, which has been observed in practice.

Inclusion of correlation coefficients - Correlation coefficients typically are known or can be reasonably inferred at one RVE. The inclusion of correlation coefficients was shown to change the simulated behaviour at scale by 30% for most material parameters. One current issue with selecting appropriate correlation coefficients is that many material parameters are obtained from destructive tests, which make it difficult to obtain accurate correlation coefficients between these material parameters. Given their impact on all material parameters, it is important to use measurable rather than speculative values for correlation coefficients when considering scale effects. Research considering how to quantify these correlation coefficients will lead to better forward estimation techniques and more reliable forward prediction methods.

The shape parameter associated with Young's Modulus - The correct selection and incorporation of variability of Young's Modulus has been shown to influence all material parameters at increased scales.

3.3 Implications of differing material parameters at increased scales

A major implication of these scale behaviour can be applied to conservative design practices. A common practice conservative design approach is to use the lowest observed strength across the entire testing campaign. Similarly, other material parameters are also selected assuming worst case conditions for example, the highest material density and lowest possible shear strength parameters. These new conservative design approaches have the following implications:

Implication 1: Engineers are 'incentivised' to test fewer and fewer samples. This is because lowest bound strength values are adopted, meaning the more samples tested, the more conservative the design parameters will be. Wording the above information into a statement:

The better quantified a material's shear strength is, the more conservative your design will be.

The above statement should alone be enough to bring into question the applicability of this highly conservative design philosophy, as it is self-contradictory. One would imagine the more understood the material is, the less conservative a design should be; however, the opposite is true. This gives Engineers an incentive to perform fewer laboratory measurements as lower strengths may make designs more problematic or uneconomic to implement.

Implication 2: The lowest strength philosophy is unjustifiably conservative. Rock does not behave as a purely frictional material, which is often the very conservative assumption adopted. Slope designed using the lowest strength bound essentially means that the overall slope angle will tend to the material's angle of repose.

Implication 3: Scale effects are very well documented. Experimental evidence presented in Chapter One, and the results in the previous section of this Chapter have shown two pronounced scale effects, an underlying scale effect and an associated homogenisation.

The extended implication of this Chapter's findings is that as the simulated volume of interest increases, the minimum observed strength relative to some smaller volume will increase. Designs considering the minimum laboratory scale strength will always be lower than the minimum value at some practical scale, even when accounting for negative scaling laws. This point again highlights the absurdity of the minimum possible value as it neglects a large amount of documented responses.

An alternative yet still conservative approach for strength selection is to consider the minimum shear strength at a practical volume as to account for both scale and homogenisation influences. While nonstandard laboratory testing is relatively uncommon, costly or impractical to implement, numerical heterogeneous analysis using PLACEBO does offer a cost effective alternative to estimate these scale effects.

To demonstrate this, the simulation results of lithology 'L5' at 8 times one RVE was chosen at a conservative 'practical volume' (equivalent to 0.17m^3) in which to define representative strength parameters compared to the typical laboratory scale (i.e., the inputs in Table 39). For both the laboratory and practical scale, the 0.01th percentile (i.e., the lowest 0.01%) was calculated from the resultant Maximum Likelihood Estimate to obtain minimum values of ϕ and c. This minimum value selection method ensures that the lowest possible value of ϕ and c are chosen, and accounts for issues associated with possible testing database sizes. Comparisons of the resulting shear strength criteria using the laboratory mean value, laboratory minimum value, scale dependant mean value and scale dependant minimum value are shown in Figure 51.

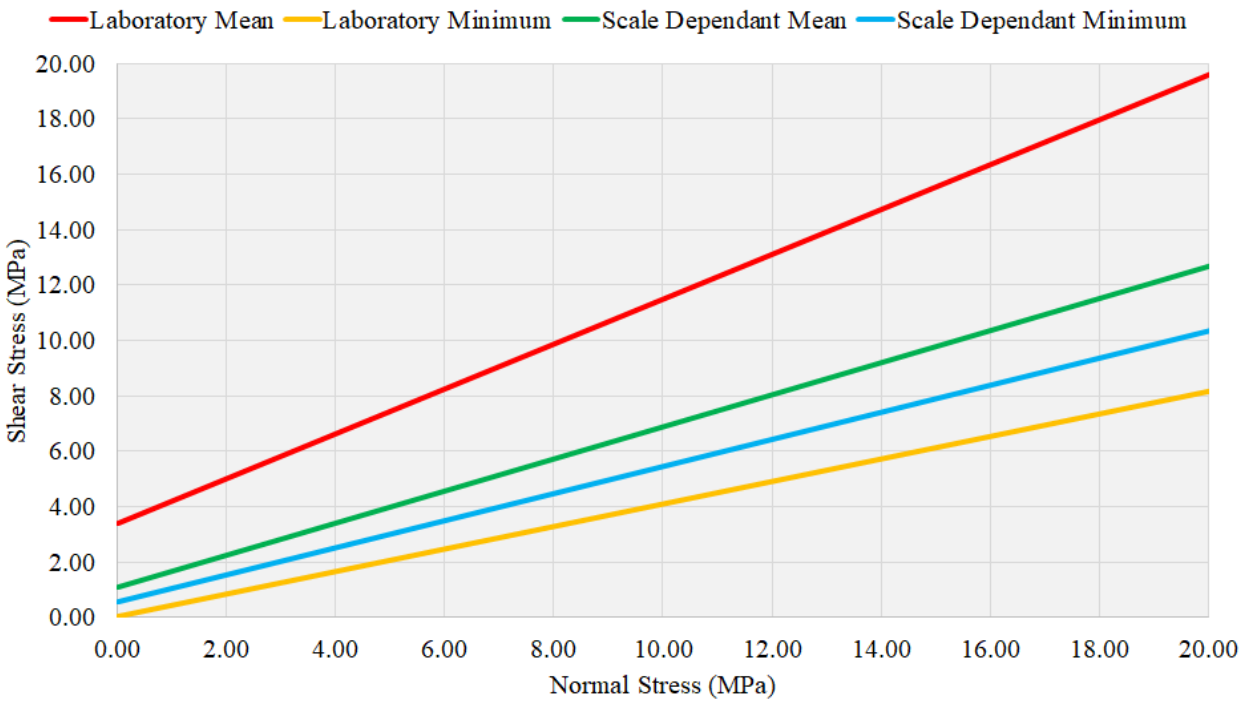

Figure 51 Comparisons of shear strength criteria for laboratory and practical scales

The material parameter values associated with each failure criterion shown in Figure 51 are summarised in Table 50.

Table 50 Comparisons of various material parameters for different selection criteria

Criterion	Friction angle	Cohesion
Laboratory minimum value	22.12°	0.03 MPa
Laboratory mean value	39.00°	3.43 MPa
Scale minimum value	26.05°	0.59 MPa
Scale mean value	30.10°	1.11 MPa

The shear strength criterion shown in Figure 51 and Table 50 demonstrate that when considering scaling laws and material homogenisation, the scale dependant minimum criterion produced is still conservative, but is comparatively stronger strength estimates than the laboratory minimum criterion.

A further complexity that also can be considered is the influences of material parameter correlation. The minimum material parameter criterion presented in Table 50 were chosen such that the correlated influences of ϕ and c are ignored. Laboratory testing considering ϕ and c are negatively correlated that is, the lower the observed friction value is the higher the associated cohesion and vice versa. For the numerical simulation completed this negative correlation is apparent and calculated as -0.68. A comparison of the numerical results and various criteria from Table 50 are shown in Figure 52.

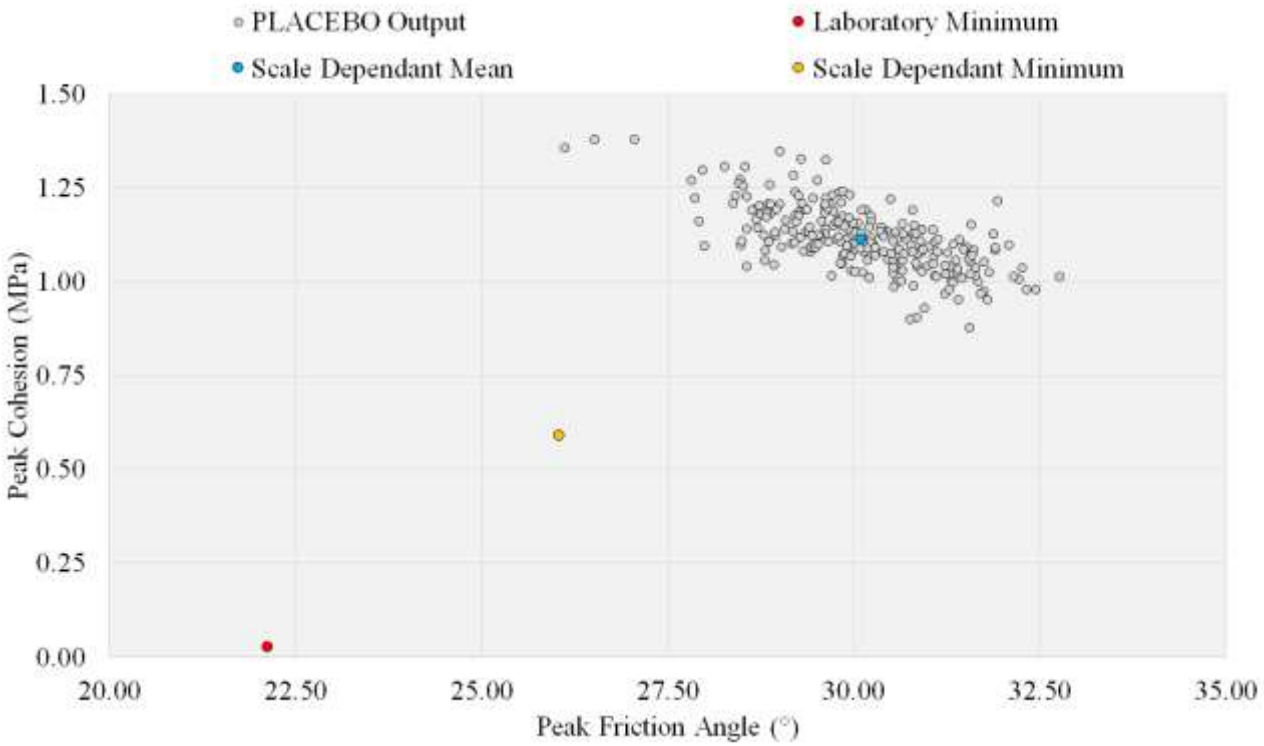

Figure 52 Scatter plot showing numerical output and various selection criteria

Note that in Figure 52 the mean laboratory material parameters are not shown to aid in the clarity of the Figure. It is evident in Figure 52 the laboratory and scale dependent minimum values are not representative of the correlated influences between ϕ and c. To account for these correlated influences, the correlated extreme values were calculated to produce two correlated minimum shear strength criteria. Comparisons of these correlated criterion and previously calculated criterion are shown in Figure 53.

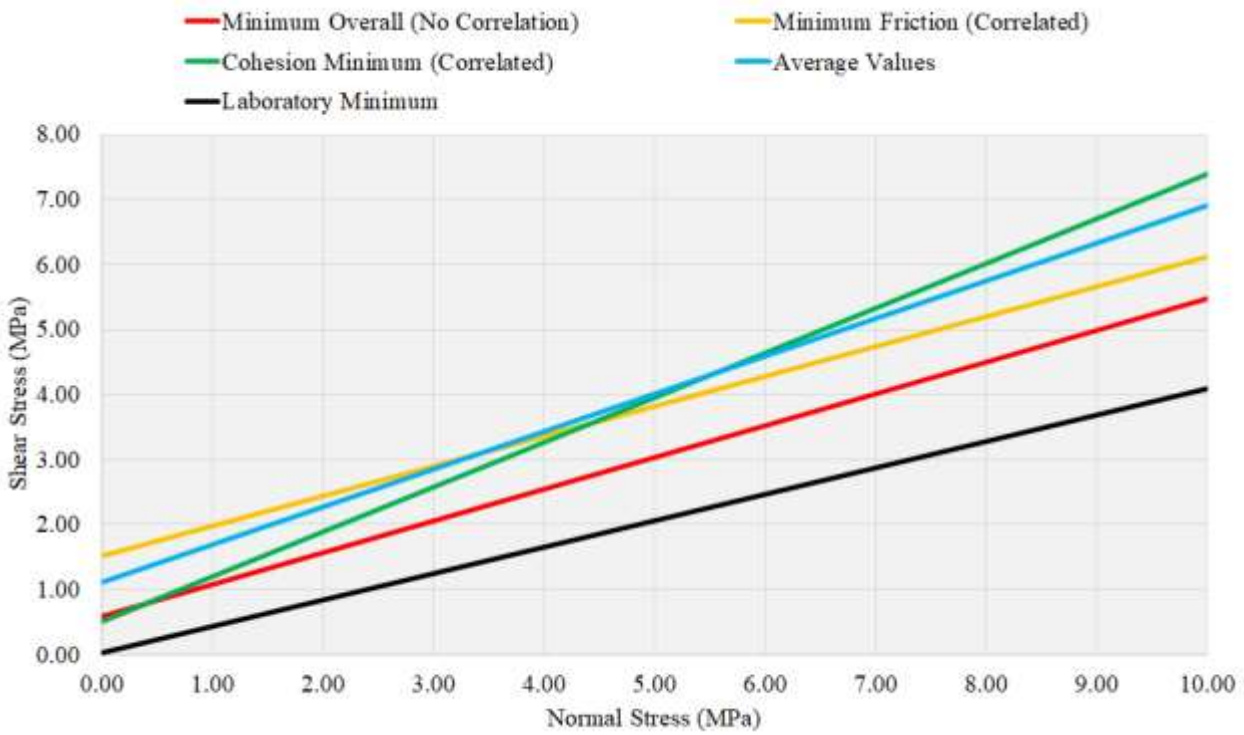

Figure 53 Comparisons of various minimum shear strength criterions considering correlations

Not shown in Figure 53 is that the minimum friction criterion crosses the overall minimum criterion at normal stresses equal to 32.30 MPa and all criteria are always higher than the laboratory minimum criterion. It is apparent in Figure 53 that which criterion produces the representative minimum shear stress depends on the acting normal stress. This stress dependant minimum value makes the problem of selecting a single representative strength envelope problematic. A simple solution to this stress dependency is to use a bi-linear shear strength criterion such that the stress dependency as well as stress path influences can be readily accounted for using a minimum strength approach. The bi-linear linear criterion appropriate for this material considering scale, heterogeneity and correlation is given in Table 51.

Table 51 Bi-linear failure criterion for the correlated minimum shear strength at scale

Normal stress	Criterion friction	Criterion cohesion	Criterion used
0.00 - 4.41 MPa	34.53°	0.51 MPa	Correlated minimum cohesion
>4.41 MPa	24.72°	1.51 MPa	Correlated minimum friction

One issue with this bi-linear strength criterion is that it can be incompatible with commercial software. In software restricted applications it is suggested that the minimum criterion that is representative over the expected normal stress range be chosen, or a linear criterion of best fit be calculated from the piece-wise linear criterion using regression techniques.

By considering scale effects in conjunction with the minimum strength approach, justifiably stronger parameters can be obtained. This new minimum approach is able to not only account for scaling laws and associated homogenisations but also considers shear strength material parameter correlations and normal stress dependencies in the final criterion. The minimum piece-wise approach derived produces the minimum possible shear strength over all normal stresses and is able to account for changing stress paths, while still remaining very conservative. While the demonstration of this new approach uses numerical methods to estimate the scale behaviour and homogenisation, the selection methodology is general enough to be applied to a-typical laboratory, or in situ testing results.

4 Universal Distribution Functions for Rock Discontinuities

4.1 Discontinuity Roughness

Mentioned in Chapter One, fractals can be classed as either fractal self-similar or fractal self-affine. With more evidence to suggest that rock discontinuities are fractal self-affine, a fractal self-affine simulation method was required. The simulation method chosen was Fractional Brownian Motion generated by the Circular Embedment method (Kroese & Botev 2014). This simulation method was chosen because of its 'exact' formulation (Dieker 2002) for a fractal self-affine process. The specified simulation resolution chosen was 2^{14} points along each generated discontinuity.

Fractional Brownian Motion $B_H = \{B_H(t): 0 \leq t < \infty\}$ with $0 < H < 1$ is defined as a stochastic fractal self-affine process with long range dependency. Fractional Brownian Motion is characterised by the following properties (Dieker 2002):

$B_H(t)$ has stationary increments, $B_H(0) = 0$, and $\mathbb{E}B_H(t) = 0$ for $t \geq 0$, $\mathbb{E}B_H^2(t) = t^{2H}$ for $t \geq 0$ and $B_H(t)$ has a Gaussian distribution for $t > 0$. These properties produce the following covariance function:

$$Cov(s,t) = \mathbb{E}B_H(s)B_H(t) = \frac{1}{2}(|t|^{2H} + |s|^{2H} - |t-s|^{2H}) \qquad \text{Equation 113}$$

for $0 < s \leq t$. As Fractional Brownian Motion has long range dependency if $H < \frac{1}{2}$ the increments are negatively correlated and if $H > \frac{1}{2}$ the increments are positively correlated.

4.1.1 Absolute roughness measurement selection routine

As the goal of this Section is to produce practical methods to quantifying roughness, more elaborate roughness measurements such as the centre line average roughness (Tse & Cruden 1979), root mean square roughness (Myers 1962), roughness profile index (Maerz & Franklin 1990), the maximum inclination angle (Tatone & Grasselli 2010) and standard deviation of the chord length (Seidel & Haberfield 1995) where not used, as they are not as easy or as practical to measure as the typical length amplitude approach used by Barton (2013). The length amplitude measure of absolute roughness was used due to its simplicity and parallels to field measurements and its closer relationship to JRC. The equation used to calculate the absolute roughness in each numerical simulation is given by:

$$R_{abs} = R_{max} - R_{min}$$ Equation 114

where R_{abs} is the absolute roughness (m), R_{max} is the maximum asperity height relative to some reference line (m) and R_{min} is the minimum asperity height relative to some reference line (m). A visual representation of R_{abs} is shown in Figure 54.

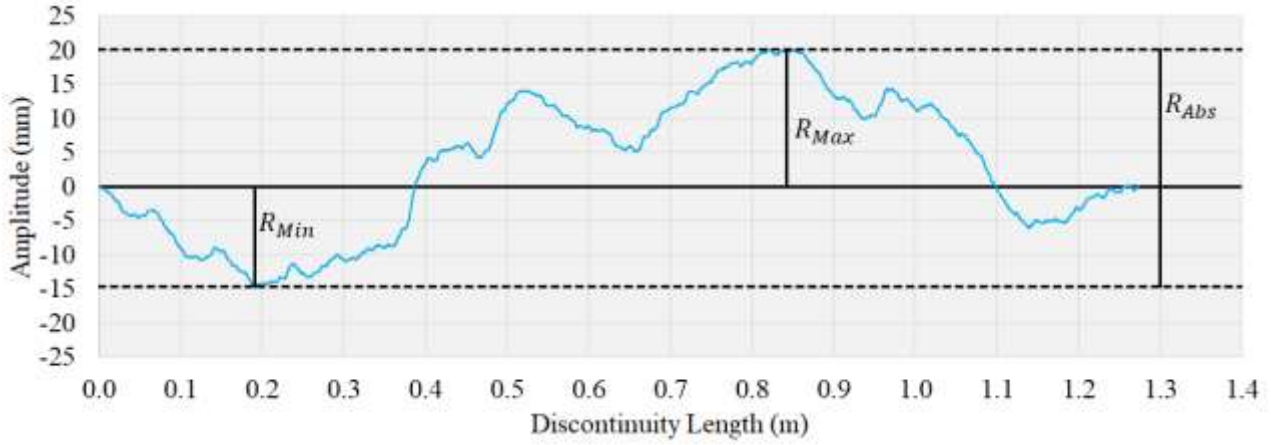

Figure 54 Visual representation of absolute roughness (R_{abs})

Fractional Brownian Motion as previously mentioned has long range dependence. This means that when the process is generated, it will have some associated correlation meaning that the generated length is longer than the specified simulation length. Before each roughness measurement can be recorded, each simulation needed to be re-orientated to reflect the required measurement length. Two re-orientation routines were initially proposed:

Bridge Centre Line Measurement - The roughness measurements are obtained perpendicular to an upper reference line that touches the surface at two fixed points. This simulation is synonymous to placing a profile comb or straight edge along a length of a discontinuity. The measurement routine is given as:

1. Generate surface $B_H(l)$ with specified H and L_0 such that $l \geq L_0$.
2. Step through each $B_H(l)$ and calculate the linear distance from $B_H(l)$ to $B_H(0)$. Find L^* such that $|B_H(L^*)| = L_0$.
3. Calculate the angle θ made between the origin and $B_H(L^*)$.
4. Apply a rotation of $-\theta$ to $B_H(l)$.
5. Calculate R_{abs}.

Linear Regression Rotation - The roughness measurements are obtained perpendicular to an average plane through the discontinuity. This simulation is synonymous with measuring roughness between two cross joints of known spacing. The measurement routine used is given as:

1. Generate surface $B_H(l)$ with specified H and L_0 such that $l \geq L_0$.
2. Step through each $B_H(l)$ and calculate the linear distance from $B_H(l)$ to $B_H(0)$. Find L^* such that $|B_H(L^*)| = L_0$.
3. Calculate the linear regression of $B_H(l)$. $\hat{B}_H(l) \approx \beta_0 + \beta_1 l$.
4. Calculate the linear regression l-axis intercept l_0.
5. Apply the offset $B_H(l) = B_H(l - l_0)$.
6. Calculate the angle θ made between the origin and the linear regression gradient β_1.
7. Apply a rotation of $-\theta$ to $B_H(l)$.
8. Calculate R_{abs}.

A visual comparison of two discontinuity profiles generated by each re-orientation routine is shown in Figure 55.

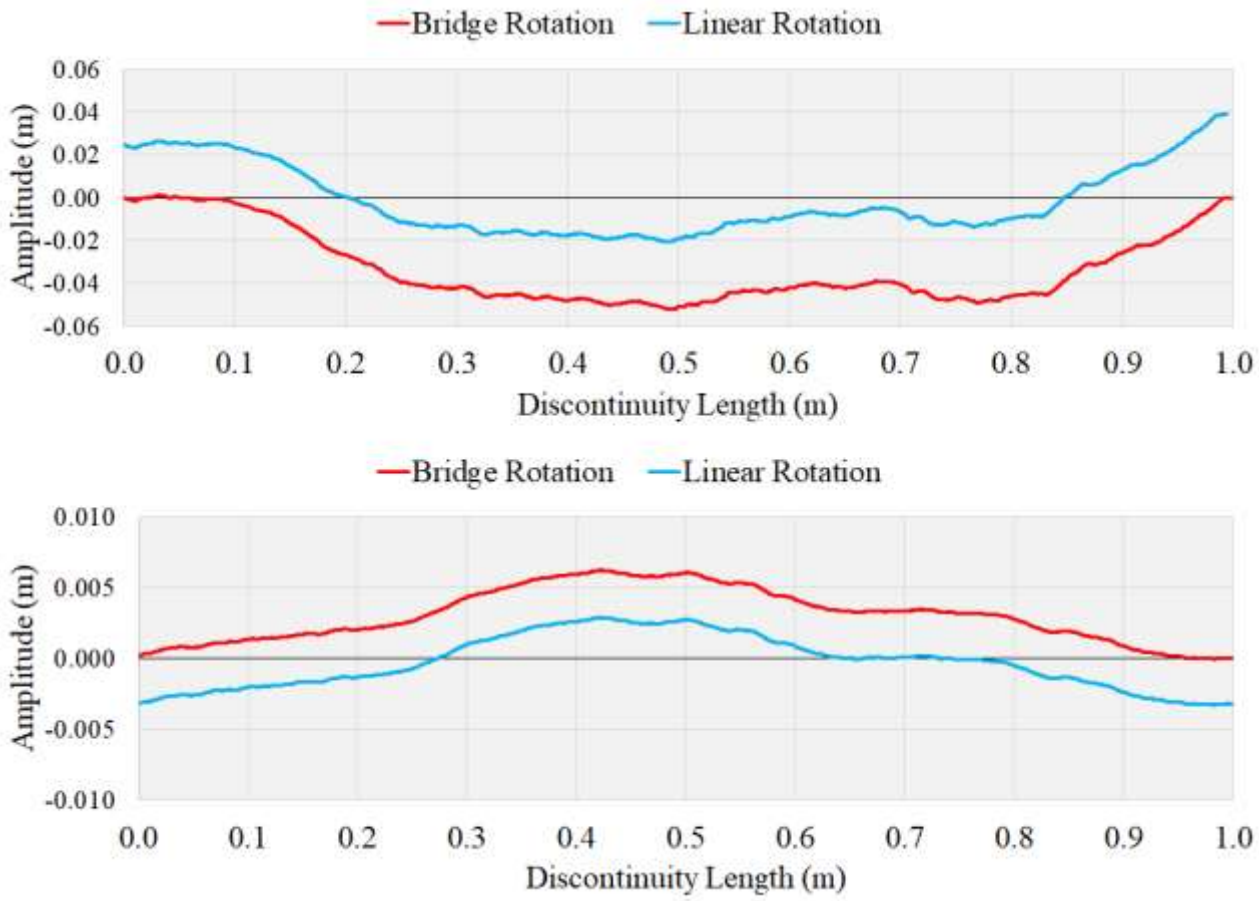

Figure 55 Comparison of absolute roughnes measurement routines. Top $H = 0.995$, bottom $H = 0.9995$

Depending on which re-orientation routine used, slightly different values of R_{abs} were obtained due to differences associated with the rotation angle. To contrast the differences between these re-orientation routines and equivalent field measurements, four input combinations of H and L were simulated 500 times for each combination for comparison. The measurement routines were then contrasted by considering the mean roughness difference and comparing EDFs using the KS test. The summary of the statistical comparisons and test decisions are shown in Table 52.

Table 52 Summary of the analysis comparing absolute roughness measurement routines

Discontinuity length	Statistical value or test	Hurst exponent 0.995	Hurst exponent 0.9995
1.0m	Mean roughness (mm) Bridge rotation	39.91	12.40
	Mean roughness (mm) Linear rotation	40.34	12.47
	Mean difference confidence interval (mm)	ND	ND
	Kolmogorov Smirnov decision	ND	ND
0.1m	Mean roughness (mm) Bridge rotation	3.82	1.22
	Mean roughness (mm) Linear rotation	3.87	1.23
	Mean difference and Confidence Interval (mm)	Detectable difference in means -0.0952 to -0.0078	Detectable difference in means -0.02969 to -0.0023
	Kolmogorov Smirnov decision	ND	ND

Note, when calculating the mean difference, the value presented in Table 52 is the bridge rotation measurement minus linear rotation. ND signifies no significant difference at a 5% significance. From the results shown in Table 52 is can be concluded at a 5% significance that the two re-orientation routines produce no significant differences in the overall distribution of measurements in each simulation, no statistically significant difference in mean values at 1.0m discontinuity length and a small but significant difference in mean roughness measurements at 0.1m. The difference in mean values for 0.1m lengths is less than a tenth of a millimetre with this discrepancy being acceptable for practical applications. The re-orientation routine selected was the bridge rotation routine due to its simpler computational requirements.

4.1.2 Testing for a Universal Distribution Function for discontinuity roughness measurements

With a representative roughness measurement and simulation method chosen, the expected behaviour of each combination of H and L was then quantified and probabilistically assessed. From preliminary testing a realistic estimate of H for rock discontinuities are values greater than 0.98 and less than 1.00. 29 different values of H were tested from within this range to cover very rough to almost planar discontinuities profiles. Values of L were simulated at 30 different lengths ranging from 0.10m through to 100m. This measurement range was selected to quantify scales ranging from practical measurements through to mine scale features. Each combination of H and L had 2000 individual realisations resulting in 1.74 million simulations in total. The simulation data was then de-scaled and assessed using non-parametric bootstrapping to determine if a UDF describing absolute roughness exists. A summary of the test decisions obtained from non-parametric bootstrapping are shown in Table 53.

Table 53 Non-parametric bootstrapping test decision summary - absolute roughness

Samples grouped by discontinuity length		Samples grouped by Hurst exponent	
Discontinuity length	Decision	Hurst exponent	Decision
0.10m	✓	0.98000	✓
0.20m	✓	0.99000	✓
0.30m	✓	0.99100	✓
0.40m	✓	0.99200	✓
0.50m	✓	0.99300	✓
1.00m	✓	0.99400	✓
1.50m	✓	0.99500	✓
2.00m	✓	0.99600	✓
2.50m	✓	0.99700	✓
3.00m	✓	0.99800	✓
3.50m	✓	0.99900	✓

4.00m	✓	0.99910	✓
4.50m	✓	0.99920	✓
5.00m	✓	0.99930	✓
6.00m	✓	0.99940	✓
7.00m	✓	0.99950	✓
8.00m	✓	0.99960	✓
9.00m	✓	0.99970	✓
10.00m	✓	0.99980	✓
12.50m	✓	0.99990	✓
15.00m	✓	0.99991	✓
17.50m	✓	0.99992	✓
20.00m	✓	0.99993	✓
25.00m	✓	0.99994	✓
30.00m	✓	0.99995	✓
35.00m	✓	0.99996	✓
40.00m	✓	0.99997	✓
50.00m	✓	0.99998	✓
75.00m	✓	0.99999	✓
100.00m	✓		

It can be concluded at a 5% significance that the distribution of de-scaled absolute roughness measurements grouped by test length L are consistent with some UDF and the distribution of de-scaled absolute roughness measurements grouped by Hurst exponent H are consistent with some UDF. These two conclusions imply that the de-scaled distribution of absolute roughness is independent of both H and L, and that is there is a single UDF that describes the distribution of de-

scaled absolute roughness measurements. With evidence that some UDF exists, a series of KS tests were then completed to test various PDF families for their goodness of fit. Parameter relationships to the median value were also used to reduce the number of independent variables in each goodness of fit test. The summary of the KS test decisions are presented in Table 54.

Table 54 Kolmogorov Smirnov goodness of fit test decision summary - descaled data for absolute roughness

Probability Density Function Family	Decision
Normal	✗
Log-normal	✗
Gamma	✗
Rayleigh	✗
Weibull	✓
Gumbel	✓
Fréchet	✗
Laplace	✗

Note that in Table 54, two additional PDF families have been included, the Gumbel and Fréchet distributions. These additional PDFs were included due to the general shape of the data's EDFs. Based on the results in Table 54 it can be concluded at a 5% significance that the UDF of de-scaled absolute roughness measurements is consistent with a Weibull or Gumbel distribution. With evidence of the existence of a UDF for absolute roughness measurements, all possible model simplifications and the applicability of the UDF to describe raw data were completed using a series of KS tests. The summary of this statistical analysis is shown in Table 55.

Table 55 Universal Distribution Function variable substitution analysis summary - absolute roughness

	Median value with variable shape parameter	Median value with constant shape parameter	Mean value with variable shape parameter	Mean value with constant shape parameter
Weibull distribution	✗	$1.838 \leq \hat{k} \leq 1.914$ $\hat{\lambda} = \frac{\bar{M}}{(\ln(2))^{\frac{1}{\hat{k}}}}$	✗	$1.845 \leq \hat{k} \leq 1.914$ $\hat{\lambda} = \frac{\bar{\mu}}{\Gamma\left(1+\frac{1}{\hat{k}}\right)}$
Gumbel distribution	$\hat{\alpha} = \bar{M} + \hat{\beta}\ln(\ln 2)$ $\hat{\beta} = c\bar{M}$ $0.512 \leq \hat{c} \leq 0.518$	✗	$\hat{\alpha} = \bar{\mu} - \gamma\hat{\beta}$ $\hat{\beta} = c\bar{M}$ $0.458 \leq \hat{c} \leq 0.466$	✗

Note that in Table 55 γ is the Euler-Mascheroni constant, $\bar{M}$ is the sample median and $\bar{\mu}$ is the sample mean. Based on all statistical tests, it can be concluded that the distribution of absolute roughness can be described by one of two UDFs, with Table 56 summarising all key deterministic and probabilistic characteristics associated with these UDFs.

Table 56 Universal Distribution Function summary - absolute roughness

	Weibull distribution	Gumbel distribution
Probability Density Function	$f_X(x) = \frac{k}{\lambda}\left(\frac{x}{\lambda}\right)^{k-1} e^{-\left(\frac{x}{\lambda}\right)^k}$	$f_X(x) = \frac{1}{\beta} e^{-\left(\frac{x-\alpha}{\beta} + e^{-\left(\frac{x-\alpha}{\beta}\right)}\right)}$
Parameter estimates using the mean	$1.845 \leq \hat{k} \leq 1.912, \hat{k} \approx \frac{3\pi}{5}$ $\hat{\lambda} = \frac{\bar{\mu}}{\Gamma\left(1+\frac{1}{\hat{k}}\right)}$	$\hat{\alpha} = \bar{\mu} - \gamma\hat{\beta}$ $\hat{\beta} = c\bar{\mu}$ $0.458 \leq \hat{c} \leq 0.466$
Parameter estimates using the median	$1.838 \leq \hat{k} \leq 1.914, \hat{k} \approx \frac{3\pi}{5}$ $\hat{\lambda} = \frac{\bar{M}}{(\ln 2)^{\frac{1}{\hat{k}}}}$	$\hat{\alpha} = \bar{M} + \hat{\beta}\ln(\ln 2)$ $\hat{\beta} = \hat{c}\bar{M}$ $0.512 \leq \hat{c} \leq 0.518$
Deterministic estimate	$\widehat{Mo} = \hat{\lambda}\left(\frac{\hat{k}-1}{\hat{k}}\right)^{\frac{1}{\hat{k}}}$	$\widehat{Mo} = \hat{\alpha}$

Note that in Table 56 Γ is the Gamma function. Although both UDFs (the Weibull and Gumbel distributions) and the associated parameter ranges shown in Table 56 are statistically acceptable and meet the required definition of a UDF, the Weibull distribution UDF with $\hat{k} = \frac{3\pi}{5}$ was chosen as a single representative UDF. This single UDF estimate was chosen based on its simpler mathematical representation and the ease and accuracy associated with deriving the theoretical scale relationships in the following Sections.

4.1.3 Development of theoretical scaling laws for fractal-self affine discontinuities

In order to estimate relationships between characteristic measurements, Hurst exponent and scale, the raw data was evaluated with linear regression techniques to find a reasonably accurate equation relating field measurements of R_{abs} to H and measurements at arbitrary scales. From a preliminary review, the simplest relationship is given by:

$$\bar{M} \approx \frac{L_0}{2}\sqrt{1-H} = 0.5 \times L_0(1-H)^{0.5} \qquad \text{Equation 115}$$

The applicability of Equation 115 was compared to the available numerical output to test for its applicability. The test hypothesis is given as:

The median value is equal to half the length multiplied by the square root of one minus the Hurst exponent.

The statistical regression a constant of 0.4990, and associated power term confidence interval of 0.4972 to 0.5001. Based on these findings it can be concluded that Equation 115 is sufficient at describing the relationship between the sample median, length and Hurst exponent. Rearranging Equation 115, the estimate of the Hurst exponent $\widehat{H}$ using the median value such that:

$$\widehat{H} \approx 1 - \left(\frac{2\bar{M}_0}{L_0}\right)^2 \qquad \text{Equation 116}$$

Equation 116 can then be used to derive a number of different estimates of $\widehat{H}$ using different statistical parameters such as the mean value, mode value or sample variance. Recall that for a Weibull distribution, the median value can be calculated using:

$$M = \lambda\left(\ln(2)^{\frac{1}{k}}\right)$$ Equation 117

Taking the constant shape estimate for k in Table 56:

$$M = \lambda\left(\ln(2)^{\frac{5}{3\pi}}\right)$$ Equation 118

By using the identities of the Weibull distribution, λ is related to other parameters such that:

$$\lambda = \frac{\mu_0}{\Gamma\left(\frac{3\pi+5}{3\pi}\right)}$$ Equation 119

$$\lambda = \frac{Mo_0}{\left(\frac{3\pi-5}{3\pi}\right)^{\frac{5}{3\pi}}}$$ Equation 120

$$\lambda = \sqrt{\frac{Var_0}{\left(\Gamma\left(\frac{3\pi+10}{3\pi}\right) - \left(\Gamma\left(\frac{3\pi+5}{3\pi}\right)\right)^2\right)}}$$ Equation 121

Substituting Equation 119, Equation 120 and Equation 121 into Equation 116 yields three additional estimates for $\widehat{H}$:

$$\widehat{H} \approx 1 - \left(\frac{2\left(\ln(2)^{\frac{5}{3\pi}}\right)}{\Gamma\left(\frac{3\pi+5}{3\pi}\right)}\right)^2 \left(\frac{\bar{\mu}_0}{L_0}\right)^2 \approx 1 - 3.44\left(\frac{\bar{\mu}_0}{L_0}\right)^2$$ Equation 122

$$\widehat{H} \approx 1 - \left(\frac{2\left(\ln(2)^{\frac{5}{3\pi}}\right)}{\left(\frac{3\pi-5}{3\pi}\right)^{\frac{5}{3\pi}}} \right)^2 \left(\frac{\overline{Mo_0}}{L_0}\right)^2 \approx 1 - 6.05\left(\frac{\overline{Mo_0}}{L_0}\right)^2 \quad \text{Equation 123}$$

$$\widehat{H} \approx 1 - \left(\frac{\left(2\left(\ln(2)^{\frac{5}{3\pi}}\right)\right)^2}{\Gamma\left(\frac{3\pi+10}{3\pi}\right) - \left(\Gamma\left(\frac{3\pi+5}{3\pi}\right)\right)^2} \right) \frac{\overline{Var_0}}{L_0^2} \approx 1 - 11.32\left(\frac{\overline{Var_0}}{L_0^2}\right) \quad \text{Equation 124}$$

It may be possible to simplify the constant terms in Equation 122 through Equation 124, however this is not necessary for practical applications. The distribution of measured percentage errors for each estimation equations are shown in Figure 56. Note that the mode value estimate is not included as this value is calculated using either the mean or median value. The errors associated with the mode value are identical to the selected generation variable.

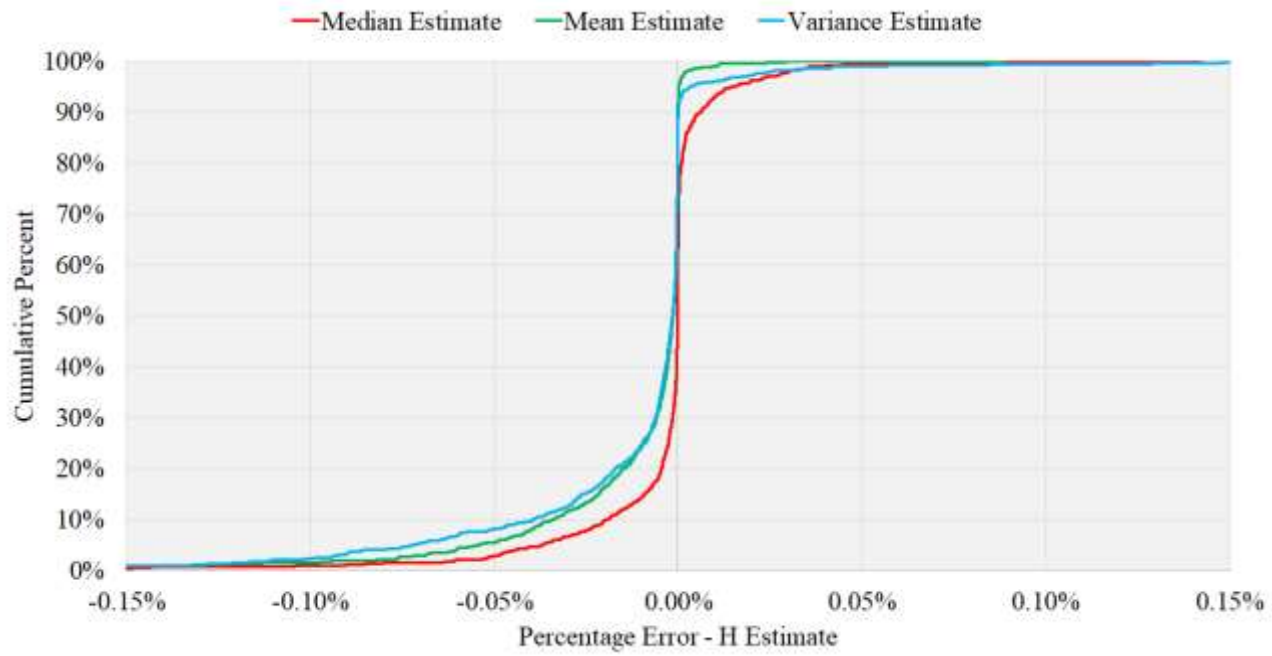

Figure 56 Cumulative Distribution Function for the percentage error for each estimation method

It can be seen in Figure 56 that the typical percentage error for estimating H by any method is very low, typically less than 0.05%. Equation 116, Equation 122 and Equation 124 are therefore valid approximations. The scale dependant relationships can also be calculated in a similar manner as the

estimation methods for $\widehat{H}$. As the true value of H is invariant of the measurement length and is an inherent parameter of each discontinuity, it can be used to relate different scales to one another such that:

$$1-\left(\frac{2M_n}{L_n}\right)^2 \approx H \approx 1-\left(\frac{2M_0}{L_0}\right)^2 \quad \text{Equation 125}$$

When simplified, Equation 125 becomes:

$$M_n \approx M_0 \frac{L_n}{L_0} \quad \text{Equation 126}$$

Equation 126 is the scale equation relating the median measurement at L_0 to the median value at the desired L_n. It then follows that:

$$\lambda_n \approx \lambda_0 \frac{L_n}{L_0} \quad \text{Equation 127}$$

$$\mu_n \approx \mu_0 \frac{L_n}{L_0} \quad \text{Equation 128}$$

$$Mo_n \approx Mo_0 \frac{L_n}{L_0} \quad \text{Equation 129}$$

$$Var_n \approx Var_0 \left(\frac{L_n}{L_0}\right)^2 \quad \text{Equation 130}$$

Two other useful identities are the relationship between the UDF scale parameter λ_n and $\widehat{H}$ and the Coefficient of Variation COV:

$$\hat{\lambda}_n = \frac{L_n\sqrt{1-\widehat{H}}}{2(\ln 2)^{\frac{5}{3\pi}}} \quad \text{Equation 131}$$

$$COV = \frac{\sqrt{\lambda^2\left(\Gamma\left(1+\frac{2}{k}\right) - \left(\Gamma\left(1+\frac{1}{k}\right)\right)^2\right)}}{\lambda\Gamma\left(1+\frac{1}{k}\right)} \approx 55.14\%$$

Equation 132

By consideration of Equation 132 the constant Coefficient of Variation implies there is no homogenisation associated with increasing scale for a purely fractal self-affine surface.

4.1.4 Comparisons to Barton's standard profiles and other studies

Studies often digitise Barton's standard roughness profiles and then estimate the associated fractal dimension or Hurst exponent to explore relationships between the two measurements. A similar comparison was completed using the theory presented in this Chapter to compare fractal characteristics of the standard profiles to those presented in other studies. The estimates of H presented in this Section are based on a probabilistic descriptions, digitising and measuring a single profile will not produce a valid estimate for H. In order to compare and contrast estimates of H across multiple studies, the amplitude of asperities equal to the standard profiles (0.10m) were used in conjunction with Equation 116, Equation 122 and Equation 123 to estimate the value of H required to produce a distribution of roughness such that the mean, median or mode value that corresponds to a particular JRC at 0.10m. Numerical estimates of H from various studies and this study are visually presented in Figure 57. Note that other studies estimating the fractal characteristics of the standard profiles using the fractal dimension have been converted to values of H using Equation 41.

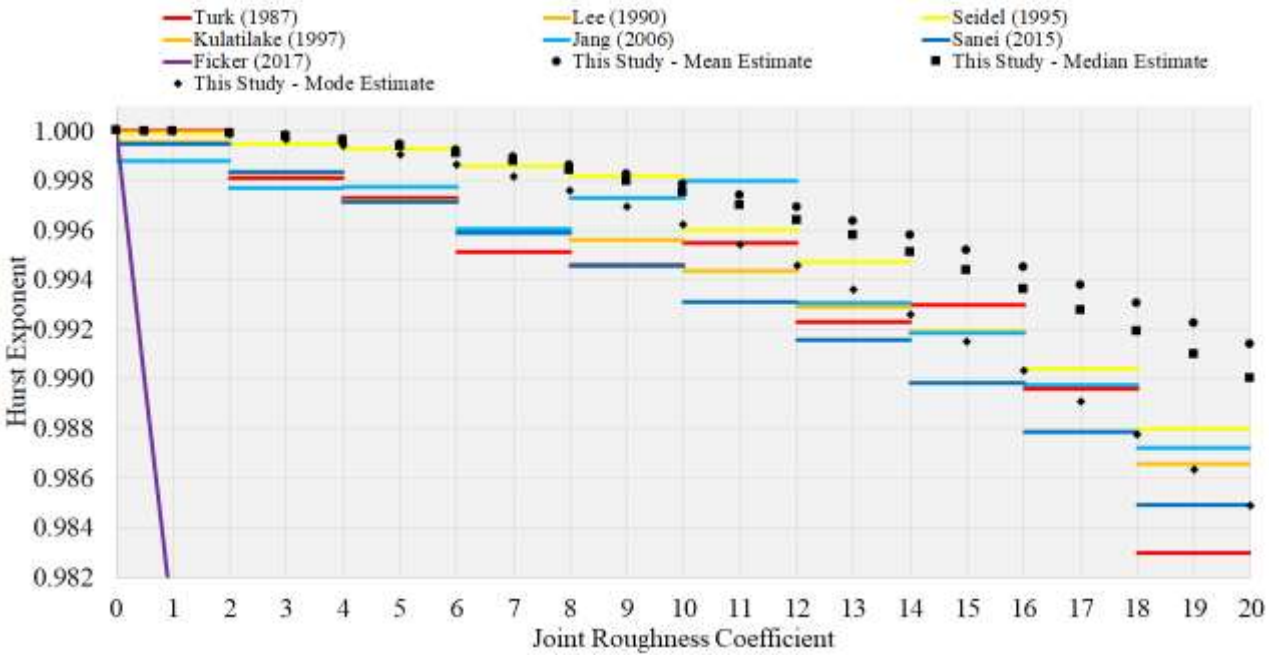

Figure 57 Graphical comparison of Joint Roughness Coefficient vs estimates of the Hurst exponent

From review of Figure 57 it can be seen that the mode JRC value estimate of H matches closest to the fractal characteristics of Barton's standard profiles, with the most comparable values from literature being those of Siedel and Haberfield (1995). It is unsurprising that the mode value corresponds closest to the standard profiles as these are deterministic or representative roughness profiles and would relate to the most likely roughness (i.e., the mode roughness value). The fact that the findings of this study do align with the results of others provides some evidence to the appropriateness of Equation 116, Equation 122, Equation 123 and Equation 124 to describe discontinuities at scales near 0.10m.

In order to estimate the equation relating values of H, D and JRC, the mode JRC estimate was fitted to an appropriate non-linear model and evaluated using regression techniques. The results of the regression produced the following two following models relating JRC, the Hurst exponent H, and fractal dimension D:

$$JRC \approx 162.64 \times \sqrt{1 - H} \qquad \text{Equation 133}$$

$$JRC \approx 162.64 \times \sqrt{D - 1} \qquad \text{Equation 134}$$

The regression r^2 of this regression is 1.00. When comparing Equation 134 to the large list of relationship equations presented in Li and Huang (2015), the closest relationship previously reported in literature was that of Wakabayashi and Fukushige (1992) whose equation is given by:

$$JRC = 150.53 \times \sqrt{D - 1} \qquad \text{Equation 135}$$

4.1.5 Comparisons to physical discontinuity measurements at various scales

The Fractal approach appears promising at being able to describe discontinuity roughness at arbitrary scales. In order to accept this mathematical description, it must be shown to be representative of real world measurements over a number of scales. In order to compare the applicability of Equation 116, Equation 122, Equation 123 and Equation 124 and the more general fractal description of discontinuities, two different discontinuities over a wide range of scales were compared to the fractal model previously presented. The first data set contained field measurements of Barton's length

amplitude approach associated with a natural Hawksbury sandstone joint with a JRC_0 approximately equal to 10. The measurement routine and data manipulation used is as followed:

1. 67 0.25m profile comb segments were taken and transferred to paper. Each segment was obtained in the same orientation to limit anisotropic influences.
2. The length amplitude measurement for each profiles was manually measured at incremental scales of 0.05m using a ruler and compass. Successive measurements at a given scale were completed such that no two segments overlapped.
3. Larger scales (i.e., lengths exceeding 0.25m) were manually measured using a straight edge and ruler. Each scale utilised a specific length straight edge to remove issues associated with measuring smaller scales using a longer straight edge. The scales measured using a straight edge covered 0.50m, 0.60m, 0.80m, 1.00m, 1.30m and 1.60m.
4. Each profile comb profile was then scanned and then finely digitised to allow for detailed numerical resampling. The average number of digitised points per segment was 660.
5. Each digitised segment was then randomly resampled to obtain many measurements over a continuum of scales. Each digitised surface was randomly resampled 1000 times using the bridge rotation method, duplicate and trivial (i.e., measurements between adjacent points) measurements were then removed. The resample lengths were then rounded to the nearest millimetre, leaving the absolute roughness as determined to aid in probabilistic evaluation.

The second data set came from laser scans of a very rough natural joint section from an operating mine. The approximate JRC_0 for this joint was close to 20. The measurement routine and data manipulation is as followed:

1. The laser scans were broken down into 196 ‘scan lines’ of the same orientation, which ranged in length from 3m to 16m and were typically between 8m and 12m with a resolution of roughly 5cm.
2. Each digitised segment was then randomly resampled to obtain many measurements over a continuum of scales. Each digitised surface was randomly resampled 500 times using the bridge rotation method, duplicate and trivial (i.e., measurements between adjacent points) measurements were then removed. The resample lengths were then rounded to the nearest centimetre, leaving the absolute roughness as determined to aid in probabilistic evaluation.

The Equation 116, Equation 122, Equation 123 and Equation 124 predicting the relationships for the mean value, median value, mode value, variance, coefficient of variation and $\widehat{H}$ were then compared

to the observed measurements to determine their effectiveness. Visual comparisons between these measured statistical values and the predicted fractal model are shown in Figure 58 through Figure 73. Note that manual and resampled measurements associated with the Hawkesbury Sandstone joint have been shown on two different plots for clarity.

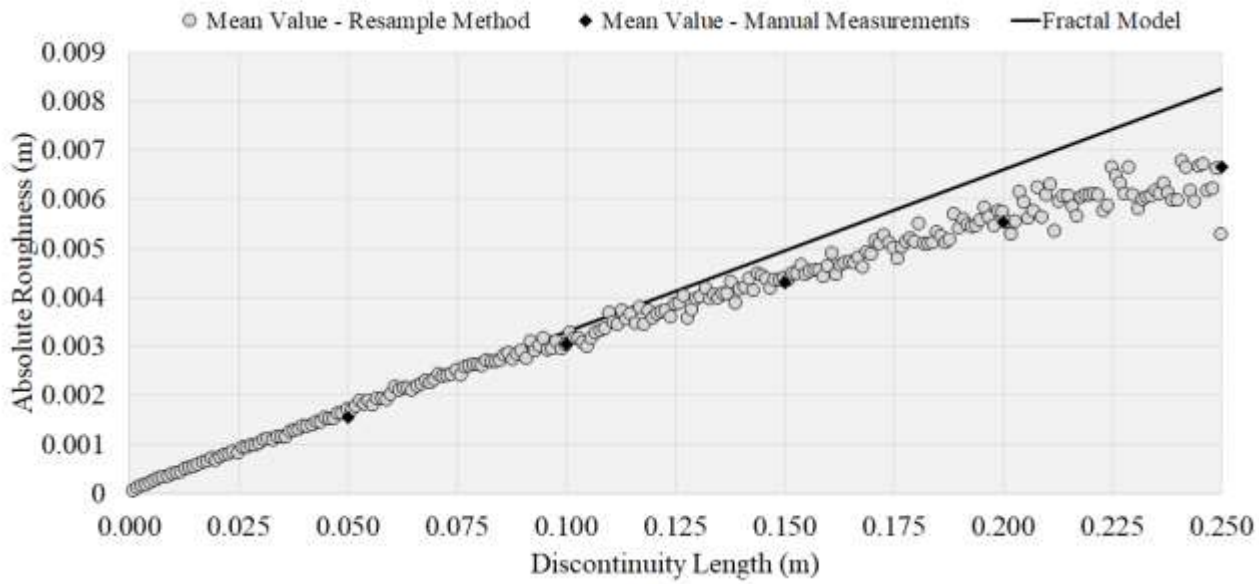

Figure 58 Absolute roughness vs discontinuity length - Hawkesbury Sandstone mean values

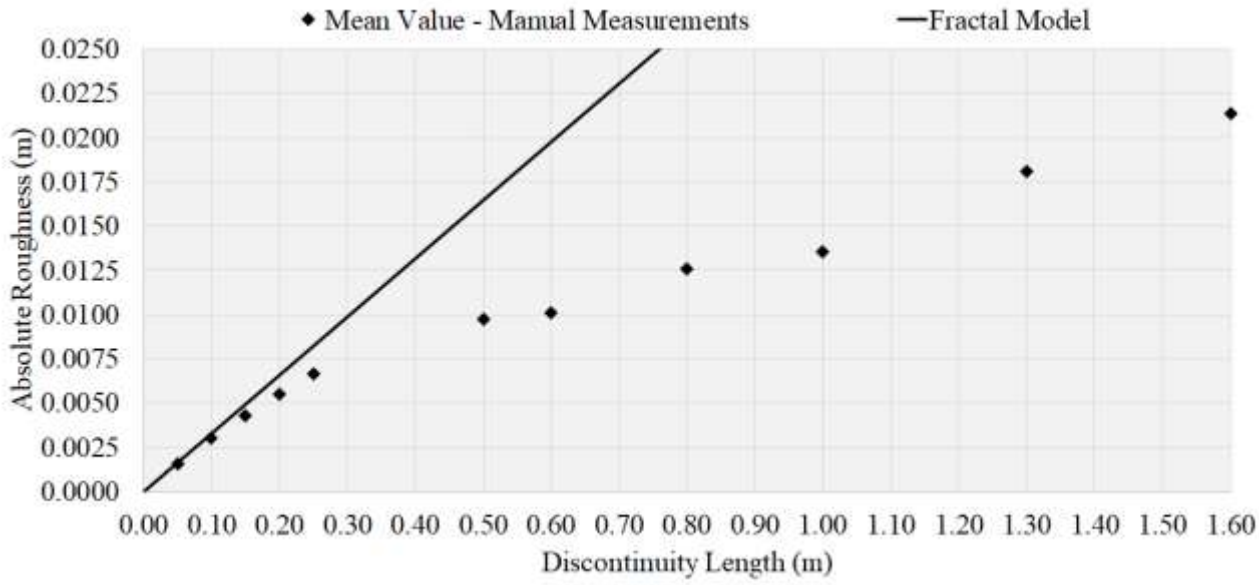

Figure 59 Absolute roughness vs discontinuity length - Hawkesbury Sandstone mean values manual measurements

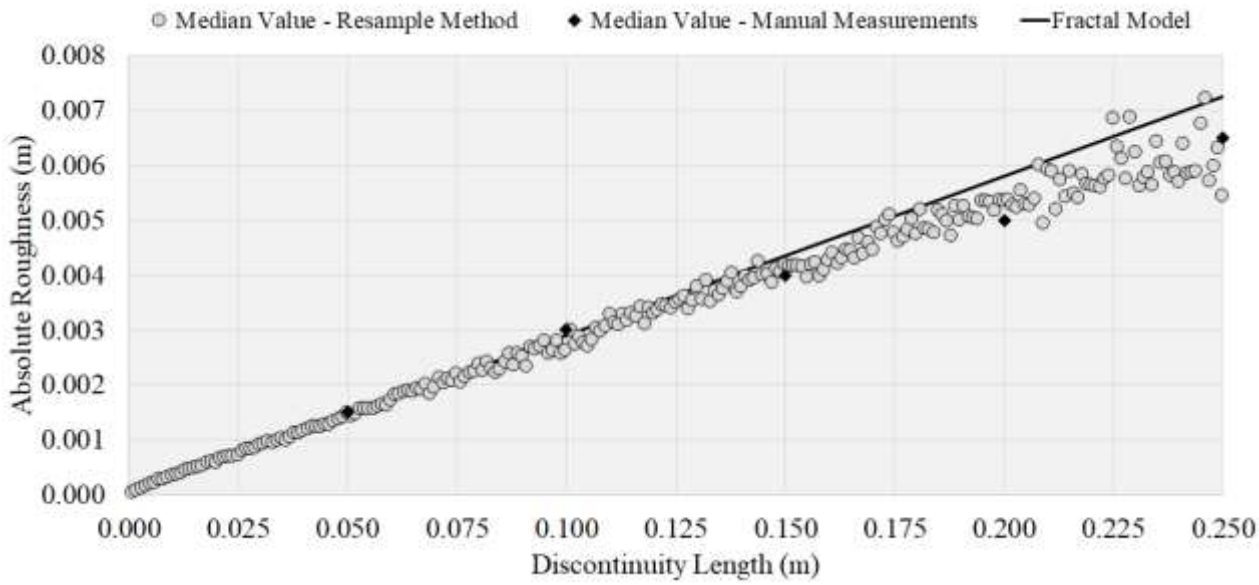

Figure 60 Absolute roughness vs discontinuity length - Hawkesbury Sandstone median values

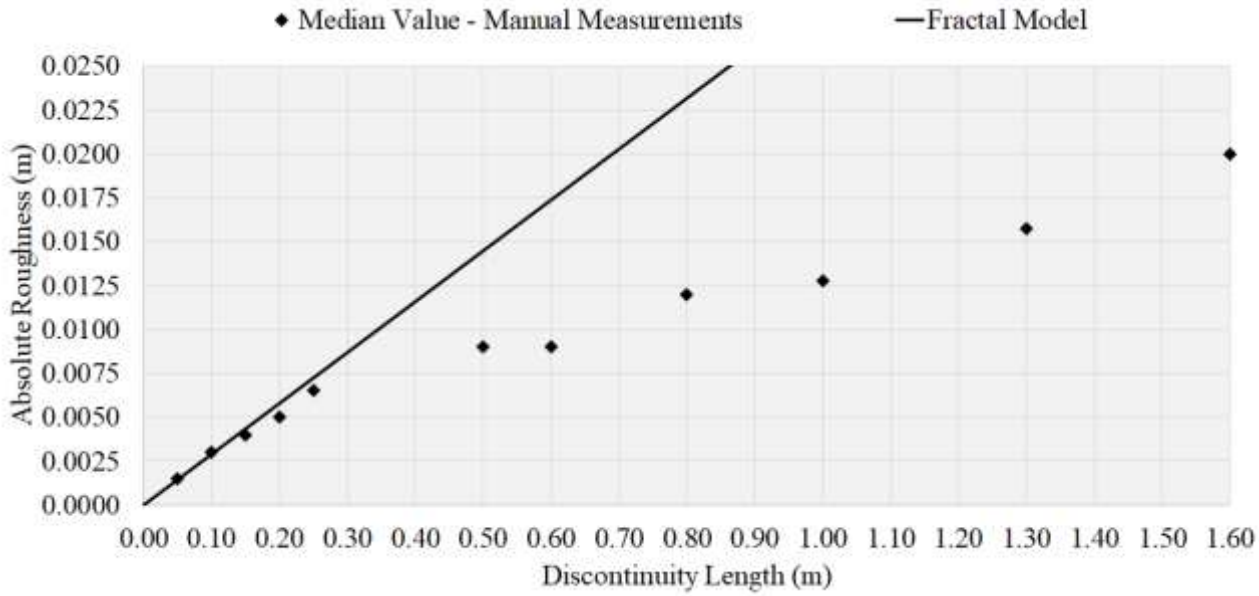

Figure 61 Absolute roughness vs discontinuity length - Hawkesbury Sandstone median values manual measurements

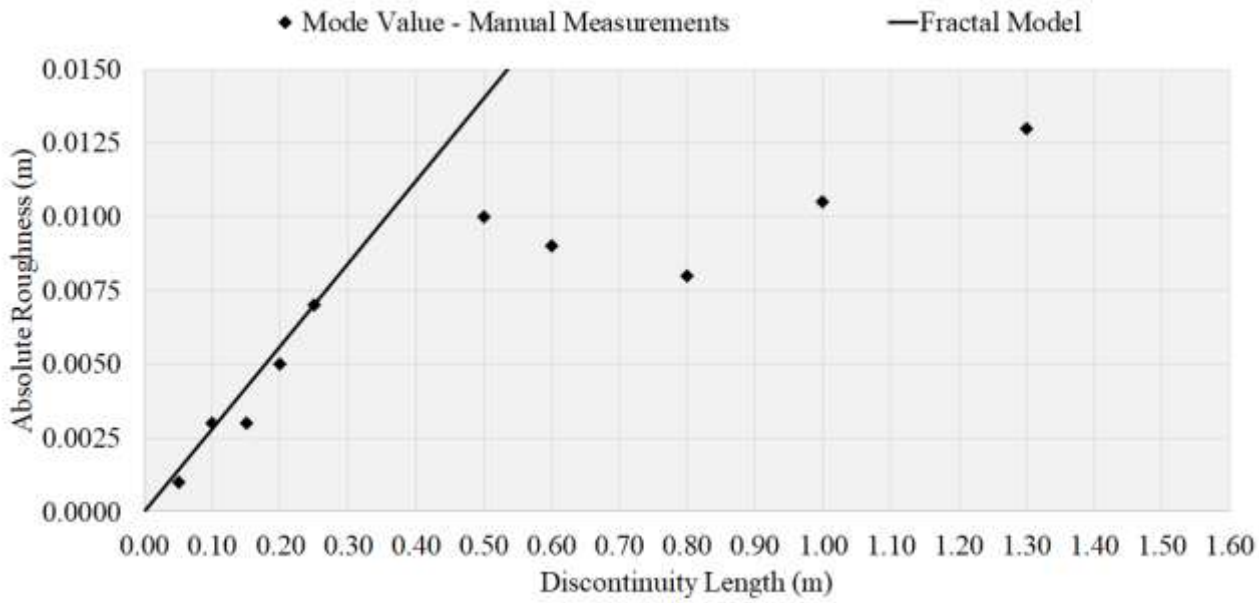

Figure 62 Absolute roughness vs discontinuity length - Hawkesbury Sandstone mode values manual measurements

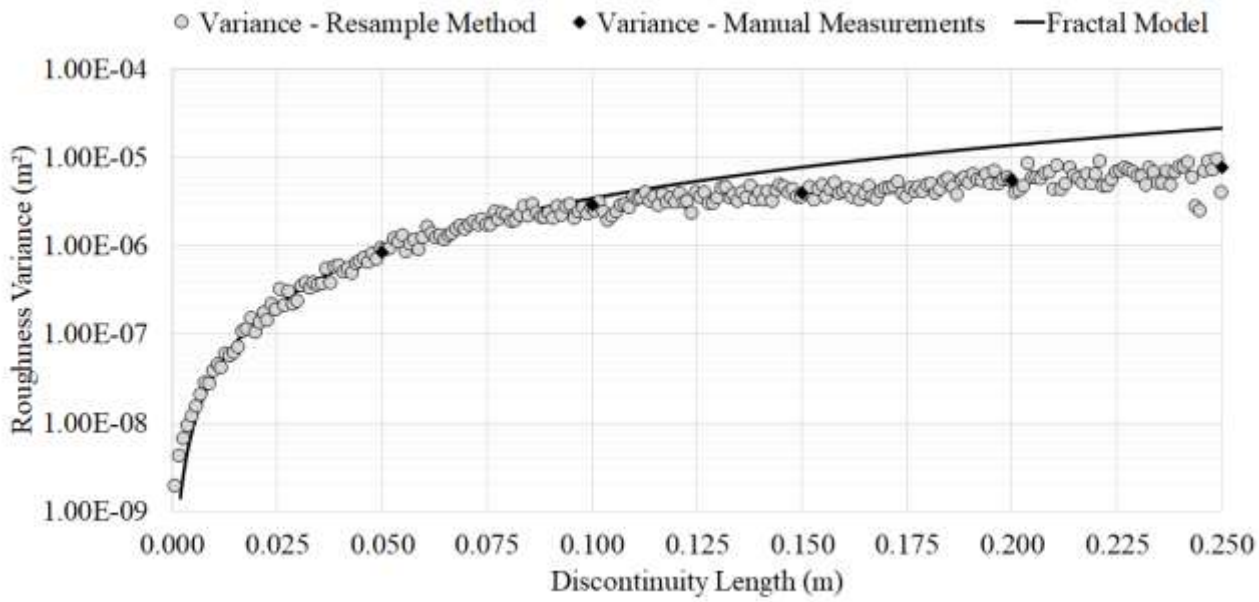

Figure 63 Absolute roughness variance vs discontinuity length - Hawkesbury Sandstone

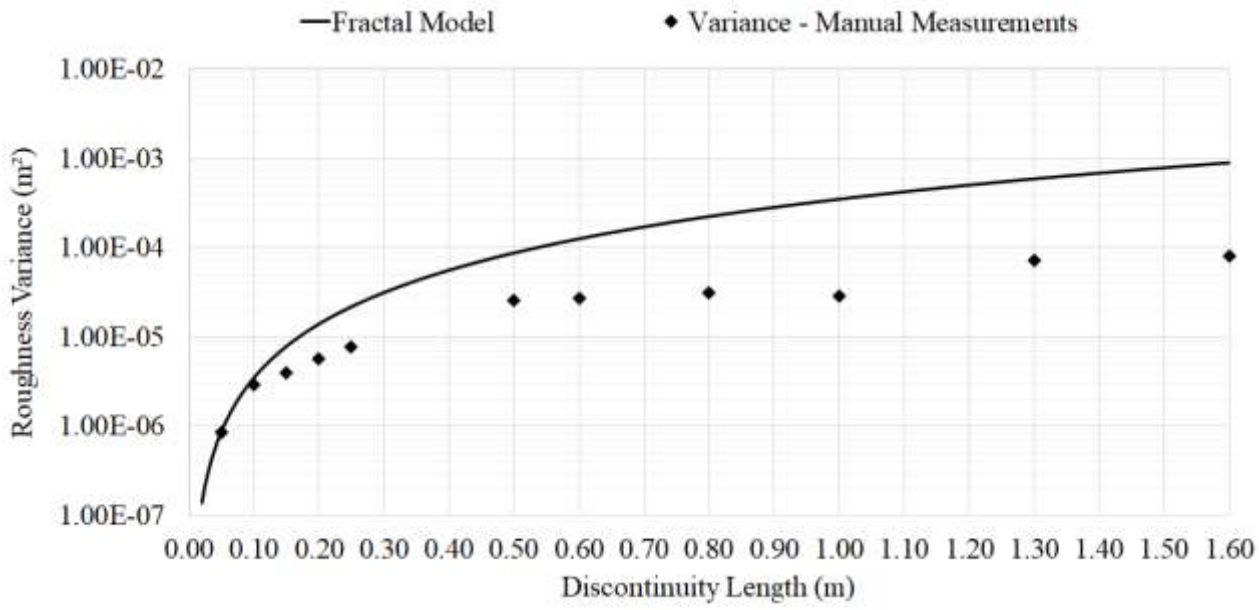

Figure 64 Absolute roughness variance vs discontinuity length - Hawkesbury Sandstone manual measurements

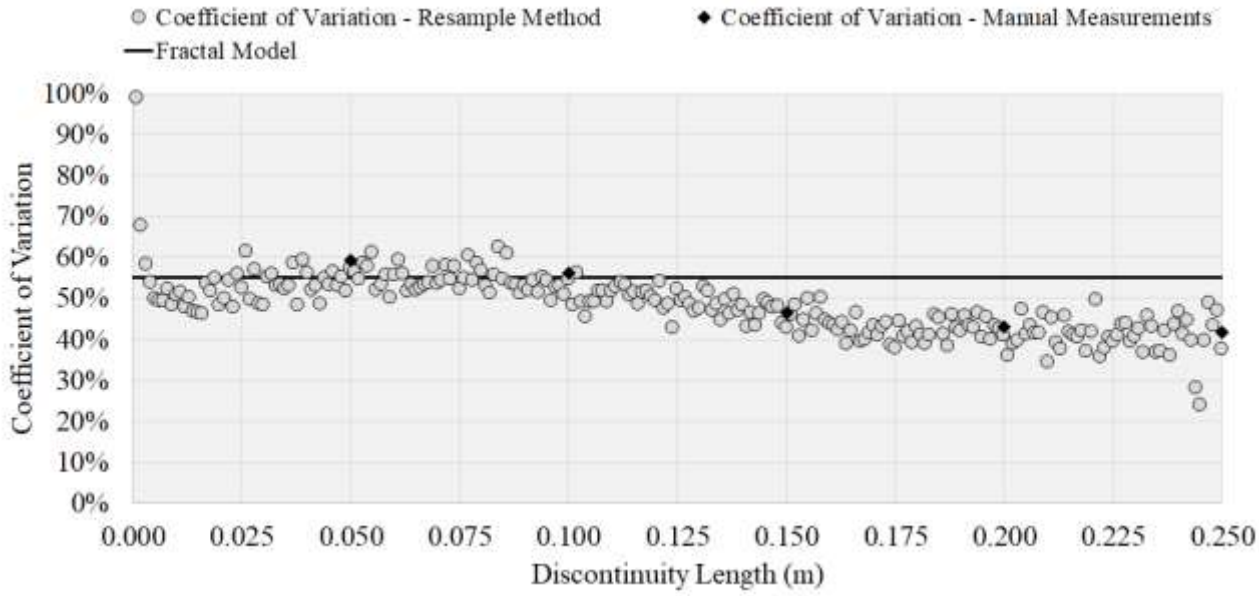

Figure 65 Coefficient of Variation vs discontinuity length - Hawkesbury Sandstone

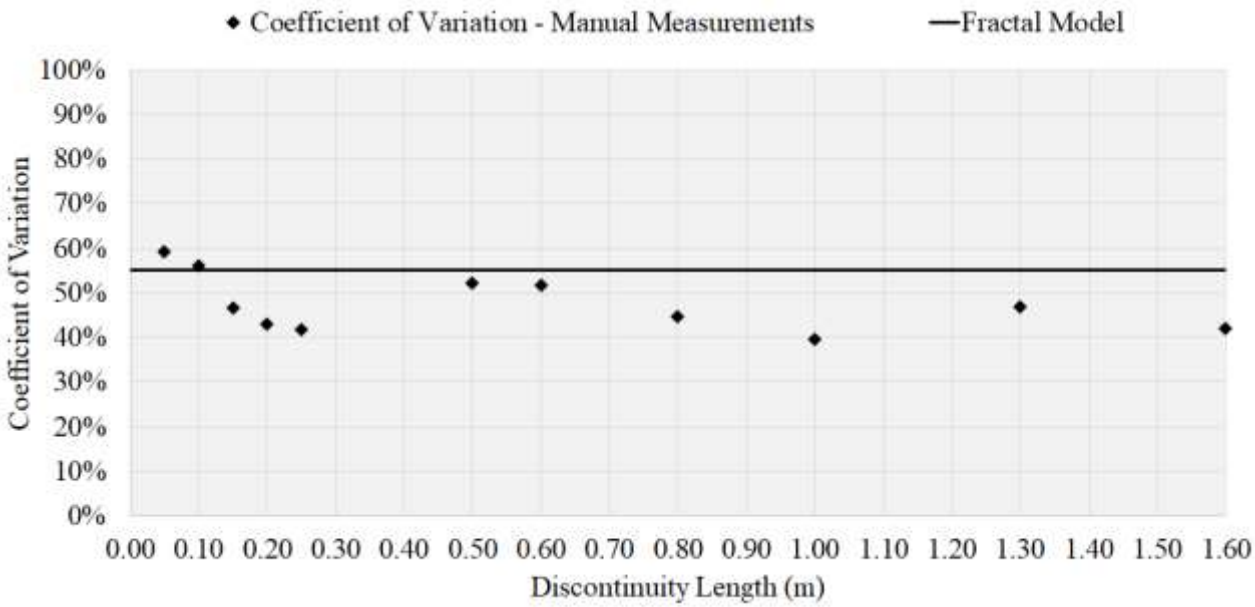

Figure 66 Coefficient of Variation vs discontinuity length - Hawkesbury Sandstone manual measurements

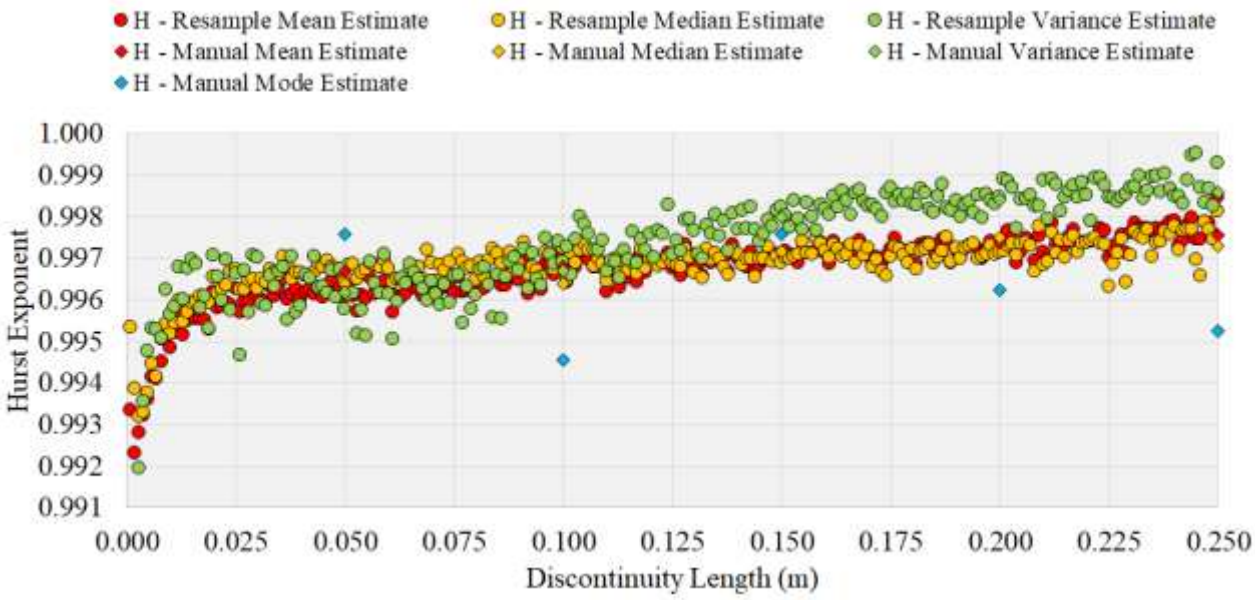

Figure 67 Hurst exponent vs discontinuity length - Hawkesbury Sandstone

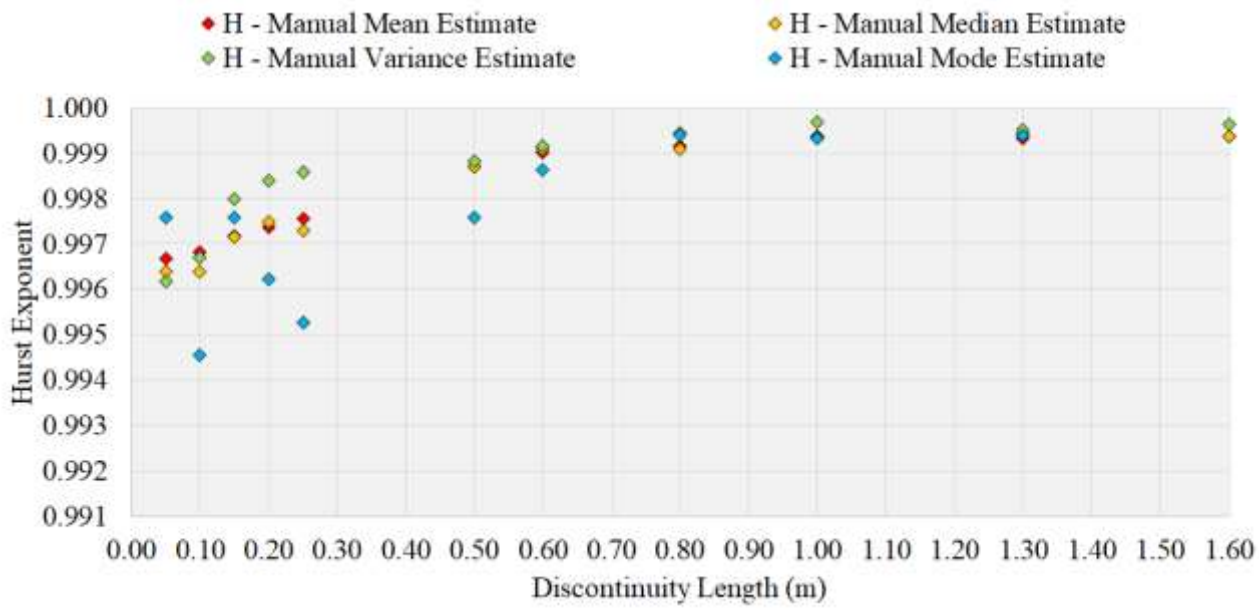

Figure 68 Hurst exponent vs discontinuity length - Hawkesbury Sandstone manual measurements

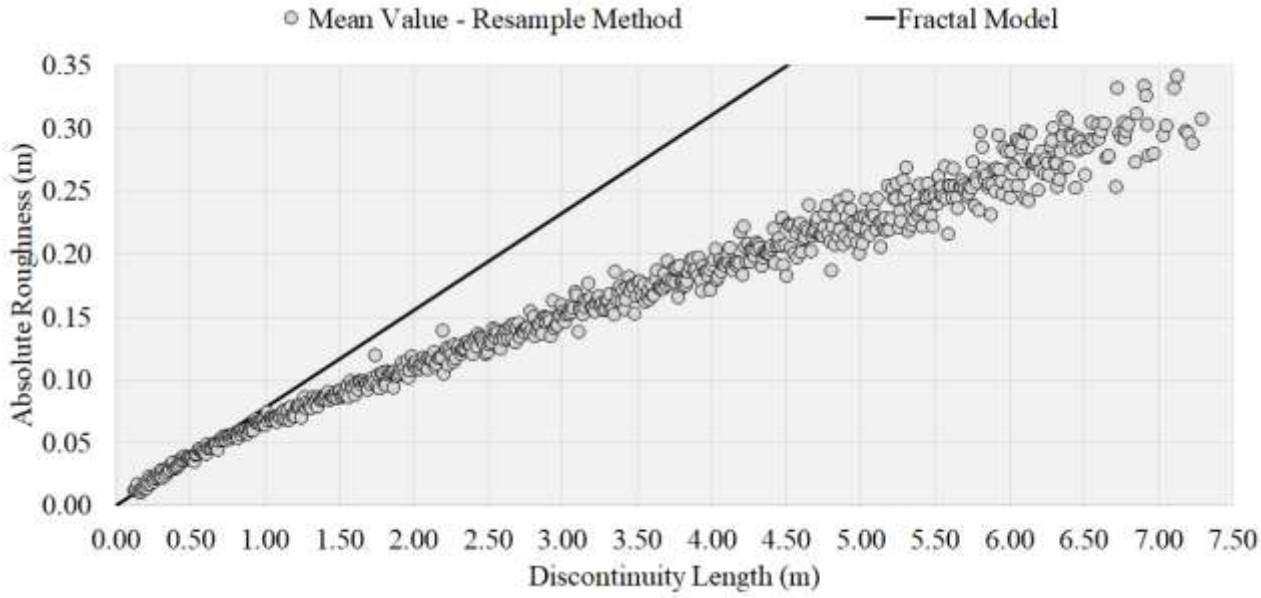

Figure 69 Absolute roughness vs discontinuity length - laser scan mean values

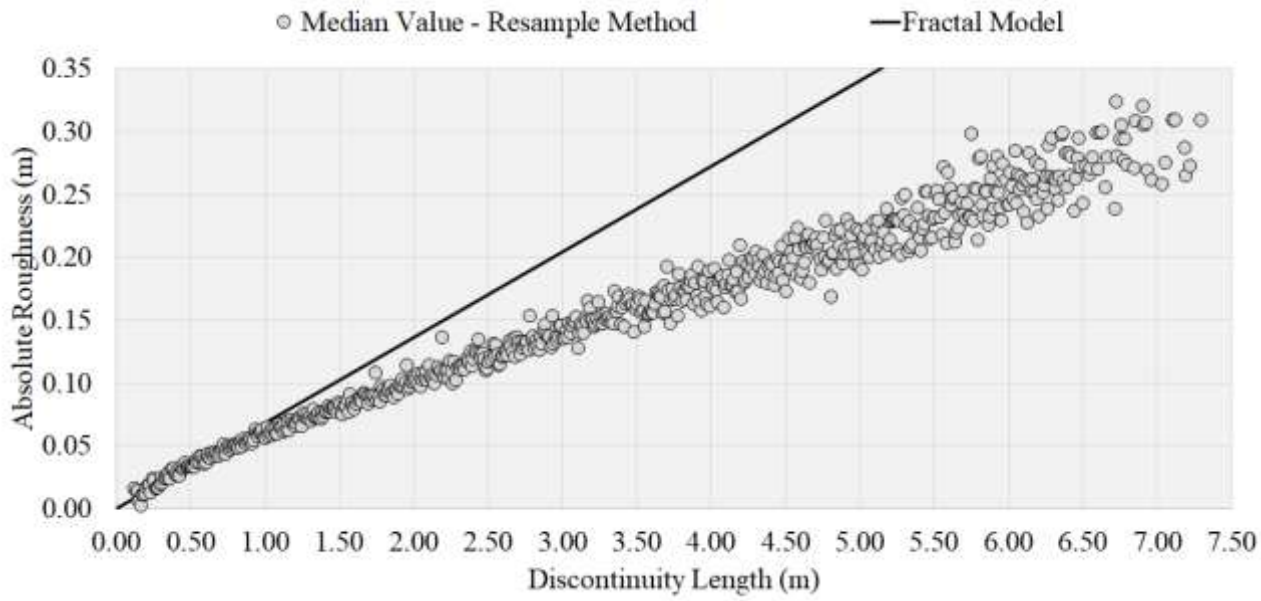

Figure 70 Absolute roughness vs discontinuity length - laser scan median values

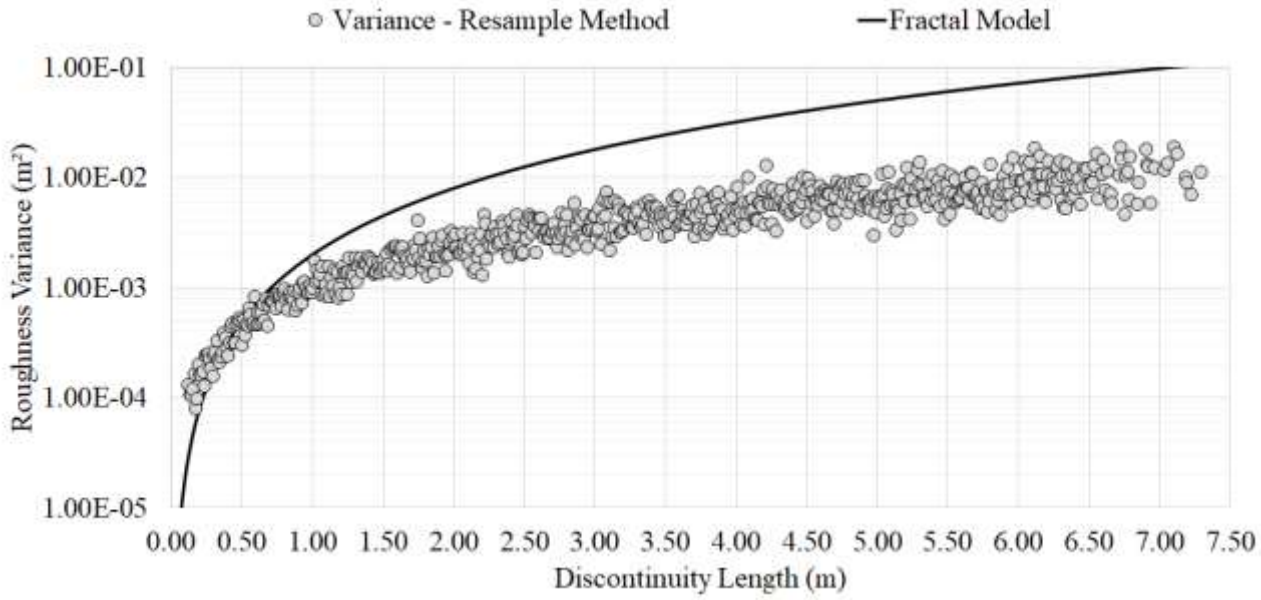

Figure 71 Absolute roughness variance vs discontinuity length - laser scan

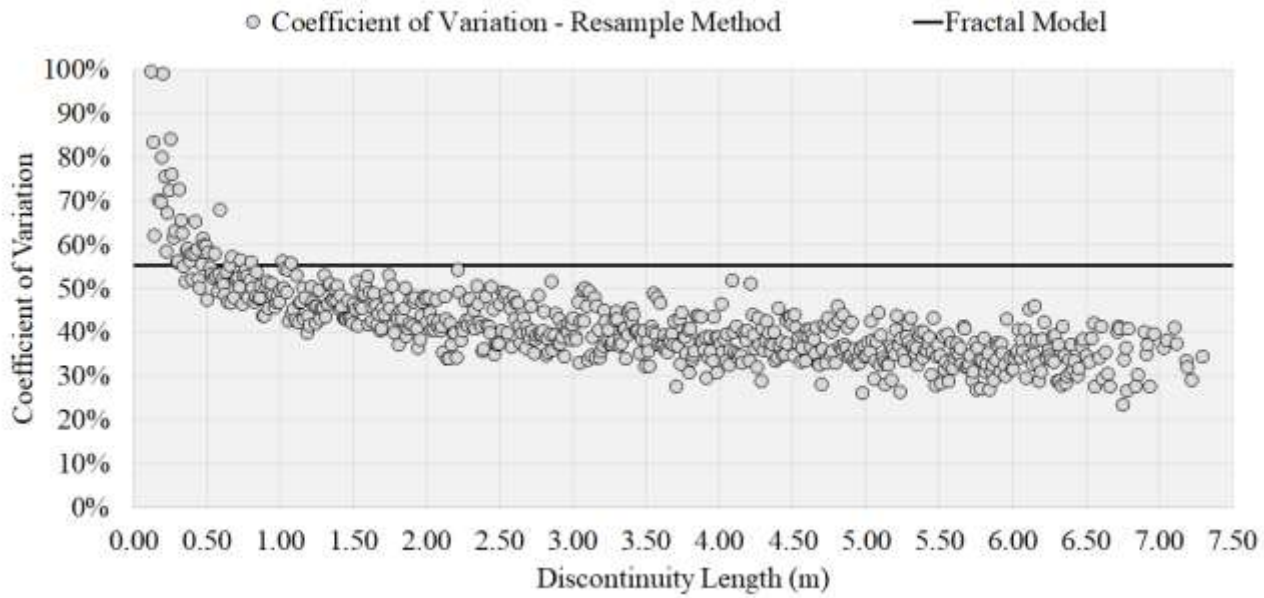

Figure 72 Coefficient of Variation vs discontinuity length - laser scan

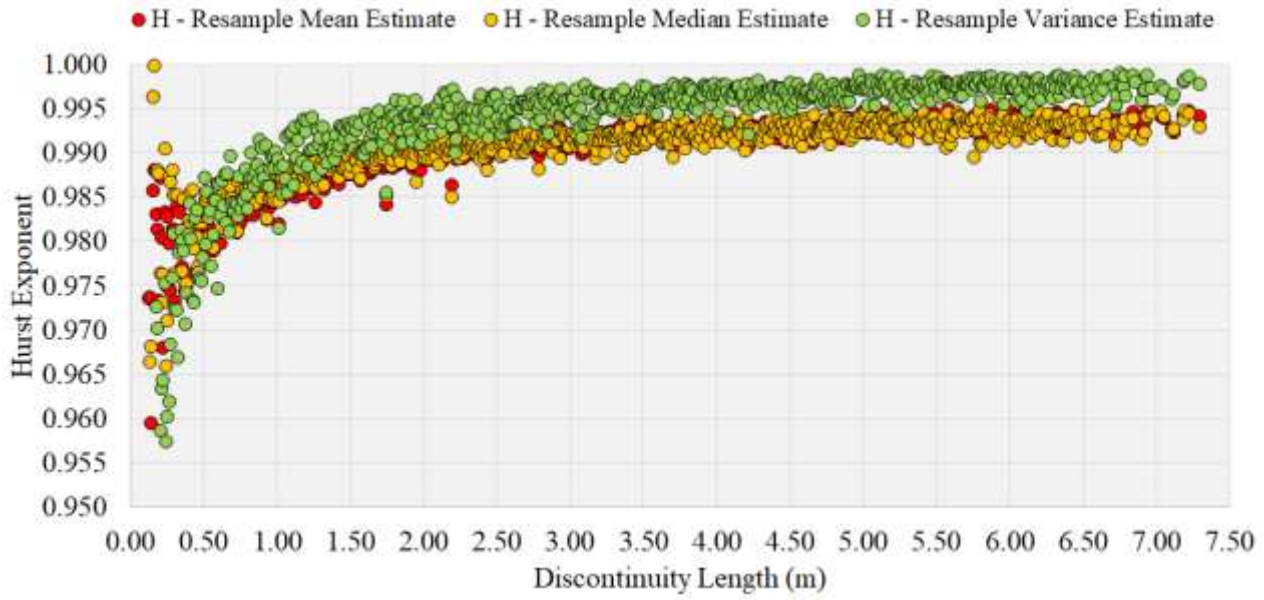

Figure 73 Hurst exponent vs discontinuity length - laser scan

Based on the above figures it is evident that a purely fractal self-affine approach is not an appropriate model to describe discontinuity roughness. It is interesting to note that at relatively small scales the fractal behaviour matches the field measurements in all statistical aspects, for example near 0.10m for the sandstone joint and near 0.50m for the laser scanned joint. It was also observed that $\widehat{H}$ was scale dependant, with the mean and median estimates remaining consistent to one another, while the

variance estimate produces larger values for $\widehat{H}$. One may try to conclude from these findings that an alternative description is that the fractal characteristics; that is, H is scale dependant as noted by Turk, Greig, Dearman & Amin (1987). This purely fractal interpretation was also discredited due to the observed reduction in the Coefficient of Variation with increasing scale. By considering Equation 132, even if the true value of H does change as a function of scale, the coefficient of variation is predicted to remain constant under the assumption a fractal description is still applicable. The change associated with the Coefficient of Variation suggests that as discontinuities increase in length there is some associated homogenisation that is; the PDF associated with R_{abs} is also scale dependant.

4.1.6 Relationships to JRC_n

Although a purely fractal description is not a viable model for discontinuity roughness, the roughness measurements from this approach do match remarkably well with Bandis' Scaling Law. This consistency is obtained by converting the scale dependant values of $\widehat{H}$ to values of JRC using Equation 133. Comparisons between the scale dependant JRC and Bandis' Scaling Law (from Table 1) are shown in Figure 74 through Figure 76.

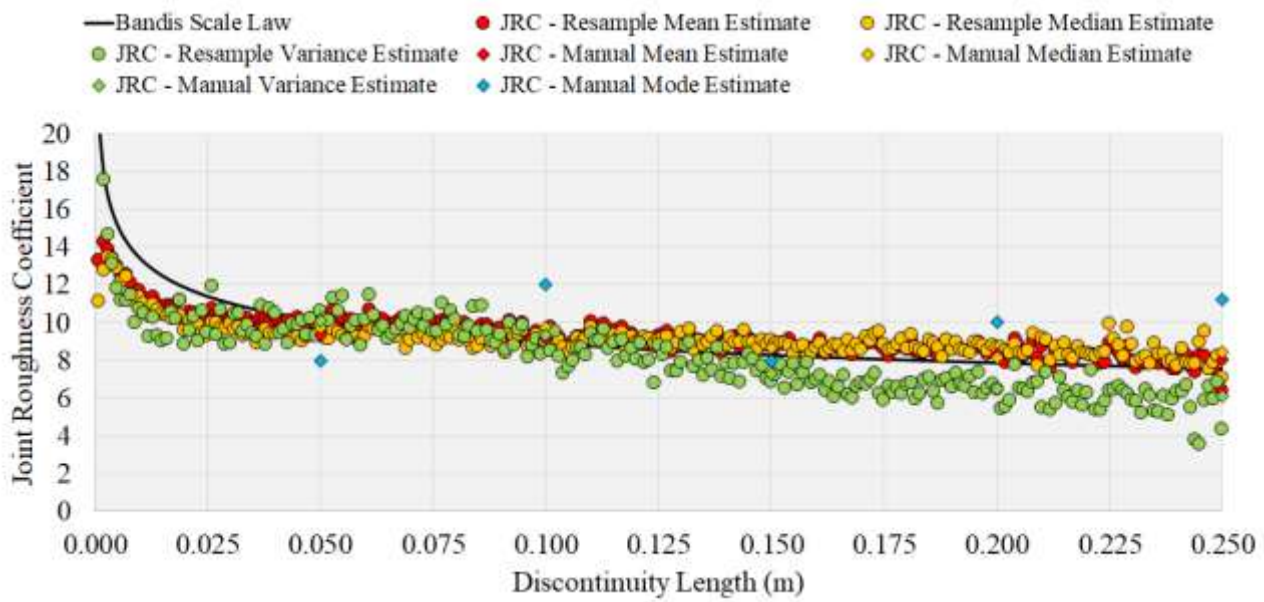

Figure 74 Joint Roughness Coefficient vs discontinuity length - Hawkesbury Sandstone $JRC_0 = 8.9$, $L_0 = 0.10$m

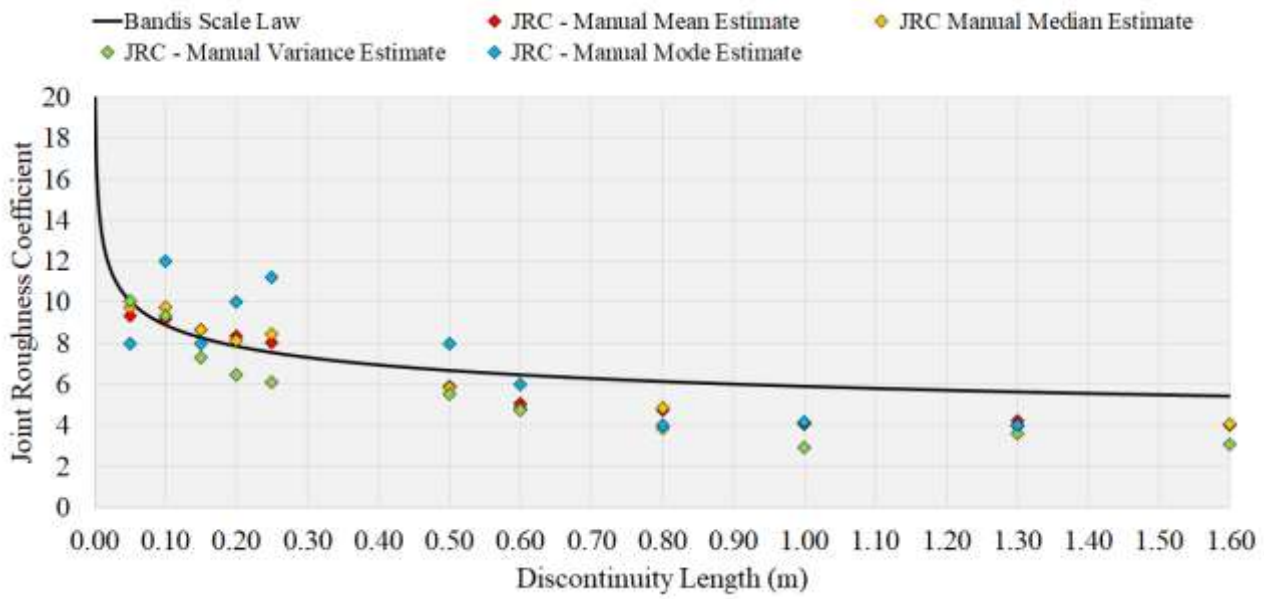

Figure 75 Joint Roughness Coefficient vs discontinuity length - Hawkesbury Sandstone manual measurements only $JRC_0 = 8.9$, $L_0 = 0.10$m

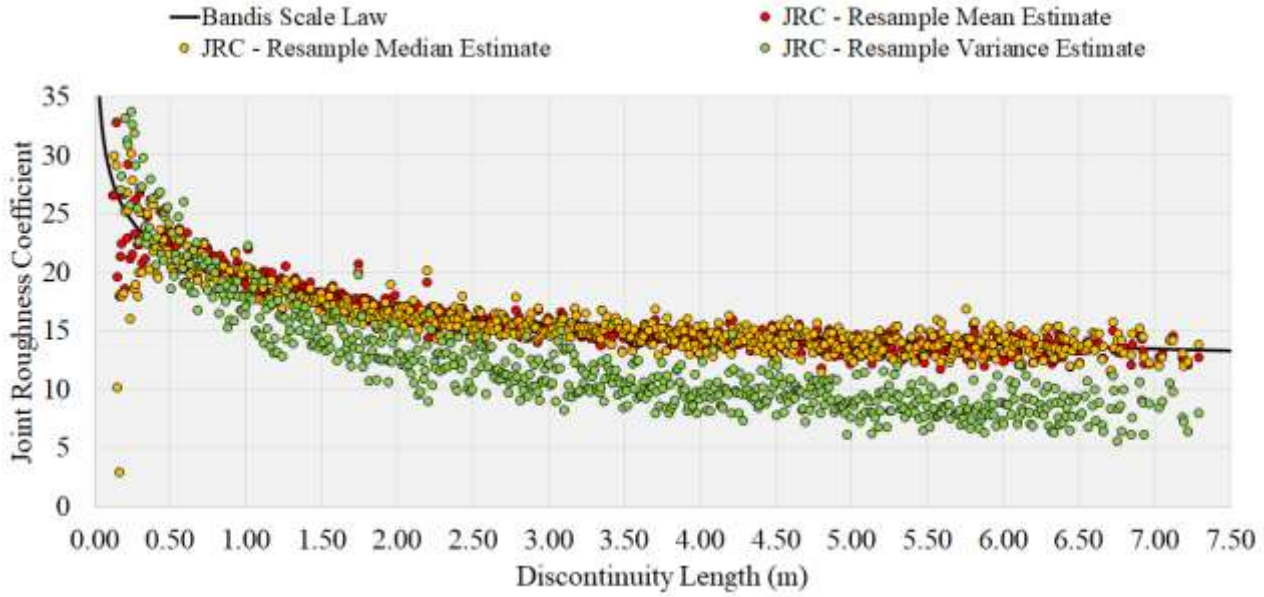

Figure 76 Joint Roughness Coefficient vs discontinuity length - laser scan $JRC_0 = 20.0$, $L_0 = 0.75$m

Note that in Figure 76 L_0 was chosen such that it corresponds to a $\mathrm{JRC}_0 = 20.0$. Note that Equation 133 and Bandis' scale equation produces values of JRC in excess of 20. By consideration of Figure 74 through Figure 76 it is apparent that by using Equation 116 or Equation 122 in conjunction with Equation 133 it is possible to closely replicate Bandis' Scaling Law. These findings suggest that even

though discontinuities are not completely described by a fractal model, scale dependant estimates of H using the methods derived in this Section are both useful and accurate in describing roughness characteristics at increased scales.

4.2 Cross Joint Spacing

So far in this Thesis, the main body of work has dealt with intact rock behaviour, while toppling failure is ultimately controlled by structure. In order to understand the POF associated with toppling, there needs to be some appreciation for the PDF associated with cross joint spacing. Recall that the FOS equation for Case 3 Toppling is given by:

$$FOS = \frac{t/h}{\tan\theta} = \frac{t}{h\ \tan\theta} \qquad \text{Equation 136}$$

where t is the bed thickness (m), h is the cross joint spacing (m) and θ is the bedding dip (˚). Two different approaches can be used to estimate a plausible UDF for joint spacing:

Physical measurements - While this method would be the most 'pure' estimation technique to derive a PDF or UDF for joint spacing estimation there are some restrictions. Firstly, the joint spacing data that was available during the duration of this Thesis was not in a usable form, as it did not consider joint spacing as a function of bed thickness. Secondly, the evolution of jointing is a complex phenomenon and is not an intrinsic 'material parameter'. As joints are formed as a result of many interacting and compounding factors, statistical analysis considering physical measurements will likely require 'site specific constants' to produce consistent fits across multiple lithology sources. While these constants are not an issue for a typical practical application, they are problematic when attempting to describe a general stability problem considering cross joint spacing. For example, a likely site specific constant would arise from some interaction between the acting field stress and rock tensile or compressive strength. While this contribution would be measureable (as in it appears as a constant), the physical meaning of this constant is lost in the analysis.

Mathematical Modelling - This approach attempts to derive a plausible PDF or UDF for joint spacing, based on some mathematical model that describes the joint formation process. This approach does lend itself to rigorous analysis, as any model component can be arbitrarily specified and varied. Site specific constants are not apparent as their relationships to measurable components is always considered. The limitation of mathematical modelling is that only the physical processes described

by the model can be considered, and the results must be validated against physical measurements to confirm their accuracy.

The methodology used in this section to estimate the UDF of joint spacing was chosen as a mathematical model, building on the theory presented by Hobbs (1967), considering how stresses are generated about a single fracture or joint within a given bed of rock (in two dimensions assuming a 1m slice). Hobbs' theory is presented in the following section:

4.2.1 Hobb's theory for cross joint generation

Given a bed of thickness d (m), with associated bed Young's Modulus E_B (Pa) and a globally applied strain of ε, the tensile load P (N) a distance x perpendicular to a vertical fracture is given by:

$$P(x) = E_B \cdot d \cdot \varepsilon(1 + A\sinh(Cx) - B\cosh(Cx)) \qquad \text{Equation 137}$$

where A, B and C are constants. When the boundary conditions $P(0) = 0$ and $\lim_{x\to\infty} P(x) \to E \cdot d \cdot \varepsilon$ are applied along with the assumption of zero slip occurs on adjacent bed contacts:

$$P(x) = E_B \cdot d \cdot \varepsilon\left(1 + \sinh\left(\frac{2x}{d}\sqrt{\frac{G_N}{E_B}}\right) - \cosh\left(\frac{2x}{d}\sqrt{\frac{G_N}{E_B}}\right)\right) \qquad \text{Equation 138}$$

where G_N is the neighbouring bed's Shear Modulus (Pa). If a secondary fracture exists a distance of l from the original fracture, the boundary conditions $P(0) = 0$ and $P(l) = 0$ can be applied to Equation 137 with the same assumption of zero slip on bed contacts to produce the following relationship:

$$P(x) = E_B \cdot d \cdot \varepsilon\left(1 - \frac{\cosh\left(\frac{2}{d}\sqrt{\frac{G_N}{E_B}}\left(\frac{l}{2} - x\right)\right)}{\cosh\left(\frac{l}{d}\sqrt{\frac{G_N}{E_B}}\right)}\right) \qquad \text{Equation 139}$$

When Equation 138 and Equation 139 are converted to stresses by dividing by the cross sectional area (d) and using the following relationship:

$$\sigma = E \cdot \varepsilon \qquad \text{Equation 140}$$

$$\sigma(x) = \sigma_0 \left(1 + \sinh\left(\frac{2x}{d} \sqrt{\frac{G_N}{E_B}} \right) - \cosh\left(\frac{2x}{d} \sqrt{\frac{G_N}{E_B}} \right) \right) \qquad \text{Equation 141}$$

$$\sigma(x) = \sigma_0 \left(1 - \frac{\cosh\left(\frac{2}{d} \sqrt{\frac{G_N}{E_B}} \left(\frac{l}{2} - x \right) \right)}{\cosh\left(\frac{l}{d} \sqrt{\frac{G_N}{E_B}} \right)} \right) \qquad \text{Equation 142}$$

where σ_0 is the equivalently acting far field tensile stress (Pa). Another simplification that can be made is to consider that adjacent beds are composed of similar rock, for example, a sandstone bed sandwiched between two similar sandstone beds. If this simplification is applied, the following relationships are produced:

$$\sigma(x) = \sigma_0 \left(1 + \sinh\left(\frac{2x}{d\sqrt{2(1+v)}} \right) - \cosh\left(\frac{2x}{d\sqrt{2(1+v)}} \right) \right) \qquad \text{Equation 143}$$

$$\sigma(x) = \sigma_0 \left(1 - \frac{\cosh\left(\frac{2}{d\sqrt{2(1+v)}} \left(\frac{l}{2} - x \right) \right)}{\cosh\left(\frac{l}{d\sqrt{2(1+v)}} \right)} \right) \qquad \text{Equation 144}$$

Equation 141 and Equation 142 produce two competing stress fields, which will dictate the growth of cross jointing occurs in a single bed. To elaborate, consider an initially intact and unbounded 1m section (in the third direction) of a bedded material with thickness d. Some constant external tensile stress σ_0 is applied due to some combination of tectonic stresses, gravitational loading or external loads. At some location, a primary fracture would form as a result of the local stresses exceeding the local tensile strength. This primary fracture is then defined with a local coordinate system such that it is located at $x = 0$. Concurrent to the formation of the primary fracture, a second fracture may also

form. The location of this fracture is then defined relative to the primary fracture and is a distance l away. Additional fractures may then form from two different processes:

Fracture Saturation - The tensile stresses between two adjacent joints (Equation 142) are sufficient to exceed local tensile strength and a new joint forms. This process then continues recursively until the joints reach a saturated state where no new joints are able to form; and

Fracture Interspersion - The tensile stresses in a region not bound by two joints exceeds the local tensile strength (Equation 141) and a new joint forms. The region between these two joints then begins the Fracture Saturation process. This process continues recursively until a geological boundary or no locally weak zones are encountered.

In order to estimate where cross joints will form in a given bed, it is possible to relate the stress field equations to the material's UTS to determine where a fracture will form as a function of the distance from an initially formed fracture. Using the hyperbolic trigonometric identities, Equation 141 can be expressed in terms of exponentials to produce:

$$\sigma(x) = \sigma_0 \left(1 - e^{-\frac{x}{\delta}}\right) \qquad \text{Equation 145}$$

where:

$$\delta = \frac{d}{2}\sqrt{\frac{E}{G}} \qquad \text{Equation 146}$$

For similarly bedded materials, G can be related to the Young's Modulus E and Poisson's Ratio v such that:

$$G = \frac{E}{2(1+v)} \qquad \text{Equation 147}$$

This gives the following relationship for the local tensile stress as a function of x:

$$\sigma(x) = \sigma_0 \left(1 - e^{-\frac{2x}{d\sqrt{2(1+v)}}} \right)$$ Equation 148

a new fracture will form when the local stresses exceed the material's tensile strength σ_t. Solving for x:

$$x = \frac{-d\sqrt{2(1+v)}}{2} \ln\left(1 - \frac{\sigma_t}{\sigma_0}\right)$$ Equation 149

Equation 149 produces a deterministic fracture spacing estimate for a homogenous material, given some combination of applied stresses and material parameters. Of interest is that Equation 149 produces undefined fracture spacing over the region $\sigma_t \geq \sigma_0$ with the deterministic joint spacing tending to infinity as σ_0 approaches σ_t. This infinite and undefined joint spacing does become mathematically problematic when considering σ_t as a random variable. To demonstrate this, consider the CDF associated with joint spacing for a problem described by $\sigma_0 = 5\ MPa$, $\bar{\mu}_{\sigma_t} = 5\ MPa$ with the UTS being described by a Rayleigh Distribution, $d = 2.5m$ and $v = 0.3$. The calculated CDF for both UTS and cross joint spacing is summarised in Table 57.

Table 57 Equivalent Cumulative Distribution Function for cross joint spacing

Percentile	Tensile Strength	Associated Cross Joint Spacing
10%	1.83 MPa	0.91 m
20%	2.67 MPa	1.52 m
30%	3.37 MPa	2.23 m
40%	4.03 MPa	3.27 m
50%	4.70 MPa	5.59 m
54%	4.99 MPa	12.53 m
54%	5.00 MPa	Undefined
75%	6.64 MPa	Undefined
95%	9.77 MPa	Undefined
100%	19.14 MPa	Undefined

Using Table 57, the interpretation is that 46% percent of all cross joints will be separated by an infinite distance, which is not physically possible. One may then try and conclude that the CDF and EDF should be calculated up until the point where $\sigma_0 = \sigma_t$ to produce a viable range, however this becomes severely limited when σ_0 is a 'realistic' value (e.g., less than 1 MPa).

4.2.2 Simulating cross joint generation processes

In order to estimate the cross joint spacing that has a more pronounced upper bound, material heterogeneity can be used to circumvent the issue of an undefined upper bound. By simulating a rock bed with a randomly distributed strength profile, at some point along the bed, the local UTS will be exceeded by chance at some location, resulting in a finite upper bound. A second benefit of this heterogeneous approach is that only Fracture Interspersion process using a bed with an initial randomly distributed tensile strength needs to be considered. The justification of this is elaborated below:

Start by randomly generating a bed of rock containing a heterogeneous distribution of UTS, in accordance to the UDF of tensile strength. The heterogeneity is discretised based on the scale that UTS is quantified (0.054m). Assume a primary crack exists at $x = 0$. Calculate the stress field as a function of distance, $\sigma(x)$. Determine the first instance (i.e., checking from $x = 0$ in the positive direction) where the local tensile strength is first exceeded. Form a crack at this new location. This process is shown in Figure 77.

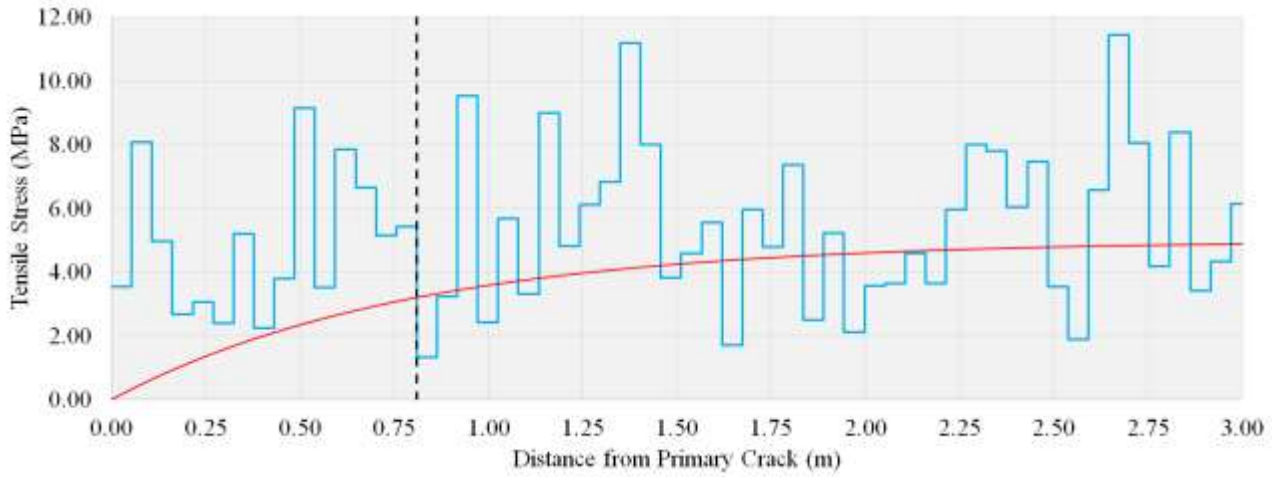

Figure 77 Initial crack formation location. Blue line represents local tensile strength

The local tensile stresses are then updated based on this new fracture. Equation 142 is used to describe the tensile stresses between the origin and the first crack and Equation 141 is then used to calculate

the stress field beyond the newly formed fracture. Note that the stress field between the origin and first fracture is always less than or equal to the original stress field. By consideration of this fact and how fracture location was checked, no new fractures are able to form between adjacent fractures, as the updated stress field (i.e., changing from using Equation 141 to Equation 142) will never exceed the initially higher stress and tensile strength at any point. The next fracture location is then determined. This process is shown in Figure 78.

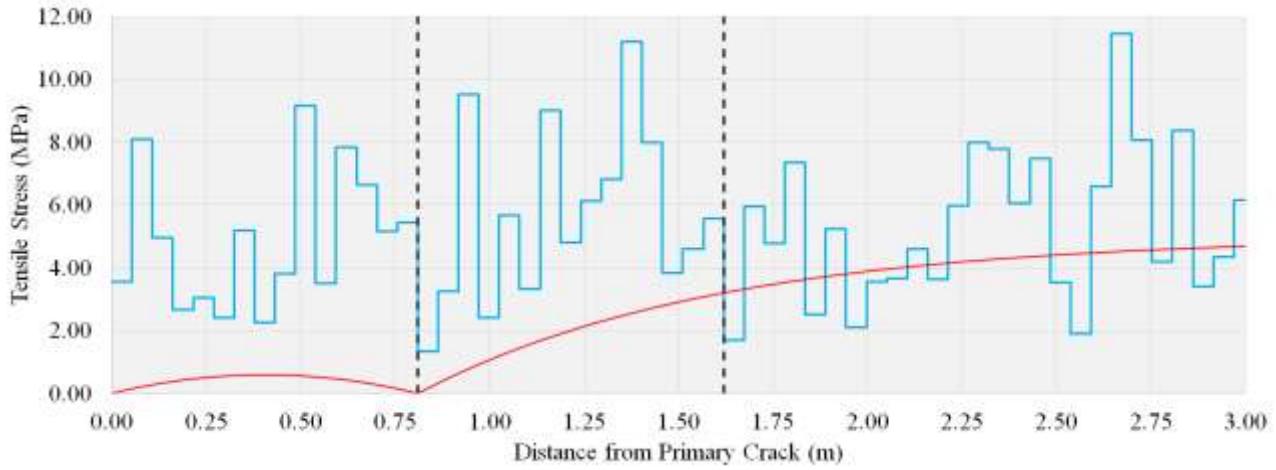

Figure 78 Stress field after the first crack forms. Blue line shows local tensile strength

This is then repeated from the new crack many times. This process is shown in Figure 79.

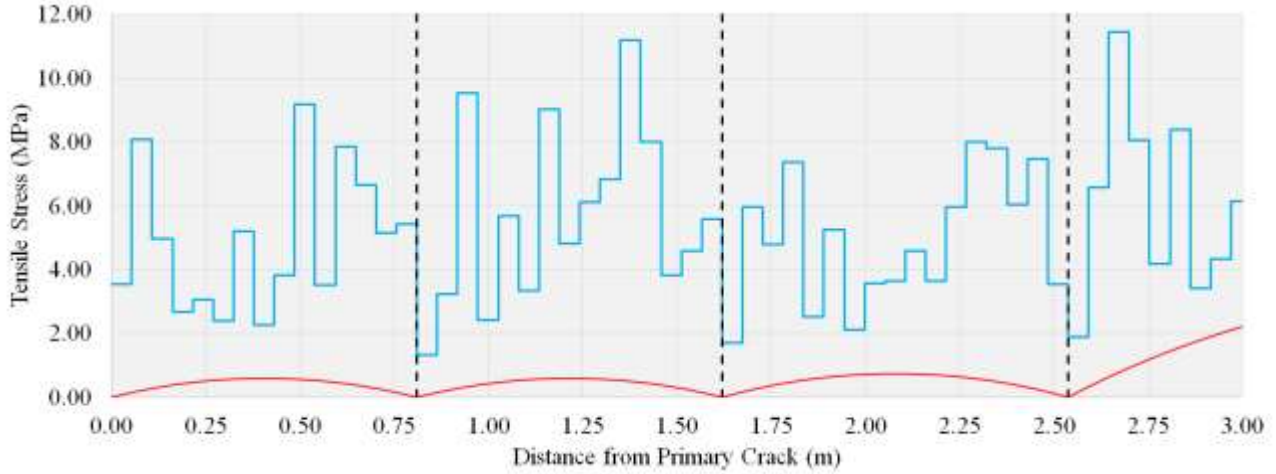

Figure 79 Updated stress field after additional cracks form. Blue line shows local tensile strength

The methodology presented ensures that the saturated fracture spacing is always achieved under the assumption that σ_0 is constant.

In order to help evaluate a general probabilistic model for joint spacing, a wide range of input combinations were assessed. The model inputs tested cover all combinations of:

- median UTS ranging from 2.5 MPa to 15.0 MPa (6 values);
- far field tensile stresses ranging from 1.0 MPa to 20 MPa (6 values);
- Poisson's Ratio ranging from 0.05 to 0.4 (5 values); and
- bed thicknesses ranging from 0.054m to 5.0m (8 values).

Each input combination (1440 total cases) were assessed to obtain an output of 2500 joint spacing measurements. To aid in producing a more continuous range of fracture spacing, while the tensile strength has a discrete distribution, the induced tensile stresses are evaluated 'continuously'. This continuous evaluation is done at 1mm increments along the length.

Limitations and Assumptions

Several assumptions have been made for the final analysis and also the methodology does pose some limitations:

Not all possible mechanisms for joint formation are assessed - The method and theory presented is as previously mentioned based on the mathematical derivation given by Hobbs, and relies on fractures being formed due to external tensile stresses. Other mechanisms such as fractures being formed due to shearing are not considered. Fractures that form parallel to some uniaxial compressive stress σ_C, are considered. In these instances, the far field tensile stress can be generated from Hooke's law to give:

$$\sigma_0 \approx -\nu\sigma_C \qquad \text{Equation 150}$$

Heterogeneity is one dimensional - The material parameter heterogeneity is modelled using a one dimensional variation. A more realistic approach would be to discretise the entire bed into a 0.054m x 0.054m x 1.0m random grid, which would then allow for another dimension of heterogeneity to be considered. If this were to be included, one would expect that the joint spacing might be smaller than the one dimensional simulation, as fractures may initiate at more than one location at some distance from an initially formed fracture. The problem with using this approach is that Hobb's theory only gives a one dimensional equation in terms of forces, which are convertible to an equivalent stress

acting over d. In order to evaluate the heterogeneity over the bed thickness, the tensile stress at each point within the bed would need to be quantified.

Only tensile strength is treated as a random variable - While it is possible to simulate all model components as random variables, only the UTS is treated as a random variable. This simplified approach was done to minimise the numerical simulation time and to produce a first pass estimate that can be compared to field measurements. Treating other variables as random (in particular G_N) can also bring into question the assumption of zero slip on contacts being true for all simulations.

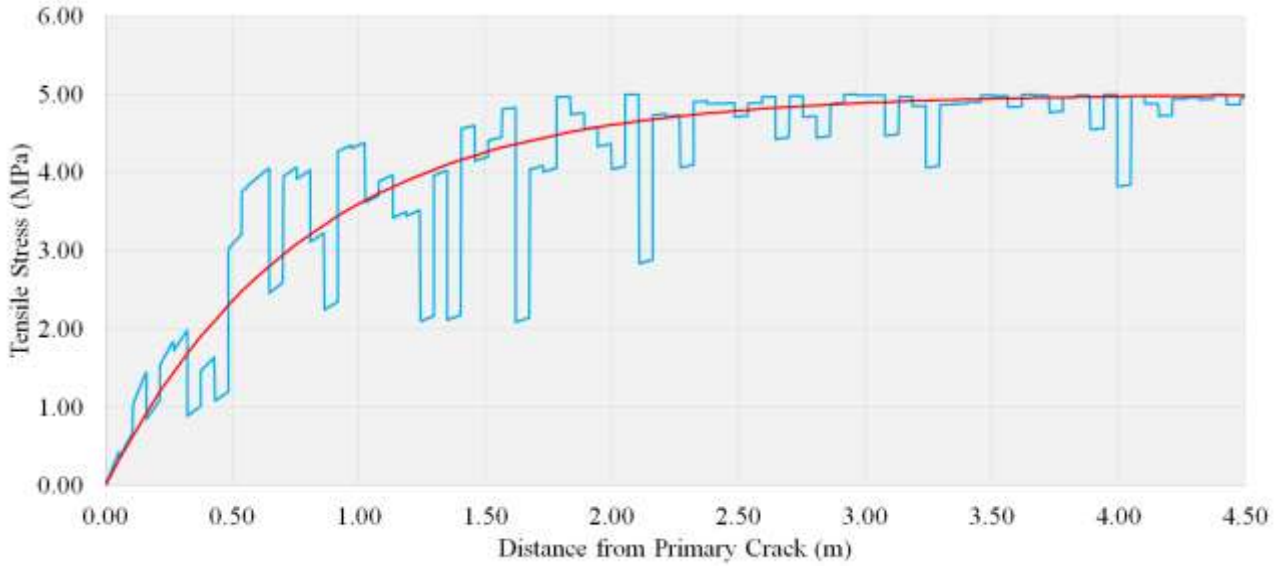

Figure 80 Example simulation of non-uniform stress field and mean stress field

4.2.3 Cross joint spacing results

Upon completing the simulation campaign, it was noted that there were considerable issues associated with the approach used. As a general conclusion, either simulations results were limited by stress field evolutions, discretisation resolution, or they produced reasonable results. Examples of these three types of simulation results are shown in Figure 81 through Figure 83.

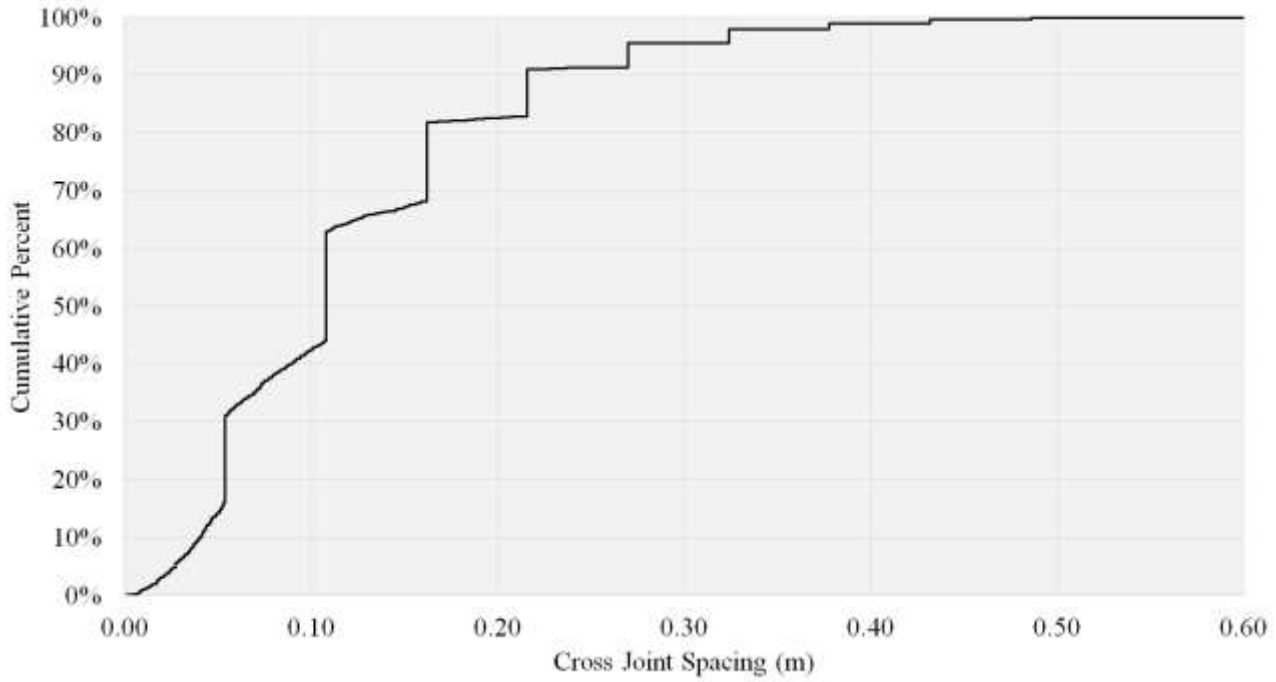

Figure 81 Example of simulation results limited by discretisation resolution

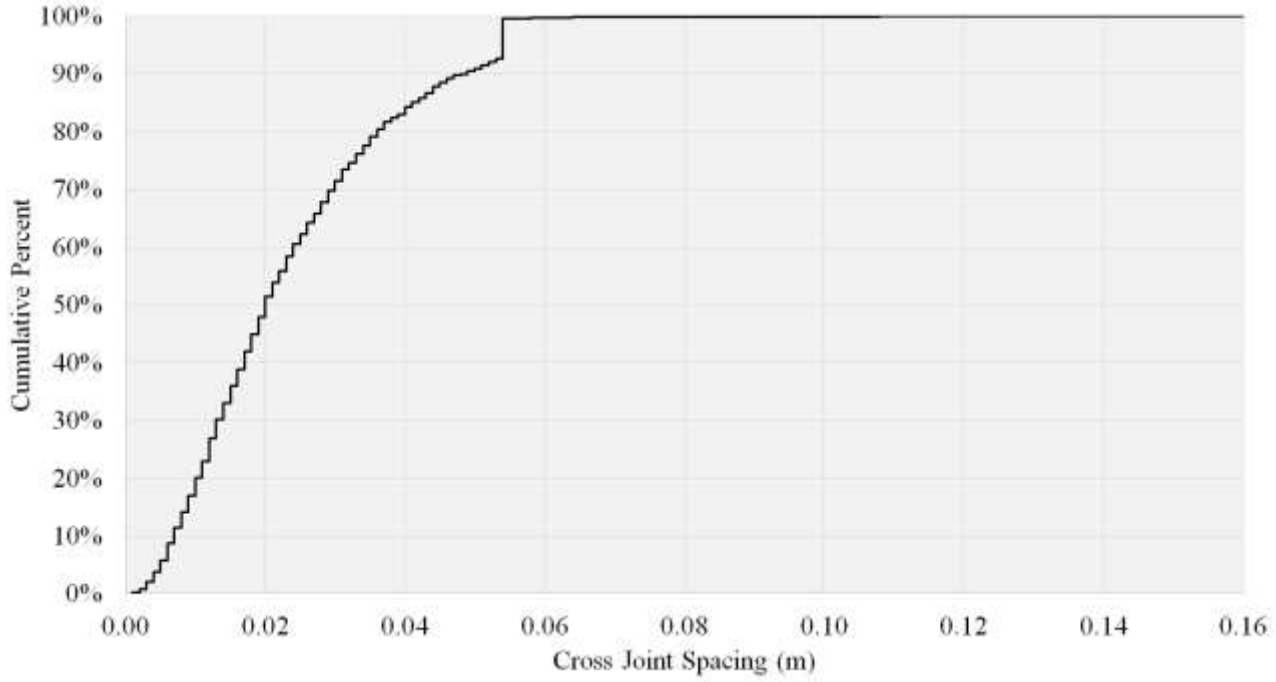

Figure 82 Example of simulation results limited by stress resolution

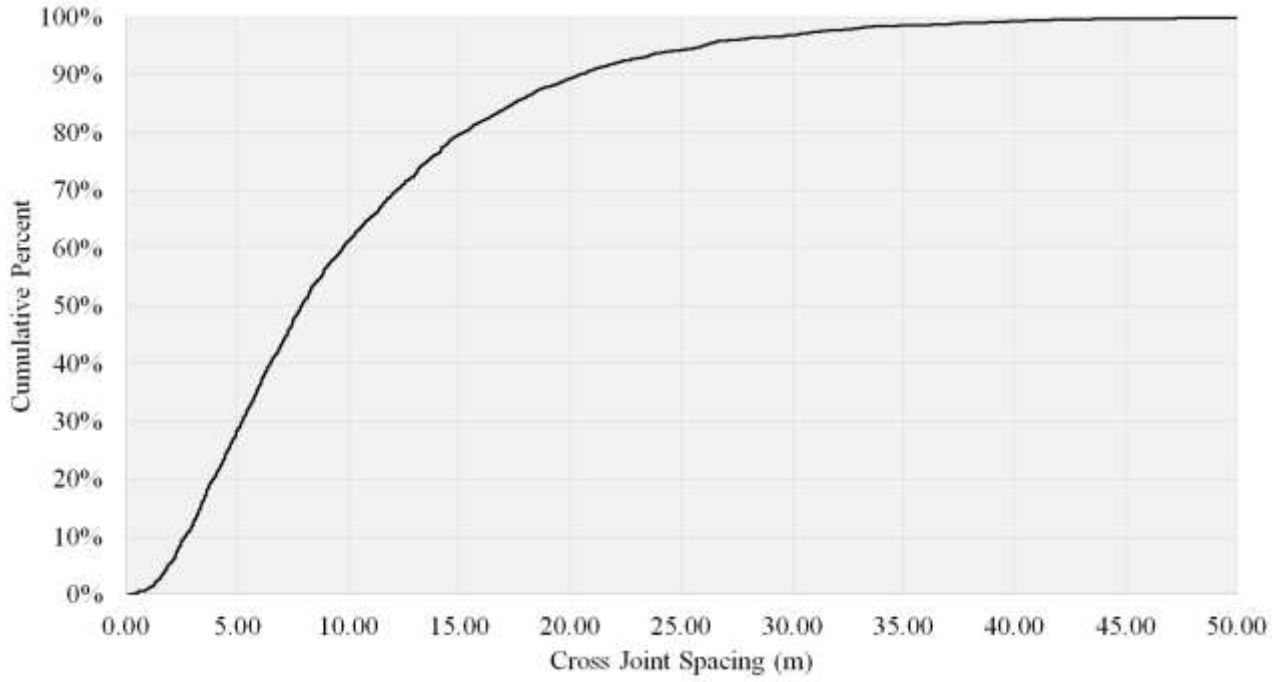

Figure 83 Example of good simulation results

While the actual simulated distributions do have the aforementioned limitations, there are some general insights that can be presented. The largest influences on the simulated cross joint spacing were associated with the bed thickness and the ratio of the applied tensile stress to the UTS. Comparisons showing the mean cross joint spacing and the associated variance as a function of these two inputs are shown in Figure 84 and Figure 85.

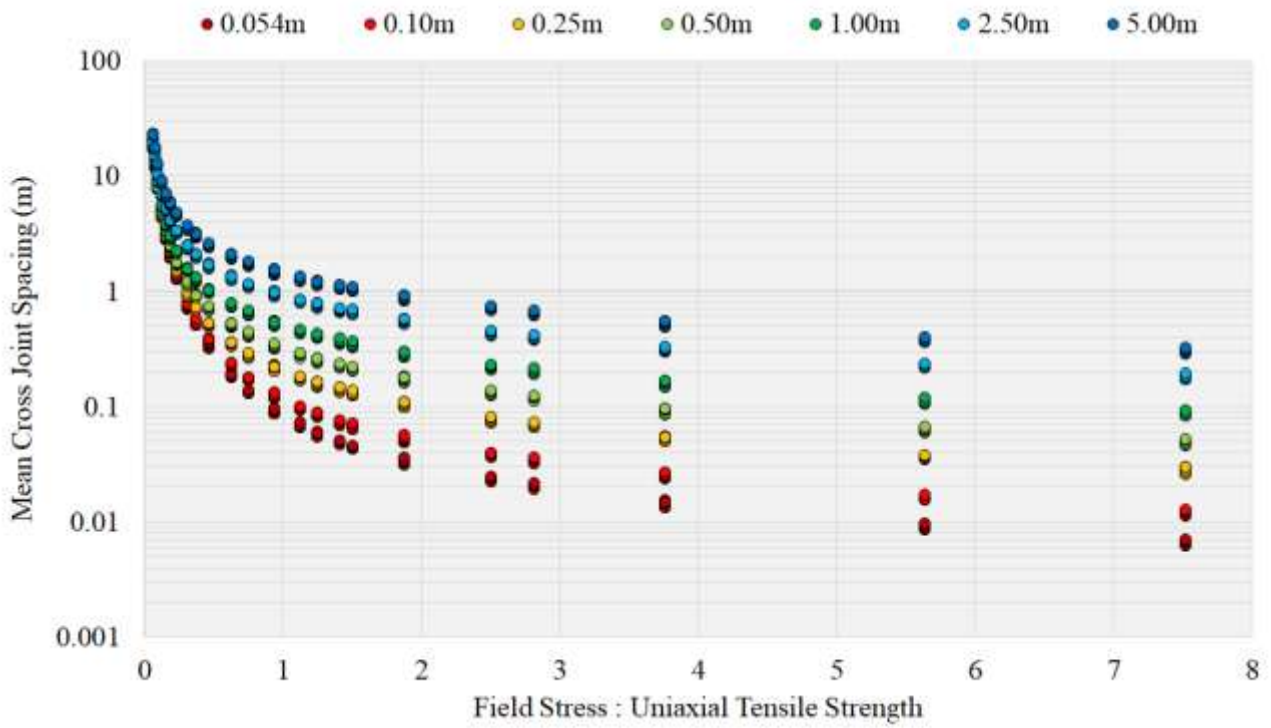

Figure 84 Mean cross joint spacing vs field stress ratio

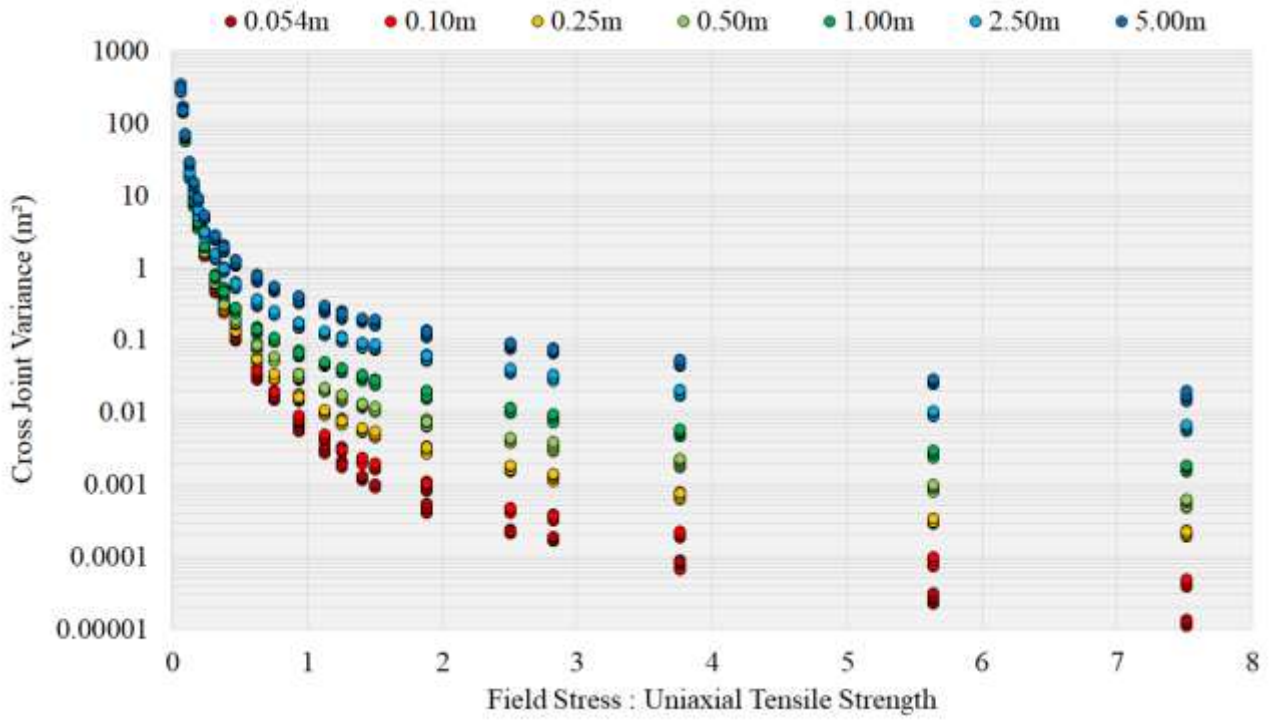

Figure 85 Cross joint spacing variance vs field stress ratio

By review of Figure 84 and Figure 85, it is apparent that:

- As the field stress ratio increases, the mean spacing decreases.
- As the field stress ratio increases the associated variance decreases.
- Thicker beds are associated with higher mean spacing and higher variances.
- Poisson's Ratio has a very small influence.

For clarification, the Poisson's ratio influence is noted to be small as that for each combination of bed thickness, UTS and applied tensile stress, all simulated Poisson's ratio values overlap or differ by a considerably small margin. Another feature that is apparent within the simulation results is the distribution of cross joint spacing at very low stress field ratios. In this region, Hobb's theory suggests an undefined cross joint spacing while the simulations produce a finite and exponential like distribution. An example of an exponential like simulation at low stress ratios is shown in Figure 86.

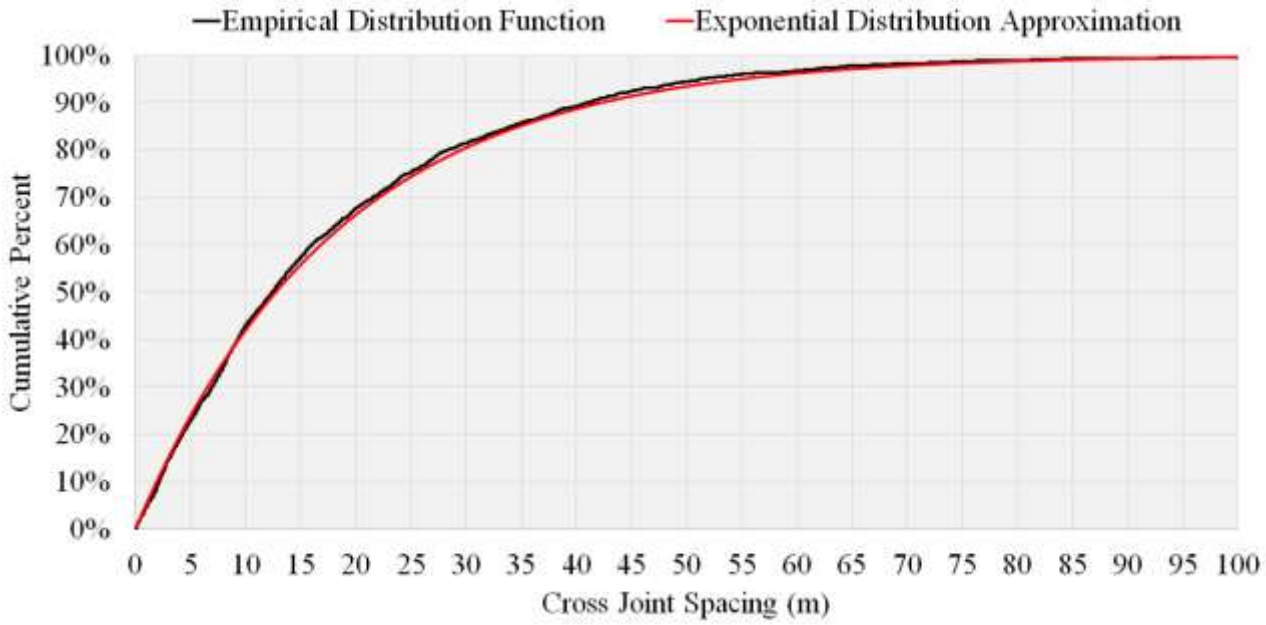

Figure 86 Example of Exponential fit

This exponential like distribution was not apparent at higher stress field ratios. This PDF behaviour does offer some deeper insights into a potential UDF for cross joint spacing. An appropriate PDF family to describe cross joint spacing needs to be able to produce exponential like and non-exponential like distributions. Two well-known PDF families, which have this behaviour are the Weibull and Gamma distributions. An example of the comparisons of a Gamma and Weibull distribution to simulated cross joint spacing data is shown in Figure 87.

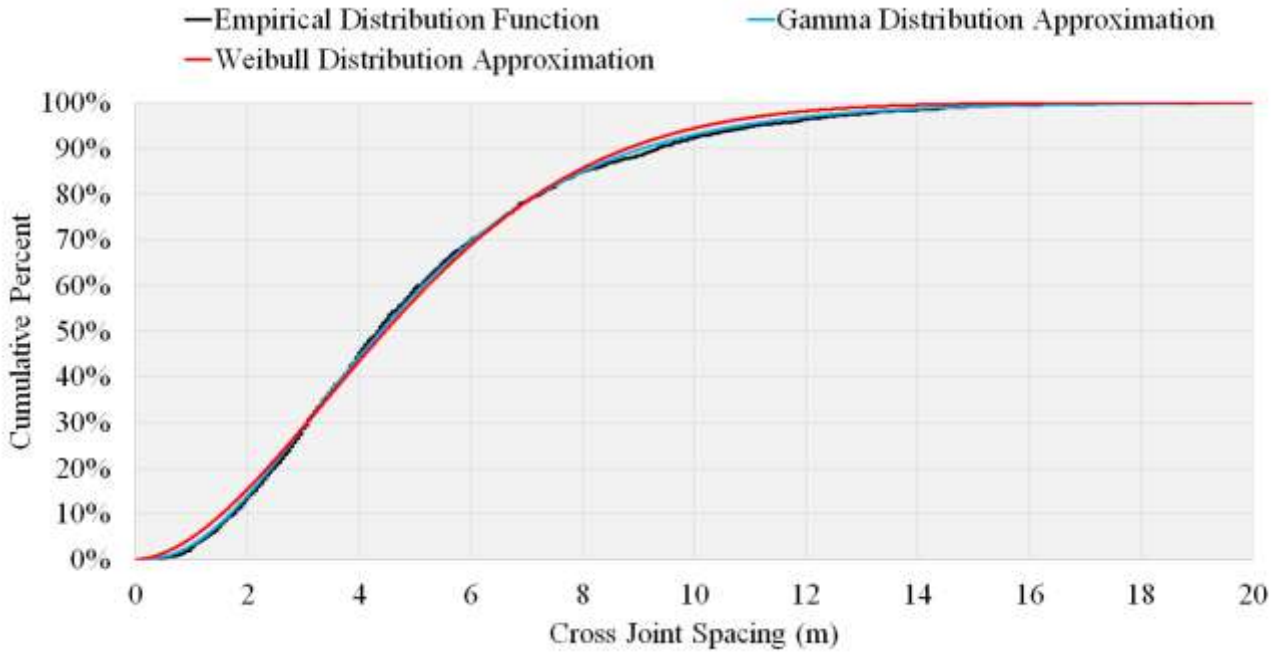

Figure 87 Example Gamma and Weibull Distribution fits

From completing KS testing using the associated Maximum Likelihood Estimates of each simulation, the Gamma distribution showed the best overall goodness of fit with 208 of the 1440 simulations being sufficiently described. The Weibull distribution showed less goodness of fit with 140 simulations being accepted. This low acceptance rate is attributed to the previously mentioned resolution limitations. The findings of this analysis indicate that the most appropriate PDF associated with cross joint spacing is a Gamma distribution.

While the results of this section were not ideal, they do offer some testable inferences. Firstly, for geological settings, which have experienced low stresses, the distribution associated with cross joint spacing should be well approximated by an exponential like gamma distribution, with a smaller average spacing being associated with thinner beds. As the applied stresses increase, the cross joint spacing should decrease and the spacing should tend to a more uniform spaced due to the reduction in associated variance. This close and uniform fracture spacing at high stresses is observed in practice, particularly evident in core disking (Lim & Martin, 2010). It is suspected that the relationship between spacing and stress in core disking is governed by the same general relationship between the acting field stress and UTS. Future research utilising physical joint spacing measurements will be able to shed more light into the formation and general applicability of a gamma distribution to describe the distribution of cross jointing.

5 Revisiting Factor of Safety and Probability of Failure

The contributions and new results presented in Chapter Two, Three and Four the relationship between FOS, POF and scale can be revisited. Recall the governing hypothesis from Chapter One:

If a geological system is sufficiently definable in terms of both variability and mechanical behaviour, a one to one relationship between Factor of Safety and Probability of Failure can be routinely calculated.

In terms of this governing hypothesis, the main findings in this Thesis has demonstrated that rock material parameter variability over scales would constitute 'sufficiently definable'.

Chapter 2 demonstrated that UDFs are a good approximation at the laboratory scale, and are suitably generalisable to any given rock problem. This result means that the input selections for each material parameter is consistent across different rock types and results in consistent equations.

Chapter 3 demonstrated is that at increased scales, the behaviour of material parameters varies systematically as a function of increasing scale. While the behaviours may be case specific, the variation is systematic and the underlying PDF family remains consistent.

Chapter 4 demonstrated that the most appropriate PDF associated with cross joint spacing is a Gamma distribution. The consistency of PDF, like with the main findings of Chapter 2 means consistent across different rock types and results in consistent equations.

Based on the previous findings in this Thesis, there are some shortcoming which do need to be highlighted:

UDF scale parameters typically have a viable range. While the distribution family for each UDF is universal, the scale parameters are often expressed in terms of some percentage range of the mean or median value. This initialised uncertainty means that a single relationship is unlikely to be determined due to these initial variations.

USFs and Homogenisation are case specific. The findings in Chapter Three demonstrate that the USF and rates of homogenisation differ between simulated samples at scale. This makes it likely impossible to solve for the relationship between FOS POF as a function of only laboratory scale material parameters, and the desired scale of interest. The UDF family remains relatively consistent over scales, meaning a routine calculation method can still be considered.

Problem geometry is completely deterministic. This is the most problematic component of calculating a relationship between FOS and POF. Variations between design and actual problem geometry is generally inevitable in mining and can vary considerably. While the geometry used is typically case specific, it is also therefore calculated on a case by case basis.

Geological features are deterministic. Major geological features (e.g., a discrete structure) need to be treated deterministically for a given problem. If the location of major structures or failure surfaces were allowed to vary, it would make it difficult to determine an appropriate POF as the FOS itself can vary for a particular problem configuration. These deterministic geological features include the angle of failure, discontinuity persistence and failure plane location.

Density can be treated as essentially deterministic. The general scale dependant behaviour of dry density was determined in closed form and is given by Equation 107 and Equation 108, the variance associated with density is very small, especially when considering larger scales. While the inclusion of a variable material density is simple to implement in Monte Carlo simulations, including this consideration in mathematical derivations is not possible without the use of numerical methods.

While these limitations will likely prohibit the formulation of a general one to one relationship considering FOS and scale, some further insights are still possible. The following sections derive and numerically validate the possible closed form relationships between FOS POF considering scale based on the main findings of this Thesis.

5.1 Factor of Safety Decomposition

One beneficial feature of the FOS equations summarised in Table 2 is the fact that each FOS calculation relationship can be decomposed into the individual FOS contributions of each relevant material parameter. This decomposing is given as:

$$FOS = FOS_{X_1} + FOS_{X_2} + \cdots + FOS_{X_n} \qquad \text{Equation 151}$$

where each FOS_{X_n} is the univariate FOS contribution associated with material parameter X_n. The number of FOS terms depends on the particular problem's complexity; for example, the number of unique lithologies, the modelled failure mode and the problem's heterogeneity interpretation. Despite having numerous FOS equations summarised in Table 2, the decomposed FOS contributions for friction, cohesion and tension are identical in each equation and are shown below:

$$FOS_{\phi} = \frac{W \cos\theta \tan\phi}{W \sin\theta} = \frac{\tan\phi}{\tan\theta}$$ Equation 152

$$FOS_{c} = \frac{cA}{W \sin\theta}$$ Equation 153

$$FOS_{\sigma_t} = \frac{tA' \sin(\alpha - \beta)}{W \sin\alpha}$$ Equation 154

$$FOS_{\sigma_t} = \frac{tA \sin(\alpha - \beta)}{W \sin\alpha \cos\beta}$$ Equation 155

$$FOS_{i} = \frac{\boldsymbol{F}_{\boldsymbol{P}_i}}{\sum_{i=1}^{n} \boldsymbol{F}_{\boldsymbol{A}_i} \cdot \hat{\boldsymbol{s}}}$$ Equation 156

Note that FOS_c (Equation 153) and FOS_{ϕ}(Equation 152) are appropriate for non-persistent cases but require the correction in terms of k to be applied. Two different Equations for FOS_{σ_t} are presented as the value is interpretation specific. Equation 156 is a general expression for all other decompositions expressed in terms of vectors. The Barton Bandis criterion (Equation 6) cannot be decomposed into its FOS components. As each FOS component is a univariate equation, the calculation of the POF for each component is straightforward. These are derived in the following sections.

A note of clarification. The above concept of decomposing the FOS into the individual components does not change the definition, or the calculated FOS. This approach is simply a mathematical construction that allows for the calculation of the POF integral to be manageable. This approach in essence is separating the FOS into the linear combinations associated with each univariate relationship. The FOS calculated as a single value and as a decomposed value will always return an identical FOS for a given problem.

5.2 Factor of Safety Probability of Failure Relationships for Frictional Components

Based on the analysis presented in Chapter Two and Three, Table 58 summarises the expected behaviour of friction over scale:

Table 58 Summary of the behaviour of friction at scale

	Peak friction	Residual friction
Laboratory UDF	Laboratory scale UDF of friction is described by a normal distribution	
USF	Negative and material specific. Stabilises quickly to 77% to 90% of Laboratory scale	Negative or non-existent. Stabilises quickly to 90% to 100% of Laboratory scale
Scale dependent UDF	Normal distribution is a very good approximation at increased scales	
Homogenisation	Pronounced homogenisation at increased scales	Material specific. Either no homogenisation or some degree of homogenisation

The behaviour of friction over scale, while not well defined behaved is at least consistent. For example, given some type of rock and a scale of interest, the friction angle can be measured from physical testing, or estimated from heterogeneous numerical methods. The measurement at this scale (assuming larger than laboratory) will typically have a lower median value, a smaller standard deviation and will be reasonably well approximated by a normal distribution. These observations will produce some combination of μ_ϕ and σ_ϕ that is applicable for the scale of interest. While this is not ideal, it still does make it possible to calculate a usable general relationship, if the POF_ϕ is calculated in terms of the case specific values of μ_ϕ and σ_ϕ and some scale V_n; that is:

$$POF_\phi = P\left(FOS_\phi \leq 1 \middle| \mu_{\phi_{V_n}}, \sigma_{\phi_{V_n}}\right) \qquad \text{Equation 157}$$

The issue with directly calculating POF_ϕ is that the PDF of ϕ is fed through the Tangent function ($\tan(\cdot)$), which will change the output distribution nonlinearly. To demonstrate this, the CDF of four different normal distributions (μ_ϕ=15°, 30°, 45° and 60°) with standard deviation of 1 were transformed using $\tan(\cdot)$. The location adjusted output PDFs are shown in Figure 88.

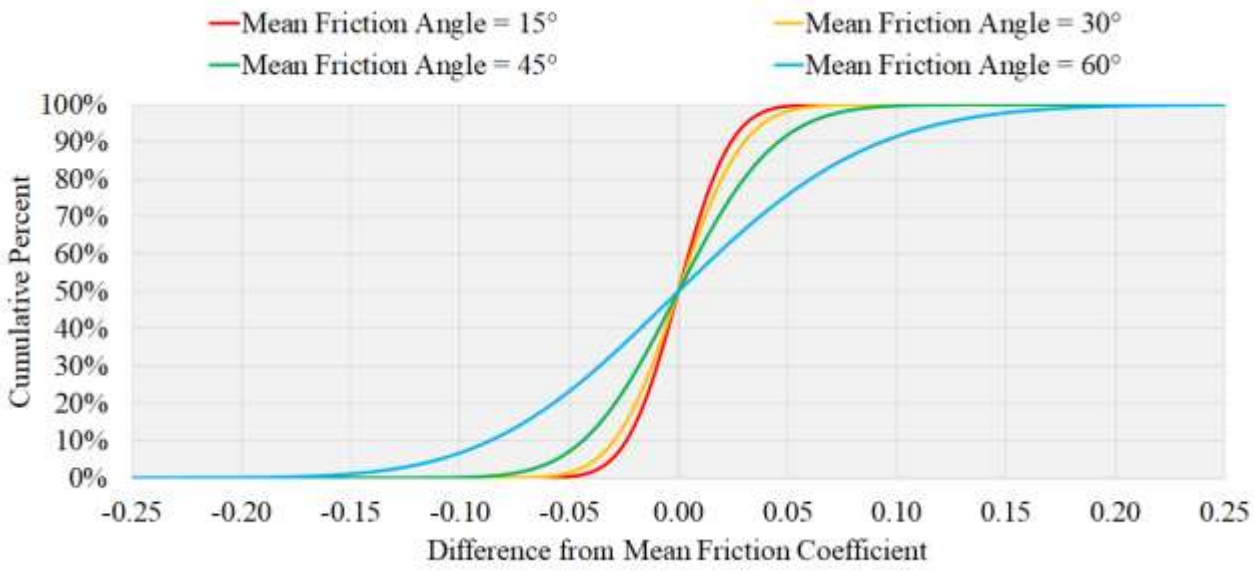

Figure 88 Cumulative Distribution Function of normalised friction coefficients

It is quite evident that the CDFs in Figure 88 are dependent on μ_ϕ. In order to calculate Equation 157, the PDF associated with $\tan\phi$ needs to be known. A very accurate approximation of the distribution of $\tan\phi$ is given by:

$$X_{tan(\phi)} \approx \mathcal{N}\left(\tan\left(\mu_\phi\right), {\sigma_\phi}^2 \sec^4\left(\mu_\phi\right)\right) \qquad \text{Equation 158}$$

With the associated standard deviation given as:

$$\sigma_{\tan(\phi)} \approx \sigma_\phi \sec^2\left(\mu_\phi\right) \qquad \text{Equation 159}$$

This approximation is derived using the delta method, where:

$$Var\left(f(X)\right) \approx \left(f'\left(E(X)\right)\right)^2 Var(X) \qquad \text{Equation 160}$$

The accuracy of Equation 158 was compared to Monte Carlo simulations (25,000 realisations per simulations) for various combinations of μ_ϕ and σ_ϕ. Values selected for μ_ϕ ranged from 1° to 64° and for each simulation and σ_ϕ was selected as 12.57% of μ_ϕ. The selection of σ_ϕ was chosen to align with the most varied distribution of ϕ possible based on the information presented in Table 58. Two comparative measurements were used to compare Equation 158 and the numerical simulations:

- mean value and standard deviation; and
- median value, and the standard deviation calculated using the Median Absolute Deviation (MAD).

MAD is a robust measurement for data variability. As this value is calculated using the median value, it is not as influenced by outliers and skewed data. MAD is defined as (Hampel 1974):

$$MAD = median|X_i - median(X)| \quad \text{Equation 161}$$

The standard deviation can be estimated using MAD (Rousseeuwm & Croux 1993):

$$\hat{\sigma} = k \times MAD \quad \text{Equation 162}$$

where k is a constant. For normal distributions k is given by:

$$k = \frac{1}{\Phi^{-1}(3/4)} \approx 1.4826 \quad \text{Equation 163}$$

The MAD was used in this instance to provide a more robust measure considering the output distribution is expected to be highly skewed. Comparisons between the percentage difference between Monte Carlo simulations and Equation 158 for the location parameter and standard deviation are shown in Figure 89 and Figure 90 respectfully.

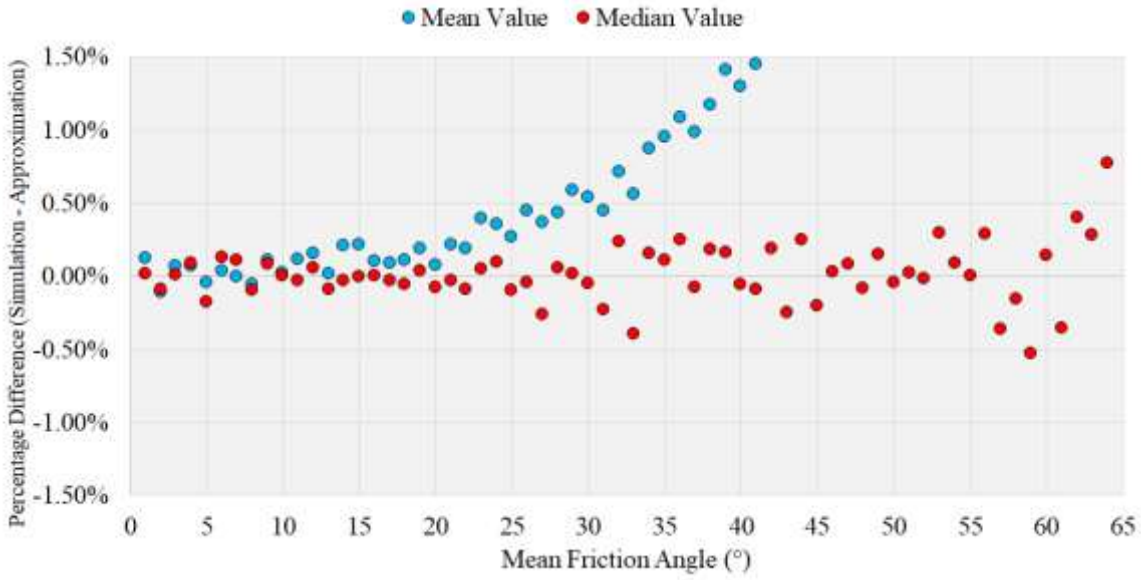

Figure 89 Percentage difference in Monte Carlo simulations and approximated location parameter

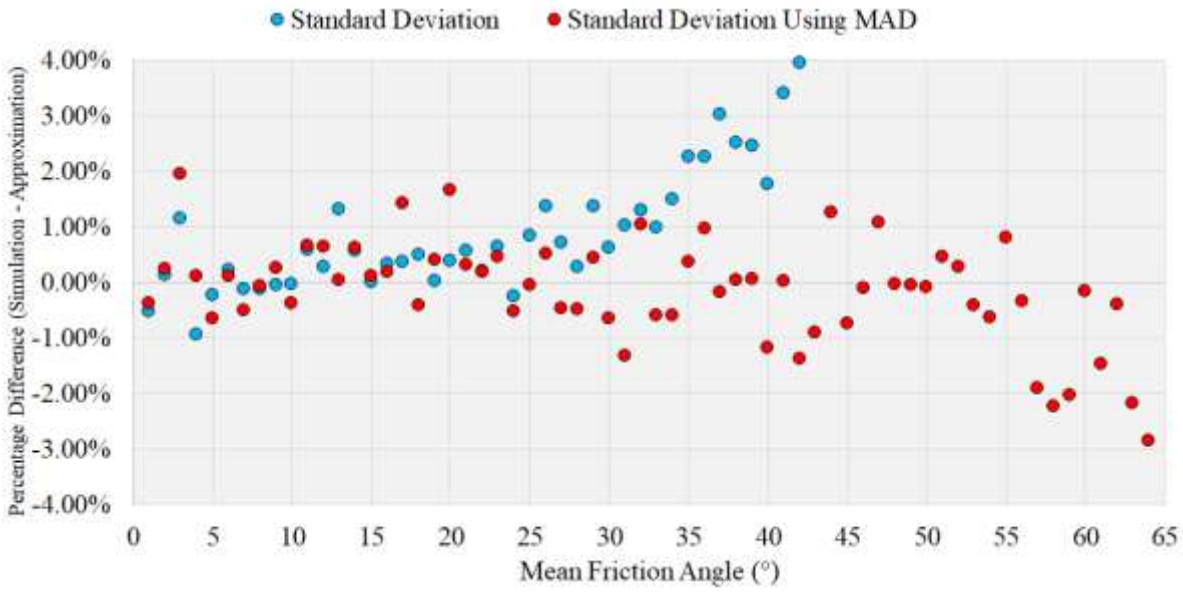

Figure 90 Percentage difference in Monte Carlo simulations and approximated standard deviation

Note the mean percentage difference for the mean value in Figure 89 continues to increase and reaches a maximum of 17.24%. The standard deviation percentage difference in Figure 90 continues to increase and reaches a maximum of 697.74%. From review of Figure 89 and Figure 90 the difference between simulated outputs and Equation 158 are very small. As expected, the highly skewed nature of $\tan(\cdot)$ is evident in the mean and standard deviation values, while more or less not apparent in measurements using MAD. Based on the simulation results, the delta method approximation given

by Equation 158 is sufficiently accurate to be used. Using Equation 152, $FOS_\phi \leq 1$ when $\tan\phi \leq \tan\theta$. POF_ϕ is then given by:

$$POF_\phi = \int_{-\infty}^{\tan\theta} \frac{e^{-\frac{(x-\tan(\mu_\phi))^2}{2\sigma_\phi{}^2 \sec^4(\mu_\phi)}}}{\sqrt{2\pi\sigma_\phi{}^2 \sec^4(\mu_\phi)}}\, dx = \frac{1}{2}\left(1 + \text{erf}\left(\frac{\tan(\theta) - \tan(\mu_\phi)}{\sqrt{2}\sigma_\phi \sec^2(\mu_\phi)}\right)\right) \qquad \text{Equation 164}$$

Use the substitution that:

$$\tan\theta = \frac{\tan\phi}{FOS_\phi} \qquad \text{Equation 165}$$

The final POF relationship obtained is:

$$POF_\phi = \frac{1}{2}\left[1 + \text{erf}\left(\frac{\sin(\mu_\phi)\cos(\mu_\phi)\,(1 - FOS_\phi)}{\sqrt{2}\sigma_\phi FOS_\phi}\right)\right] \qquad \text{Equation 166}$$

Equation 166 is the general solution for the POF for any single frictional component. Note that Equation 166 could be expressed in terms of the mean, median or mode FOS because these are all equivalent deterministic estimates. Equation 166 is also applicable to any scale of interest, as long as the mean and standard deviation of the scale of interest is known. An interesting feature of Equation 166 is that while the inputs are approximately normally distributed and have zero skew, the relationship between FOS and POF is subtly positively skewed. This is demonstrated in Figure 91 where a particular FOS POF relationship is shown, along with the symmetric normal approximation of best fit.

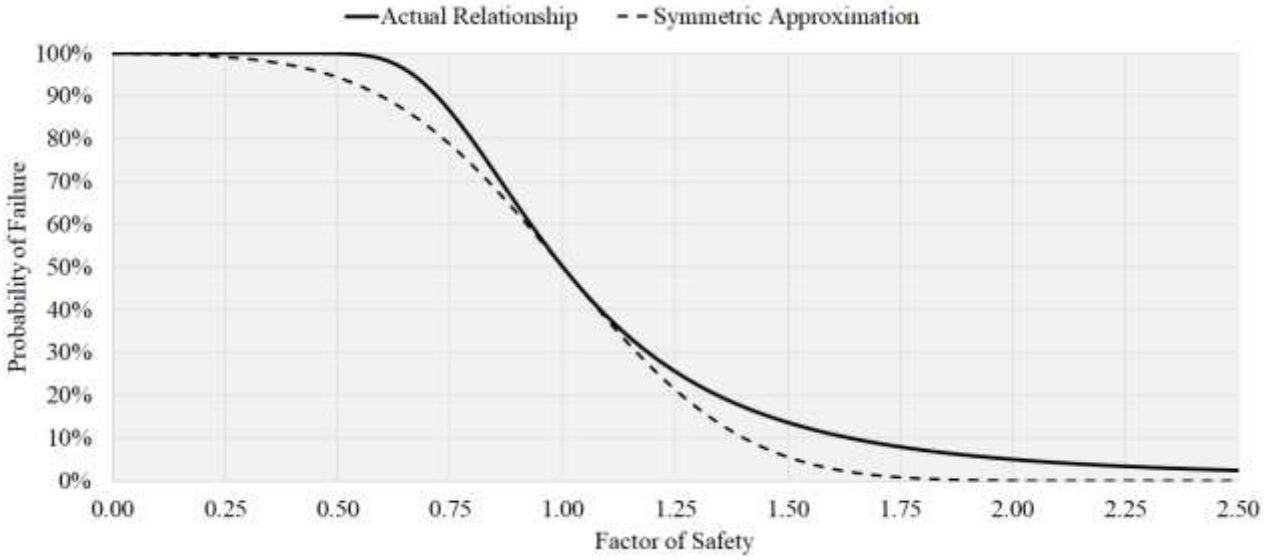

Figure 91 Demonstration of the Factor of Safety Probability of Failure relationship skewness, $\mu_\phi = 60°$, $\sigma_\phi = 7.542°$

Note the 'unrealistic' mean friction value used in Figure 91 is to exaggerate the skewness for clarity. As a final check for the accuracy of Equation 166, 1000 evaluations of FOS POF estimates calculated using Monte Carlo Sampling, with each simulation having 100,000 realisations to compare the accuracy of Equation 166. The CDF of the simulated difference is shown in Figure 92.

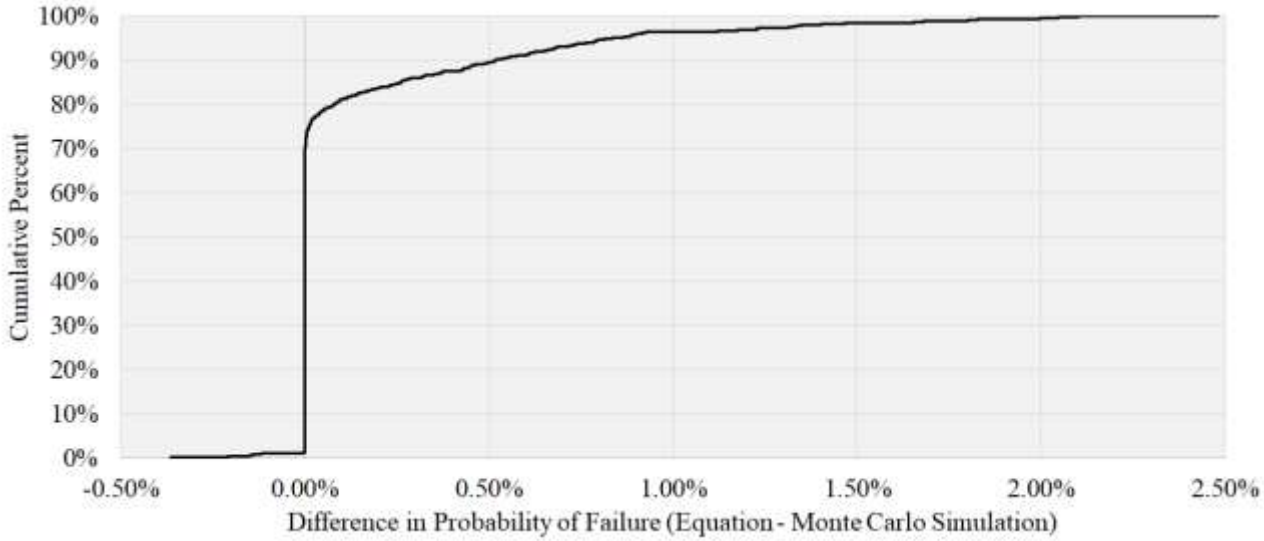

Figure 92 Difference in probability output - friction

It is apparent from Figure 92 that the Monte Carlo estimates for the POF typically match the value produced using Equation 166 and in extreme cases, overestimates the simulation POF by at most 2.5%. It was also seen that these largest differences were generally associated with Monte Carlo

simulations that had large values of both μ_ϕ and σ_ϕ. Based on the simulation results, Equation 166 is sufficiently accurate at describing POF_ϕ. It also needs to be noted that some of the error shown in Figure 92 is due to the random nature of the Monte Carlo Sampling.

5.2.1 Special case for generalised frictional components

While Equation 166 is appropriate at describing the relationship between POF_ϕ and FOS_ϕ for a single component, the generalised equation for FOS_ϕ is given as:

$$FOS_\phi = \frac{\sum_{i=1}^{n} W_i \cos\theta_i \tan\phi_i}{\sum_{i=1}^{n} W_i \sin\theta_i} \qquad \text{Equation 167}$$

Which describes the total frictional FOS contributions of an arbitrary path through an arbitrary number of unique materials. While the completely generalised expression is dealt with in the following section, the second special case is Equation 168, which describes an arbitrary failure path through a single material:

$$FOS_\phi = \frac{\tan\phi \sum_{i=1}^{n} W_i \cos\theta_i}{\sum_{i=1}^{n} W_i \sin\theta_i} \qquad \text{Equation 168}$$

From Equation 168 it is straightforward to show that $FOS_\phi \leq 1$ when:

$$\tan\phi \leq \frac{\sum_{i=1}^{n} W_i \sin\theta_i}{\sum_{i=1}^{n} W_i \cos\theta_i} \qquad \text{Equation 169}$$

Using a similar form of Equation 164 and the substitution:

$$\frac{\sum_{i=1}^{n} W_i \sin\theta_i}{\sum_{i=1}^{n} W_i \cos\theta_i} = \frac{\tan\phi}{FOS_\phi} \qquad \text{Equation 170}$$

An identical derivation follows resulting in the same result as Equation 166. What this means in practice is that for a homogenous material, the relationship between FOS_ϕ and POF_ϕ is not influenced by the complexity of the failure path. While a complex failure may have a different value of FOS_ϕ, the value of POF_ϕ can always be identically calculated.

5.2.2 Generalised friction case

The complete generalised frictional case is more cumbersome to calculate but it can be done. Expanding Equation 167:

$$FOS_\phi = \frac{W_1 \cos\theta_1 \tan\phi_1}{W_1 \sin\theta_1 + \cdots + W_n \sin\theta_n} + \cdots + \frac{W_n \cos\theta_n \tan\phi_n}{W_1 \sin\theta_1 + \cdots + W_n \sin\theta_n} = FOS_{\phi_1} + \cdots + FOS_{\phi_n} \qquad \text{Equation 171}$$

Recall that the distribution associated with each $\tan(\phi_n)$ is approximately normally distributed. Using this fact, Equation 171 can be converted to an equivalent normal distribution using linear combinations of the PDF of each; that is:

$$\sum_{i=1}^{n} \frac{W_n \cos\theta_n}{W_1 \sin\theta_1 + \cdots + W_n \sin\theta_n} X_i \sim \mathcal{N}\left(\sum_{i=1}^{n} \frac{W_n \cos\theta_n}{W_1 \sin\theta_1 + \cdots + W_n \sin\theta_n} \mu_i, \sum_{i=1}^{n} \left(\frac{W_n \cos\theta_n}{W_1 \sin\theta_1 + \cdots + W_n \sin\theta_n} \sigma_i\right)^2\right) \qquad \text{Equation 172}$$

where each σ_i is given by:

$$\sigma_i \approx \sigma_{\phi_i} \sec^2\left(\mu_{\phi_i}\right) \qquad \text{Equation 173}$$

For clarity, Equation 172 then gives us the PDF associated with FOS_ϕ. Calculating the POF_ϕ yields the completely generalised relationship:

$$POF_\phi = \int_{-\infty}^{1} \frac{1}{\sqrt{2\pi \sum_{i=1}^{n} \left(\frac{W_n \cos\theta_n}{W_1 \sin\theta_1 + \cdots + W_n \sin\theta_n} \sigma_i\right)^2}} e^{-\frac{\left(x - \sum_{i=1}^{n} \frac{W_n \cos\theta_n}{W_1 \sin\theta_1 + \cdots + W_n \sin\theta_n} \mu_i\right)^2}{2 \sum_{i=1}^{n} \left(\frac{W_n \cos\theta_n}{W_1 \sin\theta_1 + \cdots + W_n \sin\theta_n} \sigma_i\right)^2}} dFOS_\phi \qquad \text{Equation 174}$$

$$POF_\phi = P\left(FOS_\phi \leq 1\right) = \frac{1}{2}\left(1 + \operatorname{erf}\left(\frac{1 - FOS_\phi}{\sqrt{2 \sum_{i=1}^{n} \left(\frac{W_n \cos\theta_n}{W_1 \sin\theta_1 + \cdots + W_n \sin\theta_n} \sigma_i\right)^2}}\right)\right) \qquad \text{Equation 175}$$

The accuracy of Equation 175 was numerically verified utilising 2000 Monte Carlo evaluations, each with 50,000 realisations. The CDF of the simulation differences is shown in Figure 93.

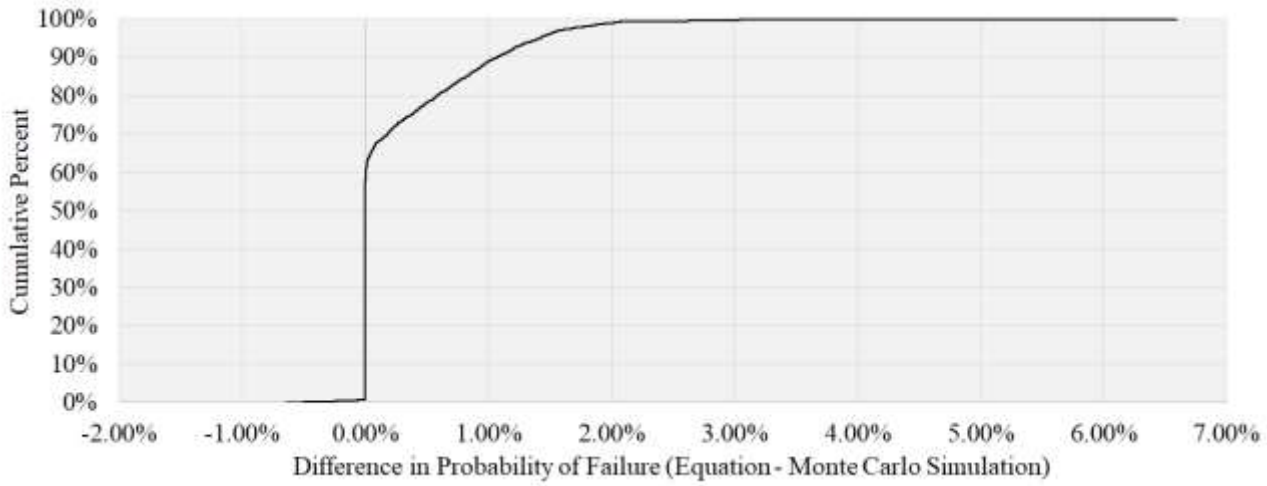

Figure 93 Difference in probability output - generalised friction

By review of Figure 93 it is apparent that the accuracy of Equation 175 is sufficiently accurate for applications.

5.3 Probability of Failure for Tensile Components

The relationship between POF_{σ_t} and FOS_{σ_t} is relatively straightforward. While the derivation presented is focused on tensile failure in open pit stability, the derivation is identical for all single component FOS equations involve a Weibull distribution, for example underground pillars acting under uniaxial compression. A summary of the expected behaviour for UTS and UCS is summarised in Table 59.

Table 59 Summary of the behaviour of tensile and compressive strength at scale

	UTS	UCS
Laboratory UDF	Laboratory scale UDF is described by a Rayleigh distribution	
USF	Negative. Stabilises to 40% to 50% of Laboratory scale	Negative. Stabilises to 30% to 35% of Laboratory scale for purely brittle materials. Higher value (up to 80%) for quasi-brittle materials
Scale dependent UDF	Weibull distribution	
Homogenisation	Pronounced homogenisation at increased scales.	

To provide a single deviation for the relationship between POF_{σ_t} and FOS_{σ_t}, the non-tensile terms in Equation 154 and Equation 155 are treated as some constant D; that is, $D = \frac{W \sin\alpha}{A' \sin(\alpha-\beta)}$ in Equation 154 and $D = \frac{W \sin\alpha \cos\beta}{A' \sin(\alpha-\beta)}$ in Equation 155. With this simplification it follows that POF_{σ_t} is given by:

$$POF_{\sigma_t} = \int_{-\infty}^{D} \frac{k_{\sigma_t}}{\lambda_{\sigma_t}} \left(\frac{\sigma_t}{\lambda_{\sigma_t}}\right)^{k_{\sigma_t}-1} e^{-\left(\frac{\sigma_t}{\lambda_{\sigma_t}}\right)^{k_{\sigma_t}}} d\sigma_t = 1 - e^{-\left(\frac{D}{\lambda_{\sigma_t}}\right)^{k_{\sigma_t}}} \qquad \text{Equation 176}$$

where λ_{σ_t} is the Scale Parameter and k_{σ_t} is the Shape Parameter. To relate Equation 176 to a calculated value of FOS_{σ_t}, we take advantage of the fact that λ_{σ_t} can be related to specific characteristic values of σ_t. These characteristic values then produce three different relationships, depending on which FOS_{σ_t} value is used. For a Weibull distribution recall that the scale parameter is described by the following relationships:

$$\lambda_{\sigma_t} = \frac{\mu_{\sigma_t}}{\Gamma\left(1 + \frac{1}{k_{\sigma_t}}\right)} \qquad \text{Equation 177}$$

$$\lambda_{\sigma_t} = \frac{M_{\sigma_t}}{(\ln 2)^{\frac{1}{k_{\sigma_t}}}} \qquad \text{Equation 178}$$

$$\lambda_{\sigma_t} = \frac{Mo_{\sigma_t}}{\left(\frac{k_{\sigma_t}-1}{k_{\sigma_t}}\right)^{\frac{1}{k_{\sigma_t}}}} \qquad \text{Equation 179}$$

where μ_{σ_t} is the mean UTS, M_{σ_t} is the median UTS and Mo_{σ_t} is the mode UTS. Using these identities and the substitution that:

$$D = \frac{\sigma_t}{FOS_{\sigma_t}} \qquad \text{Equation 180}$$

The final three relationships for FOS_{σ_t} and POF_{σ_t} are obtained:

$$POF_{\sigma_t} = P\left(FOS_{\sigma_t} \leq 1 \middle| k_{\sigma_t}, \lambda_{\sigma_t}\right) = 1 - e^{-\left(\frac{\Gamma\left(1+\frac{1}{k_{\sigma_t}}\right)}{FOS_{\mu_{\sigma_t}}}\right)^{k_{\sigma_t}}} \quad \text{Equation 181}$$

$$POF_{\sigma_t} = P\left(FOS_{\sigma_t} \leq 1 \middle| k_{\sigma_t}, \lambda_{\sigma_t}\right) = 1 - e^{-\left(\frac{(\ln 2)^{\frac{1}{k_{\sigma_t}}}}{FOS_{M_{\sigma_t}}}\right)^{k_{\sigma_t}}} \quad \text{Equation 182}$$

$$POF_{\sigma_t} = P\left(FOS_{\sigma_t} \leq 1 \middle| k_{\sigma_t}, \lambda_{\sigma_t}\right) = 1 - e^{-\frac{k_{\sigma_t}-1}{k_{\sigma_t} FOS_{Mo_{\sigma_t}}^{k_{\sigma_t}}}} \quad \text{Equation 183}$$

It needs to be noted that while the above derivation produces three different relationships between POF_{σ_t} and FOS_{σ_t}, the calculated POF is identical across all equations given some initial Weibull distribution. As previously mentioned in Chapter Two, the mode value is recommended as the deterministic value due to its intuitiveness to the problem interpretation and coincidentally produces the simplest POF_{σ_t} and FOS_{σ_t} relationship. To validate Equation 181, Equation 182 and Equation 183, 1000 random POF_{σ_t} and FOS_{σ_t} simulations were completed, each with 100,000 realisations to compare and contrast the estimates. The CDF of the simulated difference is shown in Figure 94.

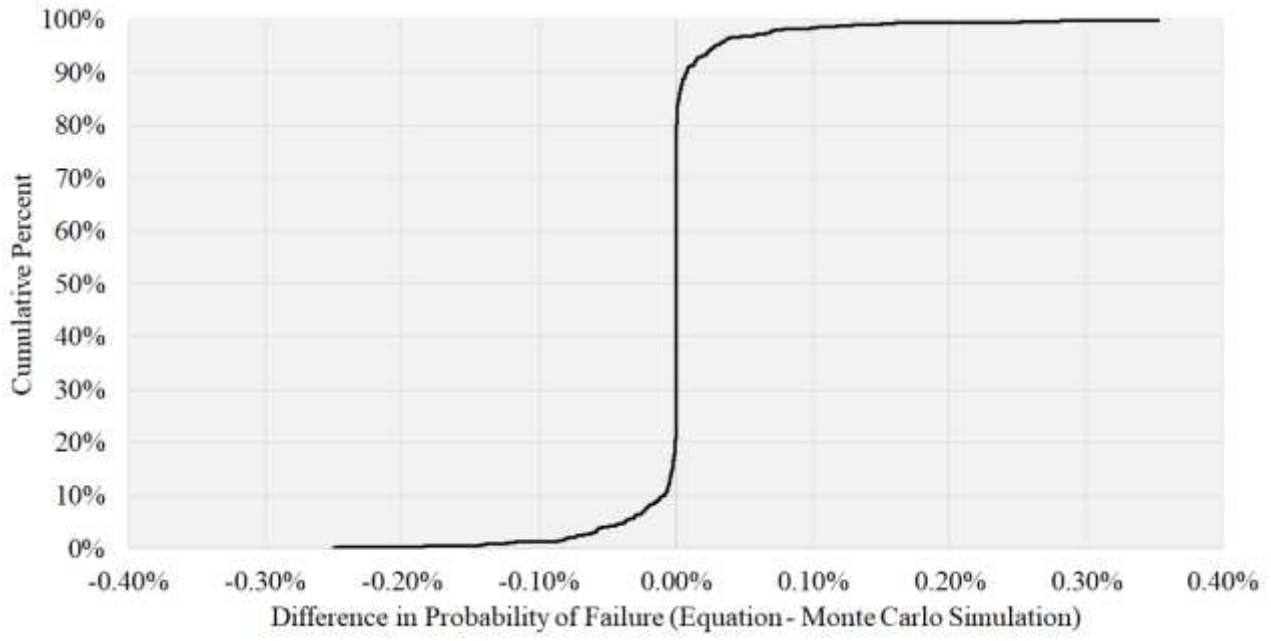

Figure 94 Difference in probability output - tension

The results shown in Figure 94 demonstrate the accuracy of Equation 181, Equation 182 and Equation 183 with an error typically at most of ±0.30%. These differences are believed to be completely due to the numerical accuracy of the Monte Carlo Sampling.

5.3.1 Special case one for generalised tensile components

A similar special case for generalised tension can be considered. For a problem where the failure surface or stress state is complex and there is only one lithology. FOS_{σ_t} in general is calculated by:

$$FOS_{\sigma_t} = \frac{\sum_{i=1}^{n} \sigma_{t_i} A_i' \sin(\alpha_i - \beta_i)}{\sum_{i=1}^{n} W_i \sin \alpha_i} \qquad \text{Equation 184}$$

Which describes the tensile FOS contribution of an arbitrary path through an arbitrary number of materials. The second special case is Equation 185, where there is only one tensile component is:

$$FOS_{\sigma_t} = \frac{\sigma_t \sum_{i=1}^{n} A_i' \sin(\alpha_i - \beta_i)}{\sum_{i=1}^{n} W_i \sin \alpha_i} \qquad \text{Equation 185}$$

From Equation 185 it is straightforward to show that $FOS_{\sigma_t} \leq 1$ when:

$$\sigma_t \leq \frac{\sum_{i=1}^{n} W_i \sin \alpha_i}{\sum_{i=1}^{n} A_i' \sin(\alpha_i - \beta_i)} \qquad \text{Equation 186}$$

In addition, using the substitution:

$$\frac{\sigma_t}{FOS_{\sigma_t}} = \frac{\sum_{i=1}^{n} W_i \sin \alpha_i}{\sum_{i=1}^{n} A_i' \sin(\alpha_i - \beta_i)} \qquad \text{Equation 187}$$

To arrive at the same three relationships as previously presented. Again this special case demonstrates that the complexity of the failure path does not change the relationship between POF_{σ_t} and FOS_{σ_t}.

5.3.2 Special case two for generalised tensile components

The calculation of the complete generalised tensile case is significantly more cumbersome than the completely generalised frictional case. Firstly, consider an arbitrary failure surface through a heterogeneous material:

$$FOS_{\sigma_t} = \frac{\sum_{i=1}^{n} \sigma_{t_i} A_i' \sin(\alpha_i - \beta_i)}{\sum_{i=1}^{n} W_i \sin \alpha_i} \qquad \text{Equation 188}$$

Note that a similar formulation of Equation 188 can be derived using Equation 155 with an almost identical derivation as the one shown below. The completely generalised POF expression for Equation 188 would be one where the PDF for each σ_{t_i} is arbitrarily specified. The slightly simpler special case is where each σ_{t_i} is an Independent Identically Distributed random variable. This simple generalised case would be equivalent to an arbitrary failure path through a homogenous material, where each section of the failure path is treated and evaluated independently, or if failure occurs through various beds of the same lithology. In order to calculate the closed form POF using this second special case, it would need to be possible to compute the n-fold convolution of the associated Weibull distribution. While the n-fold convolution is not analytically possible, work by Johnson (1960) demonstrated a very close approximation of the convolution could be obtained by using an appropriate Erlang distribution. The CDF of the sum of L Independent Identically Distributed Weibull random variables x_i can be approximated by:

$$F_{\Sigma x}(\Sigma x) \approx 1 - e^{(-u)} \sum_{i=0}^{L-1} \frac{u^i}{i!} \qquad \text{Equation 189}$$

With:

$$u = \left(\frac{\Gamma\left(L + \frac{1}{k}\right)}{L!\,\Gamma\left(1 + \frac{1}{k}\right)} \frac{\Sigma x}{\lambda} \right)^k \qquad \text{Equation 190}$$

where λ and k are the scale and shape parameters of the input Weibull distribution respectfully. Equation 190 can be simplified by taking advantage of the Weibull distribution characteristics to produce:

$$u = \left(\frac{\Gamma\left(L + \frac{1}{k}\right)}{L!} \frac{\Sigma x}{\mu_x} \right)^k \quad \text{Equation 191}$$

where μ_x is the mean value associated with the input Weibull distribution. Now consider Equation 188, the calculated FOS_{σ_t} is in terms of some deterministic estimate of the distribution associated with each L, while the approximation in Equation 189 is in terms of the sum of each individual components. To calculate the POF_{σ_t} in terms of the original calculated FOS_{σ_t}, the appropriate value for Σx needs to be determined. Using Equation 185, the value of Σx for which FOS_{σ_t} is less than or equal to one is given by:

$$\Sigma x = L\sigma_t \leq \frac{L \sum_{i=1}^{n} W_i \sin \alpha_i}{\sum_{i=1}^{n} A_i' \sin(\alpha_i - \beta_i)} \quad \text{Equation 192}$$

Substituting Equation 192 into Equation 191:

$$u = \left(\frac{\Gamma\left(L + \frac{1}{k}\right)}{L!} \frac{L \sum_{i=1}^{n} W_i \sin \alpha_i}{\mu_x \sum_{i=1}^{n} A_i' \sin(\alpha_i - \beta_i)} \right)^k \quad \text{Equation 193}$$

Substituting Equation 185 into Equation 193:

$$u = \left(\frac{\Gamma\left(L + \frac{1}{k}\right)}{L!} \frac{L}{FOS_{\mu_{\sigma_t}}} \right)^k \quad \text{Equation 194}$$

Which produces the final FOS POF approximation:

$$POF_{\sigma_t} = 1 - e^{-\left(\frac{\Gamma\left(L+\frac{1}{k}\right)}{(L-1)!FOS_{\mu_{\sigma_t}}}\right)^k} \sum_{i=0}^{L-1} \frac{1}{L!} \left(\left(\frac{\Gamma\left(L+\frac{1}{k}\right)}{(L-1)!\,FOS_{\mu_{\sigma_t}}} \right)^k \right)^L \quad \text{Equation 195}$$

A slightly modified version of Equation 195 is also proposed:

$$POF_{\sigma_t} = 1 - e^{-\left(\frac{\Gamma\left(L+\frac{\sqrt{2}}{k}\right)}{(L-1)!FOS_{\mu_{\sigma_t}}}\right)^{\frac{k}{\sqrt{2}}}} \sum_{i=0}^{L-1} \frac{1}{L!} \left(\left(\frac{\Gamma\left(L+\frac{\sqrt{2}}{k}\right)}{(L-1)!\,FOS_{\mu_{\sigma_t}}} \right)^{\frac{k}{\sqrt{2}}} \right)^L \quad \text{Equation 196}$$

In order to verify the accuracy of Equation 195 and Equation 196, 1000 individual FOS POF simulations were completed each with 5000 realisations per simulation. Comparisons between the predicted POF and Monte Carlo simulation for each of the two proposed approximations is shown in Figure 95.

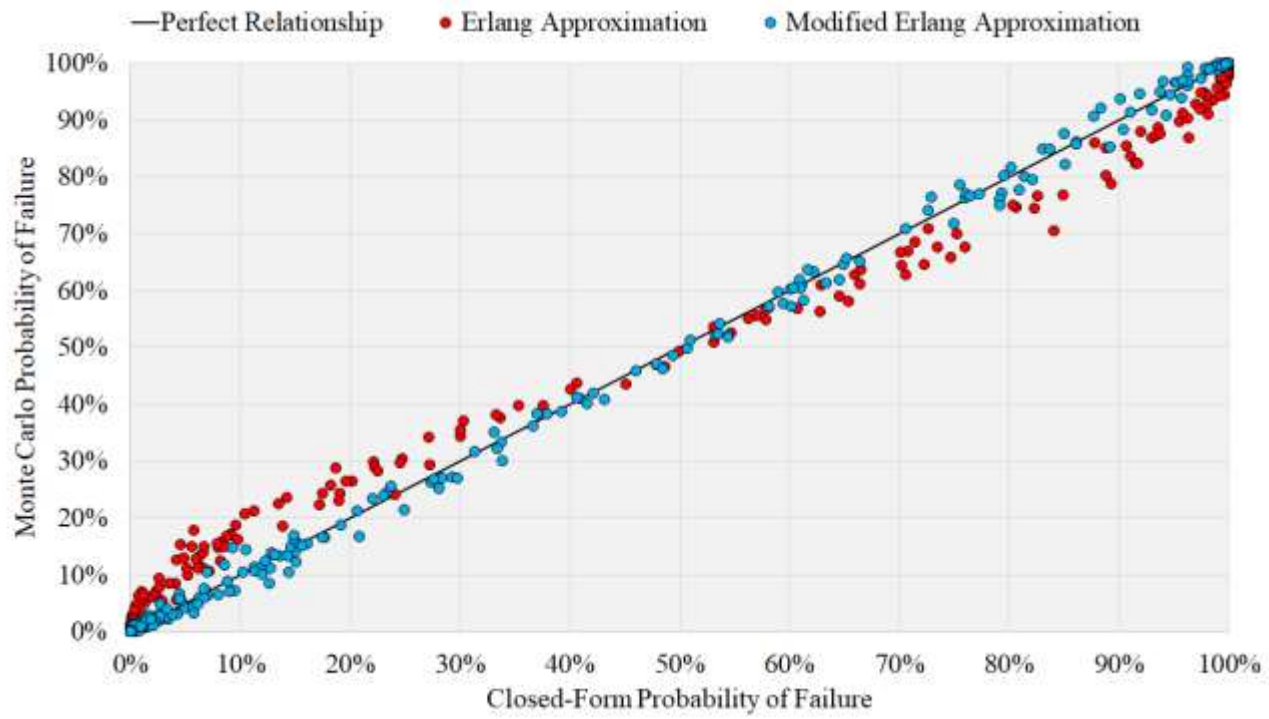

Figure 95 Comparisons of the Erlang and modified Erlang approximations to Monte Carlo Sampling

From review of Figure 95 it is apparent that the simulated POF using Equation 195 is considerably inaccurate, particularly in the 'practical' design regions (POF < 20%). The modified Erlang approximation using Equation 196 is substantially more accurate and is sufficient to use when computing this second special case. Note that the modified Erlang approximation was derived by incrementally adjusting Equation 190 to obtain a better estimate of the entire n-fold convolution distribution. There is no readily apparent mathematical basis as to why this modification produces better results.

5.3.3 Generalised tension case

The completely generalised tensile case has no analytical solution or approximation. The only currently viable method of computing the POF associated with this case is using numerical methods.

5.4 Probability of Failure for Cohesive Components

Based on the analysis presented in Chapter Two and Three, Table 60 summarises the expected behaviour of cohesion over scale:

Table 60 Summary of the behaviour of cohesion at scale

	Peak cohesion	Residual cohesion
Laboratory UDF	Implicitly defined PDF	0
USF	Negative and material specific. Stabilises to 32% to 40% of laboratory scale	Emergent positive or non-existent. Stabilises to 0% t0 10% of laboratory peak cohesion.
Scale dependent UDF	Implicitly defined PDF	
Homogenisation	Pronounced homogenisation at increased scales. Scale dependent variance is likely described by some inconsistent negative power law	No general behaviour. Simulations produce a transition period of increased variance due to the emergence of residual cohesion.

The problematic aspect of considering the scale dependant FOS POF relationships for cohesion is that the PDF describing it is implicitly defined. While it can be shown that cohesion can be very well approximated by a Weibull distribution, there is currently no reasonably accurate method of calculating the PDF of cohesion using only the known behaviour associated with the distribution of

UCS and ϕ. The fact that on a case by case basis, cohesion can be approximated by a Weibull distribution means that the univariate POF relationship relating to cohesion are is identical to those previously presented in Section 5.3.

5.5 Probability of Failure for Toppling

Based on the analysis presented in Chapter Four, the expected behaviour for cross joint spacing is not as definitive as the other parameters. The presented analysis did indicate that a representative PDF family to describe cross joint spacing is a gamma distribution. The FOS equation for Case 3 toppling is given by:

$$FOS = \frac{t/h}{\tan\theta} = \frac{t}{h\ \tan\theta} \qquad \text{Equation 197}$$

where t is the bed thickness (m), h is the cross joint spacing (m) and θ is the bedding dip (˚). The value of h where the FOS is less than one is given by:

$$\frac{t}{\tan\theta} \leq h \qquad \text{Equation 198}$$

That is, the FOS is less than one when h is greater than some specific value. In order to provide a simpler integral, complement rule is instead used:

$$P(X) = 1 - P(X') \qquad \text{Equation 199}$$

The POF is then given by:

$$P(FOS \leq 1) = 1 - \int_{-\infty}^{\frac{t}{\tan\theta}} \frac{1}{\Gamma(k)} h^{k-1} e^{-\frac{x}{\vartheta}}\, dh = 1 - \frac{1}{\Gamma(k)}\gamma\left(k, \frac{t}{\tan\theta\,\vartheta}\right) \qquad \text{Equation 200}$$

where k is the gamma distribution shape parameter, ϑ is the gamma distribution scale parameter and γ is the lower incomplete gamma function. Using Equation 200, two different FOS POF relationships can be determined using the mean and mode cross joint spacing using the following characteristic relationships:

$$h_{\mu} = k\vartheta \qquad \text{Equation 201}$$

$$h_{Mo} = (k-1)\vartheta \qquad \text{Equation 202}$$

where h_{μ} and h_{Mo} are the mean and mode cross joint spacing respectfully. Note that the median value is not presented, as there is no closed form relationship for the median value of a gamma distribution. Using the relationships in Equation 201, Equation 202 and Equation 197, the following POF relationships are obtained for Case 3 toppling:

$$POF = 1 - \frac{1}{\Gamma(k)}\gamma\left(k, kFOS_{\mu}\right) \qquad \text{Equation 203}$$

$$POF = 1 - \frac{1}{\Gamma(k)}\gamma(k, (k-1)FOS_{Mo}) \qquad \text{Equation 204}$$

To validate Equation 203 and Equation 204, 1000 random POF and FOS simulations were completed, each with 100,000 realisations to compare and contrast the estimates. The CDF of the simulated difference is shown in Figure 96.

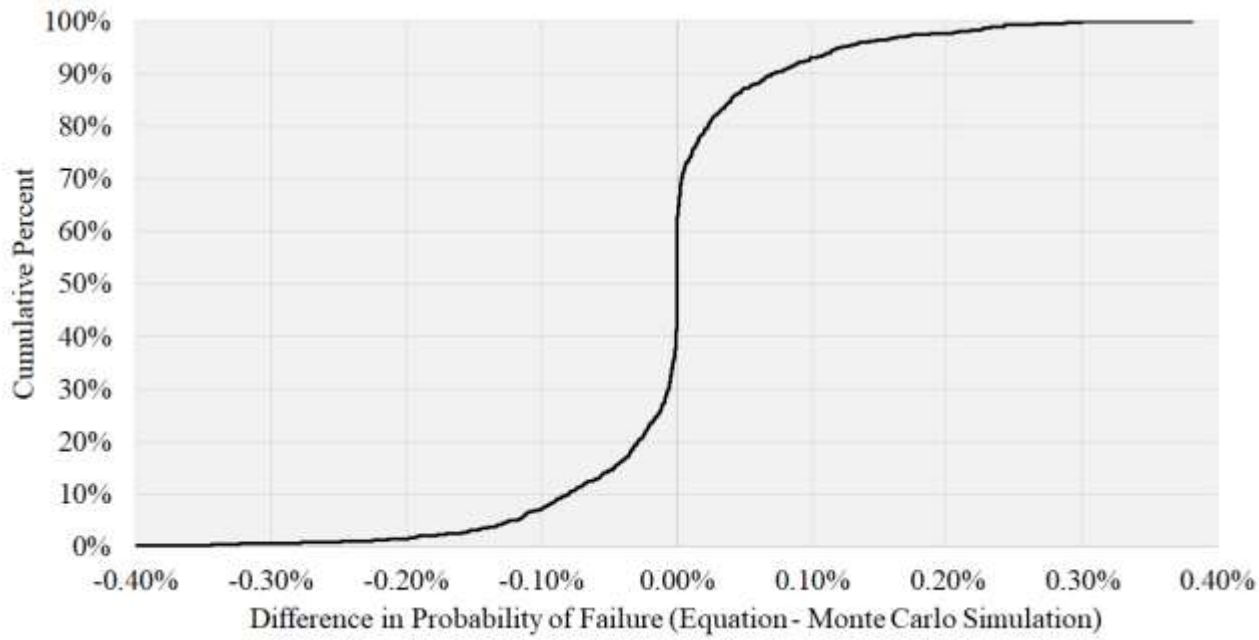

Figure 96 Difference in probability outputs - toppling

The results shown in Figure 96 demonstrate the accuracy of Equation 203 and Equation 204 with an error typically at most of ±0.40%. These differences are believed to be completely due to the numerical accuracy of the Monte Carlo Sampling.

An alternative toppling FOS relationship (Equation 18) was presented in Chapter One. The POF FOS relationships for this toppling formulation are equivalent to the previously presented frictional relationships, as they are identical formulations with a rotated coordinate system.

5.6 Factor of Safety Probability of Failure Bounds

Using the univariate relationships presented in this Chapter, it is possible to define for multi component problems, an upper and lower bound to the underlying FOS POF equation. The upper and lower bounds relating FOS and POF can be constructed by considering that for a particular design, the POF can never exceed the highest POF for a single component, and can never be lower than the lowest POF component. Using the laboratory scale UDFs, the upper and lower FOS POF bounds for failure through a Mohr Coulomb material is presented in Figure 97.

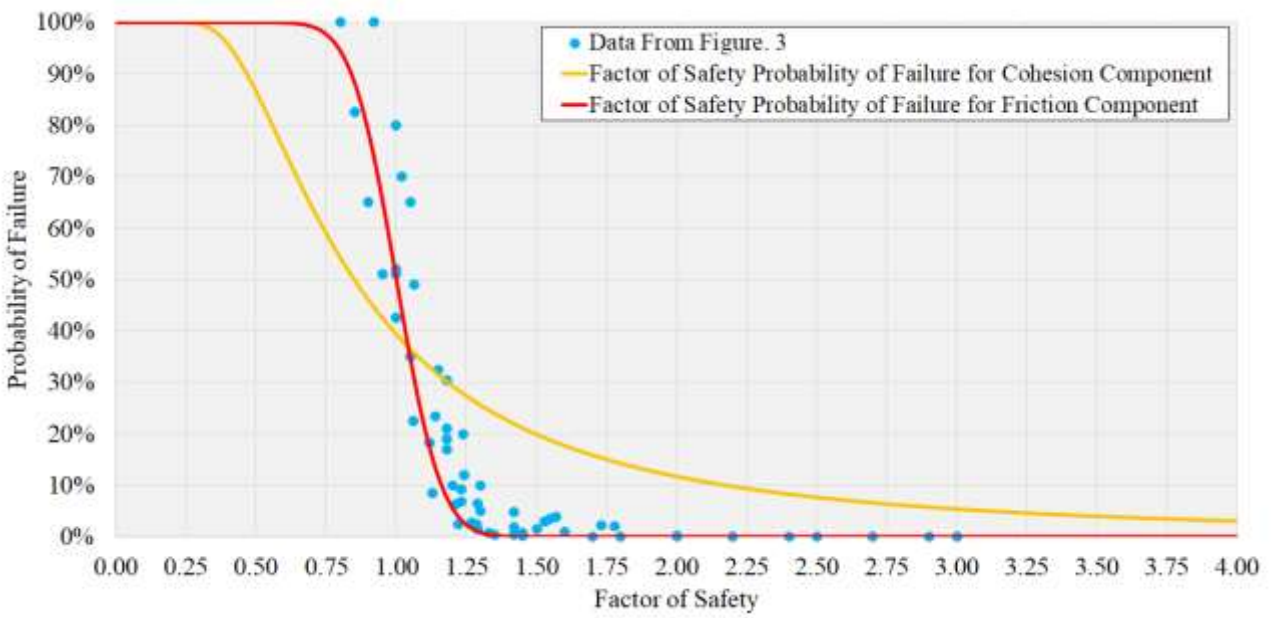

Figure 97 Factor of Safety Probability of Failure bounds using laboratory scale material parameters

By comparing the data shown in Figure 97 to the theoretical upper and lower FOS POF bounds, it can be seen that the FOS POF pairs typically plot within the specified region, or follow closely the frictional relationship. The interpretation of this is that the FOS POF relationships shown in Figure 97 and Figure 9 would have been derived using laboratory scale variability and would have primarily used normal like distributions to define each material parameter.

While the FOS POF bounds presented in Figure 97 are an interesting feature, the region they span for a given FOS is far too large to provide any practical guidance to the problem's POF. In order to produce the problem specific POF FOS relationship, the conditional probabilities associated with each univariate relationship need to be considered. In order to calculate the case specific relationship, consider the simplest two variate FOS equation:

$$FOS = \frac{cA + W\cos\theta\tan\phi}{W\sin\theta} \qquad \text{Equation 205}$$

where A, W and θ are constants, c is a Weibull distribution and ϕ is a normal distribution. c and ϕ are treated as uncorrelated for simplicity. Equation 205 can be decomposed into the values of FOS related to each random variable as was done previously. The particular area of interest is the probability where:

$$FOS_\phi + FOS_c = FOS \leq 1 \qquad \text{Equation 206}$$

The region where $FOS \leq 1$ in terms of ϕ and c is given by:

$$\frac{\tan\phi}{\tan\theta} \leq 1 - \frac{cA}{W\sin\theta} \qquad \text{Equation 207}$$

$$\tan\phi \leq \tan\theta\left(1 - \frac{cA}{W\sin\theta}\right) = \tan\theta\,(1 - FOS_c) \qquad \text{Equation 208}$$

As presented previously, it is known that the distribution associated with $\tan\phi$ is given by:

$$X_{tan(\phi)} \approx \mathcal{N}\left(\tan(\mu_\phi), {\sigma_\phi}^2\sec^4(\mu_\phi)\right) \qquad \text{Equation 209}$$

So then, the probability $\tan\phi$ falls in this region is given by:

$$P\left(\tan\phi \leq \tan\theta\,(1 - FOS_c)\right) = \int_{-\infty}^{\tan\theta(1-FOS_c)} \frac{1}{\sqrt{2\pi\sigma^2}} e^{-\frac{(x-\mu)^2}{2\sigma^2}} dx \qquad \text{Equation 210}$$

$$P\left(\tan\phi \le \tan\theta\,(1-FOS_c)\right) = \frac{1}{2}\left(1+\operatorname{erf}\left(\frac{\left(\tan\theta\,(1-FOS_c)\right)-\tan\left(\mu_\phi\right)}{\sqrt{2}\sigma_\phi \sec^2\left(\mu_\phi\right)}\right)\right) \quad \text{Equation 211}$$

Using the substitution that $tan\ \theta = \frac{\tan\mu_\phi}{FOS_\phi}$:

$$\begin{aligned} P\left(FOS_\phi \le 1-FOS_c\right) &= P\left(\tan\phi \le \tan\theta\,(1-FOS_c)\right) \\ &= \frac{1}{2}\left(1+\operatorname{erf}\left(\frac{\sin\mu_\phi\cos\mu_\phi\left(1-FOS_c-FOS_\phi\right)}{\sqrt{2}\sigma_\phi FOS_\phi}\right)\right) \end{aligned} \quad \text{Equation 212}$$

The corresponding Weibull distribution in terms of FOS_c:

$$f(FOS_c) = \frac{k}{\lambda_{FOS_c}}\left(\frac{FOS_c}{\lambda_{FOS_c}}\right)^{k-1} e^{-\left(\frac{FOS_c}{\lambda_{FOS_c}}\right)^k} \quad \text{Equation 213}$$

Note that in the above equation, λ_{FOS_c} is given by:

$$\lambda_{FOS_c} = \frac{\lambda_c A}{W\sin\theta} \quad \text{Equation 214}$$

Using the law of total probability, the probability that $FOS_\phi + FOS_c \le 1$ can be written as:

$$P\left(FOS_\phi + FOS_c \le 1\right) = \int_0^1 \frac{1}{2}\left(1+\operatorname{erf}\left(\frac{\sin\mu_\phi\cos\mu_\phi\left(1-FOS_c-FOS_\phi\right)}{\sqrt{2}\sigma_\phi FOS_\phi}\right)\right)\frac{k}{\lambda_{FOS_c}}\left(\frac{FOS_c}{\lambda_{FOS_c}}\right)^{k-1} e^{-\left(\frac{FOS_c}{\lambda_{FOS_c}}\right)^k} d(FOS_c) \quad \text{Equation 215}$$

Which cannot be computed without numerical means. While this approach can be extended indefinitely and include correlations, it becomes increasingly difficult to both formulate and compute the required POF integral. For a practical application, it is far simpler to compute the actual POF using Monte Carlo Sampling. The implication of this formulation is that based on the understanding of rock material parameters developed in this Thesis, there is no one to one relationship between FOS and POF for structured rock. While in theory, it is possible to routinely calculate this particular relationship, from a problem solving perspective it is far simpler to complete the Monte Carlo Sampling to obtain the case specific value of the POF.

5.7 The Scale of Interest Conundrum

The astute reader may have noted potential complications and inconsistencies in the final relationships between FOS and POF for a given design. These inconsistencies arrive from how an Engineer chooses to consider material parameter heterogeneity and scale in their analysis. To demonstrate this consider the following example:

A 50m high slope with a batter angle of 65° needs to be designed in a cohesionless material. The company requires that the slope's POF be at most 5%. A relevant failure surface was loosely approximated as a bilinear failure surface for the analysis. From site based testing the following relevant material parameter were obtained:

- the mean friction angle μ_ϕ is equal to 38°;
- the standard deviation associated with the friction angle is 2.66°; and
- the median material density is 2700 kg/m³.

The approximated failure surface and problem geometry is shown in Figure 98.

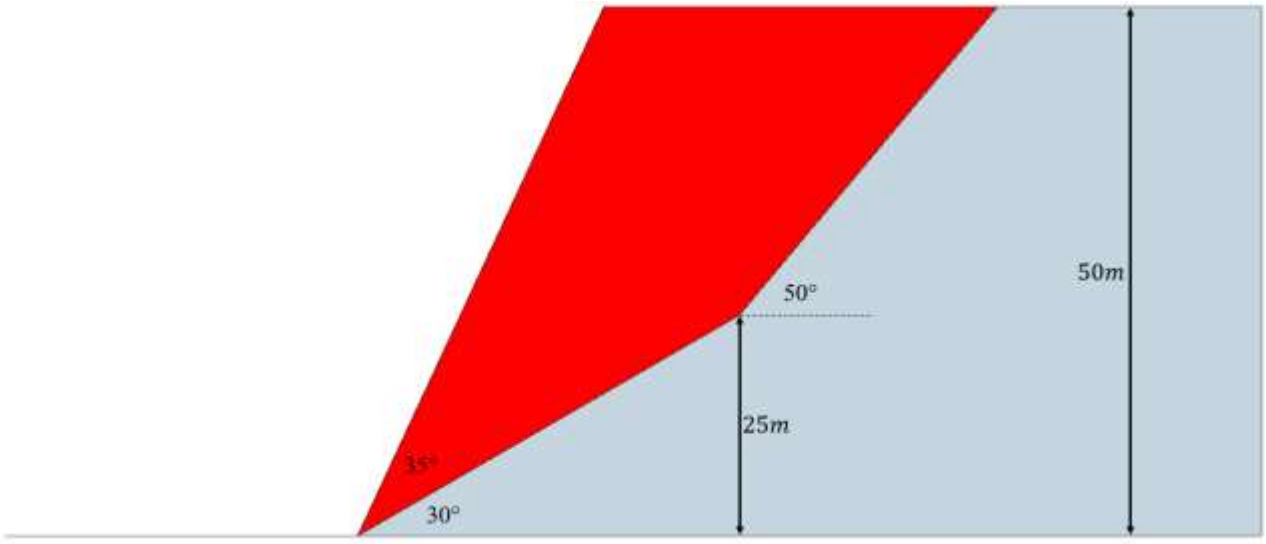

Figure 98 Example problem geometry

Using Equation 167, the slope's FOS is calculated as:

$$FOS = \frac{1040.91 \times 9.81 \times 2700 \times \tan(38°) \times \cos(30°) + 262.22 \times 9.81 \times 2700 \times \tan(38°) \times \cos(50°)}{1040.91 \times 9.81 \times 2700 \times \sin(30°) + 262.22 \times 9.81 \times 2700 \times \sin(50°)} \quad \text{Equation 216}$$

$$FOS = 1.16 \quad \text{Equation 217}$$

Using Equation 166, the POF then is given as:

$$POF = \frac{1}{2}\left[1 + \text{erf}\left(\frac{\sin(38°)\cos(38°)\,(1 - 1.16)}{\sqrt{2} \times 2.66° \times 1.16}\right)\right] = 7.47\% \quad \text{Equation 218}$$

which does not meet the design requirement of a maximum POF of 5%. For the above POF calculation, we have treated both linear segments as having the same random friction behaviour. An alternate interpretation that could be used is to treat each linear segment as having its own associated friction angle, which may be sufficient to keep the overall slope stable. To calculate the POF using this interpretation, first, we calculate the standard deviations σ_1 and σ_2 for surfaces 1 and 2 using Equation 173. The equivalent standard deviation of the linear combination is then calculated using Equation 172:

$$\sigma_1 = \sigma_2 = 2.66° \times \sec^2(38°) = 0.0748 \quad \text{Equation 219}$$

$$\sum_{i=1}^{2}\left(\frac{W_n \cos\theta_n}{W_1 \sin\theta_1 + \cdots + W_n \sin\theta_n}\sigma_i\right)^2 \quad \text{Equation 220}$$

$$= \left(\frac{1040.91 \times 9.81 \times 2700 \times \cos(30°)}{1040.91 \times 9.81 \times 2700 \times \sin(30°) + 262.22 \times 9.81 \times 2700 \times \sin(50°)} \times 0.0748\right)^2$$

$$+ \left(\frac{262.22 \times 9.81 \times 2700 \times \cos(50°)}{1040.91 \times 9.81 \times 2700 \times \sin(30°) + 262.22 \times 9.81 \times 2700 \times \sin(50°)} \times 0.0748\right)^2$$

$$= 0.009044$$

This then gives the following POF using Equation 175:

$$POF = \frac{1}{2}\left(1 + \text{erf}\left(\frac{1 - 1.16}{\sqrt{2 \times 0.009044}}\right)\right) = 4.62\% \quad \text{Equation 221}$$

Which does meet the desired POF. This raises some rather serious dilemmas as to which way should be used to truthfully calculate the slope's POF. If the stope was further subdivided, an even lower POF would be obtained, which would eventually reaches the limit distribution where POF = 100% for FOS less than 1, and 0% for any FOS greater than 1. What this means, is that if some input combination and problem geometry has a FOS greater than one, any POF can be obtained if the correct heterogeneity or scale interpretation is applied. A visual comparison between the resultant FOS POF relationships as a function of problem interpretation is shown in Figure 99.

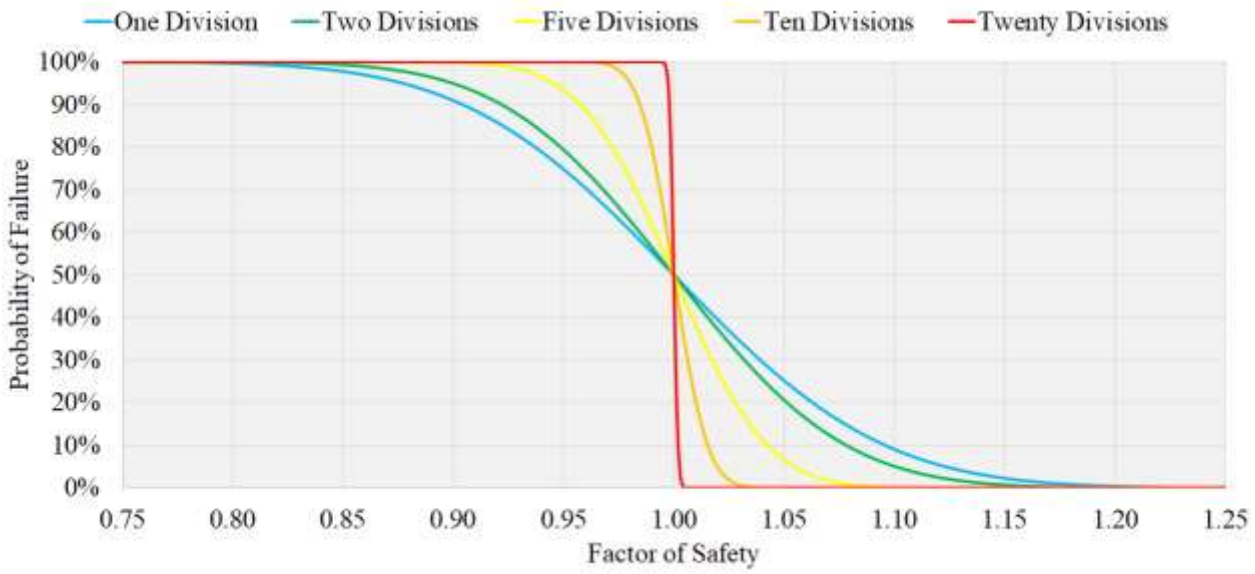

Figure 99 Factor of Safety Probability of Failure as a function of failure subdivisions

In order to meaningfully include scale effects and in turn calculate the POF, it needs to be known which material scale and heterogeneity interpretation is appropriate to use for a given problem. The issue with an 'open' problem such as slope stability analysis is that the critical volume or scale of interest is not well defined unlike a 'closed' problem such as an underground rock pillar where the volume of interest is the pillar volume. It is also expected that the appropriate scale of interest is both failure mode and failure surface dependent. For example, a piping failure in a tailings dam would require a much smaller volume of material to fail prior to total slope failure, compared to say sliding along a non-persistent joint set where a large portion of the discontinuous sections must shear before total failure occurs. The most intuitive measure of the scale of interest would relate to the critical volume or length of a failure surface that needs to fail before the overall slope to fail. This creates the issue that the particular failure surface and failure initiation point must be known prior to calculating the POF. The concept of a 'scale of interest' will need to be further researched due to the considerably large implications to probabilistic based slope designs.

6 Thesis Conclusions and Further Research Avenues

The aim of this Thesis was to explore the general relationship between Factor of Safety, Probability of Failure and problem scale. While the conclusions demonstrated that there is no general relationship between these factors, many significant contributions to the field of rock mechanics were made along the way. This Chapter outlines the major contributions and significant findings of this Thesis, as well as potential future research topics.

6.1 Significant Contributions and Main Findings

This Section summarises the significant contributions and the main findings associated with this Thesis. These findings have been grouped into each key Chapter.

6.1.1 Significant findings of Chapter Two

The initial starting point of this Thesis was to explore the notion that rock material parameters exhibit consistent universal behaviours. This Chapter focused primarily on demonstrating that Universal Distribution Functions exist and are suitably generalisable as to apply to any given rock problem at the laboratory scale. To date, no such large scale variability analysis has been completed on rock material parameters. The following main conclusions were presented:

Development of a general purpose non-parametric test methodology for quantifying Universal Distribution Functions. This non-parametric methodology presented allows for general quantification, comparison and manipulation of random data. While the application of this testing methodology within this Thesis focused on quantifying intact rock material parameters, this methodology can be used to generally compare and contrast non-parametric data.

Determined the existence of Universal Distribution Functions for laboratory scale material parameters and universal correlation coefficients. Universal Distribution Functions were shown to be an appropriate probabilistic model for laboratory scale material parameters. Universal correlation coefficients were also demonstrated to exist between many common laboratory material parameters. These universal probabilistic descriptions allow for consistent insights into the behaviour of rock at laboratory scales, as well as describe many documented phenomena.

Calculated the sampling error associated with each known Universal Distribution Function as a function of number. The number of test samples required to achieve a desired level of accuracy was derived for all deterministic and probabilistic material parameter components described by Universal Distribution Functions. These estimates can be used to ensure geotechnical data meets or exceeds the required level of accuracy.

Statistical proof as to why Uniaxial Compressive Strength, Point Load Test and Uniaxial Tensile Strength are linearly related. The universal probabilistic behaviour was able to provide a statistical explanation as to why a linear relationship is obtained between any pair of Uniaxial Compressive Strength, Point Load Testing and Uniaxial Tensile Strength measurements. While this derivation was able to show the existence of a linear relationship, it was unable to quantify the magnitude of the relationship.

Statistical proof as to why a curved relationship is apparent for Uniaxial Compressive Strength and Young's Modulus. A similar derivation used to demonstrate the linearity between intact strength measurements was able to demonstrate the nonlinear relationship between Uniaxial Compressive Strength and Young's Modulus. This relationship is typically assumed linear, as the curvature can be subtle.

New equation for the relationship between sonic velocity and Uniaxial Compressive Strength. Using Universal Distribution Functions and fundamental physics, a new equation relating sonic velocity measurements to the Uniaxial Compressive Strength of rock was presented. The applicability of this new Sonic Velocity model was compared to laboratory sonic velocity measurements and was able to replicate the laboratory data. This new relationship uses only measurable inputs and does not use empirical relationships.

Statistical evidence of downgrading strength parameters. Two commonly used deterministic 'downgrading' methods for Uniaxial Compressive Strength were replicated through statistical analysis. This statistical interpretation gives a mathematical justification for these otherwise empirical downgrading values.

6.1.2 Significant findings of Chapter Three

Chapter Three build on from the findings of Chapter Two and explores the possibility of extending Universal Distribution Functions to consider non-standard scales. This was achieved using stochastic heterogeneous numerical modelling. The following key findings were presented:

Development of PLACEBO. PLACEBO is a general purpose numerical homogenisation tool able to probabilistically quantify material parameter of intact rock at arbitrarily large scales, including material nonlinearities and material parameter correlations. This approach includes many complexities previously not implemented into stochastic numerical analysis. It was also demonstrated that PLACEBO could be used to calculate path dependant probabilities of failure for a single design.

Derived the closed form Universal Distribution Function for material density. The general probabilistic behaviour of dry density at arbitrarily large scales was mathematically derived as a function of volume. This probabilistic model is expected to be accurate for volumes greater than the laboratory scale, but decrease significantly in accuracy for volumes that approach the material's grain size.

Material parameter heterogeneity is the leading contributor of scale effects in rock. Localised zones of weakness within a larger volume dominate the failure process. It was numerically demonstrated that in order to obtain numerical results consistent with literature heterogeneous numerical models require the inclusion of stochastic effects for each relevant material parameter, selection of an appropriate constitutive model, and the inclusion of correlation coefficients between each material parameter. The inclusion of correlation coefficients was shown to be arguably the most important consideration when completing this style of numerical modelling. The inclusion of correlation coefficients was shown to change the simulated behaviour at scale by 30% for most material parameters. The inclusion of n-variate correlation coefficients has not been previously implemented in heterogeneous numerical modelling for rock.

Typical scaling laws from literature are reproducible numerically using PLACEBO - The scaling laws associated with Uniaxial Tensile Strength, Uniaxial Compressive Strength and elastic Young's Modulus were able to be reproduced numerically using PLACEBO. A negative scaling law was observed for Uniaxial Tensile Strength and Uniaxial Compressive Strength while a positive scaling law was observed for elastic Young's Modulus.

Probabilistic behaviour is reasonably consistent over increased scales. From a probabilistic perspective, the variability of material parameter at any scale was remarkably consistent, but sufficiently different to prevent a simple generalisation. The associated shape parameter for the elastic Young's Modulus for an arbitrary volume was developed, however the associated scale parameter must be specified on a case by case basis. These consistent probabilistic behaviours do hint that scale dependant generalisations for many material parameters may be possible, however physical testing results are required to better quantify the underlying relationship. The probabilistic behaviour associated with peak and residual friction angles produced statistically significant deviations from the initial input behaviours, in particular the probabilistic behaviour for the peak friction angle appears to be invariant of the initial input selection. The behaviour of residual friction angles also differ from their initial inputs but vary considerably on a case by case basis.

Intact failure at scale requires a complex failure model. From brittle failure of a Mohr Coulomb material, material behaviour at scale can be shown to exhibit complex failure. Among all simulated material types, failure at increased scales was shown to require the following complexities; a significant amount of plastic dilation must occur before the peak strength is reached, a friction hardening response between the peak and residual strengths, a cohesion softening response between the peak and residual strengths, and a nonlinear failure envelope when failure is not instantaneous. The fact that these complex failure models are used to simulate practical scale problems and were numerically reproduced without assumption suggests that they are the most appropriate failure response for rock at practical scales.

Stronger Estimates of Minimum Strength Approaches were demonstrated - Lowest bound approaches are often used in practical settings and are unjustifiably conservative. These conservative design philosophies neglect documented behaviours, in particular correlation and scale effects. By considering scale effects computed by PLACEBO in conjunction with the minimum shear strength approach, justifiably stronger shear strength parameters were obtained for practical designs. This new minimum approach is able to not only account for scaling laws and associated homogenisations but also considers material parameter correlations and stress dependencies in the final criterion. The minimum piece-wise approach derived produces the minimum possible shear strength over all possible stress paths experienced and is considerably stronger than previous lowest bound methods.

6.1.3 Significant findings of Chapter Four

Chapter Four explored the applicability of using fractal methods to derive the Universal Distribution Function and Universal Scale Functions for discontinuity roughness at arbitrary scales. This Chapter also looked at the potential of using existing mathematical theory in conjunction with heterogeneous modelling to derive a Universal Distribution Function associated with cross joint spacing in a bedded material. The following main conclusions were presented:

A theoretical model for the behaviour of discontinuities at arbitrary scales was presented. From an initial assumption that rocks exhibit fractal self-affine properties, a theoretical model was derived from using numerical simulations of Fractional Brownian Motion and non-parametric statistical techniques. This theoretical model predicted no apparent scaling law associated with discontinuity roughness, no homogenisation associated with increasing scale and a Weibull or Gumbel like Probability Density Function over all scales.

A new method of measuring discontinuity fractal characteristics was presented. A common research practice involves measuring discontinuity fractal characteristics by using complicated method routines. A simple method of estimating both the Hurst exponent and fractal dimension were presented using only Barton's length amplitude measurements. This new method was validated by estimating the Hurst exponent associated with Barton's standard roughness profiles and comparing them to fractal characteristics estimated by multiple authors. This new approach is capable of estimating a single fractal characteristic and accounts for differences between multiple measurements of a single discontinuity.

Evidence of the non-fractal nature of discontinuities at scale was presented. The theoretical scale behaviour was compared and contrasted against two different discontinuities with measurements scales ranging from 0.05m to 7.5m. The field measurements of discontinuity roughness demonstrated the non-fractal nature of discontinuities over most measured scales and the inability of the fractal model to produce the observed negative scaling law and associated homogenisation at increasing scales. These findings suggest that a purely fractal description of discontinuity roughness is not applicable at practical scales.

New relationships between fractal characteristics and Joint Roughness Coefficients were derived. A new relationship was derived relating fractal characteristics and Joint Roughness Coefficients. This new relationship was compared against Bandis' Scaling Law using the available field measurements of roughness and showed consistency in estimates of the scale dependant Joint Roughness Coefficient up to discontinuity lengths of 7.5m. This comparison with the well tested Bandis Scaling Law demonstrates the applicability and correctness of this new calculation method even at very large scales.

Cross joint spacing is expected to follow a gamma distribution. The simulation method used for cross joint spacing relied on the theory presented by Hobbs and simple heterogeneous simulations. The resulting output was able to provide a non-infinite fracture spacing at low stresses and suggested that the appropriate Probability Density Function family for cross joint spacing is a gamma distribution.

6.1.4 Significant findings of Chapter Five

Chapter five revisited the relationship between Factor of Safety and Probability of Failure using the findings in the previous three Chapters. The following key findings were presented:

Factor of Safety equations can be decomposed into individual contributions. It was demonstrated that most Factor of Safety equations could be decomposed into univariate contributions associated with each material parameter. This decomposition allows for the calculation of many closed form relationships between Factor of Safety and Probability of Failure. It was noted that the Barton Bandis shear strength criterion has no appropriate decomposition.

The completely generalised frictional Factor of Safety Probability of Failure relationship was derived. The relationship between Factor of Safety and Probability of Failure for an arbitrary frictional material and scale was derived for a number of cases. Relationships were presented for the typical case, a special case of an arbitrary failure bath through a homogenous material and the completely generalised case of an arbitrary path through an arbitrary number of materials. The resulting Factor of Safety Probability of Failure relationship was shown to be subtly positively skewed, a feature that is often not included in published relationships.

Several cases for tensile and cohesive Factor of Safety Probability of Failure relationships were derived. The relationship between Factor of Safety and Probability of Failure for tensile and cohesive components were derived for a number of cases. Relationships were presented for the typical case, a special case of an arbitrary failure bath through a homogenous material and a second special case of an arbitrary failure through a number of homogenous materials. The modified Erlang approximation used to derive the second special case was shown to be significantly more accurate compared to the currently implemented approximations. It was noted that the completely generalised relationship for tensile and cohesive components could not be computed without the use of numerical methods.

The completely generalised Factor of Safety Probability of Failure relationship was derived for Toppling. Two generalised relationships between Factor of Safety and Probability of Failure were presented for toppling failure. These relationships were based on a gamma distribution associated with cross joint spacing.

The relationship between Factor of Safety and Probability of Failure is not one to one. While the univariate relationships between Factor of Safety and Probability of Failure can be shown to be exact, when considering multiple contribution relationships the relationship is not one to one. The univariate Factor of Safety Probability of Failure relationships do form upper and lower bounds, which give an indication to the likely value. In order to calculate the case specific relationship, numerical methods are required. From a practical perspective, it is simpler to compute the case specific Factor of Safety and Probability of Failure using Monte Carlo Sampling.

The inclusion of scale effects bring into question the appropriate method of calculating the Probability of Failure. It was demonstrated that by changing the scale of interest or heterogeneity interpretation for a particular design, any desirable Probability of Failure could be calculated. The ability to justifiably change the calculated Probability of Failure raises some serious dilemmas as to how Probability of Failure should be meaningfully calculated for a given design.

6.2 Further Research Avenues

As this Thesis primarily dealt with the new concept of Universal Distribution Functions, there are an abundance of possible research topics that branch from the main findings. This section outlines possible future research topics associated with each key focus, as well as possible methods of assessment for each.

6.2.1 Further research avenues from Chapter Two

Incorporation of additional data to accept or refute the notion of Universal Distribution Functions. Although Universal Distribution Functions were shown to be statistically applicable based on the available testing database, their general applicability needs to be constantly validated. Incorporation of more geological data can be used to verify the general applicability of Universal Distribution Functions.

A better model for Poisson's Ratio, cohesion and residual friction. From the tested material parameters, the least understanding was associated with the aforementioned characteristics. Although reasonable approximations were presented, there is ample room to improve these approximations.

Assessment of additional rock parameters in terms of Universal Distribution Functions. There exist many more quantifiable rock parameters than what was explored in this Thesis. These additional rock parameters can easily be analysed using the non-parametric methodology presented in this Thesis to determine if there are viable Universal Distribution Functions approximations for other rock parameters.

An in depth study into the behaviour of material parameters over varying confinements. The probabilistic behaviour for a Mohr Coulomb material at varying confinements has only been postulated and needs physical validation for its appropriateness. The quantification of rock strength over varying confinement should also consider the Hoek Brown criterion as well in order to better understand the probabilistic behaviour of a generalised nonlinear criterion over varying confinements. This study should also look into how other material parameters, for example Young's Modulus or Poisson's Ratio, change as a function of varying confinement.

The implications of new material parameter estimates and their applications to empirical methods. Long standing empirical design methods (e.g., Rock Mass Rating, Q System and Mathew's Stability Method), which may have been initially calibrated with different deterministic estimates than the Mode value. The effectiveness of these new deterministic estimates and their applicability to these long standing empirical methods needs to be checked to ensure they provide consistent and safe design practices.

Is the ratio of Compressive Strength, Tensile Strength and Point Load Testing universal? What is the mechanism that controls this ratio? While it was possible to demonstrate that a linear relationship exists between the aforementioned material characteristics, the magnitude of this ratio is not specified. While guidelines do give estimates of this ratio, the question remains if the multiple estimates are a function of sampling error, or some inherent difference between rock types. This ratio could be assessed using the non-parametric statistical framework presented in this Thesis to more objectively validate its value. If the ratio between these parameters does fundamentally differ between lithologies, the extension would be to determine what mechanism or inherent property controls this ratio.

Comparisons between the presented sonic velocity relationship and more empirical evidence. Only a single database was evaluated using the new sonic velocity relationship presented in this Thesis. The comparison of this new relationship between sonic velocity and Uniaxial Compressive Strength to more data is required to test its general applicability.

6.2.2 Further research avenues from Chapter Three

Validation of the generalised dry density Universal Distribution Function. The appropriateness and accuracy of the generalised dry density Universal Distribution Function could not be verified during this Thesis. Validation of this probabilistic model is required.

Better measurement routines for plastic strain components for heterogeneous materials. More accurate plastic strain measurement routines are required for heterogeneous numerical modelling. Once developed, heterogeneous modelling methods such as PLACEBO could then be used to estimate the probabilistic strain dependencies as a function of scale.

Probabilistic quantification of material softening components. The assumed behaviour of probabilistic strain softening responses used while reasonable, are assumptions. Physical quantification of the probabilistic nature of material softening behaviours will lead to more accurate numerical predictions.

A better method of estimating Uniaxial Tensile Strength. The simulated uniaxial tensile strength is expected to be an overestimate of the actual tensile strength at scale. Development of new methods of estimating Uniaxial Tensile Strength will lead to more accurate numerical predictions.

Physical quantification of probabilistic material parameters at larger scales. The probabilistic behaviours at increased scales presented are based on numerical estimates. Probabilistically quantifying the material parameter behaviour over a large number of a-typical scales can be used to compare and contrast numerically predicted scale behaviours.

Quantification or estimation of material parameters at sub laboratory scales - PLACEBO operates at mesoscopic scales to bootstrap out the expected behaviour at macroscopic scales. While the inputs for this mesoscopic (laboratory) scale are well approximated, it stands to reason if microscopic material characteristics are modelled in PLACEBO, it should be able to numerically replicate the laboratory scale behaviour. Quantification and simulation of sub laboratory scales can be used to validate the initial Universal Distribution Function approximations, as well as provide a means to simulate rock from an even smaller initial starting scale.

Deriving a method of estimating the Universal Scale Function for a given material. From the completed analysis, it was apparent that no easily definable Universal Scale Function exists for rock parameters. In depth research into quantifying this underlying behaviour will aid in forward prediction and model synthesis of multi volume zone models.

6.2.3 Further research avenues from Chapter Four

A generalised probabilistic model for discontinuity roughness. The approach used in this Thesis was to derive the expected behaviour assuming a purely fractal-self affine model. It was demonstrated that this model is insufficient at describing discontinuities over a number of scales. Collecting physical discontinuity roughness measurements from a number of different discontinuities and scales can form an empirical database that can be assessed. It is suspected there is some underlying consistent behaviour that should be able to be determined form a sufficiently large database using the non-parametric framework presented in this Thesis. An empirically based description of discontinuity roughness at scale will allow for the development of mathematical or numerical methods that can truthfully describe discontinuities.

A method of simulating such discontinuity profiles. The discontinuity simulation methods used in this Thesis while very good, were insufficient at meaningly simulating large scale discontinuities. Once a better understanding of the expected behaviour of discontinuity roughness at scales is available, efforts can be made to numerically generate these surfaces. A method of routinely simulating large two or three dimensional discontinuity surfaces will be paramount for future geotechnical research.

An empirically based universal model for cross joint spacing. The approach used to quantify cross joint spacing in a bedded material proved problematic. An empirically based approach will be able to give further insights into the applicability of a gamma distribution to describe cross joint spacing. As mentioned in Chapter Four, this empirical approach does have some fundamental limitations, however it will be able to give some insight into important characteristics such as which Probability Density Function family is appropriate and general relationships between bed thickness and spacing characteristics.

6.2.4 Further research avenues from Chapter Five

Derivation of Factor of Safety Probability of Failure relationships for a wider range of failure mechanisms. The failure mechanisms explored in this Thesis do cover a wide range of cases, however this is not an exhaustive list. The incorporation of additional failure mechanisms, the incorporation of other attributes (e.g., pore water pressure) or support elements will lead to a wider range of applicable equations.

Defining the scale of interest. The scale of interest is an important concept when meaningfully calculating a slope's Probability of Failure. The issue with an 'open' problem such as slope stability analysis is that the critical volume or scale of interest is not well defined. It is expected that the appropriate scale of interest is both failure mode and failure surface dependent. For example, a piping failure in a tailings dam would require a much smaller volume of material to yield prior to total slope failure compared to say intact rock failure. An increased understanding of what an appropriate scale of interest is for slope designs is required in order to meaningfully quantify the Probability of Failure.

What are the influences of spatial correlations and variability? Rock material parameters, for example Uniaxial Compressive Strength often increase as a function of the depth below the surface. Does the inclusion of spatial correlations significantly change the Factor of Safety or Probability of Failure of a slope? Will the Probability of Failure for a failure surface change if the location of all weaker material parameters zones are known in advance? An increased understanding of the effects of spatial variability and correlations may aid in calculating more representative Factor of Safety and reduce over conservatism in slope design.

References

Abdellah, W, Mitri, H, Thibodeau, D & Moreau-Verlaan, L 2014. 'Stability of mine development intersections - a probabilistic analysis approach', *Canadian Geotechnical Journal*, vol. 51 no. 2 pp. 184-195.

Acar, E & Sun, L 2013. 'A generalised Kruskal-Wallis Test incorporating group uncertainty with application to genetic association studies', *Biometrics*, vol. 69, no. 2, pp. 427-435.

Al-Sahawneh, E 2013. 'Size effect and strength correction factors for normal weight concrete specimens under uniaxial compression stress', *Contemporary Engineering Sciences*, vol. 6, no. 1, pp. 57-68.

Amaral, P, Cruz Fernandes, J & Guerra Rossa, L 2008. 'Weibull statistical analysis of granite bending strength', *Rock Mechanics and Rock Engineering*, vol. 41, no. 6, pp. 917-928.

Annadhason, A, 2012. 'Methods of Fractal Dimension computation', *International Journal of Computer Science and Information Technology & Security*, vol. 2, no. 1, pp. 166-169.

Baecher, GB 1983. 'Statistical analysis of rock mass fracturing, *Journal of the International Association for Mathematical Geology*, vol. 15, no. 2, pp. 329-348.

Baecher GB & Christian, JT 2003, 'Reliability and statistics in geotechnical engineering', John Wiley Publications, Chichester.

Baecher, GB, Lanney, NA & Einstein, HH 1977, 'Statistical description of rock properties and sampling', Proceedings of the 18th U.S. Symposium on Rock Mechanics, pp. 1-8.

Bahaaddini, M 2014, 'Numerical study of the mechanical behaviour of rock joints and non-persistent jointed rock masses', PhD thesis, The University of New South Wales, Sydney.

Bandis, S, Lumsden, A & Barton, N 1981, ' Experimental studies of scale effects on the shear behaviour of rock joints', *International Journal of Rock Mechanics and Mining Sciences & Geomechanics Abstracts*, vol. 18, no. 1, pp. 1-21.

Barton, NR 1976. 'The shear strength of rock and rock joints', *International Journal of Rock Mechanics and Mining Sciences & Geomechanics Abstracts*, vol. 13, no. 9, pp. 255-279.

Barton, N 2013. ‘Shear strength criteria for rock, rock joints, rock fill and rock masses: Problems and some solutions’, *Journal of Rock Mechanics and Geotechnical Engineering*, vol. 5, no. 4, pp. 249-261.

Barton N 1982, ‘Modelling rock joint behaviour from in situ block tests: implications for nuclear waste repository design’. Office of Nuclear Waste Isolation ONWI-308: Columbus, OH; p. 96.

Barton, NR & Choubey, V 1977. ‘The shear strength of rock joints in theory and practice’, *Rock Mechanics and Rock Engineering*, vol. 10, no. 1, pp. 1-54.

Barton, NR & Pandey, SK 2011. ‘Numerical modelling of two stoping methods in two Indian mines using degradation of c and mobilization of ϕ based on Q-parameters’, *International Journal of Rock Mechanics and Mining Sciences & Geomechanics Abstracts*, vol. 48, no. 7, pp. 1095-1112.

Baumberger, T & Caroli, C 2006. ‘Solid friction from stick-slip down to pinning and aging’, *Advances in Physics*, vol. 55, no. 3, pp. 279-348.

Bažant, ZP 1999. ‘Size effect on structural strength: A review’, *Archive of Applied Mechanics*, vol. 69, no. 9, pp. 703-725.

Bažant, ZP 2008. ‘Mechanics based statistical prediction of structure size and geometry effects on safety factors for composites and other quasi-brittle materials’, *Theoretical and Applied Mechanics*, vol. 35, no. 1, pp. 53-71.

Bažant ZP & Le, J 2011. ‘Size effect on strength and lifetime probability distributions of quasibrittle structures’, *Sadhana*, vol. 37, no. 1, pp. 17-31.

Bieniaswski, ZT 1968. ‘The effect of specimen size on compressive strength of coal’, *International Journal of Rock Mechanics and Mining Sciences & Geomechanics Abstracts*, vol. 5, no. 4, pp. 325-326.

Bieniawski, ZT & Bernede MJ 1979. ‘Suggested methods for determining the uniaxial compressive strength and deformability of rock materials’, *International Journal of Rock Mechanics and Mining Sciences & Geomechanics Abstracts*, vol. 16, no. 2, pp. 138-140.

Bieniawsky, ZT & Hawkes, I 1978. ‘Suggested methods for determining tensile strength of rock materials - 1. Suggested method for determining direct tensile strength’, *International Journal of Rock Mechanics and Mining Sciences & Geomechanics Abstracts*, vol. 15, no. 3, pp. 99-103.

Bieniawski, ZT & Van Heerden, WL 1975. 'The significance of in-situ tests on large rock specimens', *International Journal of Rock Mechanics and Mining Sciences & Geomechanics Abstracts*, vol. 12, no. 4, pp. 101-113.

Borr-Brunetto, M, Carpinteri, A & Chiaia, B 1999. 'Scaling phenomena due to fractal contact in concrete and rock fractures', *International Journal of Fracture,* vol. 95, pp. 221-238.

Barton, NR 2013. 'Shear strength criteria for rock, rock joints, rockfill and rock masses: Problems and some solutions', *Journal of Rock Mechanics and Geotechnical Engineering*, vol. 5, no. 4, pp. 249-261.

Bauer, J & Paula, W 2000. 'Reliability with respect to settlement limit-states of shallow foundations on linearly-deformable subsoil', *Computers and Geotechnics*, vol. 26, no. 3, pp. 281-308.

Belem, T, Homand-Etienne, F & Souley, M 1997. 'Fractal analysis of shear joint roughness', *International Journal of Rock Mechanics and Mining Sciences & Geomechanics Abstracts*, vol. 34, no. 3, pp. 130 - 146.

Belem, T, Homand-Etienne, F & Souley, M 2000. 'Quantitative parameters for rock joint surface roughness', *Rock Mechanics and Rock Engineering*, vol. 33, no. 4, pp. 217-242.

Brook, N 1985. 'The equivalent core diameter method of size and shape correction in point load testing', *International Journal of Rock Mechanics and Mining Sciences & Geomechanics Abstracts*, vol. 22, no. 2, pp. 61-70.

Brooks, S 1998. 'Markov chain Monte-Carlo methods and its application', *Journal of the Royal Statistical Society Series D (the statistician),* vol. 47, no. 1, pp. 69-100.

Brown, SR 1987. 'A note on the description of surface roughness using fractal dimension', *Geophysical Research Letters,* vol. 14, no. 11, pp. 1095-1098.

Butel N, Hossack A & Kizil, MS 2014, 'Prediction of in situ rock strength using sonic velocity', Proceedings of the 14th Coal Operators Conference, pp. 89-102.

Canbulat, I 2010, 'Roadway roof support design in critical areas at Anglo American Metallurgical Coal's underground operations', Proceedings of the 10th Underground Coal Operator's Conference, pp. 50-72.

Carvajal, C, Peyras, L & Bacconnet C 2011. 'On the loading / shear strength coupling in the probabilistic formulation on the limit state in shear for gravity dams', *European Journal of Environmental and Civil Engineering*, vol. 14, no. 3, pp. 283-301.

Chandong, C, Zoback, MD & Khaksar, A 2006. 'Empirical relations between rock strength and physical properties in sedimentary rocks', *Journal of Petroleum Science and Engineering*, vol. 51, no. 3, pp. 223-237.

Cheng, J & Druzdzel, M 2000, 'Latin Hypercube sampling in Bayesian networks', Proceedings of the Florida AI Research Society Conference, pp. 287-292.

Chiwaye, H 2010. 'A comparison of the limit equilibrium and numerical modelling approaches to risk analysis for open pit mine slopes', MPhil thesis, University of the Witwatersrand, Johannesburg.

Christian, J & Baecher, G 1999. 'The point estimate method as numerical quadrature', *Journal of Geotechnical and Geoenvironmental Engineering*, vol. 125, no. 9, pp. 779-786.

Coulson, JH 1970. 'The effects of surface roughness on the shear strength of joints in rock', PhD thesis, University of Urbana, Illinois.

Daniels, HE 1945. 'The statistical theory of the strength of bundles of threads', Proceedings of the Royal Society of London. Series A, *Mathematical and Physical Sciences*, vol. 183, no. 995, pp. 405-435.

Dehkordi, A 2008, '3D Finite Element Cosserat continuum simulation of layered geomaterials', PhD thesis, University of Toronto, Toronto.

Department of Minerals and Energy – Western Australia, 1999. Geotechnical Considerations in Open Pit Mines – Guidelines.

Dieker T 2002. 'Simulation of Fractional Brownian Motion', Masters thesis, Vrije University, Amsterdam.

DuFour, J, Farhat, A, Gardiol, L & Khalaf, L 1998. 'Simulation-based finite sample normality tests in linear regression', *Econometrics Journal*, vol. 1, no. 1, pp 154-173.

Efron, B 1979. 'Bootstrap methods: Another look at the jackknife', *The Annals of Statistics*, vol. 7, no. 1, pp. 1-26.

Einstein, HH, Veneziano, D, Baecher, GB & O'Reilly, KJ 1983. 'The effect of discontinuity persistence on rock slope stability', *International Journal of Rock Mechanics and Mining Sciences & Geomechanics Abstracts*, vol. 20, no. 5, pp. 227-236.

Fardin, N 2003. 'The effect of scale on the morphology, mechanics and transmissivity of single rock fractures', PhD thesis, Royal Institute of Technology, Stockholm.

Fattahi, H, Shojaee, S, Ebrahimi Farsangi, MA & Mansouri, H 2013. 'Using Latin Hypercube sampling based on the ANN-HPSOGA model for estimation of the creation probability of damaged zone around underground spaces', *International Journal of Optimisation in Civil Engineering*, vol. 3, no. 3, pp. 389-408.

Fellenius, W 1936. 'Calculation of the stability of earth dams', Proceedings of the 2nd congress on large dams, vol. 4, pp. 445-463.

Fenton, GA & Griffiths, DV 2003. 'Bearing-capacity prediction of spatially random c-ϕ soils', *Canadian Geotechnical Journal*, vol. 40, no. 1, pp. 54-65.

Ficker, T 2017. 'Fractal Properties of Joint Roughness Coefficients', *International Journal of Rock Mechanics and Mining Sciences*, vol. 94, pp. 27-31.

Fisher, R 1922. On the interpretation of X^2 from contingency tables, and the calculation of P, *Journal of the Royal Statistical Society*, vol. 85, pp. 57-94.

Fisher ARA. Biometrika Trust Frequency Distribution of the Values of the Correlation Coefficient in Samples from an Indefinitely Large Population Published by : Oxford University Press on behalf of Biometrika Trust Stable URL : http://www.jstor.org/stable/2331838 Accessed : 20-06-2016 01 : 04 UTC. 2016;10(4):507-521.

Franklin, JA et al. 1985. 'Suggested method for determining point load strength', International *Journal of Rock Mechanics and Mining Sciences & Geomechanics Abstracts*, vol. 22, no. 2, pp. 51-60.

Fredlund, DG 1984. 'Analytical methods for slope stability analysis' Proceedings of the 4th international symposium on landslides, state of the art, pp. 229-250.

Friedman J. On Multivariate Goodness–of–Fit and Two–Sample Testing. http//www.slac.stanford. edu/econf C. 2004:1-3. doi:10.2172/826696.

Gao, FQ & Kang, HP 2016. ‘Effects of pre-existing discontinuities on the residual strength of rock mass- Insight from a discrete element method simulation’, *Journal of Structural Geology*, vol. 85, pp. 40-50.

Gao, FQ, Stead, D & Kang, HP 2014. ‘Numerical investigation of the scale effect and anisotropy in the strength and deformability of coal’, *International Journal of Coal Geology*, vol. 136, pp. 25-37.

Giacomini, A, Buzzi, O & Krabbenhoft, K 2008. ‘Modelling the asperity degradation of a sheared rock joint using FEM’, Proceedings of the 8th World Congress on Computational Mechanics and the 5th European Congress on Computational Methods in Applied Sciences and Engineering, Venice, Italy.

Ge, Y, Tang, H, Ez Eldin, MAM, Wang, L, Wu, Q & Xiong, C 2017. ‘Evolution process of natural rock joint roughness during direct shear tests’, *International Journal of Geomechanics*, vol. 17, no. 5, pp. 1-10.

Gill, DE, Corthésy, R & Leite, MH 2005. ‘Determining the minimal number of specimens for laboratory testing of rock properties’, *Engineering Geology*, vol. 78, no. 2, pp. 29-51.

Glass, GV, Peckham, PD & Sanders, JR 1972. ‘Consequences of failure to meet assumptions underlying the fixed effect analysis of variance and covariance’, *Review of Educational Research*, vol. 42, no. 3, pp. 237-288.

Goodman, RE & Bray, J 1976, ‘Toppling of rock slopes’, Proceedings of the speciality conference rock engineering for foundations and slopes, pp. 201-234.

Goodman, RE & Shi G 1985. ‘Block theory and its application to rock engineering’, Prenticle-Hall Inc, Englewood Cliffs, New Jersey.

Goodman, RE, Talyor, RL & Brekke TL 1968. ‘A model for the mechanics of fractured rock’, *Journal of the soil mechanics and foundations division*, vol. 94, pp. 637-660.

Goldstein, M, Goosev, B, Pyrogovsky, N, Tulinov, R & Turovskaya, A 1966, ‘Investigations of mechanical properties of cracked rock’ Proceedings of the 1st Congress of the Society of Rock Mechanics, Lisbon, pp. 521-524.

Griffith, AA 1921. ‘The phenomena of rupture and flow in solids’, Philosophical Transactions of the Royal Society. Series A, *Mathematical, Physical and Engineering Sciences,* vol. 221, no. 582, pp. 163-198.

Griffiths, DV, Fenton, GA & Tveten, DE 2002. ‘Probabilistic geotechnical analysis: how difficult does it need to be?’, Proceedings of the international conference on probabilististics in geotechnics, pp. 3-20.

Guarascio, M & Oreste, P 2012. ‘Evaluation of the stability of underground rock pillars through a probabilistic approach’, *American Journal of Applied Science,* vol. 9, no. 8, pp. 1273-1282.

Gumede, TR & Stacey, H 2007. ‘Measurement of typical joint characteristics in south African gold mines and the use of these characteristics in the prediction of rock falls’, *Journal of the Southern African Institute of Mining and Metallurgy,* vol. 107, no. 5, pp. 335-344.

Guohua, S 1994. ‘Joint roughness characterization and effect of rockiness on peak shear strength of joints’, PhD thesis, The University of Arizona, Arizona.

Hajiabdolmajid, V, Kaiser, PK & Martin, CD 2002. ‘Modelling brittle failure of rock’, *International Journal of Rock Mechanics and Mining Sciences,* vol. 39, no. 6, pp. 731-741.

Hammah, R and Yacoub, T, 2009. ‘Probabilistic slope analysis with the Finite Element Method’, Proceedings of the 43rd U.S Rock Mechanics Symposium and 4th US-Canada Rock Mechanics Symposium, Asheville, NC, 28th June – 1st July 2009.

Hampel, FR 1974. ‘The influence curve and its role in robust estimation’, *Journal of the American Statistical Association,* vol. 69, no. 346, pp. 383-393.

Harding, B, Tremblay, C & Cousineau, D, 2014. ‘Standard errors: A review and evaluation of standard error estimators using Monte Carlo simulations’, *Tutorials in Quantitative Methods for Psychology,* vol. 10, no. 2, pp. 107-123.

Hawkins, AB 1998. ‘Aspects of rock strength’, *Bulletin of Engineering Geology and the Environment,* vol. 57, no. 1, pp. 17-30.

Helton, JC & Davis, DJ 2003. ‘Latin Hypercube sampling and the propagation of uncertainty in analyses of complex systems’, *Reliability Engineering & System Safety,* vol. 81, no. 1, pp. 23-69.

Hoek, E & Bray, JW 1981, Rock slope engineering, 3rd edn, The Institute of Mining and Metallurgy, London.

Hoek, E & Brown, ET 1980, 'Empirical strength criterion for rock masses', *Journal of Geotechnical Engineering Division*, vol. 106, no. GT9, pp. 1013–1035.

Hoek, E & Brown ET 1988. 'The Hoek-Brown failure criterion - a 1988 update', Proc. 15th Canadian Rock Mechanics Symposium, pp. 31-38.

Hoek, E, Carranza-Torres, C & Corkum, B 2002. 'Hoek-Brown criterion – 2002 edition'. Proc. NARMS-TAC Conference, Toronto, pp. 267-273.

Hoek, E & Marinos, P 2007. 'A brief history of the development of the Hoek-Brown failure criterion', *Solids and Rocks*, no.2.

Hoek, E & Martin, CD 2014. 'Fracture initiation and propagation in intact rock - A review', *Journal of Rock Mechanics and Geotechnical Engineering*, vol. 6, no. 4, pp. 287-300.

Hobbs, DW 1967. 'The formation of tension joints in sedimentary rocks: An explanation', *Geological Magazine*, vol. 104, no. 6, pp 550-556.

Hormazabal, E, Rovira, E, Walker, M & Carranza-Torres, C 2009. 'Analysis and design of slopes for Rajo Sur, an open pit mine next to the subsidence crater or El Teniente mine in Chile'. Proc. Slope Stability 2009, 9 – 11 September Santiago, Chile.

Hoskin, T 2009. 'Parametric and Nonparametric: Demystifying the Terms', Mayo Clinic Department of Health Sciences. Available from http://www.mayo.edu/mayo-edu-docs/center-for-translational-science-activities-documents/berd-5-6.pdf accessed 16 September 2015.

Hustrulid, WA 1975. 'A review of coal pillar strength formulas', *Rock Mechanics and Rock Engineering*, vol. 8, no. 2, pp. 115-145.

Idris, MA, Saiang, D & Nordlund, E 2012. 'Consideration of the rock mass property variability in numerical modelling of open stope stability', Bergmakanikdag 2012: 12/03/2012 - 12/03/2012.

Iman, RL & Conover, WJ 1980. 'Small sample sensitivity analysis techniques for computer models, with an application to risk assessment', *Communications in Statistics - Theory and Methods*, vol. 9, no. 17, pp. 1749-1842.

Irigaray, C, El Hamdouni, R, Jiménez-Perálvarez, JD, Fernández, P & Chacón, J 2012. 'Spatial stability of slope cuts in rock massifs using GIS technology and probabilistic analysis', *Bulletin of Engineering Geology and the Environment*, vol. 71, no. 3, pp. 569-578.

Itasca Consulting Group, Inc. 2014, UDEC — Universal Distinct Element Code, Ver. 6.0. Minneapolis: Itasca.

Itasca Consulting Group, Inc. 2014, PFC — Particle Flow Code, Ver. 5.0. Minneapolis: Itasca.

Jang, BA, Jang, HS & Park, HJ 2006. 'A new method for determination of joint roughness coefficient' Proceedings of IAEG, Paper number 95.

Javankhoshdel, S & Bathurst, RJ 2014. 'Simplified probabilistic slope stability design charts for cohesive and cohesive-frictional (c-ϕ) soils' *Canadian Geotechnical Journal*, vol. 51, no. 9 pp. 1033-1045.

Jefferies, M, Lorig, L & Alvares, C 2008. 'Influence of rock strength spatial variability on slope stability, Proceedings of the 1st International FLAC/DEM Symposium on Numerical Modelling, Minneapolis.

Jang, Y, Li, B & Tanabashi, Y 2006. 'Estimating the relation between surface roughness and mechanical properties of rock joints', *International Journal of Rock Mechanics and Mining Sciences*, vol. 43, no. 6, pp. 837-846.

Johansson, F 2016. 'Influence of scale and matedness on the peak shear strength of fresh, unweathered rock joints', *International Journal of Rock Mechanics and Mining Sciences*, vol. 82, pp. 36-47.

Kalita, K & Rajbongshi, P 2014. 'Variability characterisation of input parameters in pavement performance evaluation', *Road Materials and Pavement Design*, vol. 16, no. 1, pp. 172-185.

Karakus, M, Liu, Y, Zhang, G & Tang, H 2016. 'A new shear strength model incorporating influence of infill materials for rock joints', *Geomechanics and Geophysics for Geo-Energy and Geo-Resources*, vol. 2, no. 3, pp. 183-193.

Karami, A & Stead, D 2008. 'Asperity degradation and damage in the direct shear test: A hybrid FEM/DEM approach', *Rock Mechanics and Rock Engineering*, vol. 41, no. 2, pp. 229-266.

Kim, BH, Cai, M, Kaiser, PK & Yang, HS 2007. 'Estimation of block sizes for rock masses with non-persistent joints', *Rock Mechanics and Rock Engineering*, vol. 40, no. 2, pp. 169-192.

Kim, H & Mission, JL 2011. 'Probabilistic evaluation of economical factor of safety for the geotechnical design of pile axial load capacity', *KSCE Journal of Civil Engineering*, vol. 15, no. 7, pp. 1167-1176.

Krahn, J & Morgenstern NR 1979. 'The ultimate frictional resistance of rock discontinuities', *International Journal of Rock Mechanics and Mining Sciences & Geomechanics Abstracts*, vol. 16, no. 2, pp. 127-133.

Kroese, DP & Botev, ZI 2014. 'Spatial process generation', In: V. Schmidt (Ed.). Lectures on Stochastic Geometry, Spatial Statistics and Random Fields, Volume II: Analysis, Modelling and Simulation of Complex Structures, Springer-Verlag, Berlin. arXiv: 1308.0399.

Krumbholz, M, Hieronymus, C, Burchardt, S, Troll, V, Tanner, D & Friese, N 2014. 'Weibull-distributed dyke thickness reflects probabilistic character of host-rock strength', *Nature Communications*, 5:3272.

Kruskal, W & Wallis, W 1952. 'Use of ranks in one-criterion variance analysis', *American Statistical Association*, vol. 47, no. 260, pp. 583-621.

Kuehn, GA, Schulson, EM, Jones, DE & Zhang, J 1992. 'The compressive strength of ice cubes of different sizes', Proc. OMAE Conf., Vol. IV, ASME, pp. 349-356.

Kulatilake P 1986. 'Bivariate normal distribution fitting on discontinuity orientation clusters', *Mathematical Geology*, vol. 18, no. 2, pp. 181-195.

Kulatilake, PHS, Chen, J, Teng, J, Pan, G & Shufang, X 1995. 'Discontinuity network modelling of the rock mass around a tunnel close to the proposed permanent shiplock area of the three gorges dam site in China', Proceedings of the 35th U.S. Rock Mechanics Symposium, pp. 807-812.

Kulatilake, PHSW, Um, J & Pan, G 1997. 'Requirements for accurate estimation of fractal parameters for self-affine roughness profiles using the line scaling method', *Rock Mechanics and Rock Engineering*, vol. 30, no. 4, pp. 181-206.

Kumar, R, Bhargava, K & Choudhury, D 2017. 'Correlations of uniaxial compressive strength of rock mass with conventional strength properties through random number generation', *International Journal of Geomechanics*, vol. 17, no. 2, pp. 1-9.

Kveldsvik, V, Nilsen, B, Einstein, H & Nadim, F 2008. 'Alternative approaches for analyses of a 100,000 m3 rock slide based on barton-bandis shear strength criterion', *Landslides*, vol. 5, no. 2, pp. 161-176.

Kwašniewski M & Wang J 1993. 'Application of laser profilometry and fractal analysis to measurement and characterization of morphological features of rock fracture surfaces', *Géotechnique*, pp. 163-176.

Lacey DW 2015. 'Assessment of some engineering properties and testing methods of residual soil and highly weathered rock materials in QLD, Australia', PhD thesis, The University of Queensland, Brisbane.

Lanaro, F 2001. 'Geometry, mechanics and transmissivity of rock fractures', PhD. thesis, The Royal Institute of Technology, Stockholm.

Lambert, C & Coll, C 2009. 'A DEM approach to rock joint strength estimate'. *Journal of Rock Mechanics and Geotechnical Engineering*, vol. 6, no. 1, pp. 1-12.

Laubscher, DH 1990. 'A geomechanics classification system for the rating of rock mass in mine design', *Journal of the South African Institute of Mining and Metallurgy*, vol. 90, no. 10, pp. 257-273.

Laubscher, D. H. & Jakubec, J. 2001. The MRMR rock mass classification for jointed rock masses. In: Hustrulid, W. A. & Bullock, R. L. (eds.) Underground Mining Methods: Engineering Fundamentals and International Case Histories. Littleton, CO: Society for Mining, Metallurgy and Exploration.

Lazzari, E 2013. 'Analysis of shear strength of rock joints with PFC2D', Masters Thesis, Royal Institute of Technology, Stockholm.

Lee, HS, Park, YJ, Cho, TF & You, KH 2001. 'Influence of asperity degradation on the mechanical behaviour of rough rock joints under cyclic shear loading', *International Journal of Rock Mechanics and Mining Sciences*, vol. 38, no. 7, pp. 967-980.

Lee, YH, Carr, JR, Barr, DJ & Haas, CJ 1990. 'The fractal dimension as a measure of the roughness of rock discontinuity profiles', *International Journal of Rock Mechanics and Mining Sciences & Geomechanics Abstracts*, vol. 27, no. 6, pp. 453-464.

Li, Y & Huang, R 2015. 'Relationship between joint roughness coefficient and fractal dimension of rock fracture surfaces', *International Journal of Rock Mechanics and Mining Sciences*, vol. 75, pp. 15-22.

Li, Y, Oh, J, Mitra, R & Canbulat, I 2017. 'A fractal model for the shear behaviour of large-scale opened rock joints', *Rock Mechanics and Rock Engineering*, vol. 50, no. 1, pp. 67-79.

Lim, SS & Martin, CD 2010. 'Core disking and its relationship with stress magnitude for Lac du Bonnet granite', *International Journal of Rock Mechanics and Mining Sciences*, vol. 47, no. 2, pp. 254-264.

Liu, HY 2004. 'Numerical modelling of the rock fragmentation process by mechanical tools', PhD thesis, Lulea University of Technology, Lulea.

Lobbestael, J, Athanasopoulos-Zekkos, A & Colley, J 2013. 'Factor of Safety reduction factors for accounting for progressive failure for earthen levees with underlying thin layers of sensitive solids', *Mathematical Problems in Engineering*, vol. 2013, Article ID 893602, 13 pages.

Lobo-Guerrero, S & Vallejo, LE 2006. 'Application of Weibull Statistics to the tensile strength of rock aggregates', *Journal of Geotechnical and Geoenvironmental Engineering*, vol. 132, no. 6, pp. 786-790.

Lorig, L 2015. Personal communication.

Lu, C & Xie, H 1995. 'A physical limit of Weibull Modulus in rock fracture, *International Journal of Fracture*, vol. 72, pp. 55-58.

Maerz NH & Franklin JA 1990. 'Roughness scale effect and fractal dimension'. In Proceedings of the first International Workshop on Scale Effect in Rock Masses, Leon, Amsterdam, pp. 121-125.

Malinverno, A 1990. 'A simple method to estimate the fractal dimension of a self-affine series', *Geophysical Research Letters*, vol. 17, no. 11, pp. 1953-1956.

Mandelbrot B. B. 1982. The Fractal Geometry of Nature, W.H. Freeman and Company New York.

Maheshwari, P, Valadkar, M & Venkatesham, E 2009. 'A new probabilistic approach for analysis of compressive strength test data of rock specimens', *Geomechanics and Geoengineering: An International Journal*, vol. 4, no. 2, pp. 163-169.

Manteufel, R 2000, 'Evaluating the convergence of Latin Hypercube Sampling', Proceedings of the 41st structures, structural dynamics and materials conference and exhibit.

Marsland, A 1971. 'The use of in-site tests in a study of the effects of fissures on the properties of stiff clays', Proc. First Aust. - N.Z. Conf. on Geomechanics, Melbourne, vol. 1, pp. 180-189.

Martin, CD & Chandler, NA 1994. 'The progressive fracture of Lac du Bonnet granite', *International Journal of Rock Mechanics and Mining Sciences & Geomechanics Abstracts*, vol. 31, no. 6, pp. 643-659.

Martin, CD, Christiansson, R & Soderhall, J 2001. 'Rock stability considerations for siting and constructing a KBS-3 repository', Technical Report TR-01-38, Swedish Nuclear Fuel and Waste Management Company, Stockholm.

Masoumi, H 2013. 'Investigation into the mechanical behaviour of intact rock at different sizes', PhD thesis, The University of New South Wales, Sydney.

Mas Ivars, D, Pierce, ME, Darcel, C, Reyes-Montes, J, Potyondy, PO, Young RP & Cundall, PA 2011. 'The synthetic rock mass approach for jointed rock mass modelling', *International Journal of Rock Mechanics and Mining Sciences*, vol. 48, no. 2, pp. 219-244.

Meemum, P 2014. 'Shear strength testing of rock fractures under constant normal load and constant normal stiffness as affected by displacement rates'. Masters thesis, Suranaree University of Technology, Thailand.

Mehotcheva, T, 2008. The Kruskal-Wallis Test, Seminar in Methodology and Statistics Linguistics Research - University of Groningen, Netherlands 23rd April 2008.

Metropiolis, N & Ulam, S 1949. 'The Monte Carlo method', *Journal of the American Statistical Association*, vol. 44, no. 247, pp. 335-341.

Metya, S & Bhattacharya, G 2014. 'Probabilistic critical slip surface for earth slopes based on the first order reliability method', *Indian Geotechnical Journal*, vol. 44, no. 3, pp. 329-340.

Miller, LH 1956. 'Table of percentage points of Kolmogorov statistics', *Journal of the American Statistical Association,* vol. 51, no. 273, pp. 111-121.

Minh, T & Le, H 2014. 'Reliability of heterogeneous slopes with cross-correlated shear strength parameters', *Georisk: Assessment and Management of Risk for Engineered Systems and Geohazards*, vol. 8, no. 4, pp. 250-257.

Mogi, K 1962. 'The influence of the dimensions of specimens on the fracture strength of rocks', Bull. Earthquake Res. Inst., 40(1962), 175-185 13th International Conference on Fracture June 16–21, 2013, Beijing, China.

Montgomery DC & Runger GC 2014. Applied statistics and probability for engineers -6th edition. Wiley Publishing, New Jersey.

Moore, D & McCabe, G 2006. Introduction to the Practice of Statistics- 6th Edition W.H.Freeman, New York.

Morelli, GL 2014. 'On joint roughness: Measurements and use in rock mass characterization', *Geotechnical and Geological Engineering*, vol. 32, no. 2, pp. 345-362.

Motulsky, H, 2007. Prism 5 Statistics Guide, GraphPad Software Inc., San Diego CA, www.graphpad.com.

Mumby, PJ 2002. 'Statistical power of non-parametric tests: A quick guide for designing samples strategies', *Marine Pollution Bulletin*, vol. 44, no. 1, pp. 85-87.

Myers, NO 1962. 'Characterisation of surface roughness', *Wear*, vol. 5, no. 3, pp. 182-189.

Nakamura, H, Gu, W, Tajima, S & Hazama, O 2015. 'Automated fracture mechanics and fatigue analyses based on three-dimensional finite elements', *Journal of Pressure Vessel Technology*, vol. 137, no. 6, Paper no. PVT-14-1170.

Nazir, R, Momeni, E, Armaghani, DJ & Amin, MF 2013. 'Correlation between unconfined compressive strength and indirect tensile strength of limestone rock samples', *Electronic Journal of Geotechnical Engineering*, vol. 18, no. 1, pp. 1737-1746.

Nejati, HR, Ghazvinian, A, Moosavi, SA & Sarfarazi, V 2014. 'On the use of the RMR system for estimation of rock mass deformation modulus', *Bulletin of Engineering Geology and The Environment*, vol. 73, no. 2, pp. 531-540.

Norton, RM 1984. 'The double exponential distribution: using calculus to find a Maximum Likelihood Estimator', *The American Statistician,* vol. 38, no. 2, pp. 135-136.

Pang, SD, Bažant, ZP & Le, JL 2008. 'Statistics of strength of ceramics: finite weakest-link model and necessity of zero threshold', *International Journal of Fracture,* vol. 154, no. 1, pp. 131-145.

Park, HJ, Um, JG, Woo, I & Kim, JW 2012. 'The evaluation of the probability of rock wedge failure using the point estimate method', *Environmental Earth Sciences,* vol. 65, no. 1, pp.353-361.

Park, JW & Song, JJ 2009. 'Numerical simulation of a direct shear test on a rock joint using a bonded-particle model', *International Journal of Rock Mechanics and Mining Sciences,* vol. 46, no. 8, pp. 1315-1328.

Pearce, H 2001. 'Experimental and analytical investigation into the shear behaviour of rock joints', PhD thesis, Monash University, Melbourne.

Perras, MA & Diederichs, MS 2014. 'A review of the tensile strength of rock: Concepts and testing', *Geotechnical and Geological Engineering,* vol. 32, no. 2, pp. 525-546.

Petrik, T, Hrubesova, E & Mohyla, M 2014. 'The use of stochastic simulation method latin hypercube sampling in the study of the response of soil exposed to dynamic load', Proceedings of the SGEM2014 Geoconference, vol. 2, pp. 971-978.

Pierce, M, Gadia, M and DeGagne, D, 2009. Estimation of rock block strength, RockENG09, proceedings of the 3rd CANUS rock Mechanics Symposium, Toronto, May 2009.

Poulsen, BA, Adhikary, DP, Elmouttie, MK & Wilkins, A 2015. 'Convergence of synthetic rock mass modelling and the Hoek-Brown strength criterion', *International Journal of Rock Mechanics and Mining Sciences,* vol. 80, pp. 171-180.

Pratt, HR, Black, AD, Brown WS & Brace, WF 1972. 'The effect of specimen size on the mechanical properties of unjointed diorite' *International Journal of Rock Mechanics and Mining Sciences & Geomechanics Abstracts,* vol. 9, no. 4, pp. 513-516.

Pula, W & Zaskorski, L 2014. 'Estimation of the probability distribution of the random bearing capacity of cohesionless soil using the random finite element method', *Structure and Infrastructure Engineering: Maintenance, Management, Life-Cycle Design and Performance,* vol. 11, no. 5, pp. 707-720.

Rabinovitch, A, Bahat, D & Greenber, R 2012. 'Statistics of joint spacing in rock layers', *Geological Magazine*, vol. 149, no. 6, pp. 1065-1076.

Ramachandran, K & Tsokos, C 2009. Mathematical Statistics with Applications. Academic Press: Elsevier.

Razali, NM, Yap, BW 2011. 'Power comparisons of Shapiro Wilk, Kolmogorov Smirnov, Lillefors and Anderson Darling tests', *Journal of Statistical Modelling and Analytics*, vol. 2, no. 1, pp. 21-33.

Rienstra SW & Hirschberg A 2009. 'An introduction to acoustics', Eindhoven University of Technology, Eindhoven.

Robertson, AM 1977. 'The determination of the stability of slopes in jointed rock with particular reference the determination of strength parameters and mechanics of failure', PhD thesis, University of Witwatersrand, Johannesburg.

Rousseeuwm PJ & Croux C 1993. 'Alternatives to the Median Absolute Deviation', *Journal of the American Statistical Association*, vol. 88, no. 424, pp. 1273-1283.

Rosenblueth, E 1975. 'Point estimates for probability moments', Proceedings of the National Academy of Sciences of the United States of America, vol. 72, no. 10, pp. 3812-3814.

Rosenblueth, E 1981. 'Two-point estimates in probabilities', *Applied Mathematical Modelling*, vol. 5, no. 5, pp. 329-335.

Rusnak J & Mark, C 2000. 'Using the Point Load Test to determine the Uniaxial Compressive strength of coal measure rock', 19th Int Conf Gr Control Mining, 8-10 August. 2000, pp. 362-371.

Ruffolo, RM & Shakoor, A 2009. 'Variability of unconfined compressive strength in relation to number of test samples', *Engineering Geology*, vol. 108, no. 1, pp. 16-23.

Ruofeng, Q & Guangli, X 2013. 'Application of Rosenblueth method to stability analysis of abandoned mine spoil slope', *Electronic Journal of Geotechnical Engineering*, vol. 18, pp. 2133-2142.

Russelli, C 2008. 'Probabilistic methods applied to the bearing capacity problem', PhD thesis, University of Stuttgart, Stuttgart.

Sainsbury, BL, Pierce, M & Mas Ivars D 2008. 'Analysis of caving behaviour using a synthetic rockmass (SRM)–ubiquitous joint rock mass (UJRM) modelling technique'. In: Potvin Y, Carter J, Dyskin A, Jeffrey R, editors. Proc1st S Hemisphere Int Rock Mech Symp, vol. 1. Australia:Perth;2008, pp. 243–53.

Sanei M, Faramarzi L, Goli S, Fahimifar A, Rahmati A & Mehinrad A 2015. 'Development of a new equation for joint roughness coefficient (JRC) with fractal dimension: a case study of Bakhtiary Dam site in Iran', *Arabian Journal of Geosciences,* vol. 8, no. 1, pp. 465-475.

Saliba, A, Saliba, F, Panitz, J, Figueiredo, R & Duarte, F 2014. 'A probabilistic Assessment of open-pit slope failures in the post-closure phase', Proceedings of Mine closure solutions 2014.

Saroglou, H & Tsiambaos, G 2008. 'A modified Hoek-Brown failure criterion for anisotropic intact rock', *International Journal of Rock Mechanics and Mining Sciences,* vol. 45, no. 2, pp. 223-234.

Seidel, JP & Haberfield, CM 1995. 'Towards an understanding of joint roughness', *Rock Mechanics and Rock Engineering,* vol. 28, no. 2, pp. 69-92.

Shapiro, SS & Wilk, MB 1965. 'An analysis of variance test for normality (complete samples)', *Biometrika,* vol. 52, no. 3, pp. 591-611.

Sharma, KG & Pande, GN 1988. 'Stability of rock masses reinforced by passive, fully grouted rock bolts', *International Journal of Rock Mechanics and Mining Sciences,* vol. 25, no. 8, pp. 273-285.

Shen, H 2012. 'Non-deterministic analysis of slope stability based on numerical simulation', PhD thesis, Technische Universität Bergakademie Freiberg, Freiberg.

Shrivastava, AK, Rao, KS & Rathod, GW 2012. 'Numerical simulation of direct shear test on rock joint', GeoCongress 2012: State of the Art and Practice in Geotechnical Engineering. Oakland, California.

Singh, MM 1981. Chapter 5: Strength of rock. In Y.Touloukian, W. R. Judd & R. Roy (Eds.), Physical properties of rock and minerals, Vol. II-2 (pp.83–121). New York: McGraw-Hill.

Simon, R & Deng D 2009. 'Estimation of scale effects of intact rock using dilatometer tests results', In proceeding of 62nd Canadian Geotechnical Conference, Halifax, pp. 481-488.

Sjoberg, J 1996. 'Large scale slope stability in open pit mining – a review', division of rock mechanics Lulea university of technology Sweden.

Srivastava, A 2012. ‘Spatial variability modelling of geotechnical parameters and stability of highly weathered rock slopes’, *Indian Geotechnical Journal*, vol. 42, no. 3, pp. 179-185.

Stacey, P 2009. ‘Fundamentals of Slope Design’ in JR Read and P Stacey, P (eds.) 2009. Guidelines for open pit slope design. CSIRO Publishing.

Stephens, MA 1974. ‘EDF statistics for goodness of fit and some comparisons’ *Journal of the American Statistical Association*, vol. 69, no. 347, pp. 730-737.

Strouth, A & Eberhardt, E 2009. ‘Integrated back and forward analysis of rock slope stability and rockslide runout at Afternoon Creek, Washington’, *Canadian Geotechnical Journal*, Vol. 46, pp. 1116-1132.

Sullivan, TD, Duran, A & Eggers MJ 1992. ‘The use and abuse of oriented core in open pit mine design’, Proceedings of The Third Large Open Pit Mining Conference Mackay, 30 August-3 September 1992, pp 387 - 395.

Tang, CA, Liang, ZZ, Zhang, YB, Chang, X, Tao, X, Wang, DG, Zhang, JX, Liu, JS, Zhu, WC & Elsworth, D 2008. ‘Fracture spacing in layered materials: A new explanation based on two-dimensional failure process modelling’, *American Journal of Science*, vol. 308, no. 1, pp. 49-72.

Tatone, BSA & Grasselli, G 2010. ‘A new 2D discontinuity roughness parameter and its correlation with JRC’, *International Journal of Rock Mechanics and Mining Sciences*, vol. 47, no. 8, pp. 1391-1400.

Tatone, BSA & Grasselli, G 2013. ‘An investigation of discontinuity roughness scale dependency using high-resolution surface measurements’, *Rock Mechanics and Rock Engineering*, vol. 46, no. 4, pp. 657-681.

Terbrugge, P, Wesseloo, J, Venter, J & Steffens, O 2006, ‘A risk consequence approach to open pit slope design’, *Journal of the South African Institute of Mining and Metallurgy*, vol. 106, pp. 503-514.

Thuro, K, Plinninger, R, Zah, S & Schuts, S 2001. ‘Scale effects in rock strength properties. Part 1: Unconfined compressive test and Brazilian test’, in ISRM Regional Symposium Eurock 2001 – Rock mechanics a challenge for society, pp. 169-174.

Tse, R 1979. ‘Strength of rough rock surfaces in shear’, PhD thesis, University of Alberta, Alberta.

Tse, R & Cruden, DM 1979. 'Estimating joint roughness coefficients', *International Journal of Rock Mechanics and Mining Sciences & Geomechanics Abstracts*, vol. 16, no. 5, pp. 303-307.

Turk, N, Greig, MJ, Dearman, WR & Amin, FF 1987. 'Characterisation of rock joint surfaces by fractal dimension', In Proceedings of the 28th U.S. Symposium on Rock Mechanics, Tucson, Balkema, Rotterman, pp. 1223-1236.

Um, J 1997. 'Accurate quantification of rock joint roughness and development of a new peak shear strength criterion for joints', Ph.D. thesis, The University of Arizona, Arizona.

Vakili, AM, Albrecht, J & Sandy, M 2014. 'Rock Strength Anisotropy and its importance in Underground Geotechnical Design', AusRock 2014: Third Australasian Ground Control in Mining Conference, Paper Number 035.

Valley, B & Duff, D 2011. 'Probabilistic analyses in Phase2 8.0', Rocscience <http://www.rocscience.com/library/rocnews/spring2011/Phase2stat-Probabilistic-Analyses-in-Phase2.pdf>.

Valley, B, Kaiser, P & Duff, D 2010. 'Consideration of uncertainty in modelling the behaviour of underground excavations', Proceedings of the 5th international seminar on deep and high stress mining, pp. 423-436.

Vantanpour, N, Ghafoori, M & Talouki, H 2014. 'Probabilistic and sensitivity analyses of effective geotechnical parameters on rock slope stability: a case study of an urban area in northeast Iran', *Natural Hazards*, vol. 71, no. 3, pp. 1659-1678.

Van Hecke, T 2012. 'Power study of ANOVA vs Kruskal-Wallis test', *Journal of Statistics and Management Systems*, vol. 15, no. 2, pp. 241-247.

Van Mier, JGM 1986. 'Multiaxial strain-softening of concrete', *Materials and Structures*, vol. 19, no. 3, pp. 190-200.

Van Vliet, MRA & Van Mier, JGM 2000. 'Experimental investigation of size effect in concrete and sandstone under uniaxial tension', *Engineering Fracture Mechanics*, vol. 65, no.2, pp. 165-188.

Villaescusa, E & Brown ET 1992. 'Maximum likelihood estimation of joint size from trace length measurements', *Rock Mechanics and Rock Engineering*, vol. 25, no. 2, pp. 67-87.

Wakabayashi N & Fukushige I 1992, 'Experimental study on the relation between fractal dimension and shear strength', In: Proceedings of the international symposium for fractured and joint rock masses. Berkeley: California, pp. 101-110.

Walsh, JE 1962, 'Handbook of Nonparametric Statistics', New York: D.V. Nostrand.

Wei, MY, Liu, HH, Li, CH & Wang, EY 2013. 'A fractal-based model for fracture deformation under shearing and compression', *Rock Mechanics and Rock Engineering*, vol. 46, no. 6, pp. 1539-1549.

Weibull, WA 1951. 'A statistical distribution function of wide applicability', *Journal of Applied Mechanics*, vol. 18, no. 1, pp. 293-297.

Weiss, J, Girard, L & Amitrano, D 2013. 'Size effects on compressive strength from a statistical physics perspective', Proceedings of the 13th International Conference on Fracture 13th international conference on fracture, Paper 6.

Whitman, RV 1984, 'Evaluating calculated risk in geotechnical engineering', *Journal of Geotechnical Engineering*, vol. 110, no. 2, pp. 143-188.

Wiles, TD 2006. 'Reliability of numerical modelling predictions', *International Journal of Rock Mechanics and Mining Sciences*, vol. 43, no. 2, pp. 454-472.

Wong, TF, Wong, RHC, Chau, KT & Tang, CA 2006. 'Microcrack statistics, Weibull distribution and micromechanical modelling of compressive failure in rock', *Mechanics of Materials*, vol. 38, no. 7, pp. 664-681.

Wyllie, D & Mah, C 2004, Rock Slope Engineering - Civil and Mining, 4th edn, Taylor & Francis group, London and New York.

York, G, Canbulat, I and Jack, B, 2000. Coal Pillar Design Procedures, Safety in Mines Research Advisory Committee, CSIR Mining Technology, Project Number COL 337.

Young, DS 1987. 'Indicator kriging for unit vectors: Rock joint orientations', *Mathematical Geology*, vol. 19, no. 6, pp. 481-501.

Zadhesh, J, Jalali, SME & Ramezanzadeh, A 2014. 'Estimation of joint trace length probability distribution function in igneous, sedimentary and metamorphic rocks', *Arabian Journal of Geosciences*, vol. 7, no. 6, pp. 2353-2361.

Zengchao, F, Yangsheng, Z & Dong, Z 2009. 'Investigating the scale effects in strength of fractured rock mass', *Chaos, Solitons & Fractals*, vol. 41, no. 5, pp. 2377-2386.

Zhang, H, Zhao, Y & Li, C 2010. 'Probabilistic slope stability analysis based on the upper bound theorem', Presented at the 2010 international conference on E-product E-service & E-entertainment (ICEEE).

Zhang, Q, Zhu, H, Zhang, L & Ding, X 2011. 'Study of scale effect on intact rock strength using particle flow modelling', *International Journal of Rock Mechanics and Mining Sciences*, vol. 48, no. 8, pp. 1320-1328.

Zhang, Y, Stead, D & Elmo, D 2015. 'Characterisation of strength and damage of hard rock pillars using a synthetic rock mass method', *Computers and Geotechnics*, vol. 65, pp. 56-72.

Zhang, Y & Zhao X 2016. 'Characterisation of confinement effect on jointed rock pillars using a synthetic rock mass approach', *International Journal for Numerical and Analytical Methods in Geomechanics*, vol. 40, no. 12, pp. 1690-1711.

Zhao, YG & Ono, T 2000. 'New point estimates for probability moments', *Journal of Engineering Mechanics*, vol. 126, no. 4, pp. 433-436.

Zhu, WC 2008. 'Numerical modelling of the effect of rock heterogeneity on dynamic tensile strength', *Rock Mechanics and Rock Engineering*, vol. 41, no. 5, pp. 771-779.

Appendix - Rock Testing Database Summary

Uniaxial Compressive Strength database summary

Main Rock Type	Sample Count	Average UCS
Sedimentary	158	41.31
Sedimentary	155	38.76
Sedimentary	88	24.71
Sedimentary	84	10.15
Sedimentary	74	27.37
Sedimentary	39	24.39
Sedimentary	34	156.26
Sedimentary	30	9.87
Sedimentary	27	23.47
Sedimentary	23	25.89
Sedimentary	22	29.03
Sedimentary	19	4.22
Sedimentary	17	164.55

Sedimentary	15	4.07
Sedimentary	15	17.06
Sedimentary	14	79.07
Sedimentary	13	14.73
Sedimentary	12	14.37
Sedimentary	11	24.27
Sedimentary	11	18.48
Sedimentary	10	135.10
Sedimentary	8	14.92
Sedimentary	8	74.23
Sedimentary	7	13.90
Sedimentary	5	65.26
Sedimentary	5	170.40
Sedimentary	5	184.64
Igneous	73	120.22

igneous	62	105.00
Igneous	23	110.27
Igneous	12	94.58
Igneous	10	113.25
Igneous	10	131.12
Metamorphic	24	182.35
Metamorphic	13	150.46
Metamorphic	8	195.00
Metamorphic	8	194.00
Metamorphic	8	191.33
Metamorphic	8	146.25
Metamorphic	7	165.86
Metamorphic	7	240.50

Point Load Database Summary

Main Rock Type	Sample Number	Average Point Load Index
Sedimentary	157	0.50
Sedimentary	100	2.59
Sedimentary	26	1.23
Sedimentary	22	2.20
Sedimentary	13	5.19
Sedimentary	12	1.45
Sedimentary	9	0.79
Igneous	464	0.99
Igneous	279	1.20
Igneous	228	6.51
Igneous	206	0.46
Igneous	191	3.65
Igneous	139	0.61

Igneous	118	2.70
Igneous	109	4.01
Igneous	100	2.53
Igneous	83	5.85
Igneous	43	5.49
Igneous	35	4.03
Igneous	34	1.23
Metamorphic	152	4.73
Metamorphic	33	2.30
Metamorphic	26	3.60
Metamorphic	14	3.38
Metamorphic	11	7.52
Metamorphic	10	2.74
Metamorphic	8	4.76
Only Logging code known	21	0.58

Only Logging code known	14	7.34
Only Logging code known	11	0.44
Only Logging code known	6	1.07
Only Logging code known	4	2.11
Only Logging code known	4	3.22
Only Logging code known	4	0.17

Tensile Strength database summary

Main Rock Type	Sample Number	Average Tensile Strength
Sedimentary	24	2.60
Sedimentary	16	5.92
Sedimentary	10	16.46
Sedimentary	11	11.36
Sedimentary	9	2.84
Sedimentary	9	1.66
Sedimentary	7	2.35
Sedimentary	7	10.71
Sedimentary	6	8.66
Sedimentary	5	1.17
Sedimentary	5	13.40
Igneous	42	12.65
Igneous	13	11.37

Igneous	8	8.04
Igneous	5	12.58
Igneous	5	23.45
Igneous	5	11.89
Metamorphic	12	15.28
Metamorphic	8	9.96
Metamorphic	8	16.30

Dry density database summary

Main Rock Type	Sample Number	Average Density
Sedimentary	158	2.43
Sedimentary	88	2.42
Sedimentary	84	2.32
Sedimentary	53	2.11
Sedimentary	44	2.03
Sedimentary	39	2.41
Sedimentary	34	2.57
Sedimentary	31	2.87
Sedimentary	27	2.30
Sedimentary	24	2.17
Sedimentary	19	1.27
Sedimentary	18	1.68
Sedimentary	15	2.22

Sedimentary	14	2.37
Sedimentary	13	2.28
Sedimentary	13	2.80
Sedimentary	13	2.68
Sedimentary	12	2.55
Sedimentary	10	2.55
Sedimentary	10	2.73
Sedimentary	8	2.16
Sedimentary	8	2.75
Sedimentary	8	2.60
Sedimentary	6	2.63
Sedimentary	6	2.49
Igneous	84	2.75
igneous	46	2.59
Igneous	23	2.67

Igneous	15	2.81
Igneous	10	2.77
igneous	7	1.85
Metamorphic	12	2.63
Metamorphic	8	2.73
Metamorphic	5	3.32
Metamorphic	5	2.78

Elastic parameter database summary

Main Rock Type	Sample Count	Average Young's modulus	Average Poisson's Ratio
Sedimentary	158	15.03	0.11
Sedimentary	155	11.65	0.27
Sedimentary	88	7.14	0.17
Sedimentary	84	5.16	0.10
Sedimentary	74	7.75	0.27
Sedimentary	39	7.63	0.16
Sedimentary	27	5.71	0.11
Sedimentary	23	26.54	0.10
Sedimentary	22	6.84	0.28
Sedimentary	19	1.52	0.05
Sedimentary	15	2.17	0.10
Sedimentary	13	2.98	0.13
Sedimentary	11	24.82	0.08

Sedimentary	11	5.73	0.30
Sedimentary	8	3.00	0.14
Sedimentary	7	12.30	0.04
Sedimentary	7	70.70	0.08
Sedimentary	5	46.78	0.07
Igneous	62	37.06	0.14
Igneous	43	67.80	0.31
Igneous	12	57.32	0.13
Igneous	12	66.85	0.18
Igneous	10	62.47	0.17
Igneous	8	71.71	0.14
Metamorphic	8	58.61	0.27
Metamorphic	5	72.38	0.29
Metamorphic	5	75.50	0.29

Friction database summary

Main Rock Type	Sample Numbers	Average Peak friction	Average Residual friction
Sedimentary	76	31.26	-
Sedimentary	27	21.54	-
Sedimentary	6	31.30	-
Sedimentary	5	27.40	-
Sedimentary	8 samples, for 6 different preparations	29.03 - 36.52	33.51 - 38.01
Sedimentary	7 samples, for 6 different preparations	26.95 - 34.77	23.95 - 35.52
Sedimentary	6 samples, for 6 different preparations	33.89 - 36.90	34.47 - 38.29
Sedimentary	7 or 9 samples, for 6 different preparations	22.91 - 35.30	29.48 - 33.38
Sedimentary	7 and 8	29.69 - 31.21	30.93 - 31.35
Sedimentary	7 samples, for 6 different preparations	28.43 - 31.97	29.59 - 32.69
Sedimentary	4 samples for 3 different preparations and 2 loading styles	33.50 - 43.00	-
Igneous	13	22.35	-

Igneous	4 samples for 3 different preparations and 2 loading styles	30.50 - 38.06	-
Igneous	7 samples, for 6 different preparations	24.39 - 32.38	31.00 - 35.92
Igneous	7 samples, for 4 different preparations	30.18 - 32.22	31.36 - 34.87
Igneous	7 samples, for 6 different preparations	28.45 - 34.83	35.57 - 37.44
Metamorphic	7 samples, for 6 different preparations	22.97 - 29.54	24.96 - 33.70